



HAL
open science

Coupled temperature and strain rate effects on non-linear mechanical behaviour of amorphous polymers: Experimental characterisation and modelling of strain rate-temperature superposition

Carlos Federico

► **To cite this version:**

Carlos Federico. Coupled temperature and strain rate effects on non-linear mechanical behaviour of amorphous polymers: Experimental characterisation and modelling of strain rate-temperature superposition. Materials. Université Paris sciences et lettres, 2018. English. NNT : 2018PSLEM009 . tel-02096837

HAL Id: tel-02096837

<https://pastel.hal.science/tel-02096837>

Submitted on 11 Apr 2019

HAL is a multi-disciplinary open access archive for the deposit and dissemination of scientific research documents, whether they are published or not. The documents may come from teaching and research institutions in France or abroad, or from public or private research centers.

L'archive ouverte pluridisciplinaire **HAL**, est destinée au dépôt et à la diffusion de documents scientifiques de niveau recherche, publiés ou non, émanant des établissements d'enseignement et de recherche français ou étrangers, des laboratoires publics ou privés.

THÈSE DE DOCTORAT

de l'Université de recherche Paris Sciences et Lettres
PSL Research University

Préparée à MINES ParisTech

Coupled temperature and strain rate effects on non-linear mechanical
behaviour of amorphous polymers. Experimental characterisation and
modelling of strain rate-temperature superposition

Effets couplés de la température et de la vitesse de déformation sur le
comportement mécanique non-linéaire des polymères amorphes.

Caractérisation expérimentale et modélisation de la superposition vitesse
de déformation-température

Ecole doctorale n°364

Science Fondamentales et Appliquées

Spécialité Mécanique Numérique et Matériaux

Soutenue par Carlos Eloy FEDERICO
le 18 Juin 2018

Dirigée par **Noëlle BILLON**
Jean-Luc BOUVARD



COMPOSITION DU JURY :

Mme Julie DIANI
Ecole Polytechnique, France. Rapporteur

M. John SWEENEY
University of Bradford, UK. Rapporteur

M. Fabrice PIERRON
University of Southampton, UK. Président
du jury

M. Aurélien MAUREL PANTEL
Laboratoire de Mécanique et
d'Acoustique, France. Membre du jury

M. Jean-Luc BOUVARD
MINES ParisTech, France. Membre du
jury

Mme Noëlle BILLON
MINES ParisTech, France. Membre du
jury

Acknowledgments

First of all, I would like to thank my supervisors Noëlle Billon, Jean-Luc Bouvard and Christelle Combeaud for their constant support during the thesis. You gave me the opportunity for coming to France to do research and also helped me to growth as a person and as a professional. I will be always grateful for your trust and help. It was a real pleasure to work with you. Additionally, I want to express my sincere gratefulness to the members of my PhD committee, Julie Diani, John Sweeney, Fabrice Pierron and Maurel-Pantel. Thank you for your time, feedback and interesting discussions. Also, I want to show my gratitude to Pierre Gérard from Arkema for providing us with the material used in this PhD and for the interesting talks we had about the matter.

Next, I would like to thank several people from the staff of CEMEF. Thanks to Gilbert Fiorucci and Christophe Pradille, who were always willing to help me during my time performing experimental testing. Thank you also for the nice talks and laughs. I want to thank Marc Bouyssou and Arnaud Pignolet, for helping me in every aspect related to sample preparation and machine modifications. I also want to thank Romain Castelani, for his advises and help concerning rheological testing. Next, I want to thank Marie-Françoise for her attention in every administrative matter and for being so sweet and cheerful.

I want to thank the people who helped me to stablish at my arrival at Nice: Charles, Gwendal, Julien, Soline and Maha. Thank you for welcoming me in the French Riviera and for your friendship. I would also like to thank my international friends, Danae, José Antonio, Luca, Ghalia, Shitij, Carlos, Charazade, Wafa, Gabriel, Marie-Agathe, Dmitri, Margaux and Grégoire. Thank you for all the laughs, funny talks, cultural exchanges, support and beautiful time. Your friendship is something valuable that I will always carry with me. Special thanks to my dear Venezuelans friends, Victor, José, Luis, Miren, Rubén, Geraldine and Laura. You always made my days happier, more relaxed and cheerful. You also allowed me to have a part of our beloved country in my heart. You are all family to me.

I would like to acknowledge my family, more especially to my grandparents for all the love they give me and for teaching me the fundamentals and ethics that allowed me to overcome the challenges during my life. Thanks to my uncles Carlos and Eloy, my aunt Milena for all their support, love and care.

Finally, I want to thank my two pillars, my mother Maria Daniela and my beloved Juliana. Thank you for the unconditional love, for your advices, for your support and for cheering me up. Your presence along these three years was fundamental for succeeding in this PhD. You always gave me strength when I needed the most and made me believe it was possible. I have no words to express my gratitude. I love you.

Content

| | | |
|-------|------------------------------------------------------------------------------------------------------------------|----|
| 1 | INTRODUCTION..... | 1 |
| 1.1 | Project framework | 2 |
| 1.1.1 | General approach | 3 |
| 2 | Material and methodology | 8 |
| 2.1 | Material | 8 |
| 2.1.1 | Material description | 9 |
| 2.1.2 | Glass transition temperature of the different polymers..... | 10 |
| 2.2 | General methodology | 13 |
| 2.2.1 | Linear viscoelastic domain tests | 13 |
| 2.2.2 | Large strain tests using Digital Image Correlation | 17 |
| 2.2.3 | Parameters identification: Inverse analysis..... | 26 |
| 2.3 | Summary..... | 27 |
| 3 | Linear viscoelastic domain on PMMA..... | 31 |
| 3.1 | Isotropy validation | 31 |
| 3.2 | Introduction to Secondary transitions in PMMA and influence on T_{α} | 31 |
| 3.3 | Results and Discussions | 33 |
| 3.3.1 | Mechanical relaxations on the investigated PMMA..... | 33 |
| 3.3.2 | Viscoelastic zones of PMMA | 37 |
| 3.3.3 | Time/temperature superposition principle on PMMAs with different molecular weight and cross-linking degree | 39 |
| 3.4 | Summary..... | 49 |
| 4 | Mechanical Behaviour of PMMAs at Large Deformation: Coupling of Temperature/Strain Rate Effects | 53 |
| 4.1 | Importance of non-monotonic mechanical tests..... | 54 |
| 4.2 | Effect of the temperature and strain rate on the mechanical behaviour of polymers | 55 |
| 4.2.1 | Temperature effect..... | 55 |
| 4.2.2 | Strain rate effect..... | 56 |
| 4.3 | First approaches on extrapolating the time/temperature superposition temperature at large deformation..... | 57 |
| 4.4 | Topological effects on the mechanical behaviour of polymers | 63 |
| 4.5 | Results and Discussions | 65 |

| | | |
|-------|--------------------------------------------------------------------------------------------------------------------------|-----|
| 4.5.1 | Global mechanical response | 65 |
| 4.5.2 | Effect of the temperature on PMMA | 67 |
| 4.5.3 | Effect of the strain rate on PMMA | 69 |
| 4.5.4 | Coupling the temperature/strain rate effect at large deformations: Equivalent strain rate at reference temperature | 71 |
| 4.5.5 | Stress state effect on the mechanical response | 85 |
| 4.5.6 | Molecular Weight and Cross-linking Effect on the Mechanical Response at Large Deformation..... | 89 |
| 4.6 | Summary..... | 95 |
| 5 | Modelling of the Mechanical Behaviour of PMMA with Different Molar Mass and Crosslinking Degree | 99 |
| 5.1 | Literature review on the modelling of mechanical response of polymers | 100 |
| 5.1.1 | Phenomenological models | 100 |
| 5.1.2 | Physically based models | 100 |
| 5.1.3 | Combining phenomenological and physical approaches | 102 |
| 5.1.4 | Summary..... | 107 |
| 5.2 | Viscohyperelastic modelling | 107 |
| 5.2.1 | Model definition | 107 |
| 5.2.2 | Internal state variables evolution | 111 |
| 5.2.3 | Model summary..... | 113 |
| 5.2.4 | 1D Case: Incompressible visco-hyperelastic model..... | 113 |
| 5.3 | Results and Discussions | 115 |
| 5.3.1 | Relevance of the model..... | 116 |
| 5.3.2 | Physical contribution of each branch on the overall mechanical response..... | 124 |
| 5.3.3 | Role of the branches when varying the equivalent strain rate..... | 126 |
| 5.3.4 | Dependence of the EV's parameters with the equivalent strain rate | 131 |
| 5.3.5 | Sensitivity to the material parameters..... | 135 |
| 5.4 | Summary..... | 137 |
| 6 | Conclusions and Perspectives | 138 |
| 6.1 | General Conclusions | 138 |
| 6.2 | Perspectives..... | 140 |
| 7 | BIBLIOGRAPHY..... | 142 |
| 8 | APENDIX..... | 153 |

| | | |
|-----|-------------------------------------------------------------------------------------------------------------------------------|-----|
| 8.1 | Digital Image Correlation | 153 |
| 8.2 | Estimation of the stress correction factor, C_s | 156 |
| 8.3 | Piecewise function for describing shift factors on PMMA 3500 | 159 |
| 8.4 | Experimental validation of the equivalent strain rate for macroscopic load-unload tensile tests on PMMA 93 and PMMA 120 | 159 |
| 8.5 | Edward-Vilgis model in function of the principal stretch ratios | 161 |
| 8.6 | 3D Constitutive modelling..... | 161 |
| 8.7 | Strain energy function derivatives..... | 169 |
| 8.8 | Model parameters for uniaxial tensile loading..... | 170 |
| 8.9 | Parameters Evolution | 172 |

CHAPTER I

INTRODUCTION

This Chapter present the motivation of this project and introduce the general approach employed in this PhD.

The motivation of the project comes from the need of finding a strategy to reduce the number of mechanical testing needed to properly characterize the mechanical behaviour of amorphous polymers. In this context, the present work propose to extrapolate the time-temperature superposition principle from the linear viscoelastic domain to the large of deformation domain by using the so-called “equivalent strain rate at reference temperature”. The next step is to use the experimental data to calibrate constitutive model developed at “Centre de Mise en Forme des Matériaux” and verify the capabilities of this model in describing the mechanical behaviour of the material.

Ce chapitre présente la motivation de ce projet et introduit l'approche générale utilisée dans ce doctorat.

La motivation de ce projet vient du besoin de trouver une stratégie pour réduire le nombre des essais mécaniques nécessaires pour caractériser correctement le comportement mécanique des polymères amorphes. Dans ce contexte, le présent travail a proposé d'extrapoler le principe de superposition temps-température du domaine viscoélastique linéaire aux grandes déformations en utilisant ce que l'on appelle la "vitesse de déformation équivalent à la température de référence". L'étape suivante consiste à utiliser les données expérimentales pour calibrer le modèle constitutif développé au Centre de Mise en Forme des Matériaux et à vérifier les capacités de ce modèle à décrire le comportement mécanique du matériau.

CHAPTER I

1 INTRODUCTION

Polymer materials have a mix of good mechanical properties and low density, making them attractive for numerous applications. For instance, they are found in everyday use products as cups, food packaging, plastic bottles, adhesives, automotive parts, phone's components and others. To take advantage of these materials, it is of main interest to understand and to predict how the mechanical behaviour will vary with the polymer nature and use conditions. Indeed, mechanical properties are ruled by the mobility of the polymer chains, which is greatly affected by temperature, loading rate, entanglement density and other factors. More especially, mechanical behaviour strongly changes near the glass transition temperature, T_g . Thus, the final performance of these materials is strongly sensitive to their intrinsic properties and also to the thermomechanical environment they are subjected, making the prediction of their mechanical properties a challenging task.

In this context, constitutive equations can be used to model the mechanical behaviour of the polymer when deformed under specific conditions. This allows predicting the final properties of the desired product. So as to successfully model the mechanical behaviour of polymers, the evolution of internal parameters (entanglements, secondary bonds and others) needs to be accounted in the material model. Therefore, we need to somehow address how the polymer internal parameters change with the deformation, temperature and strain rate and to establish a link with the final mechanical properties.

To understand how external factors affect the internal parameters and mechanical behaviour of polymers, mechanical testing is performed at the conditions of interest. For example, tensile uploading-unloading tests can be performed at different temperatures and strain rates to link the stress-strain curves to physical mechanisms. However this is a highly challenging task specially when near T_g and its rubbery state. An example is shown in Figure 1.1 a) for cyclic tensile tests performed on a poly(methyl methacrylate). We can see that the mechanical response changes considerably depending on the temperature and strain rate.

Additionally, Figure 1.1 b) displays a cyclic tensile test on two poly(methyl methacrylate) at constant set of temperature/strain rate but with different architecture (in this case different molar mass). We can see that the curves are significantly different, revealing that the macroscopic mechanical response also depends of the chain architecture of the polymer.

This variety of results shows that polymers behaviour has a coupled dependency on strain rate and temperature as well as a strong sensitivity to its architecture (molar mass or other as

crosslinks). Indeed, the polymer mechanical behaviour combines several features as elastoplasticity, viscoplasticity, viscoelasticity, hyperelasticity, strain hardening, softening and viscohyperelasticity. Under the same conditions, a polymer may display a mix of these behaviours without a clear threshold between them, which means that characterization and modelling of mechanical behaviour of polymers is a challenging task.

At this point, we find ourselves with different problematics. From the experimental aspect, we have a highly coupled mechanical response that depends on the temperature, strain rate, stress state and chain factors, pushing us to perform a large number of experimental tests to fully characterize our polymer (which is time consuming and economically expensive from an industrial point of view). From a theoretical point of view, the literature is missing constitutive models able to fully describe multiple responses accounting for the physical aspects.

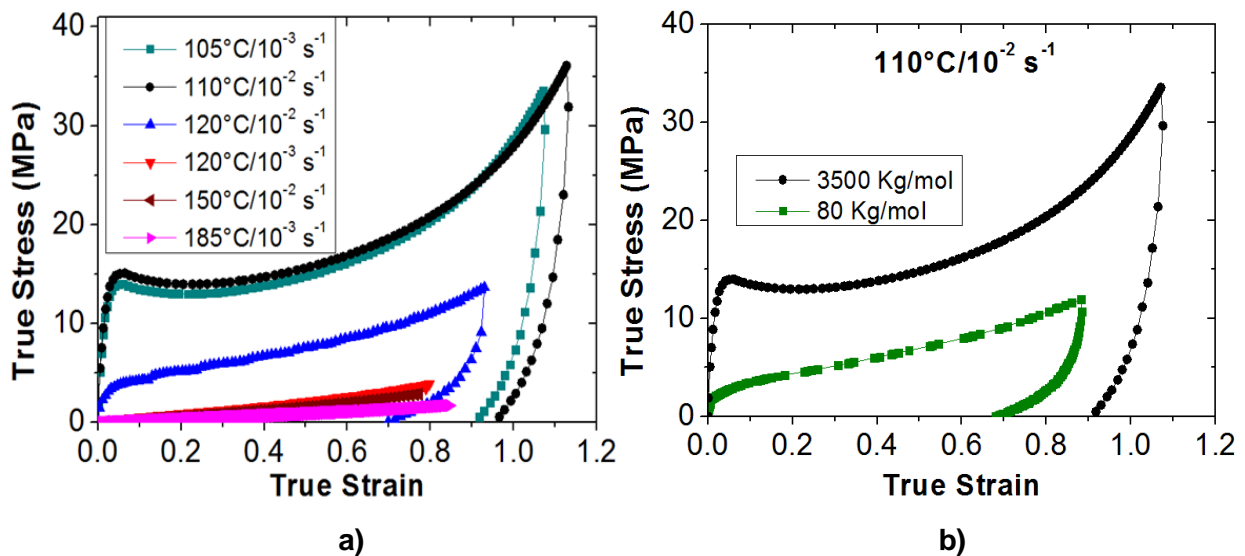


Figure 1.1: True stress-true strain curves for PMMA at a) various temperatures and strain rates, b) different molecular weights.

1.1 Project framework

In front of these challenges, the “Centre de Mise en Forme des Matériaux”, CEMEF, develops since many years a strategy to adapt mechanical characterization and modelling to polymers near to alpha transition relying on the use of so-called time-temperature superposition principle. This PhD takes place in this strategy as validation and a first insight on relationships between chain architecture and mechanical modelling. This work was sponsored by a CARNOT project.

In this project, we choose to work with a homogeneous amorphous material of controlled architecture for performing mechanical characterization at different level of deformation, strain rate and temperature, corresponding to behaviours near the fluid state up to the glassy state.

The idea of this work is to first validate the use of the time-temperature principle even at high strain level for amorphous polymers of different architecture. Then, we aim to determine and to model the influence of the molar mass and crosslinks on the mechanical response of amorphous polymers from the quasi-fluid state up to the solid state. Thus, the goal of this work is to characterize and to model in a simplified and accurate manner, the mechanical behaviour of amorphous polymers with different architectures.

1.1.1 General approach

The material chosen for this project was an amorphous poly(methyl methacrylate), PMMA of controlled molar mass, which allows producing different grades of PMMA with remarkable differences in their behaviour. The versatility of this material together with well-known relaxations will help to enrich the study by including the effect of architecture factor in the mechanical behaviour. Materials and experimental protocol are presented in Chapter II.

Then, to achieve the points previously mentioned, specific goals are established in this work. These are presented in Figure 1.2. They can be classified into three categories.

First, we aim to characterize the mechanical behaviour in the linear domain of deformation from the flow state up to the glassy state. Also, we want to understand the influence of the molecular weight and crosslinking in the time/temperature dependence at infinitesimal deformations. Indeed, PMMA have been found to exhibit various mechanical relaxations which display different sensitivity to the temperature and loading rate [1]–[4]. Additionally, other authors [5]–[10], have found that the main mechanical relaxation is also strongly dependent on the molar mass and crosslinking degree. To identify the dependence to the mechanical relaxations, analysis in the linear viscoelastic domain will be performed through rheology tests and dynamic mechanical thermal analysis in the range of interest. This will allow identifying the different viscoelastic region for then targeting our material characterization at larger deformations. The reader will find more details in Chapter III.

Secondly, we targeted to obtain a material data base at large strain for different temperatures, strain rates and stress states (tensile and shear loading). Following previous work [11], we want to validate the coupling of strain rate and temperature dependencies by means of the “equivalent strain rate at a reference temperature” for a wide range of conditions (rubbery, viscoelastic and near glassy), for different loading states and different architectures. Finally, we expect to link the experimental results at large deformations to the molecular motions of the polymer changes when varying temperature, strain rate, density of entanglements and crosslinks.

Indeed, polymer chains are highly sensitive to the effect of temperature and strain rate [12]–[14] as also to the molecular weight and crosslinking degree [15]–[18]. To generate a reliable

material data base, we will perform mechanical tests for the different PMMAs under different temperatures, strain rates and loading modes while measuring the displacement field through Digital Image Correlation [19]. Additionally, to simplify the number of tests and constitutive parameters needed to characterize the mechanical behaviour of the polymer, works of Billon et al. [11], [20], [21] will be used. Such studies suggested that the strain rate and temperature could be coupled, allowing to identify sets of temperature and strain rate leading to the same mechanical behaviour. In this project, we will take advantage of the well-known time temperature superposition principle in the linear domain [22] to define the so-called “equivalent strain rate at a reference temperature” that will help us to reduce the number of experimental tests and to link constitutive parameters to this variable. This study is depicted in Chapter IV.

Third, we aim to verify the constitutive model developed in CEMEF [11], [21] to describe the mechanical behaviour of the PMMAs under 1D tensile loading conditions for the different equivalent strain rates, corresponding to near-liquid, rubbery state, viscoelastic and near glassy state. Through this study, we expect to link the internal parameters evolution (entanglements, secondary bonds and others) with the equivalent strain rate to have a full understanding of the temperature/strain rate effect in the elastic and inelastic components.

To include the physical aspects of the internal parameters evolution when the polymer is deformed under different conditions, we proposed to use a thermodynamic framework accounting for the hyperelastic model of Edward and Vilgis [23] combined with the evolution of internal state variables (ISVs) to incorporate inelastic mechanisms. The approach used in this project was inspired by the works of Gorlier [24], Baquet [20], Billon et al. [11], [21], Gehring et al. [25] and Quandalle [26]. Additionally, the purpose is to include the “equivalent strain rate at reference temperature” into the modelling to establish a clear link between the internal parameter evolution and the elastic and inelastic mechanisms of the polymer under deformation. This is presented in Chapter V.

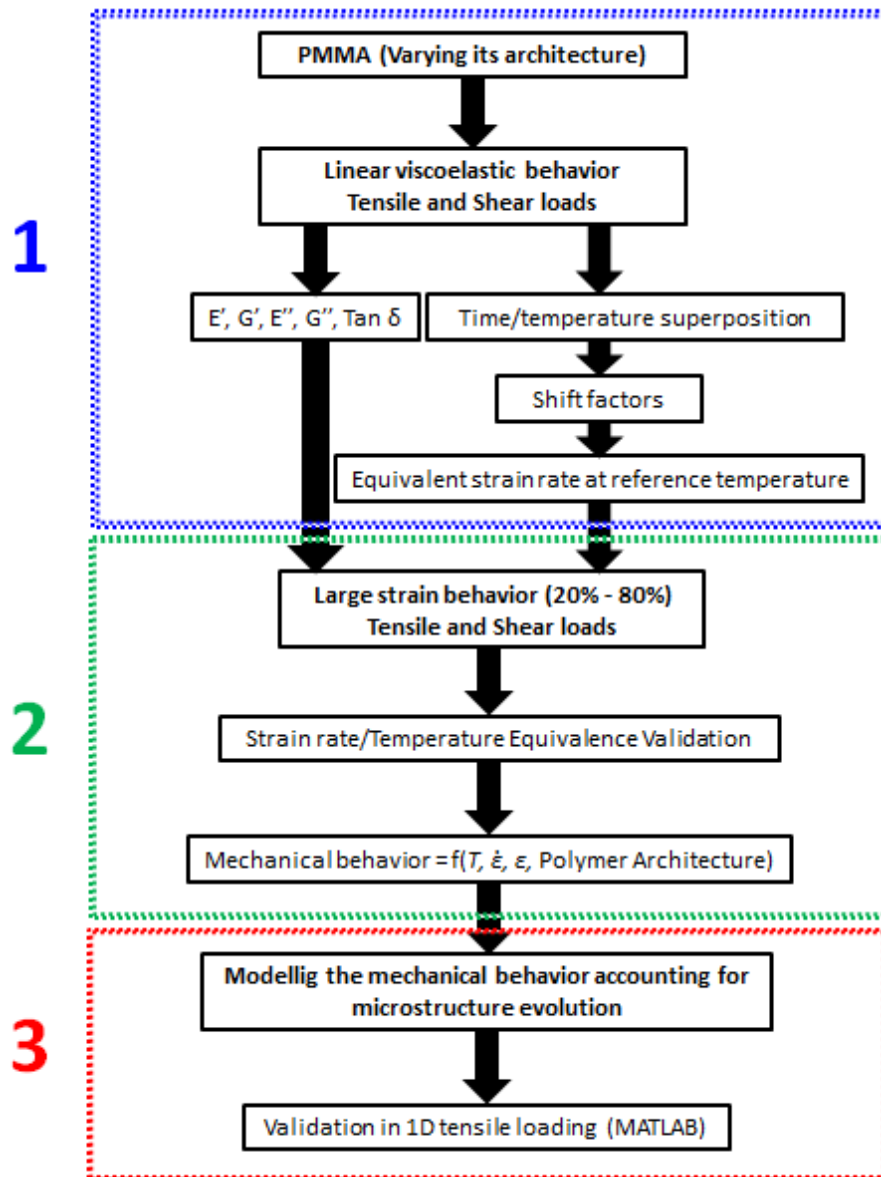


Figure 1.2: Schematic representation of the methodology employed in this project. E' , G' : Storage modulus under tensile and shear loading, E'' , G'' : Loss modulus under tensile and shear loading, $\tan \delta$: damping factor.

CHAPTER II

EXPERIMENTAL AND METHODOLOGY

This Chapter aims first at presenting the general features of the materials used in this research.

The second part of this Chapter illustrates the general methodology used to characterize the mechanical behaviour of the material. Presenting first, the linear viscoelastic behaviour study which was carried out through dynamic mechanical thermal analysis in tensile load and shear rheology. Then, the protocol for large deformation tests is detailed. This consisted in cycling tests in tensile and shear loadings using Digital Image Correlation.

Finally, a brief description of the use of inverse analysis for parameters identification will be shown. These concepts will give a glimpse on how the experimental results were compared to constitutive equations and theoretical models.

Ce chapitre cible d'abord à présenter les caractéristiques générales des matériaux utilisés dans cette étude.

La deuxième partie de ce chapitre illustre la méthodologie générale utilisée pour caractériser le comportement mécanique du matériau. En présentant d'abord l'étude du comportement viscoélastique linéaire qui a été réalisée par analyse thermique mécanique dynamique en charge de traction et en rhéologie de cisaillement. Ensuite, le protocole pour les tests de grande déformation est détaillé. Cela a consisté à effectuer des essais de cyclique dans des chargements de traction et de cisaillement en utilisant la corrélation d'image numérique.

Enfin, une brève description de l'utilisation de l'analyse inverse pour l'identification des paramètres sera présentée. Ces concepts donneront un aperçu de la façon dont les résultats expérimentaux ont été comparés aux équations constitutives et aux modèles théoriques.

CONTENT

| | | |
|---------|-------------------------------------------------------------|----|
| 2 | Material and methodology | 8 |
| 2.1 | Material | 8 |
| 2.1.1 | Material description | 9 |
| 2.1.2 | Glass transition temperature of the different polymers..... | 10 |
| 2.2 | General methodology | 13 |
| 2.2.1 | Linear viscoelastic domain tests | 13 |
| 2.2.1.1 | Tensile loading | 14 |
| 2.2.1.2 | Shear loading | 15 |
| 2.2.2 | Large strain tests using Digital Image Correlation | 17 |
| 2.2.2.1 | Tensile tests | 18 |
| 2.2.2.2 | Shearing tests | 21 |
| 2.2.3 | Parameters identification: Inverse analysis..... | 26 |
| 2.2.3.1 | Optimization method | 27 |
| 2.3 | Summary..... | 27 |

2 Material and methodology

2.1 Material

The material of this study is a poly(methyl methacrylate), PMMA, which is a linear amorphous polymer with transparent properties (transmitting up to 92% of visible light). It is synthesized from methyl methacrylate, MMA, by radical polymerization (see Figure 2.1) involving peroxides as initiators at temperatures up to 100°C.

Substituents on the α -carbon atom restrict chain mobility, leading to a significantly high glass transition temperature, T_g . Typical values of this temperature may vary between 105°C and 120°C depending on the molar mass. From this point of view, two kinds of synthesis routes allow a wide range of molar weights.

As an example, suspension polymerization leads to low molar mass, 10^3 g/mol, and fluidity at high temperature. This PMMA are compatible with classical molten state processing. A second route is casting, which allows higher molar masses, i.e. 10^6 g/mol. In such a case, viscosity is so high that the material is almost unable to flow below its degradation temperature. Yet, it is basically used for rubbery state processing such as thermoforming [27]. Additionally to that, copolymerization can be used and casting route makes possible to crosslink PMMA in a controlled manner.

This versatility in controlling the molar mass and crosslinking makes PMMA a good candidate for studying the response of the material between the glass transition temperature and the flowing temperature, accounting also for the effect of the molecular weight and crosslinking degree on the mechanical behaviour of the material.

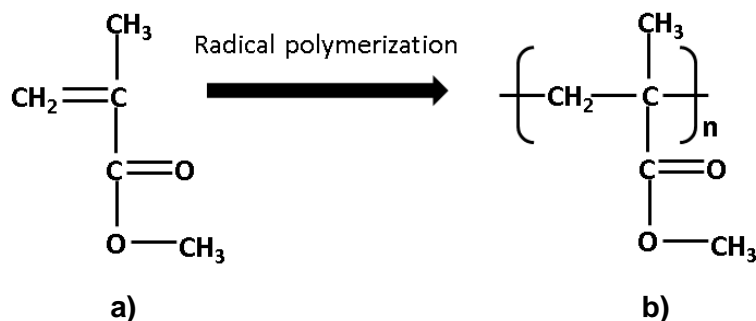


Figure 2.1: a) Methyl methacrylate. b) Poly(methyl methacrylate). [27]

2.1.1 Material description

The study was carried out using five semi-industrial PMMAs with different molecular weights and cross-linking degree. In three of these PMMAs, a comonomer, ethyl acrylate, was added for improving their process ability. The glass transition temperature, T_g , of this comonomer is ranging from -25°C to -22°C , adding flexibility to the chain backbone of PMMA [28]. Thus, copolymerizing methyl methacrylate with ethyl acrylate may decrease the glass transition temperature of the material.

The material was provided by Arkema under the commercial name ALTUGLAS[®]. Table 2.1 summarizes the molar masses (in weight, M_w , and in number M_n), the density at room temperature (ρ) and the comonomer content. Let's add that the crosslinked PMMA is not highly crosslinked (<1%). Those different molar masses cannot be processed the same way. Therefore, Table 2.1 reminds the different processes used to supply the different PMMAs received as isotropic plaques.

The PMMAs with lower molar weight ($M_w=80$ Kg/mol and $M_w=93$ Kg/mol) were supplied as injection moulded 4mm thick plaques. Injection gate was located through the width of a lateral side of the plaque. The third PMMA ($M_w=120$ Kg/mol) was processed as 4 mm thick extruded plaques. The last two materials ($M_w=3500$ Kg/mol and crosslinked) were acrylic sheet prepared by pouring the methyl methacrylate based syrup into a casting cell with controlled temperature. Material was processed as 4 mm thick. No comonomer was added in the cast sheet. Processing conditions were chosen according to the state of the art. Resulting mechanical anisotropy in the plane of the plaques was found to be negligible (see section 3.1)

Table 2.1: Material Properties.

| Processing/Grade | Comonomer (wt%) | ρ (g/cm ³) | M_w (Kg/mol) | M_n (Kg/mol) |
|---------------------------|-----------------|-----------------------------|-----------------------|----------------|
| Injection moulding/VM100 | 10 | 1.18 | 80 | 42 |
| Injection moulding/V825T | 0.6 | 1.19 | 93 | 45 |
| Extrusion moulding | 4 | 1.19 | 120 | 62 |
| Casting moulding/CN | 0 | 1.20 | 3500 | 880 |
| Casting moulding/ShieldUp | 0 | 1.21 | Crosslinked Copolymer | |

For clarity, through this manuscript the PMMAs are referred to using their molar mass in weight. For instance, the PMMAs with $M_w=80$ Kg/mol, $M_w=93$ Kg/mol were named “PMMA 80” and “PMMA 93”, respectively. Finally the crosslinked PMMA was named “PMMA CL”.

2.1.2 Glass transition temperature of the different polymers

The glass transition temperature is the temperature where cooperative motions of the main chain, involving 10-20 bonds in the amorphous phase, are possible. This brings relevant changes in the mechanical properties of such polymers, related to a sharp decrease on the mechanical stiffness. At this point, the material has more deformability, making the glass transition temperature a starting point for processing at the solid state [1], [4], [29], [30]. Therefore, it is important to address this temperature and to observe how it is affected by factors as molecular weight, cross-linking and copolymerization.

To verify the dependence of T_g with the molar mass, differential scanning calorimetry, DSC, were performed on the five materials. The material was cut into small pieces and settled into aluminium pans which were encapsulated using a universal crimper press. The weight of the samples was close to 8 mg. The calorimetric analyses were carried out in a DSC *Perkin Elmer 8500*, calibrated with indium. All the DSC tests were realized three times for each material in a nitrogen atmosphere at a heating rate of 10°C/min from room temperature up to 160°C.

Figure 2.2 shows a thermogram obtained for PMMA 120. Below 100°C, the polymer heat capacity corresponds to a solid state. Then, a gradual increase on the heat capacity takes place, which is related to the onset of cooperative motions of the main-chain bonds, linked to the glass transition temperature [31]. This transition does not occur suddenly, but takes place over a temperature range. For measuring a discrete T_g , we used the software *Pyris* which takes the interceptions between the baselines and the slope in transition range, for then choosing the middle point of these interceptions as the glass transition temperature. This is illustrated in Figure 2.2

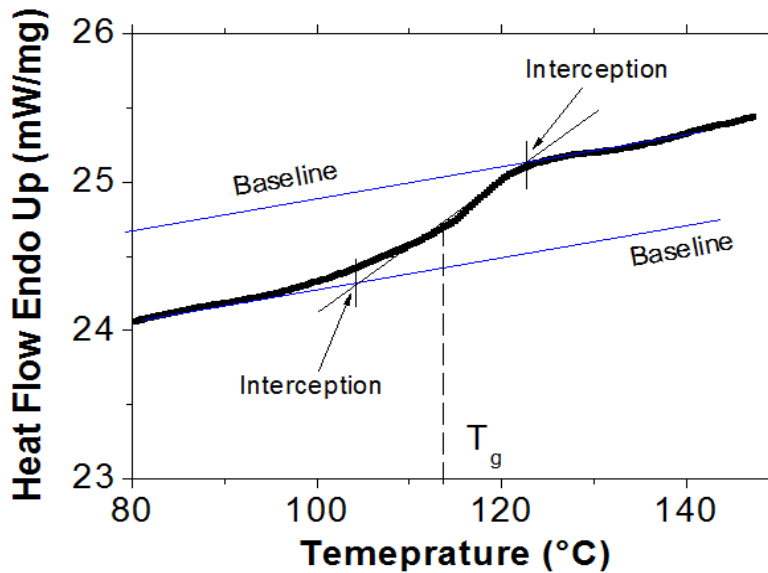


Figure 2.2: DSC thermogram for PMMA 120 at a heating rate of 10°C/min. Graphical illustration of the glass transition temperature determination.

Results were confronted to Flory–Fox equation [32] which relates the molar mass to the transition temperature as:

$$T_g = T_{g\infty} + \frac{K}{M_n}, \quad 2.1$$

where $T_{g\infty}$ is the maximum glass transition temperature that can be achieved at a theoretical infinite molecular weight and K is an empirical parameter that is related to the free volume present in the polymer sample. A good agreement is observed between the experimental data and the theoretical equation by using $T_{g\infty} = 119^\circ\text{C}$ and $K = 422^\circ\text{C}\cdot\text{Kg/mol}$.

Two things can be concluded from Figure 2.3: i) low molecular weight PMMAs result in lower glass transition temperatures whereas increasing values of molecular weight results in an asymptotic approach to $T_{g\infty}$. This has been reported by other authors [9], [32], [33]. This asymptote starts around 400 Kg/mol, showing that PMMAs with higher molar mass should not display any relevant changes in their T_g . ii) The maximum transition temperature identified from the Flory-Fox model is about the same than that of PMMA 3500.

Figure 2.3 also suggests that PMMA 120 has a lower glass transition temperature than PMMA 93, which seems to disagree with the general trend. This can be attributed to the comonomer content in both polymers. As shown in Table 2.1, PMMA 120 has a higher amount of

comonomer than PMMA 93, increasing the flexibility of its chain backbone and reducing its glass transition temperature of the PMMA.

Another relevant factor is the crosslinking degree; where polymer chains are chemically joined by other chains at points along their length. Similarly to the molecular weight, the increase of the crosslinking degree is expected to raise the glass transition temperature [7], [9]. We can observe in Figure 2.3 that the glass transition temperature of PMMA CL is higher than PMMA 3500. This suggests that the presence of crosslinks reduces the chain mobility of the polymer [7], [34] more than having high molecular weights, leading to an increase on its glass transition temperature.

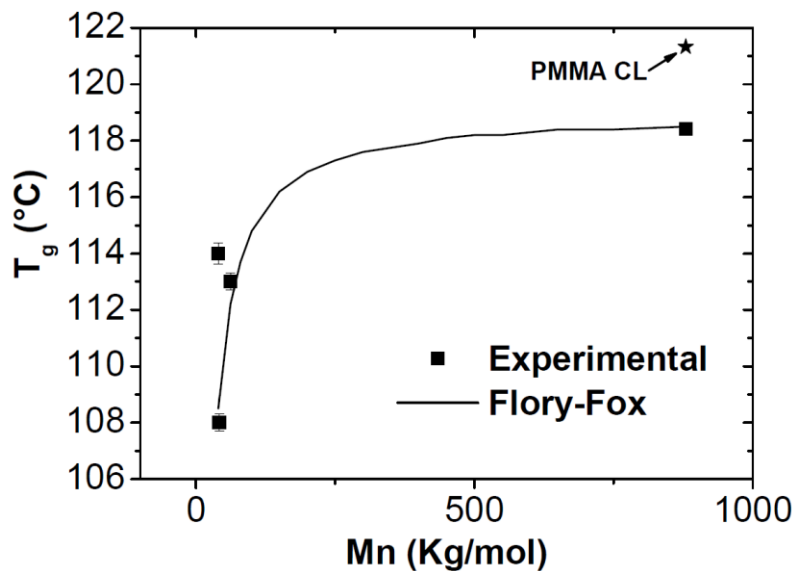


Figure 2.3: Glass transition temperature evolution with the molecular weight on PMMA.

These results highlight the influence of the molecular weight and crosslink degree on the glass transition temperature of PMMA. As a conclusion, we are facing five polymers with very distinguishable glass transitions attributed to discrepancies in molecular weights and also in chains architecture.

Characterizing and understanding how these factors affect the mechanical behaviour at low and large strains accounting for the coupled strain rate and temperature effect is one of the purposes of this study. To answer this, we designed a methodology to fully characterize the linear and non-linear mechanical response in an optimized manner. This is presented in the next Section.

2.2 General methodology

As mentioned in the Introduction, the main goal of this project is to explore coupled dependences of the mechanical behaviour of polymers of different architecture upon temperature and strain rate and more especially, the relevance of so-called time temperature superposition principle to define a constitutive parameter. To achieve that point, a general methodology has been built up following previous observations on PMMA [11], PA66 [20], [21] and PET [25], [26].

Starting with sample preparation, materials were tested as received, i.e. without any annealing treatment. Samples were carefully tooled using a computer controlled milling machine (CharlyRobot[®]) to get appropriate specimens geometries for the different experimental technics. Thanks to this, heating during machining in the samples was avoided. Geometries were such that strain fields obey general assumptions in the zone of interest: uniaxiality (when required) and uniformity.

The next sections present details regarding the experimental set-up used for characterizing the material.

2.2.1 Linear viscoelastic domain tests

Dynamic mechanical analysis is a well-known technique used to characterize the viscoelastic behaviour of a polymer at small deformation, i.e. in the linear domain. A low amplitude sinusoidal strain is applied to the sample while the load is recorded to compute the resulting stress. For viscoelastic materials, a characteristic delay, δ , is observed between the applied strain and material stress response:

$$\varepsilon_{(t)} = \varepsilon_0 e^{i\omega t}, \quad 2.2$$

$$\sigma_{(t)} = \sigma_0 e^{i(\omega t + \delta)}, \quad 2.3$$

where σ_0 is the maximum stress and ε_0 is the maximum strain. The complex dynamic modulus can be expressed as:

$$E^* = \frac{\sigma_{(t)}}{\varepsilon_{(t)}} = \frac{\sigma_0}{\varepsilon_0} e^{i\delta} = \frac{\sigma_0}{\varepsilon_0} (\cos \delta + i \sin \delta). \quad 2.4$$

Equation 2.4 allows to identify the storage modulus, E' , and the loss modulus, E'' . These different moduli give a better understanding of the ability of the material to store energy (E') and to dissipate energy (E''): [35]

$$E' = \frac{\sigma_0}{\varepsilon_0} \cos \delta. \quad 2.5$$

$$E'' = \frac{\sigma_0}{\varepsilon_0} \sin \delta. \quad 2.6$$

The delay δ is expressed through the damping factor, $\tan \delta$, which represents the ratio of energy dissipated during a strain cycle. It is defined as:

$$\tan \delta = \frac{E''}{E'}. \quad 2.7$$

2.2.1.1 Tensile loading

Linear viscoelastic behaviour under tensile loading was studied using samples of dimensions 30mm x 4mm x 1mm. The effective length was 5mm. The tests were carried out on a DMTA Tritec 2000 machine (see Figure 2.4). Each type of tests was performed five times. The error of the temperature measurements was lower than 1°C.

The linear domain was validated performing strain scans from room temperature up to 200°C. Figure 2.5 displays strain scans of PMMA 3500. The linear relationship between the monitored dynamic stress and strain is an indicator of the limit in the linear viscoelastic response of the material. A strain of 0.1% was enough to ensure a linear behaviour; therefore all the viscoelastic properties measurements were performed at this strain level.

Temperature scans at frequencies of 0.1 Hz, 1 Hz and 10 Hz were performed to identify the mechanical relaxations. Investigated temperatures ranged from -20°C up to 150°C for PMMAs 80, 93 and 120 and from -20°C up to 200°C for PMMA 3500 and crosslinked PMMA at a heating rate of 1°C/min.

Then, isothermal frequency sweep tests were performed for frequencies ranging from 0.1 Hz up to 100 Hz and for temperatures ranging from 25°C up to 150°C every 10°C for PMMA 80, 93

and 120 and ranging from 25°C up to 200°C for the PMMA 3500 and crosslinked PMMA. Shift factor were graphically determined using storage modulus, E' . It was checked that shift factor were relevant for both storage and loss moduli. No vertical shifts were applied. Higher temperatures were not studied in this configuration since the material turned into a liquid. At this point rheological tests were needed.

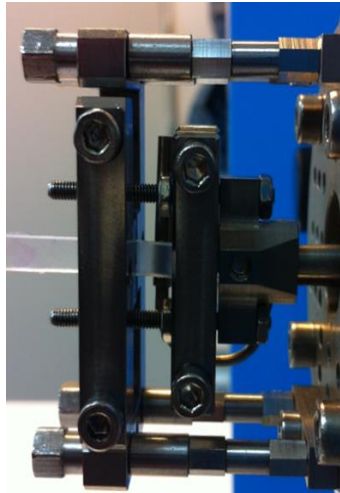


Figure 2.4: DMTA setup for tensile test sample

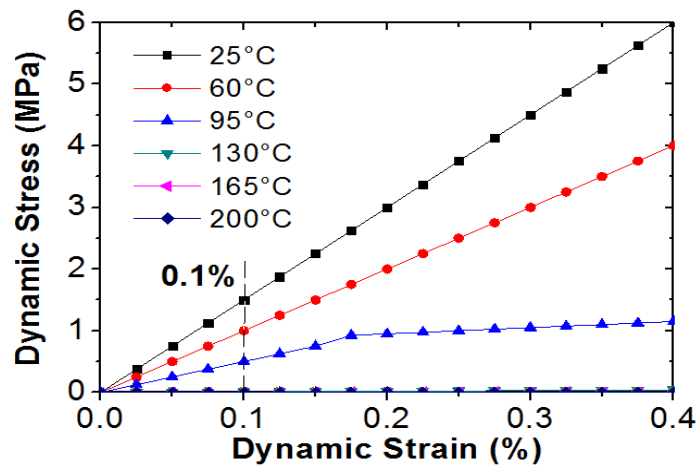


Figure 2.5: Strain scans for PMMA 3500 at different temperatures.

2.2.1.2 Shear loading

To study the linear viscoelastic behaviour of the material under shear loading and at higher range of temperatures than DMTA, rheological tests were performed using a Rheometer Ares with two configurations: torsion and parallel plates (see Figure 2.6 a) and b)). The torsional mode allowed characterizing the material under a shear loading in its solid state (rectangular samples 30mm x 4 mm x 1 mm) while the parallel discs were used for the flowing state (discs

with a diameter of 25mm and 1mm thickness). Equations for computing the modulus and stress are presented in Appendix 8.1.

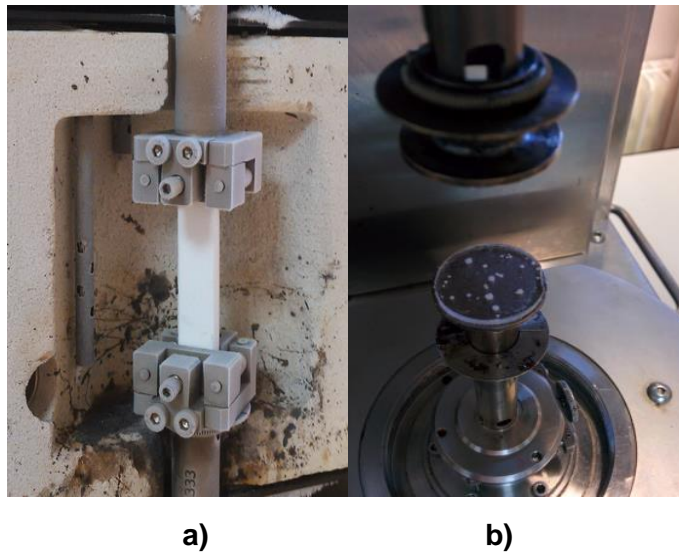


Figure 2.6: a) Rheometer setup using: a) torsional mode and b) parallel plates.

As it was done for the tensile loading, we first verified that the tests were performed in the linear viscoelastic region. Figure 2.7 a) displays the evolution of the shear storage modulus with the strain for PMMA 3500 at 260°C. The modulus remained constant in the studied strain range. For all the tests, a strain of 0.1% was used to ensure that the material was in its linear viscoelastic region whatever the temperature was. This range was also validated for the different PMMAs.

Isothermal frequency sweep tests were performed from 0.1Hz to 100 Hz. For PMMA 3500 and PMMA CL, the material did not show any flow at the tested conditions, i.e. at temperatures ranging from 40°C to 260°C. For this reason a torsion configuration was used in this temperature range. For PMMA 80, 93 and 120 we tested the material as a solid at temperatures ranging from 40°C to 110°C for the torsional mode and as a fluid from 120°C to 210°C for the parallel plates mode.

The maximum applied temperature was determined by measuring the evolution of the storage modulus versus time at different temperatures when applying a dynamic strain of 0.1%. This is illustrated on Figure 2.7 b) where three temperatures are used for PMMA 3500. For 260°C the modulus remains nearly constant up to 300 seconds, which is enough time for performing the study. However, increasing temperature leads to a stronger decrease of G' with time. Therefore, we concluded that PMMAs 80, 93 and 120 could be tested up to 230°C while PMMAs 3500 and CL could be tested up to 260°C, to avoid degradation.

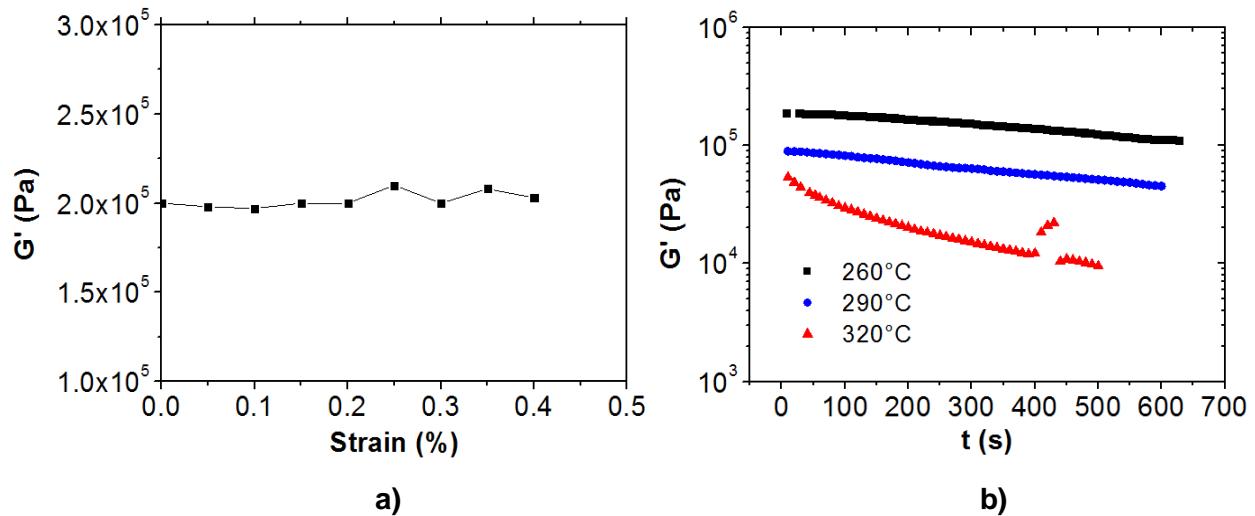


Figure 2.7: a) Strain scan at 260°C b) Shear storage modulus evolution with time for different temperatures. Study performed on PMMA 3500.

2.2.2 Large strain tests using Digital Image Correlation

For a correct characterization at large deformation, experimental tests with controlled conditions are required. This implies, to ensure a homogeneous temperature, strain and strain rate in a representative volume of the material. Additionally, this results will also be used as database for revisiting constitutive models [11], [21], [25] which describes mechanical response of the polymers. Therefore, consistent boundary conditions (local temperature, displacement and deformation) are needed. Moreover, incompressibility assumption needs to be validated especially regarding modelling. Along this Chapter, we will present the methodology used to guarantee such condition.

Behaviour at large strain was obtained by performing uploading-unloading tensile and shearing tests on an Instron 596 electro-mechanical testing machine with a thermal chamber. The unloading was imposed until a zero force. Strain-rate was the same during uploading and unloading. For obtaining a homogenous temperature and local constant true strain rate, the following protocol was used:

- Homogeneous temperature: pre-heating was required. Its duration was calibrated using thermocouples located on the sample surfaces and in the bulk of the material. Ten minutes ensured a homogeneous temperature prior performing the mechanical test. For the materials with lower molecular weights, 80 Kg/mol up to 120 Kg/mol, the temperatures were chosen ranging from 90°C up to 140°C while for high molecular weight and cross-linked PMMAs, temperatures were chosen ranging from 110°C up to 200°C.
- Local constant true strain rate, $\dot{\epsilon}_T$: it was obtained during stretching by imposing an exponential cross-head velocity, v , defined as:

$$v = l_0 \cdot \dot{\epsilon}_T \cdot \exp(\dot{\epsilon}_T \cdot t),$$

2.8

where l_0 is the initial gage length and t is the time. The local constant true strain rates were chosen from 10^{-3} s^{-1} to 10^{-2} s^{-1} . DIC allowed verifying that strain-rate remained locally constant.

2.2.2.1 Tensile tests

The set-up for tensile tests is depicted in Figure 2.8. Pneumatic clamps and sand paper were used to avoid sample sliding. Samples were home designed dog bone shapes of dimensions which allow promoting a transversally uniform uniaxial loading in the central zone. One head of the sample was fixed in the clamp while the other one was free during the pre-heating time. This allowed a free thermal expansion. After fixing the two heads of the sample, a “specimen protection mode” available on the testing machine was enabled for keeping the force close to zero. The displacement field on the front face of the sample was followed from images recorded using a stereovision system of two cameras (previously calibrated through a calibration grid). And then Digital Image Correlation (DIC) was used to compute the strain fields. A more detailed explanation is presented in Appendix 8.2.

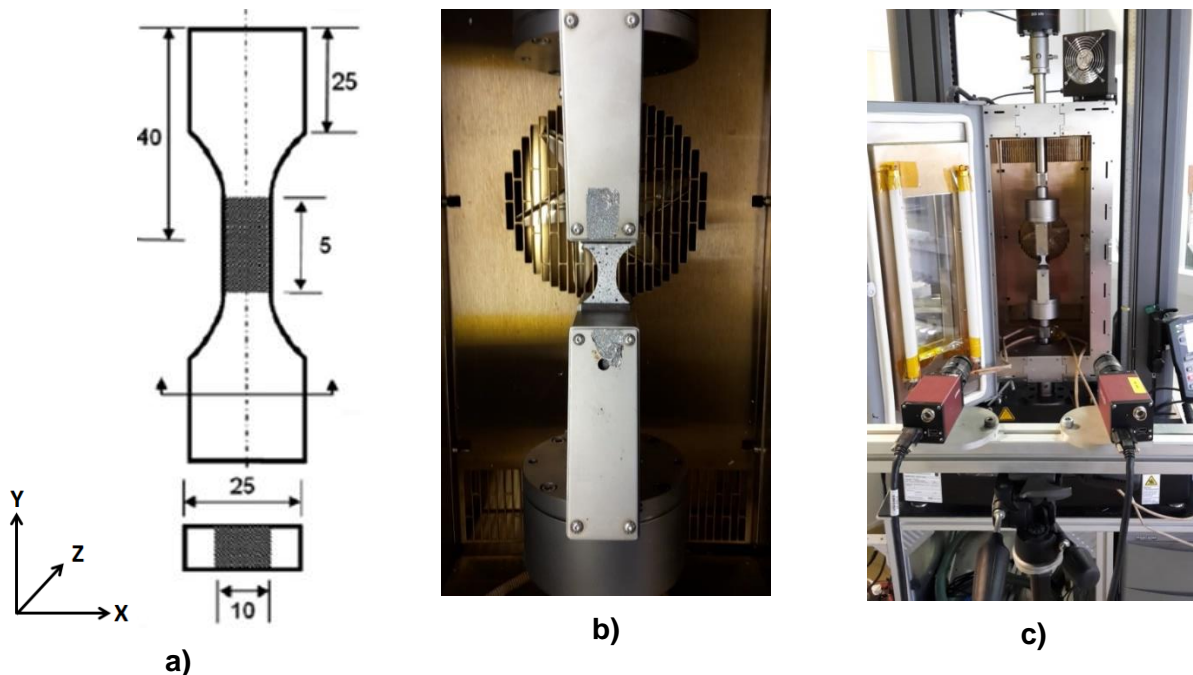


Figure 2.8: a) Geometry of tensile sample. Sample had 4mm thickness. b) Pneumatic clamps used on a tensile test specimen. c) Experimental set-up displaying the mechanical testing machine with a thermal chamber, stereovision system and lightening.

The Hencky's or true strain was chosen as the deformation indicator, which is convenient for accounting the strain path at large strain levels [36]:

$$\varepsilon = \int_{l_o}^{l(t)} \frac{\partial l}{l_o} = \ln\left(\frac{l(t)}{l_o}\right) = \ln(\lambda), \quad 2.9$$

where l_o is the initial length, $l(t)$ is the instantaneous length and λ is the stretch ratio. We define ε_{yy} as the true strain in the loading direction and ε_{xx} as the true strain in the transverse direction. Figure 2.9 shows an example of the strain field in the loading direction.

After choosing the DIC parameters (subset size of 21 pixels, step size of 2 pixels and filter size of 15) for obtaining an accurate strain field (detailed in Appendix 8.2), the homogeneity of the strain field was examined. Figure 2.9 shows the iso-strain maps in the longitudinal direction for PMMA 93 subjected to a tensile loading at a strain rate of $1.5 \times 10^{-2} \text{s}^{-1}$ and a temperature of 140°C . Different levels of maximum local strain are shown: 20%, 40%, 60% and 80%. We can observe a longitudinal strain gradient increasing with the applied loading along the y-axis. From this strain field, a homogeneous longitudinal Hencky's strain, ε_{yy} , within the central zone can be observed over the whole sample width. This homogeneous ε_{yy} in the central area was observed for all PMMAs stretched at different ranges of temperature and strain rate. Thus, all the data used to generate the stress-strain curves and the local strain rates was obtained from the information within the central zone of the samples.

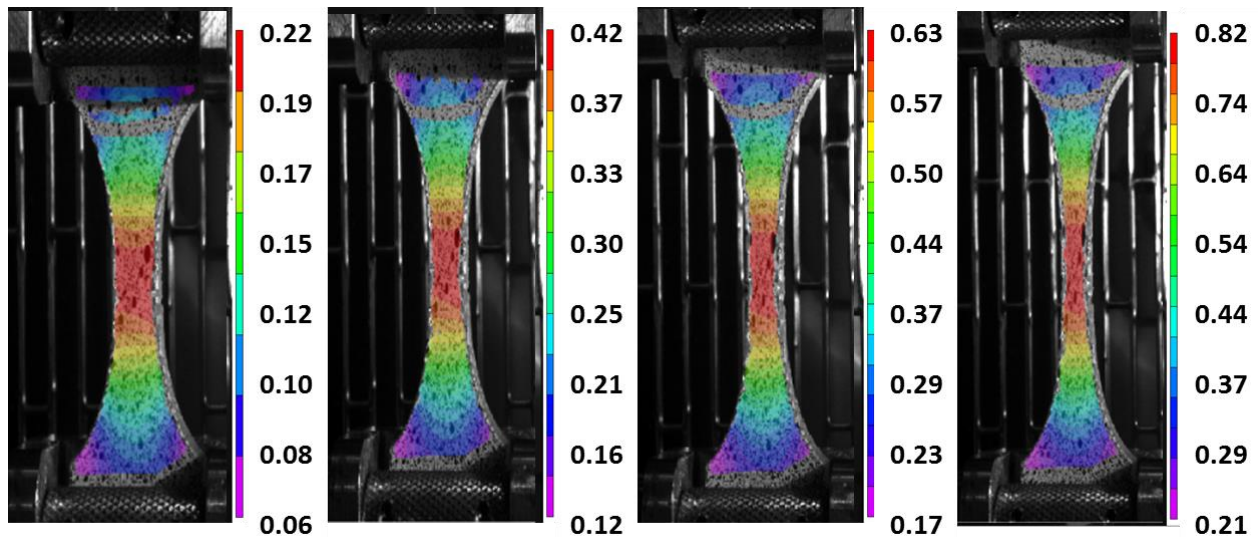


Figure 2.9: Iso-longitudinal Hencky strain maps of PMMA 93 stretched at $140^\circ\text{C} - 1.5 \times 10^{-2} \text{s}^{-1}$.

After validating the homogeneity of the strain, the next step was to verify if the exponential cross-head velocity used for the tensile tests promoted a constant local true strain rate within the central zone. Having a constant true strain rate during the mechanical testing will allow comparing the experimental results in a more accurate manner. Figure 2.10 presents the evolution of the true strain and true strain rate in the longitudinal and transverse directions (measured within the central zone). We can observe that the true strain evolves linearly with time. In the same way, we observe that the true strain rate remains constant close to $1.5 \times 10^{-2} \text{s}^{-1}$. Strain rate appeared less constant during unloading phase. However, such variation is small enough to be considered as negligible. The use of an exponential velocity profile (Equation 2.8) is appropriate for obtaining a constant true strain rate.

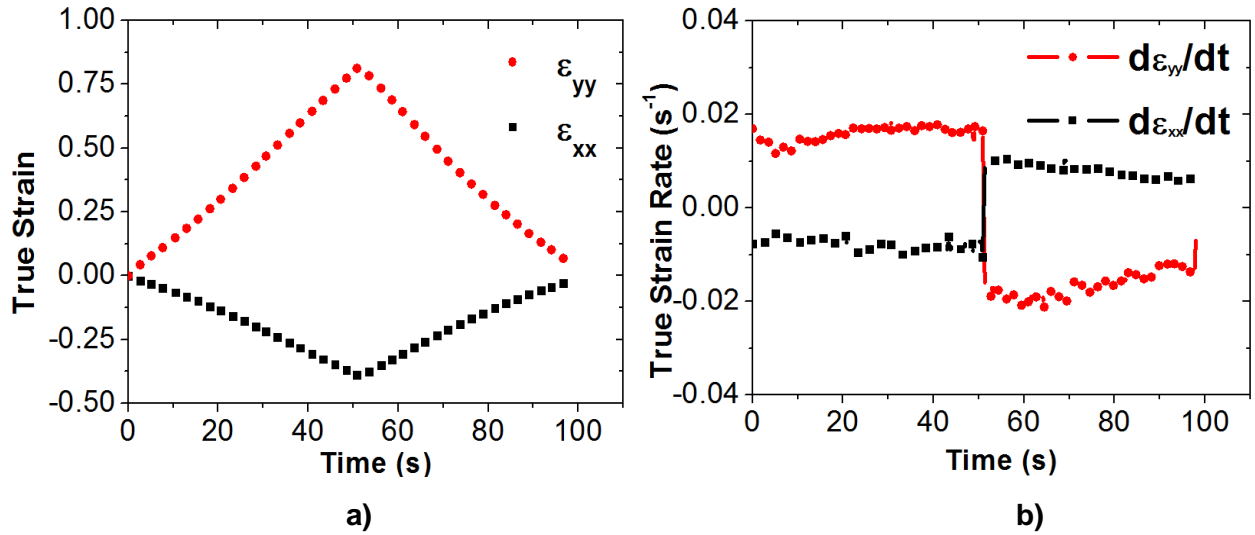


Figure 2.10: a) Longitudinal and transverse true strains vs time and b) Longitudinal and transverse true strain rates vs time for PMMA 93 stretched at 140°C and $1.5 \times 10^{-2} \text{s}^{-1}$.

Last point is the compressibility of the material during the uploading/unloading. In consequence, the volumetric strain during the test was calculated following [37]:

$$\frac{\Delta V}{V_0} = \exp(\epsilon_{xx} + \epsilon_{yy} + \epsilon_{zz}) - 1, \quad 2.10$$

where ϵ_{zz} is the true strain in the thickness direction and V_0 is the initial volume. Previous work on injection moulded PMMA [11] showed that the material is transversally isotropic. In this work, casted plaques were assumed to be also isotropic. This choice was made due to the difficulty of measuring the strain in transversal direction. Additionally, non-simultaneous tensile tests confirmed previous assumption. Therefore, we generally assumed that $\epsilon_{xx} = \epsilon_{zz}$. Thus, it was possible to compute the volumetric strain by using Equation 2.10.

Figure 2.10 displays the evolution of the volumetric strain with the longitudinal true strain for PMMA 93 at $140^{\circ}\text{C} - 1.5 \times 10^{-2} \text{s}^{-1}$. The figure reveals that the volume remains quite low in the range of investigated deformation. Therefore, we have assumed that the material is close to be incompressible for these test conditions, as reported by other authors [38]. This assumption of incompressibility was verified for all the different experimental conditions and for all PMMAs (from 90°C up to 200°C and 10^{-2}s^{-1} up to 10^{-3}s^{-1}), by obtaining a similar response. Thus, future modelling of these materials will account for an incompressible behaviour.

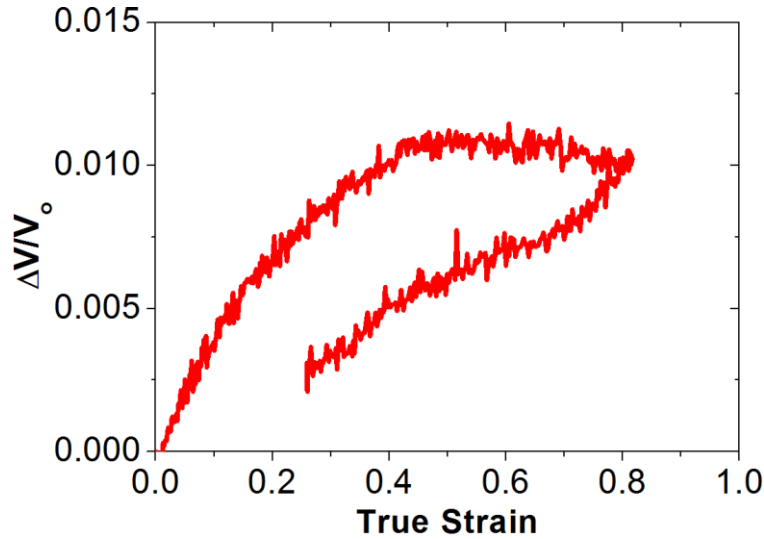


Figure 2.11: Volume strain vs Longitudinal true strain for PMMA 93 tested at $140^{\circ}\text{C} - 1.5 \times 10^{-2} \text{s}^{-1}$.

Finally, the true stress can be computed using Equation 2.11:

$$\sigma_{yy} = \frac{F}{A_{(t)}} = \frac{F}{A_0 \exp(\varepsilon_{xx} + \varepsilon_{zz})} \quad 2.11$$

where F is the loading force, $A_{(t)}$ and A_0 are the instantaneous cross section and the initial cross section of the sample. Once again, a transverse isotropy hypothesis was assumed.

2.2.2.2 Shearing tests

Experimental setup for imposing local shearing strain have been validated in polymers at room temperature [21] and at high temperatures for composites [39]. However, studies at high temperature on polymers, coupling the Iosipescu configuration with Digital Image Correlation is not abundant in the literature. In the present study, we aim at carrying out this test to enrich the mechanical characterization of the material, for several sollicitation modes.

An Iosipescu configuration, as described in standard “ASTM D 5379” [40], was used. The shear sample geometry was chosen for promoting shear strain localization in the central zone of the sample. Indeed, Pierron and Vautrin [41] showed that a triangular notch shape with a specific angle of 90° promoted a local shear condition. The geometry and experimental set-up of the Iosipescu system is displayed in Figure 2.12.

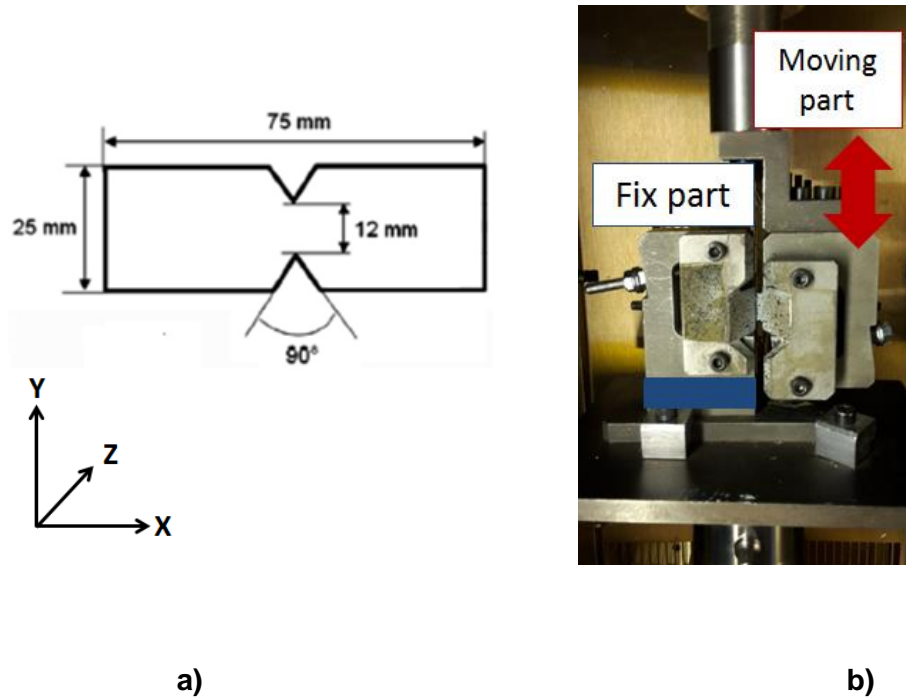


Figure 2.12: a) Geometry of shear sample with 4mm thickness and a notch radius of 2mm. b) Iosipescu configuration. The left side is fixed while the right side moves up and down for performing the sample upload-unload.

As in the case of tensile loading tests, an exponential cross-head velocity was imposed (Equation 2.8) to promote a local true strain rate. Moreover, the displacement field on the front face of the sample was followed from images recorded using two cameras in stereo-correlation and then post-treated using VIC-3D. Since the speckle size distribution was similar than the one used for the tensile geometry (see Figure 8.1 b) in Appendix 8.2), the mesh parameters were found to be the same for both shear and tensile tests, i.e. subset size of 21 pixels, step size of 2 pixels and filter size of 15. This was also verified by performing a sensitivity study of the DIC parameters as depicted in Appendix 8.2.

Prior using this set-up, a validation was made to assure that the local strain was mainly under shear condition. Such condition means that the other strain components (ϵ_{xx} and ϵ_{yy}) remained close to zero during loading. Figure 2.13 shows the strain field corresponding to each iso-strain field when the shear strain, ϵ_{xy} , was about 25%. Figure 2.13 a) stands for the lateral true strain,

ϵ_{xx} , b) for the longitudinal true strain, ϵ_{yy} , and c) for the shear true strain, ϵ_{xy} . It can be noticed that the first two strains remain quite low within the central zone while the shear strain is localized homogeneously between the notches. Thus, we will make the assumption that the central zone of the sample displays in between the notches apparent pure shear behaviour. The maximum values of ϵ_{xx} and ϵ_{yy} are located next to the notches. These could affect the measurements since a pure shear is no longer present. These results have also been reported by other authors [21], [42]. However, these strains at the notch remain quite low, less than 5%, and far from the apparent pure shear zone. Therefore, as for tensile loading tests, an analysis zone (indicated as a 2px square in Figure 2.13) was chosen within the central zone between the notches, where an apparent pure shear state was observed.

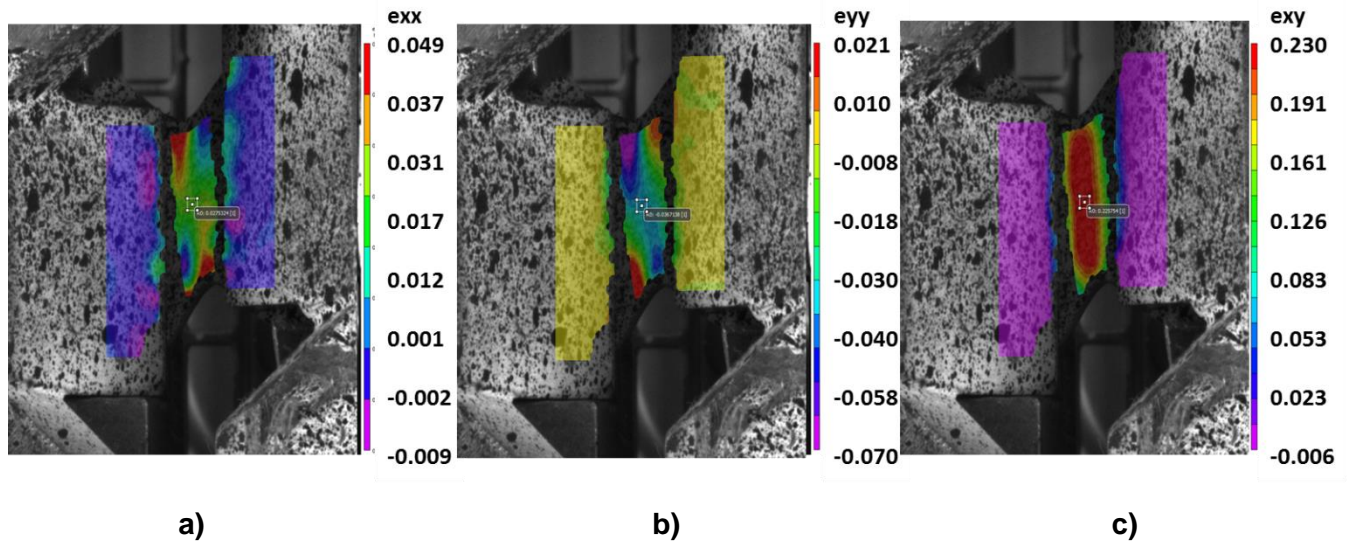


Figure 2.13: a) Iso-lateral Hencky strain map b) Iso-longitudinal Hencky strain map and c) Iso-shear Hencky strain map of PMMA CL stretched at $118^{\circ}\text{C} - 1.5 \times 10^{-2} \text{ s}^{-1}$.

We need also to address the evolution of the strain components with time to verify that ϵ_{xx} and ϵ_{yy} remain close to zero. The variation of the different strain components with time and the local shear strain rate, $\dot{\gamma}$, are depicted in Figure 2.14. The shear strain components increase almost linearly up to 30% at a constant shear true strain rate of $1.5 \times 10^{-2} \text{ s}^{-1}$. In this range, the other two strain components remain lower than 5%, which may be considered as “negligible”. Thus, we assume a “pure” local shearing stress state for these conditions. However, it was observed during the tests that, at around 30% of shear strain, the material started sliding from the clamps, making the measurement inaccurate. Therefore, a value of 25% was chosen as a maximum strain to guarantee “pure” local shearing condition with no sliding. This maximum shear strain was used for all the PMMAs at the different temperatures and strain rates.

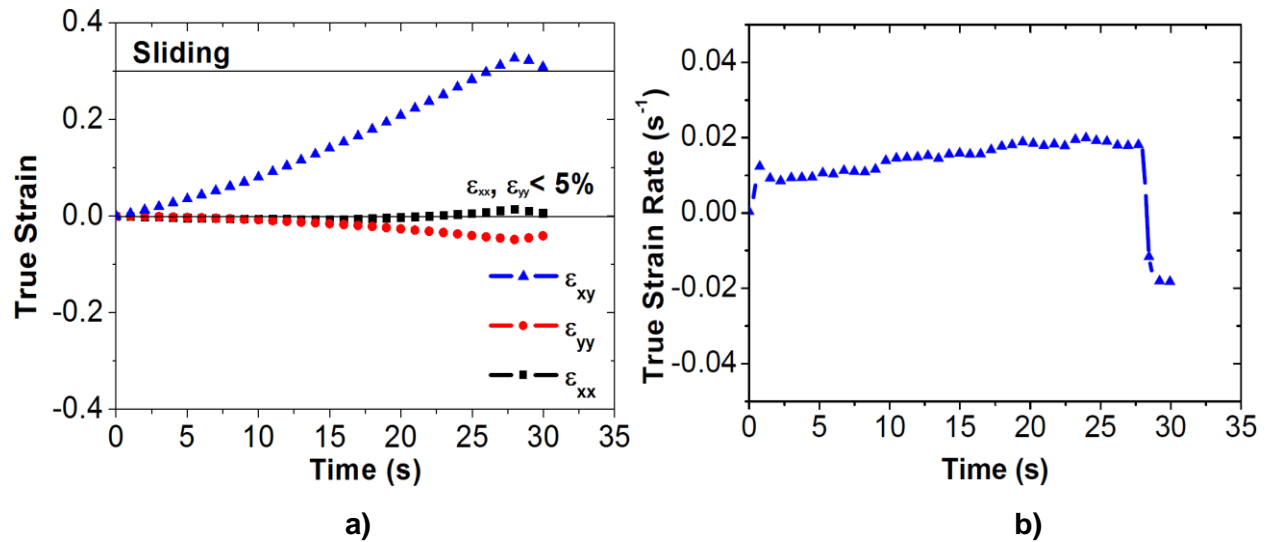


Figure 2.14: a) Shear, longitudinal and transverse true strains vs time. b) Shear true strain rate vs time for PMMA CL stretched at 118°C - $1.5 \times 10^{-2} \text{ s}^{-1}$.

Nevertheless, some authors [41], [43]–[45] have stated that shear strain may be distributed heterogeneously between the notches due to bending during the tests, leading to inaccurate estimation of the shear strain and stress. For verifying this, we tracked the shear strain along the “Y” direction, between the notches, and along the “X” direction, perpendicular to the notches. This is depicted in Figure 2.15 a). The shear strain evolution along these axes is presented in Figure 2.15 b) and c) respectively. It can be observed that the deformation is quite homogeneous in the central zone. However, the tracking performed along “Y” reveals that the shear strain near the notches front is about 15% lower than the average value in the central zone.

As stated for the standard “ASTM D 5379” [40], the mechanical response under shear loading can be characterized by the true shear stress, which stands in Equation 2.12 following:

$$\sigma_{xy} = \frac{F}{AB \cdot h} \quad 2.12$$

where AB is the length between the notches and h is the thickness. However, as it was illustrated in Figure 2.15 b) and c), the shear strain along AB was not constant. Therefore, if the whole length is accounted when computing the shear stress, an overestimation of the stress may occur. This was also reported by other authors [44] on composites. Morton et al. [43] and Pierron et al. [41], [45] proposed to introduce a correction factor, C_s , to account for the non-uniformity of the stress state in the midsection of the sample, and average the stress. The correction factor, C_s , may be determined from the ratio between the local shear stress in the

midsection of the sample, τ_{xy} , and the average shear stress in the midsection, defined in Equation 2.12. Thus, a corrected shear stress, σ^c_{xy} , can be calculated based on the correction factor following:

$$C_s = \frac{\tau_{xy}}{F/(AB \cdot h)} \quad 2.13$$

$$\sigma^c_{xy} = \frac{F}{C_s \cdot AB \cdot h} \quad 2.14$$

For estimating this correction factor, finite element simulations were carried out by using ABAQUS 6.14-1 package. Two simulations were performed: the first one assuming hyperelastic behaviour for the PMMA (rubbery regime) and the second one accounting for elastoplastic behaviour (glassy state). Both behaviours were taken from experimental results on PMMA. More details about the simulations and calculations are presented in Appendix 8.3.

For the hyperelastic material, the stress correction factor is equal to 1.091. This result is similar to those found by Morton et al. [43] and Pierron et al. [41], [45] on elastic materials. However, the correction factor for the elastoplastic simulation was 1.342, which is higher than the one for elastic and hyperelastic materials. This suggests that the correction factor may vary following the constitutive behaviour used for the material.

Therefore, the correction factor is sensitive to the mechanical behaviour and should be determined for the different investigated mechanical behaviours. For the studied PMMAs under shear loading, the plastic behaviour did not show any strain hardening, thus a factor of 1.342 was used for the different cases. Additionally, viscoelastic and hyperelastic behaviours seemed to be well described by a correction factor of 1.091.

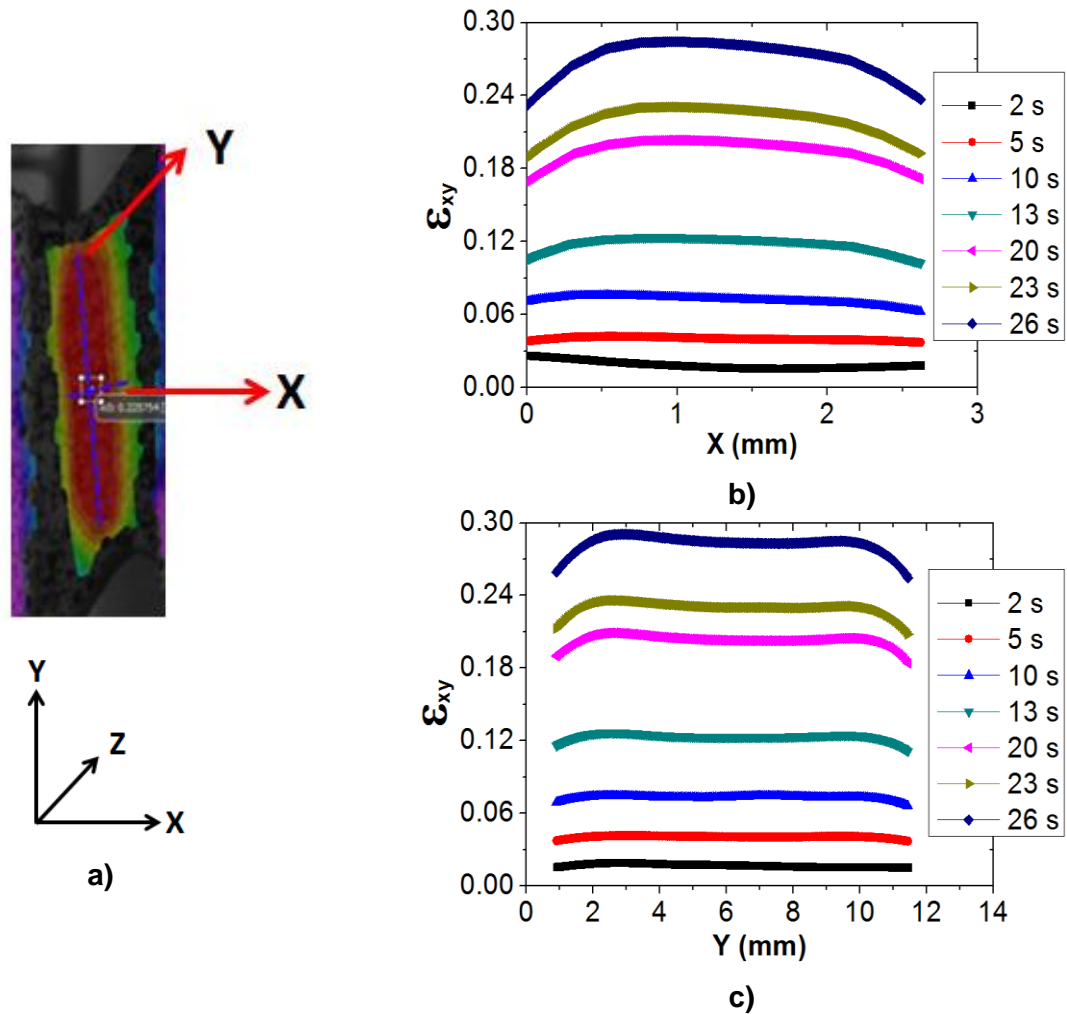


Figure 2.15: a) Local shear strain map measurement along the “X” and “Y” direction. Evolution of the shear strain during loading in function of: b) the distance perpendicular to the notches and c) between the notches.

2.2.3 Parameters identification: Inverse analysis

After performing an experimental characterization of the material, it is important to be able to reproduce the main results by working with material constitutive equations. However, identifying the material parameters that properly describe the material behaviour is not always a trivial task. To overcome this difficulty, the use of inverse analysis is a reliable option.

Classically, a direct modelling of a physical indicator, as the stress, consists in expressing its response, S^m , using a behaviour law that may depend on intrinsic properties (p_i), geometry and boundary conditions:

$$S^m = f(p_1, p_2, p_3, \dots, p_n). \quad 2.15$$

Inverse analysis consist in identifying the optimal parameters “ $p_1^o, p_2^o, p_3^o, \dots, p_n^o$ ” that lead to a similar experimental response, S^{exp} :

$$S^m(p_1^o, p_2^o, p_3^o, \dots, p_n^o) = S^{exp}. \quad 2.16$$

Thus, the goal of using inverse analysis is to find the set of parameters that minimizes the difference between the values determined experimentally and those computed through a model. Such difference is quantified through a scalar called “cost function”, CF . If the cost function is low, the results from constitutive equation and those from the experiment are similar. The idea is to minimize the cost function. In this work, the cost function was defined in a classical mean square method based on experimental and theoretical values (Equation 2.17). This form as been previously used for identifying physical and mechanical parameters on uniaxial tensile tests by [21], [25].

$$CF = \frac{1}{n} \left[\sqrt{\frac{\sum_{i=1}^n (S_i^m - S^{exp})^2}{\sum_{i=1}^n (S^{exp})^2}} \right]. \quad 2.17$$

2.2.3.1 Optimization method

Many methods may be used for minimizing the cost function [46]–[48]. In this study minimizations were conducted by means of the simplex algorithm of the “fminsearch” MATLAB[®] function. This function uses the Nelder-Mead simplex algorithm [49] as described in Lagarias et al. [50]. This method uses a simplex of $n+1$ vertices, where n is the number of variables. The algorithm initially makes a simplex around the initial guess of parameters by adding 5% of each component. Then, the cost function is computed in each vertex (including the initial guess) and ordered from the lowest to the highest. At each iteration the algorithm discards the worst point (or highest cost function) and modifies it according different procedures: reflection, expansion, contraction and shrinkage [50]. Each of these operations constantly modifies the simplex until it converges to a minimum of the cost function.

2.3 Summary

This Chapter described the investigated material by presenting its general features, synthesis and some of its physical properties. We also gave a glimpse about the effect of the molecular

weight and cross-linking on the glass transition temperature. Low molecular weight PMMAs exhibit lower glass transition temperatures whereas increasing values of molecular weight results in reaching an asymptotic value to $T_{g\infty}$.

Section 2.2.1 gives an introduction of dynamical analysis for linear viscoelastic properties measurement. At this level, we presented the two configurations used in this study: tensile and shear loading. It was verified that for both conditions the imposed strain remain in the linear viscoelastic region. Moreover, it was shown that shear tests could be performed for PMMAs 80, 93 and 120 up to 230°C and up to 260°C for PMMAs 3500 and CL. Higher temperatures may promote degradation.

In Section 2.2.2 tests used at the macroscopic level were presented regarding uploading-unloading tensile and shear tests. The displacement field on the front face of the sample was followed accurately from images recorded using a stereovision system of two cameras. Computation of the strain was done using VIC-3D. By performing a mesh sensitivity study, we concluded the appropriate set of parameters to have the best compromise between accuracy and computing time: a subset size of 21 pixels, a step size of 2 pixels and a filter size of 15.

All the data post-treatment was issued from the information obtained within the central zone of the samples, where true strain fields were homogeneous. The use of an exponential velocity profile (equation 2.8) was appropriate to obtain constant true strain rates. Moreover, the incompressibility was verified for all the different experimental conditions and for all PMMAs, by obtaining similar responses. For characterizing the material behaviour under shearing, an Iosipescu configuration was used at high temperature coupled with Digital Image Correlation. The maximum ε_{xy} was chosen to be around 25%. This maximum shear strain was used for all the PMMAs at different temperatures and strain rates. To account for non-homogeneity of the shear strain between the notches, correction stress factors were calculated from finite element simulations. The values were found equal to 1.342 for elastoplastic behaviour, and to 1.091 for viscoelastic and hyperelastic behaviour.

Finally, a brief description of inverse analysis, cost function and Nelder-Mead simplex algorithm was given to illustrate the methodology employed for identification of model parameters. Such methodology will be used for calibrating all the parameters in the following Sections.

CHAPTER III

LINEAR VISCOELASTIC DOMAIN

This Chapter focuses on the mechanical relaxations of PMMA in the linear viscoelastic domain. Additionally, the effect of the loading frequency, molecular weight and cross-linking degree on these relaxations is addressed.

Temperature scans in the linear domain allowed identifying the secondary and primary relaxations on PMMA as well as their sensitivity to frequency. These relaxations will considerably rule the mechanical behaviour since they modify the elastic and loss moduli. Such study was performed for all PMMAs by evaluating if the molecular weight and cross-linking influence the way mechanical relaxations vary with frequency. The time/temperature superposition principle was used to build the master curves of the five PMMAs. Such curves described the viscoelastic response of the material along wide ranges of frequency at a reference temperature. Because material may be subjected to different stress state when processed, master curves were performed for tensile and shear loading. Additionally, the topology of the PMMAs was examined for relating it with the linear viscoelastic response. More precisely, we aimed to correlate the entanglement density with the elastic and inelastic response of the material.

Ce chapitre se concentre sur les relaxations mécaniques du PMMA dans le domaine viscoélastique linéaire. De plus, l'effet de la fréquence de chargement, de la masse molaire et du degré de réticulation sur ces relaxations est adressé.

Les balayages de température dans le domaine linéaire ont permis d'identifier les relaxations secondaires et primaires sur PMMA ainsi que leur sensibilité à la fréquence. Ces relaxations régiront considérablement le comportement mécanique puisqu'ils modifient les modules d'élasticité et de perte. Cette étude a été réalisée pour tous les PMMA en évaluant si la masse molaire et la réticulation influencent la façon dont les relaxations mécaniques varient avec la fréquence. Le principe de superposition temps/température a été utilisé pour construire les courbes maîtresses des cinq PMMA. De telles courbes décrivent la réponse viscoélastique du matériau sur de larges plages de fréquence à une température de référence. Étant donné que le matériau peut être soumis à différents états de contrainte lors de la mise en forme, des courbes maîtresses ont été réalisées pour la traction et le cisaillement. De plus, la topologie des PMMA a été examinée pour la relier à la réponse viscoélastique linéaire. Plus précisément, nous avons cherché à corrélérer la densité des enchevêtrements avec la réponse élastique et inélastique du matériau.

CONTENT

| | | |
|-------|------------------------------------------------------------------------------------------------------------------|----|
| 3 | Linear viscoelastic domain on PMMA..... | 31 |
| 3.1 | Isotropy validation | 31 |
| 3.2 | Introduction to Secondary transitions in PMMA and influence on T_{α} | 31 |
| 3.3 | Results and Discussions | 33 |
| 3.3.1 | Mechanical relaxations on the investigated PMMA..... | 33 |
| 3.3.2 | Viscoelastic zones of PMMA | 37 |
| 3.3.3 | Time/temperature superposition principle on PMMAs with different molecular weight and cross-linking degree | 39 |
| 3.4 | Summary..... | 49 |

3 Linear viscoelastic domain on PMMA

3.1 Isotropy validation

Recalling Section 2, we saw that some of the plaques were obtained by injection and extrusion moulding, which could generate a preferential molecular orientation and thus, an anisotropic mechanical behaviour. Thus, we have to validate that these curves are representative whatever the orientations of the samples is, before performing any further analysis.

Figure 3.1 shows the evolution of the storage modulus, a), and loss modulus, b), for two samples of PMMA 120 that were machined in two orientations: aligned with the injection flow (0°) and perpendicular to it (90°). We can see that moduli do not show any difference ($< \sim 1\%$) along the viscoelastic regions. We can therefore conclude that there is no appreciable effect of the orientation in the mechanical properties, meaning that plaques exhibit an isotropic behaviour. This was verified for all the PMMAs.

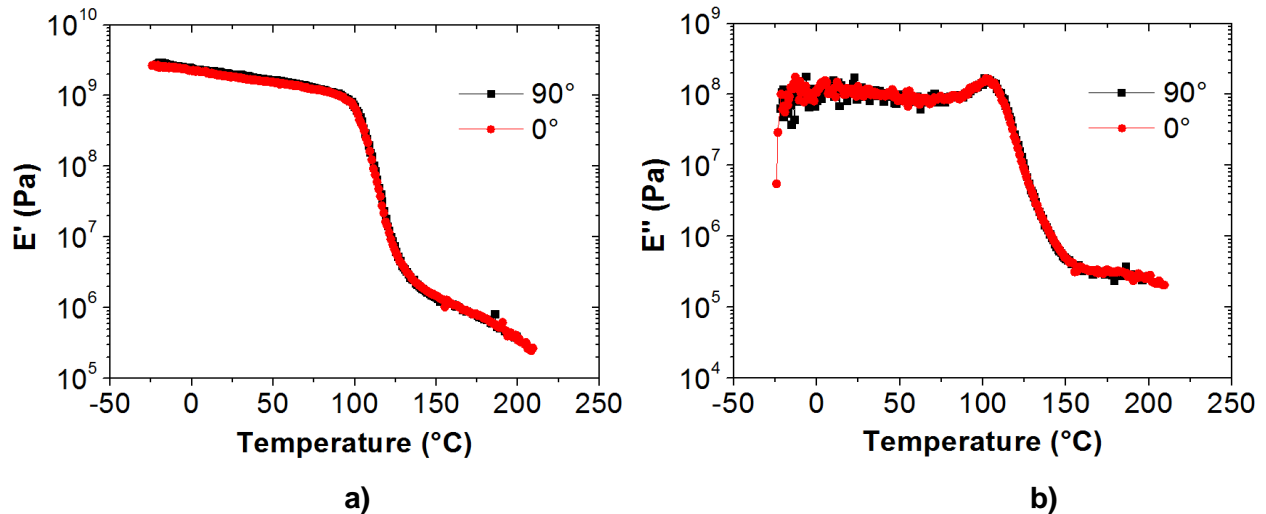


Figure 3.1: Temperature scans at 1 Hz for PMMA 120 in two directions. a) Storage modulus and b) loss modulus

3.2 Introduction to Secondary transitions in PMMA and influence on T_α

According to literature [1]–[3], PMMA exhibits three secondary relaxations, namely δ , γ and β (Figure 3.2). The δ transition is associated to the rotation of the methoxy group (O-CH₃) at a temperature close to -270°C at 1 Hz. The γ transition is related to the rotation of methyl group (CH₃) at a temperature close to -180°C at 1 Hz. Those two relaxations are not of importance in our study since they occur far from the α -transition. However, the β transition, which

corresponds to the rotations of ester group (O–C=O), takes place close to 10°C at 1 Hz, having chances of interacting with the α -relaxation we are focusing on [51].

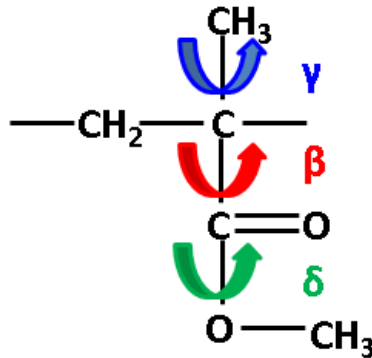


Figure 3.2: Secondary transitions in PMMA. [2]

Mechanical relaxations are often addressed by identifying the local maximum of the loss modulus evolution with temperature. Figure 3.3 displays the temperature dependence of the loss modulus for a PMMA at 1 Hz, having two maxima that correspond to the β -relaxation and α -relaxation. We can notice that the loss peak in β transition have a partial overlapping with the α -relaxation peak. Indeed, this β -relaxation leads to a broader relaxation peak when frequency increases, and shifts toward higher temperature with higher proportion than α -transition. So it may happen that the two processes merge in one unique so-called $\alpha\beta$ process [52]–[54]. In this temperature range, the intramolecular cooperative mechanisms are high enough to consider the molecular motions as the precursors of the large amplitude molecular motions in the α -relaxation [52].

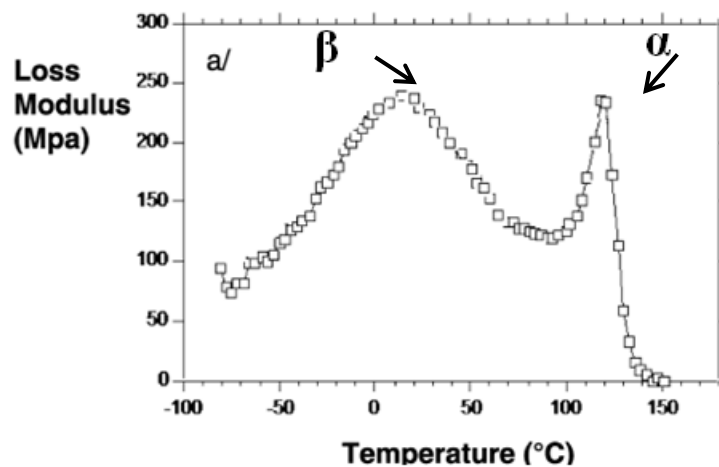


Figure 3.3: Temperature dependence of the loss modulus for a PMMA at 1 Hz. [1]

Indeed, Schmidt-Rohr et al. [3] suggested that motions during β -relaxation can be associated to fast π -flips of the ester group which brings reorientations of an angle of 20° around the local chain axis, producing a slight deformation in the molecular surroundings as displayed in Figure 3.4. This distortion in the molecular surrounding may facilitate the cooperatives chain motions related to the α -relaxation.

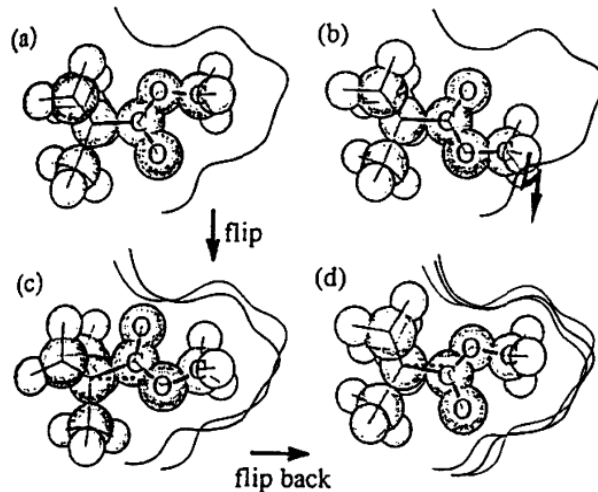


Figure 3.4: Dynamics of the ester side group in its environment. (a) Initial orientation of the side group. (b) π -flip without main-chain motion: steric clash with the environment. (c) Twist around the local chain axis: slight deformation in the environment. (d) Second jump occurs and returns the group back near to its original orientation in (a). [3]

3.3 Results and Discussions

3.3.1 Mechanical relaxations on the investigated PMMA

Interaction between α and β relaxations may be an issue when applying the time-temperature superposition principle since two types of molecular motions with different frequency dependence would take place. Thus, before building the master curves, it is necessary to address whether the secondary relaxation of the different PMMAs will superimpose or not with the α -relaxation.

Figure 3.5 displays the evolution of the loss modulus as a function of the temperature for different frequencies for PMMA 3500. Taking the local maxima of the loss modulus at 1 Hz as the moment where mechanical relaxations will occur, the β -transition and α -relaxation can be observed around 26°C and 113°C respectively. By varying the loading frequency, we can observe that β -transition shift for a decade of frequency around three times faster to higher temperatures than α -relaxation. Specifically, the β -transition shifts around 24°C per decade of frequency while α -relaxation shifts 8°C , which means that β -transition is more sensitive to

frequency. This observation has also been reported in PMMA by Schmidt et al. [3] and Mulliken et al. [54].

To represent the sensitivity of each molecular relaxation to the frequency effect, a relaxation map was plotted in Figure 3.6 for PMMA 3500. In this figure, we can observe the evolution of the frequency logarithm as a function of $1000/\text{Temperature}$ (expressed in kelvins). These temperatures correspond to the transition temperatures determined by the maximum of either E'' or $\tan \delta$. It can be seen that in this range of frequency the α -relaxation and β -relaxation nicely obey an Arrhenius form:

$$f = f_0 \exp\left(-\frac{Q_j}{RT}\right), \quad 3.1$$

where f_0 is a pre-exponential frequency factor, Q_j is an activation energy for the onset of a specific molecular motion and T is the temperature in kelvin. Through this relationship it was possible to determine the activation energies for the α and β relaxations, denoted as Q_α and Q_β respectively. The β -relaxation has an activation energy of 65 KJ/mol, while the α -relaxation has higher activation energy, 441 KJ/mol. Similar results have been reported by [51], [55]. This relationship between the activation energies, i.e. $Q_\beta < Q_\alpha$, confirms that the secondary relaxation activates with more ease and has higher sensitivity to the frequency than the α -relaxation.

Figure 3.6 also suggests that both relaxations tend to merge at high frequency, as reported elsewhere [52]–[54]. For example, by extrapolating the evolution of the mechanical relaxations of a PMMA 3500, the $\alpha\beta$ -process would occur around 3750 Hz for a temperature of 158°C. However, within our range of frequencies, overlapping remains low for all the PMMAs.

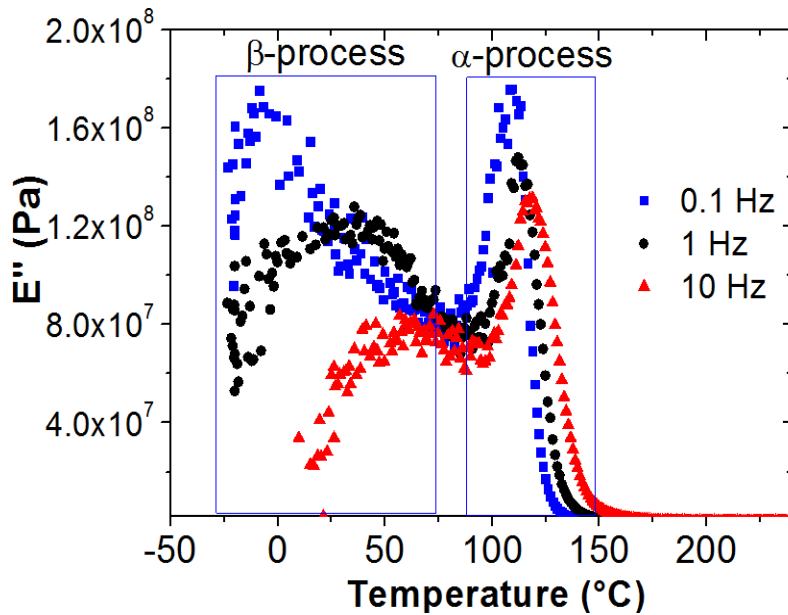


Figure 3.5: Loss modulus as a function of temperature at 0,1Hz, 1Hz and 10Hz for PMMA 3500.

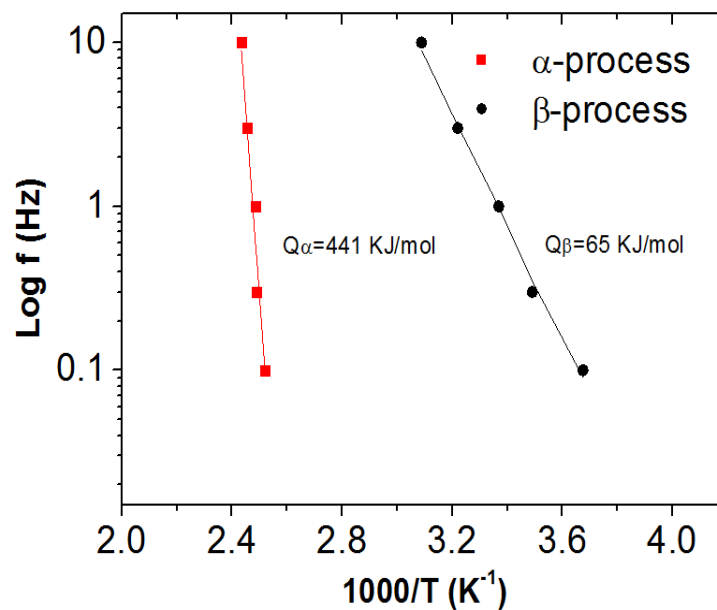


Figure 3.6: Relaxation map of PMMA 3500 obtained using the maxima of α and β relaxations.

Figure 3.7 shows the evolution of the loss modulus as a function of the temperature for the different PMMAs at 1 Hz. A shift on the α -relaxation peak to higher temperature can be seen as the molecular weight and cross-linking increase. This is related to an increase of the α -transition temperature. This may be due to the rise in the number of entanglements and to the presence of chemical crosslinks. These topological constraints, hinder the molecular motions that will introduce higher energy (in this case temperature) to activate the cooperative motions.

Regarding the secondary relaxation, we can observe a shift to higher temperatures when the molecular weight increases. As it was explained for the α -relaxation, entanglement restricts the

molecular mobility, which also seems to slow down the secondary relaxation. However, chemical crosslinks seems to have the opposite effect, decreasing considerably the β -relaxation temperature.

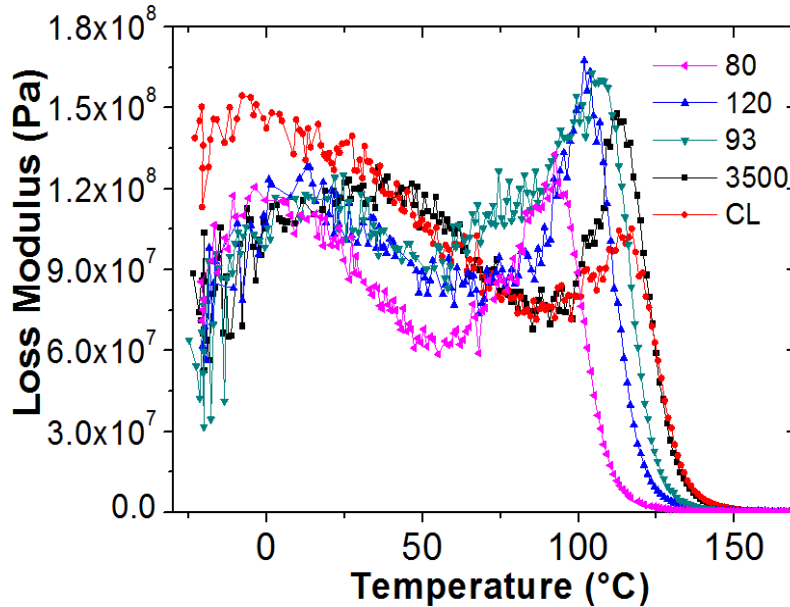


Figure 3.7: Loss modulus as a function of temperature at 1Hz for all PMMAs.

For having a better representation of the mechanical relaxation dependence with the molecular weight and cross-linking, we plotted relaxation map for the different PMMAs to determine their activation energies. Figure 3.8 shows how these activation energies vary for each PMMA. The activation energy for the α -relaxation was described through a Flory-Fox equation, increasing sharply with the molecular weight and then reaching asymptotically a maximum value around 441 KJ/mol. Additionally, PMMA CL has a higher Q_α , 483 KJ/mol, than any other PMMA. Thus, chemical crosslinks seem to impose more restriction than physical entanglements for the primary relaxation. These results display the same trend than the glass transition temperatures as displayed in previous Chapter.

Additionally, the differences for the activation energy on β -relaxation between PMMA 80 and PMMA 3500 are quite small, approximately 2 KJ/mol. Thus, even if the β -temperature rises with the molar mass, its activation energy remains nearly constant, meaning that its dependency with frequency is the same whatever the molar mass is. Moreover, Q_β is considerably lower, 36 KJ/mol, when chemical crosslinks are present. This result seems to be counterintuitive since crosslinks are supposed to slow down molecular motions. Similar observations have been reported by Casalini et al. [56] where they reported a decrease on Q_β when increasing crosslinking degree for a polyvinylethylene. For the purpose of this project, further explanations are not required. Future research on this topic may be useful for applications such as impact that induces higher loading frequencies.

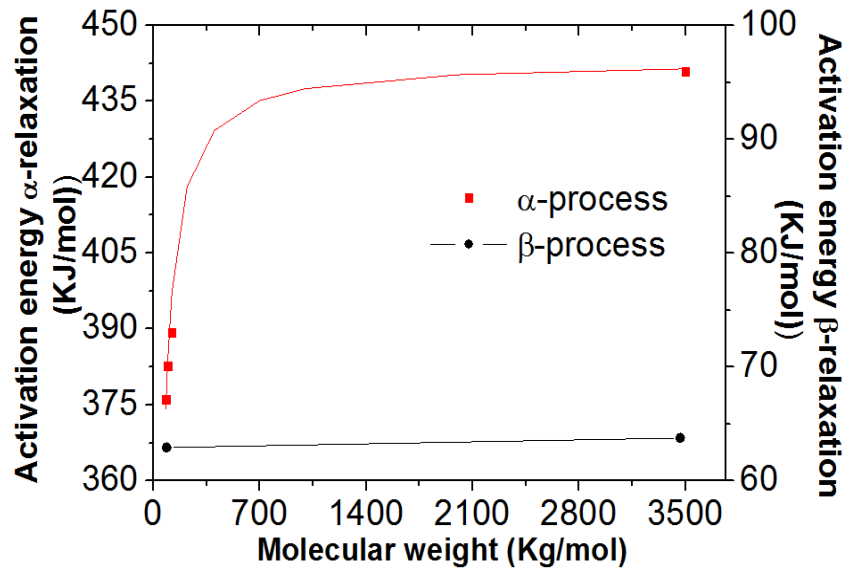


Figure 3.8: Evolution of activation energies with PMMA molecular weights.

3.3.2 Viscoelastic zones of PMMA

In the previous section, we addressed the main mechanical relaxations on PMMA and investigated how the temperature, frequency, molecular weight and crosslinking affect them. To draw a global picture of the material linear viscoelastic response, we characterized in this section the different viscoelastic regions of the five PMMAs.

First, a temperature scan gives an insight of the polymer viscoelastic response. Figure 3.9 shows the evolution of the storage modulus, loss modulus and damping for PMMA 3500 at 1 Hz. In this figure the classical viscoelastic regions are identified:

- A glassy region from -25°C up to 100°C with a high storage modulus and low energy dissipation. Storage modulus exhibits a slight progressive decrease. This is likely due to the secondary relaxation which acts as a precursor of molecular motions.
- Then, a viscoelastic region from 100°C up to 150°C is observed. At this point, there is a sharp decrease of E' and high energy dissipation. $\tan \delta$ exhibits a peak which is related to the α -transition temperature.
- Later, a rubbery plateau is observed from 150°C up to 250°C where the dissipation is quite low and E' gradually decreases while increasing the temperature. The increase in temperature provides enough energy to the polymer network, promoting a gradual disentanglement process that leads to a decrease of the storage modulus and an increase

of the energy dissipation. In fact, this rise of dissipation appears around 225°C and seems to have a tendency to overcome the storage modulus at higher temperatures, reaching the flowing region. In this test configuration (temperature scan performed under tensile loading), we could not analyse the flowing region since the material was too fluid and displayed an important thermal dilatation.

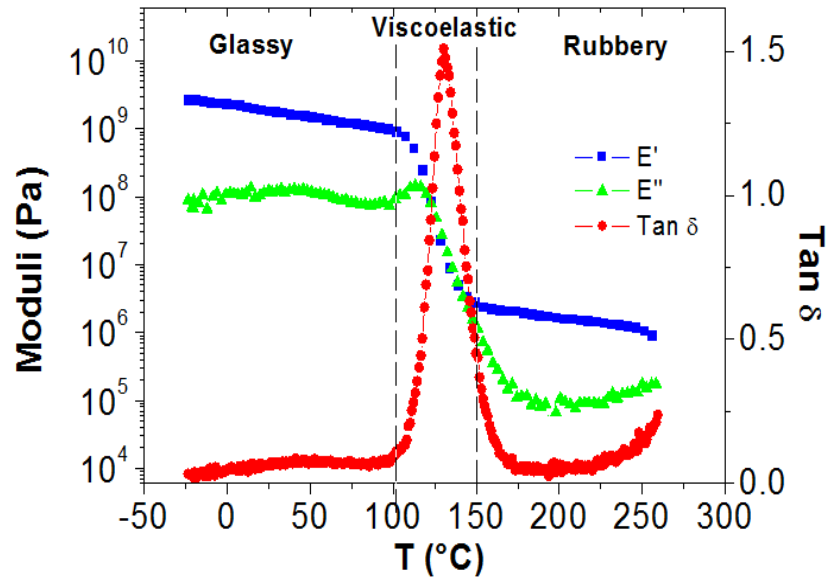


Figure 3.9: Moduli and $\text{Tan } \delta$ evolution with the temperature for PMMA 3500 at 1 Hz.

For understanding the effect of the loading frequency on the viscoelastic response, temperature scans were performed at three different frequencies. Figure 3.10 shows two examples of temperature scan where the storage and loss moduli evolve with the temperature at 0.1 Hz, 1 Hz and 10 Hz for PMMA 80 and PMMA 3500.

We can see that moduli at rubbery plateau of PMMA 3500 barely change. This suggests that viscoelasticity is not dominant in this region. For PMMA 80, the extension of the rubbery plateau is so short that the material seems to display viscoelastic behaviour in the studied conditions. Thus, the molecular weight appears to have an influence in the viscoelastic regime of the material.

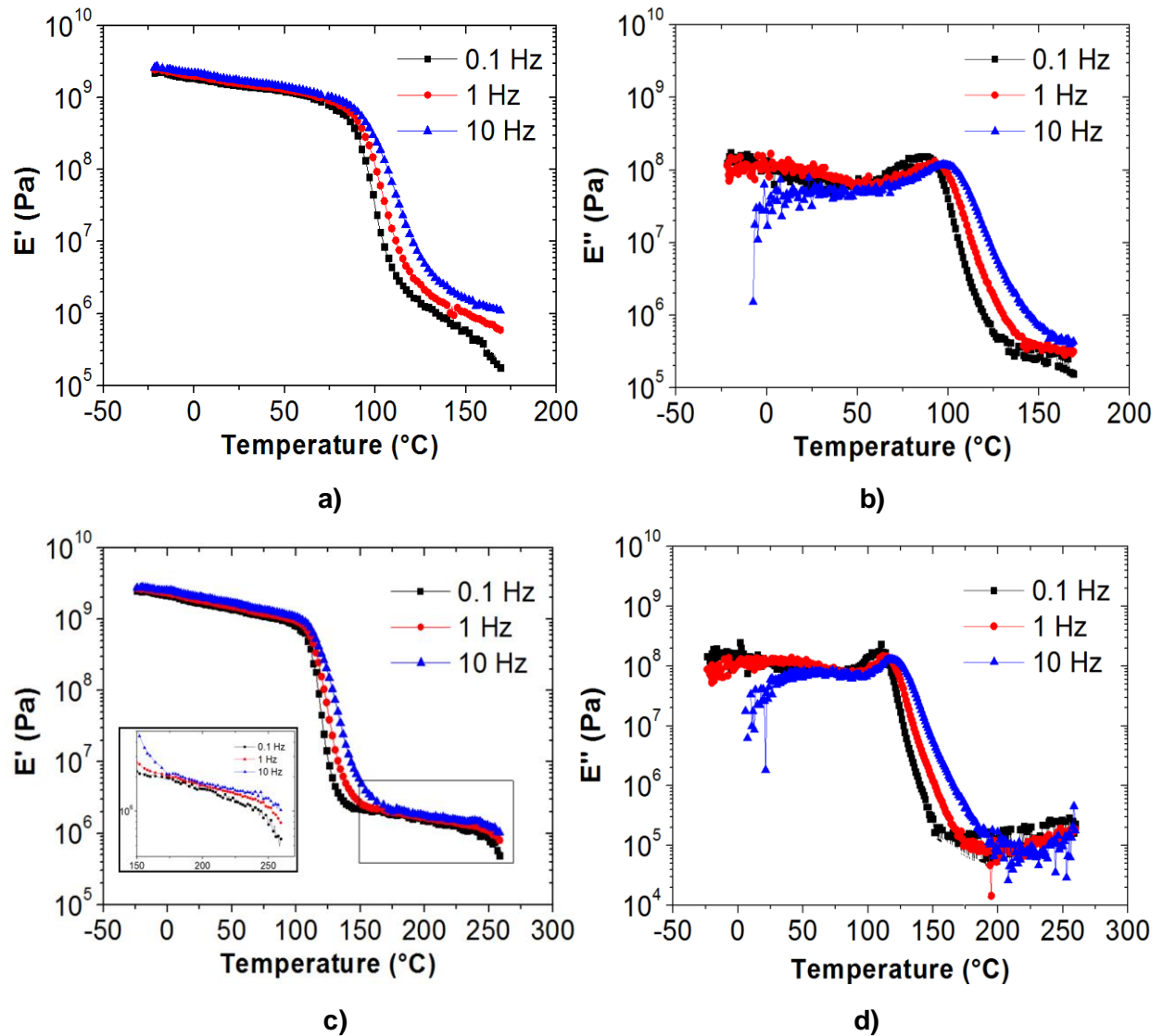


Figure 3.10: Storage and loss moduli evolutions with temperature at 0.1 Hz, 1 Hz and 10 Hz for a), b) PMMA 80 and c), d) PMMA 3500.

3.3.3 Time/temperature superposition principle on PMMAs with different molecular weight and cross-linking degree

Previous section introduced the overall linear viscoelastic response of PMMAs as a function of temperature, at constant frequencies for tensile loading. In this section, the goal is to address how the different PMMAs behave in a wide range of frequency. For this, we will use the time/temperature superposition principle for two types of loading: tensile and shear. This principle allows representing viscoelastic properties in terms of an equivalent frequency at reference temperature, f_0 , using a horizontal shift factor, a_{T_j/T_0} [4], [22], [57]:

$$f_0 = a_{T_j/T_0} f_j$$

3.3.3.1 PMMA Master Curves at Tensile and Shear Loading

First, frequency sweeps were performed under tensile loading. Figure 3.11 shows the master curves for the storage and loss moduli which were successfully built up for PMMA 80 with “horizontal” shift factors. This was done with a unique reference temperature, chosen at 130 °C for convenience since this temperature is near to the viscoelastic region for all the PMMAs. Thanks to this protocol, the linear viscoelastic response of the material was addressed over a wide range of frequencies, from 10^{-3} s^{-1} to 10^{16} s^{-1} , where the glassy region, viscoelastic zone and rubbery plateau are depicted. However, despite these tests, we were not able to observe the response in the flowing region.

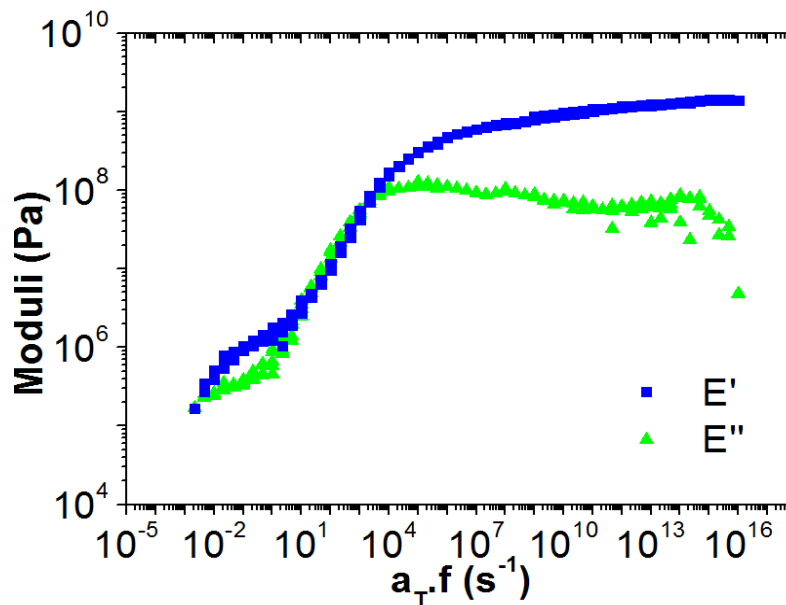


Figure 3.11: Master Curves of the storage and loss moduli in tensile loading for PMMA 80 at a reference temperature of 130°C.

For better characterizing the flowing region, we proceed by building master curves by using shear loading in two configurations: torsion and parallel discs. The torsional mode was used for characterizing the solid state and parallel discs mode for the flowing state. Figure 3.12 shows the master curves obtained for the storage and loss moduli on PMMA 80 for shear loading combining both configurations. The torsional mode allowed building the master curves from 10^{-3} s^{-1} up to 10^{12} s^{-1} using a reference temperature of 130°C, and addressing the glassy region, viscoelastic zone and rubbery plateau. At lower equivalent angular frequency, the material was too fluid for being analysed through torsional mode. We complemented these master curves in the flowing region by using parallel discs configuration, at a reference temperature of 130°C.

Figure 3.12 indicates that master curves built in shear loading can be superimposed by using the same reference temperature, even if the test configuration was different. Similar observation was made by Halary et al. for a copolymer [58]. This methodology allowed obtaining all the viscoelastic regions of our PMMAs for a wide range of angular frequency.

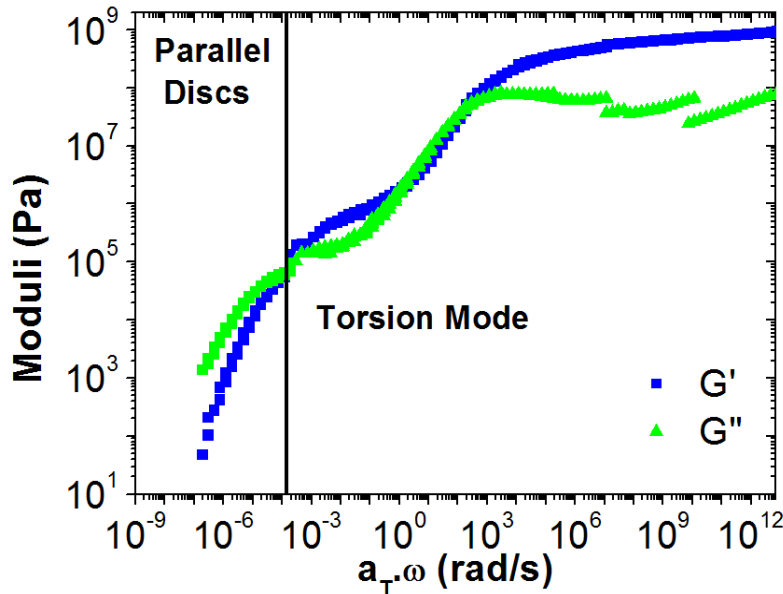


Figure 3.12: Master curves of the storage and loss moduli in shear loading for PMMA 80 at 130°C.

We will now compare the two loading modes (tensile and shear). Figure 3.13 a) displays the master curves of the storage shear modulus, G' , obtained by torsional loading and the tensile storage modulus, E' , obtained by DMTA for PMMA 80. The reference temperature of 130°C was used in both cases. We can notice that shear modulus is lower than the tensile one. In fact, both shear and tensile moduli were assumed to be related by the Hooke's Law expression as:

$$G^* = \frac{E^*}{2(1 + \nu_p^*)}, \quad 3.3$$

where ν_p^* is the Poisson's ratio. In the case of incompressibility, $\nu_p^*=0,5$ and therefore $E'=3G'$. For future studies, we recommend to perform confined compression tests to determine the bulk modulus, K^* , and obtaining a more accurate value of the Poisson's ratio in the studied conditions.

In our case, dividing E^* by a factor of 3 allowed to superimpose the tensile and shear measurements, as shown in Figure 3.13 b) at least in the viscoelastic and rubbery zones where assumptions concerning Poisson's ratio are valid. This suggests that rheology and DMTA are complementary techniques that can be used to characterize viscoelasticity up to the flow at small strain. Thanks to these master curves, the influence of the molecular weight and crosslinking on the viscoelastic response can be studied in the linear domain for PMMA materials.

The framework of this study is built for characterizing the mechanical response from the onset of the viscoelastic region up to the end of the rubbery plateau. Master curve will be used as a reference for defining the experimental conditions at the macroscopic level.

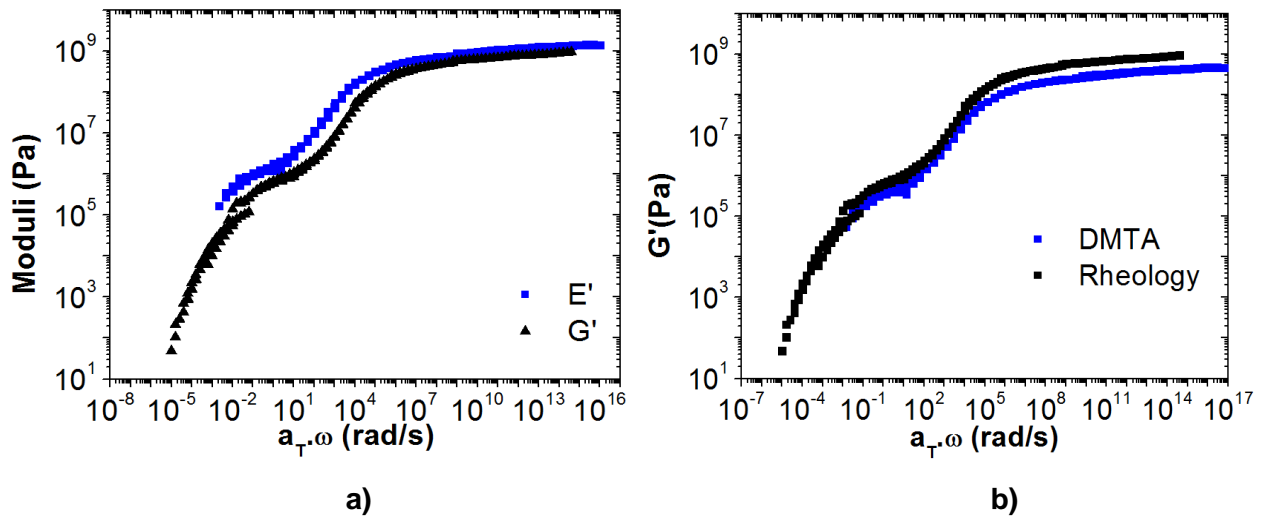


Figure 3.13: a) Comparison between master curves for tensile storage modulus, E' , and shear storage modulus, G' . b) Master curves of G' obtained by superposing DMTA and rheology results. Both curves were done for PMMA 80 at reference temperature of 130°C.

Since β -relaxation did not overlap with α -relaxation, shift factors were successfully identified manually using storage modulus, E' . Figure 3.14 shows the shift factors for PMMA CL determined from tensile and shear loadings. Shift factors nicely obey to Williams-Landel-Ferry, WLF, equation [22] (see Equation 3.4) at least in the viscoelastic region and rubbery zone.

$$a_{T_j/T_0} = 10^{\left(\frac{-C_1(T_2 - T_0)}{C_2 + T_2 - T_0}\right)}, \quad 3.4$$

where C_1 and C_2 are parameters related to T_0 , named reference temperature. Very often, C_1 may vary between 8 to 25 and C_2 from 25°C to 80°C.

Figure 3.14 reveals that the shift factor evolution varies with the loading state: higher values are found in tensile loading below the reference temperature while there are inferior above it. This suggests that frequency dependence of the material may depend on the loading state, being slightly less sensitive when material is submitted to shear condition. The physical origin of this observation is not fully understood, but these results will be relevant for future mechanical characterization at large deformations.

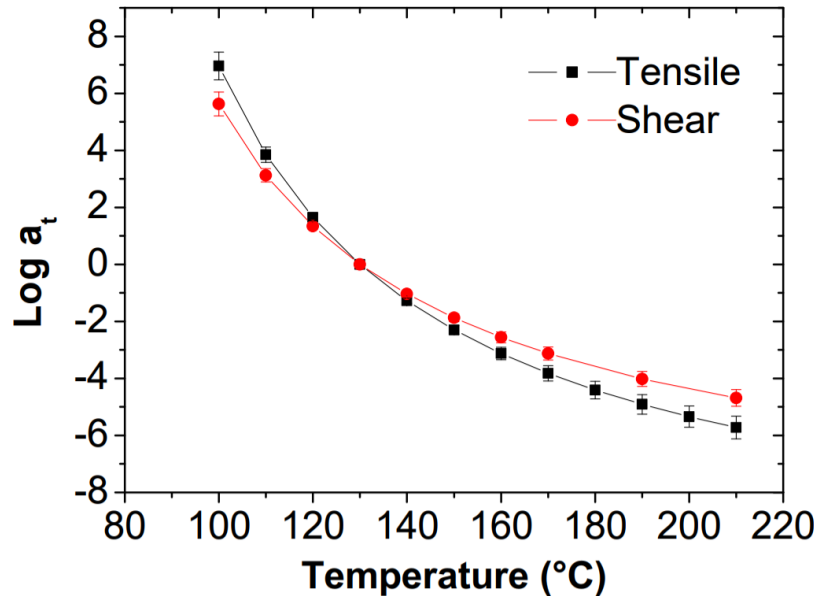


Figure 3.14: Shift factor evolution with temperature for PMMA CL for tensile and shear loadings. Reference temperature was taken at 130°C. Symbols indicate experimental values while the lines correspond to the identified WLF Equation.

3.3.3.2 Influence of the Molecular Weight and Cross-linking

After studying the effect of temperature, frequency and loading state on the mechanical behaviour of the material, we will investigate the influence of the polymer architecture, i.e. the molar mass and cross-linking. Figure 3.15 and Figure 3.16 display the master curves for the storage and loss moduli successfully built up for the five PMMAs with “horizontal” shift factors. A unique reference temperature, chosen at 130 °C was used for convenience. Regarding the molecular weight effect on viscoelastic region, results suggest that:

- The glassy region does not exhibit major variations.
- In the viscoelastic region, the storage and loss moduli increase with the molar mass due to the higher number of entanglements, which is coherent with the bibliography. However, PMMA 93 displays higher moduli in this region than PMMA 120, which seems to be

contradictory considering that PMMA 120 should have more entanglements. As explained in Section 2, this may be attributed to the high content of comonomers on PMMA 120 that grants more mobility to the polymer backbone in the viscoelastic region.

- In the rubbery plateau, increasing the molar mass leads to an increase of the storage and loss moduli and a wider rubbery plateau over the frequency range. For instance, PMMA 80 displays a rubbery plateau in a range of $10^{-2} \text{ s}^{-1} < a_{T_j/T_0} < 10^0 \text{ s}^{-1}$ while PMMA 3500 does at $10^{-12} \text{ s}^{-1} < a_{T_j/T_0} < 10^{-3} \text{ s}^{-1}$. These observations are likely due to a larger number of physical entanglements that will restrict the molecular motion.
- In the flowing region, PMMAs with the lowest molecular weight, i.e. PMMAs 80, 93 and 120, display flowing with moduli that rise with the molecular weight. For PMMA 3500, physical entanglements are so important that flowing does not take place in the studied range of frequency. This means that E'' was constantly lower than E' .

Concerning the crosslinking effect, we can notice that this material is equivalent to PMMA 3500 except in the flowing region that disappears or is postponed toward lowest equivalent frequencies. Indeed, the moduli for PMMA CL remain constant since crosslinking inhibits flow at high temperatures or low frequencies.

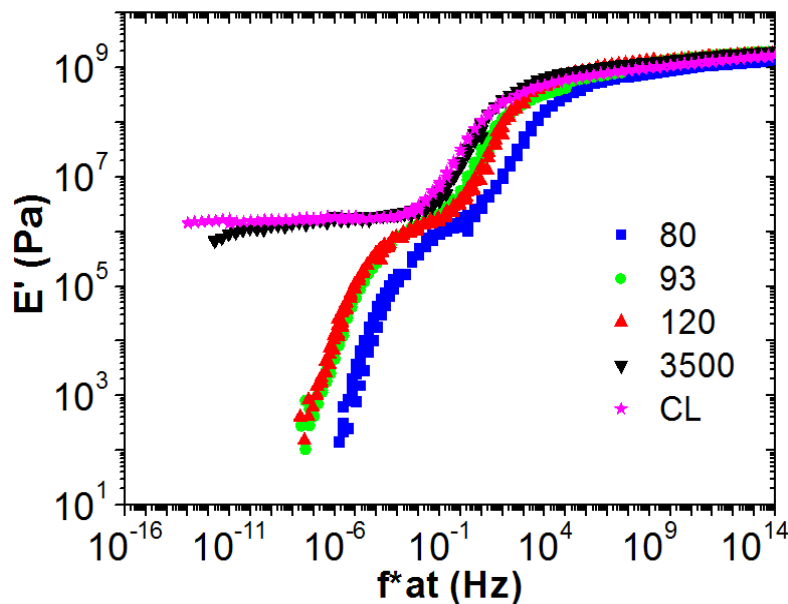


Figure 3.15: Storage modulus master curves for all PMMAs at a reference temperature of 130°C.

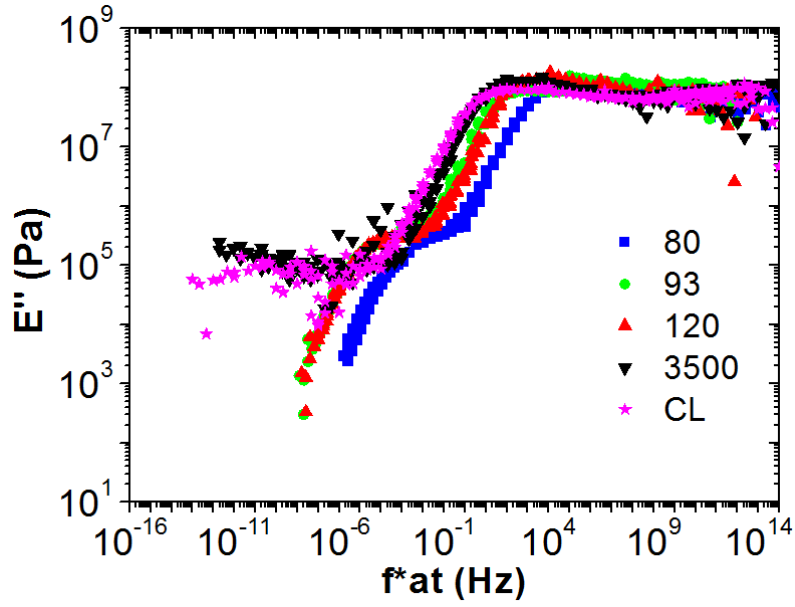


Figure 3.16: Loss modulus master curves for all PMMAs at a reference temperature of 130°C.

It has been seen that the increase on the molecular weight and the presence of crosslinking directly affect the viscoelastic response of PMMA in the linear domain. At this point, we have assumed that this is related to an increase in the number of entanglements with the molecular weight.

According to rubber elasticity theories [59], the shear modulus at the rubbery plateau, G_N^0 (corresponding to the shear storage modulus at the minimum of $\tan \delta$), allows estimating the average mass between crosslink. Extending this to entanglements, the mass between entanglement, M_e , should be such as [5], [23], [60], [61]:

$$G_N^0 = (G')_{\tan \delta \rightarrow \text{minimum}} = g_0 \frac{\rho RT}{M_e}, \quad 3.5$$

where ρ is the polymer density at the absolute temperature T and R is the gas constant. g_0 is equal to 1 if entanglements are considered as chemical cross-links [22], and 4/5 otherwise according to reptation theory.

The density of entanglements is then:

$$\nu_e = \frac{\rho N_A}{M_e}, \quad 3.5$$

where N_A is the Avogadro number. According to [1] and [61], a polymer network has a number of entanglements of the order of 10^{25} or 10^{26} per cubic meter.

Additionally, entanglements appear after overcoming a critical molecular weight, M_{cr} . Direct empirical relationship between this magnitude and the molecular weight between entanglements, M_e , has been previously used by [15] and [62]:

$$M_{cr} = 2M_e, \quad 3.6$$

Figure 3.17 depicts the evolution of the critical molecular weight for entanglements apparition, M_{cr} , the molecular weight between entanglements, M_e , and the entanglements density, ν_e , with the molecular weight. These results were deduced from DMTA analysis and equations 3.-3.6. All the experimental data were described by a Flory-Fox equation.

First, the critical molecular weight for entanglement apparition of each PMMA was lower than its respective molecular weight (see Table 2.1). This means that entanglements are present and a temporary network already exists for all the materials. Figure 3.17 also suggests that the molecular weight between entanglements decreases with the material molecular weight. This confirms that polymer chains tend to entangle more when they are longer. Moreover, if the molecular weight between entanglements decreases with M_w , this means that the average number of entanglements should increase when the molecular weight is higher. This is depicted in Figure 3.17 where the average entanglements density increased from 0.8×10^{26} entanglements per cubic meter for PMMA 80 to 1.6×10^{26} entanglements per cubic meter for PMMA 3500. This increase in the average number of entanglements restricts the molecular mobility, which agrees with the effect of the molecular weight on the moduli observed in Figure 3.15 and Figure 3.16.

For the crosslinked PMMA, results reveal that the molecular weight between entanglements is higher than the one on PMMA 3500 and therefore, the average density of entanglements for PMMA CL is lower than for PMMA 3500. This may be attributed to the factor g_0 in Equation 3.5. This suggests that crosslinks are more effective to hinder molecular motions than physical entanglements. Indeed, results reveal that a higher density of entanglements is needed to promote the same storage modulus of a crosslinked PMMA.

As depicted in Figure 3.8 and Figure 3.17, physical parameters were described with the Flory-Fox equation. However, this is just a hypothesis since some data points are missing by the lack of PMMAs showing different molecular weights. As perspective, we will recommend to work with PMMAs of different molecular weights such as 300 Kg/mol, 700 Kg/mol, 1000 Kg/mol and 2000 Kg/mol for proving if Flory-Fox equation are describing the kinetics of the parameters showed in these Figures, or to propose any other empirical relationship.

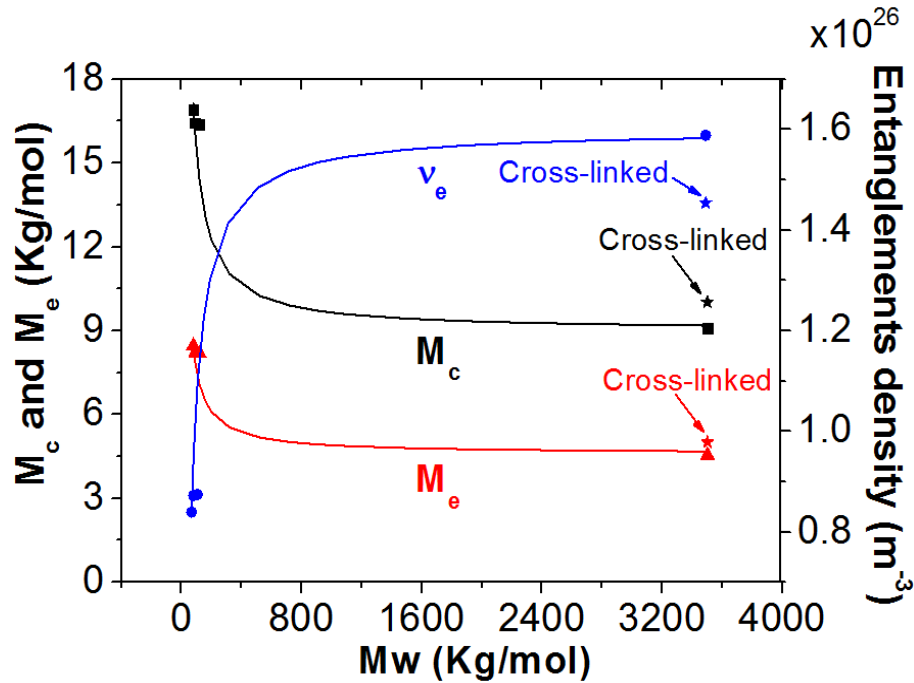


Figure 3.17: Evolution of the critical molecular weight between entanglements, M_{cr} , molecular weight between entanglements, M_e , and entanglements density, v_e , with the weight average molecular weight.

So far, shift factors were determinant for obtaining master curve of the PMMAs. These were successfully identified for tensile and shear loading. Figure 3.18 displays these values for the different PMMAs under tensile load. Shift factors nicely obey to the WLF equation (see Equation 3.) at least in the viscoelastic region and rubbery zone (i.e., up to 170°C for entangled PMMAs and up to 230°C for cross-linked PMMA).

Regarding PMMA 3500, a double kinetic process for the shift factor was obtained. Especially, WLF was accurate up to 180°C and was then no longer valid. Indeed, an Arrhenius law was more relevant from 180°C up to 230°C to describe the shift factors:

$$a_{T_j/T_0} = \exp\left(\frac{Q_{plateau}}{R} \left(\frac{1}{T} - \frac{1}{T_0}\right)\right) \quad 3.7$$

where $Q_{plateau}$ is the activation energy in the rubbery plateau and T_0 is the reference temperature in Kelvin. Using WLF and Arrhenius relationships allowed describing shift factors in an accurate manner for a wide range of temperatures. However, notice that the transition between the two expressions (in the range of 170°C and 180°C) is not continuous and may lead to inaccurate predictions. Nevertheless, this was not a big issue as the shift factor values were discrete, and could be experimentally determined if needed. Another option is to use a piecewise function as suggested in Appendix 8.4.

The values obtained for the parameters C_1 , C_2 and $Q_{plateau}$ are displayed in Table 3.1 for those computed from tensile loading and Table 3.2 for the ones computed from shear loading. These were determined using 130°C as reference temperature.

Table 3.1: WLF and Arrhenius parameters for the different PMMAs under tensile loading.

| PMMA | C_1 | C_2 (K) | $Q_{plateau}$ (K.J/mol) |
|-------------|-------------------------|-----------------------------|-------------------------------------------|
| 80 | 4.5 | 66.3 | - |
| 93 | 6.6 | 64.7 | - |
| 120 | 7.8 | 77.7 | - |
| 3500 | 8.8 | 68.1 | 344.1 |
| CL | 11.5 | 79.2 | - |

Table 3.2: WLF and Arrhenius parameters for the different PMMAs under shear loading.

| PMMA | C_1 | C_2 (K) | $Q_{plateau}$ (K.J/mol) |
|-------------|-------------------------|-----------------------------|-------------------------------------------|
| 80 | 6.6 | 87.8.0 | - |
| 93 | 9.2 | 80.0 | - |
| 120 | 8.5 | 75.8 | - |
| 3500 | 10.3 | 83.3 | 329.3 |
| CL | 9.5 | 80.0 | - |

Regarding the effect of the molecular weight on these shift factors, Figure 3.18 suggests that the kinetics of the shift factors with the temperature varies for the different PMMAs, tending to occur faster when the molecular weight increases and/or with the presence of crosslinking. Shift

factors were determined mainly in the viscoelastic region and rubbery plateau, so they could be related to the activation energy of the α -relaxation (Figure 3.8). It was previously observed that Q_α increased with the molecular weight. Thus, it seems that the activation energies and the rate with which shift factors change could be linked since both increases with the molecular weight.

As described in Section 3.3.1, the increase of the activation energies with the molecular weight suggests that the α -transition requires higher frequencies to be affected. Indeed, shift factors relate the difference of loading frequency that have to be applied for having the same transition at two different temperatures. Thus, their increase with the molecular weight may suppose that higher variation of frequency is needed to have the same response. This will be a main factor for characterizing the macroscopic mechanical behaviour of PMMAs in the next Section.

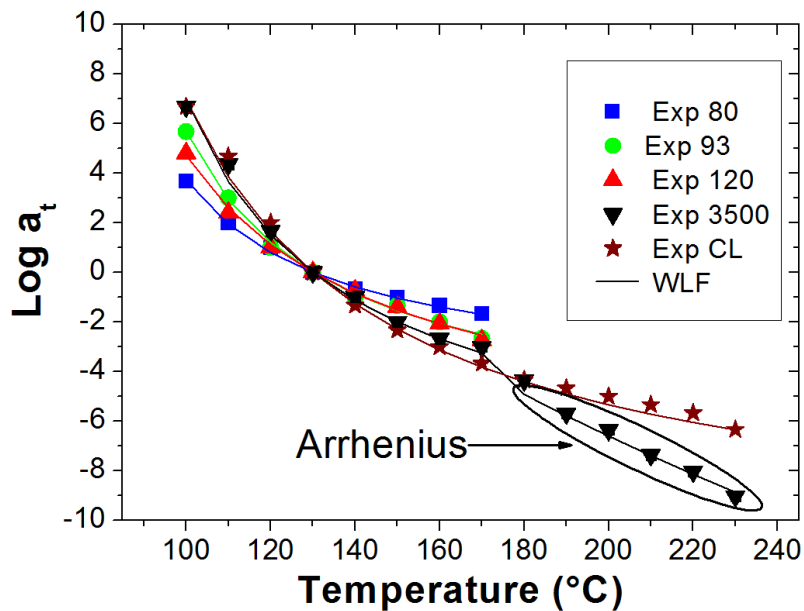


Figure 3.18: Shift factor vs temperature for the different PMMAs. Symbols represent experimental data. Straight lines represent Equations 2 and 5 with parameters from Table 3.1.

3.4 Summary

In this Chapter, a characterization of the linear viscoelastic behaviour of the five PMMAs was done by submitting the materials to tensile and shear loadings.

Two mechanical relaxations were addressed on PMMA: a solid state β -transition related to the rotation of the ester group and a main α -relaxation related with cooperative motions in the amorphous phase. The activation energy for secondary transition was considerably lower than the activation energy of α -relaxation, indicating that the secondary relaxation has higher sensitivity to the frequency. Results showed that the experimental conditions did not promote

$\alpha\beta$ -process. Moreover, it was found that the activation energy for the α -transition increases with the molecular weight as it did for the transition temperature.

Master curves were built up for all PMMAs employing “horizontal” shift factors, with a unique reference temperature, chosen at 130 °C. Using these master curves, the linear viscoelastic response of the material was addressed accounting for the glassy region, viscoelastic zone and rubbery plateau. For studying the flowing region, rheological tests in shear loading were used. By relating the tensile and shear storage moduli through $E' = 3G'$, it was possible to overlap both curves obtaining a global picture of the viscoelastic response. Thanks to these master curves, the influence of the molecular weight and cross-linking on the viscoelastic response at the linear domain for PMMA was deeply studied.

Regarding the effect of the molecular weight on the linear viscoelastic response, we observed that in the viscoelastic region, rubbery plateau and flowing state, the storage and loss moduli increased with the molar mass. Additionally, the extension of the moduli over the frequency in the rubbery plateau was enlarged with the increase of the molar mass. This is likely due to the rise of physical entanglements that restricted the molecular motions.

Concerning the crosslinking effect on the linear viscoelastic response, we made a comparison with PMMA 3500. In the glassy and viscoelastic regions the storage and loss moduli are similar, suggesting that physical entanglements and chemical crosslinks restrict in a similar manner the molecular motion. In the rubbery plateau, E' remained constant for PMMA CL while on PMMA 3500 gradually decreased when reducing the equivalent frequency. This confirmed that chemical crosslinks do not disappear with time/temperature.

Shift factors were successfully identified for the five PMMAs under tensile and shear loadings. They nicely obeyed to WLF equation at least in the viscoelastic region and rubbery zone. PMMA 3500 presented a double kinetic process for the shift factor, described by the WLF and Arrhenius laws. Shift factors evolution also shows dependence to the stress state and to the polymer architecture. Moreover, variation of shift factors with temperature were more relevant when the molecular weight increases and with the presence of crosslinking.

CHAPTER IV

MECHANICAL BEHAVIOUR OF PMMA_s AT LARGE DEFORMATION: COUPLING OF TEMPERATURE/STRAIN RATE EFFECTS

This Chapter presents experimental evidence of the effect of the temperature, strain rate, stress state, entanglement density and crosslinking degree on the mechanical properties of PMMA at large deformation levels. This study was carried out by coupling the temperature/strain rate effects in one parameter called “equivalent strain rate” at reference temperature which allowed simplifying the experimental characterization. First, we illustrate the individual effect of the temperature and strain rate on the finite domain of deformation. After verifying that they have inverse effects, we extrapolated the time/temperature superposition principles from the linear domain to the large deformation domain. We experimentally proved for several temperature/strain conditions that the stress-strain curves were similar as far as the equivalent strain rate was the same. This was proven for tensile and shear loading, and for five different PMMA_s with different molecular weights and crosslinking degrees. By choosing specific equivalent strain rate, the effect of stress state, molecular weight and crosslinking degree were then studied. It was found that the type of loading strongly affects the mechanical response likely to the mechanisms of the molecular motions during the deformations. Moreover, the molar mass and crosslinking were found to govern the macroscopic mechanical response, and more especially the elastic and inelastic responses.

Ce chapitre présente des résultats expérimentaux de l'effet de la température, de la vitesse de déformation, de l'état de contrainte, de la densité d'enchevêtrement et du degré de réticulation sur les propriétés mécaniques du PMMA à des niveaux de déformation importants. Cette étude a été réalisée en couplant les effets température/vitesse de déformation en un paramètre appelé «vitesse de déformation équivalent» à température de référence qui a permis de simplifier la caractérisation expérimentale. Dans un premier temps, nous illustrons l'effet individuel de la température et de la vitesse de déformation sur le domaine de déformation linéaire. Après nous avons extrapolé les principes de superposition temps/température du domaine linéaire aux grandes déformations. Nous avons expérimentalement prouvé que les courbes contrainte-déformation étaient similaires dans la mesure où la vitesse de déformation équivalente était la même. Ceci a été prouvé pour la charge de traction et de cisaillement, et pour cinq PMMA avec topologies différents. En choisissant une vitesse de déformation équivalente spécifique, l'effet de l'état de contrainte, de la masse molaire et du degré de réticulation a ensuite été étudié. Il a été constaté que le type de chargement affecte fortement la réponse mécanique. De plus, la masse molaire et la réticulation se sont avérées gouverner la réponse mécanique macroscopique, et plus particulièrement les réponses élastiques et inélastiques.

CONTENT

| | | |
|-------|--------------------------------------------------------------------------------------------------------------------------|----|
| 4 | Mechanical Behaviour of PMMAs at Large Deformation: Coupling of Temperature/Strain Rate Effects | 53 |
| 4.1 | Importance of non-monotonic mechanical tests..... | 54 |
| 4.2 | Effect of the temperature and strain rate on the mechanical behaviour of polymers | 55 |
| 4.2.1 | Temperature effect..... | 55 |
| 4.2.2 | Strain rate effect..... | 56 |
| 4.3 | First approaches on extrapolating the time/temperature superposition temperature at large deformations | 57 |
| 4.4 | Topological effects on the mechanical behaviour of polymers | 63 |
| 4.5 | Results and Discussions | 65 |
| 4.5.1 | Global mechanical response | 65 |
| 4.5.2 | Effect of the temperature on PMMA | 67 |
| 4.5.3 | Effect of the strain rate on PMMA..... | 69 |
| 4.5.4 | Coupling the temperature/strain rate effect at large deformations: Equivalent strain rate at reference temperature | 71 |
| 4.5.5 | Stress state effect on the mechanical response | 85 |
| 4.5.6 | Molecular Weight and Cross-linking Effect on the Mechanical Response at Large Deformation..... | 89 |
| 4.6 | Summary..... | 95 |

4 Mechanical Behaviour of PMMAs at Large Deformation: Coupling of Temperature/Strain Rate Effects

In the previous Chapter, it was shown that the mechanical response in the linear domain was strongly dependent of the loading frequency, temperature, molar mass and crosslinking degree. Thus, these factors need to be taken into account for the material characterization at large deformation levels.

Authors [11], [21], [63]–[67] have suggested that mechanical characterization can be simplified by extrapolating the time/temperature equivalence from the linear domain of deformation to the large strain domain. However, this area has also some room for improvement.

Indeed, most of the work addressed the validity of the time/temperature equivalence at large deformation for monotonic loading under conditions either above or below the glass transition. However, few studies have validated this equivalence to the overall viscoelastic region for non-monotonic loading. Additionally, most of the studies have been performed under tensile and compression loadings. Few validations of the equivalence have been done yet for other stress states. Finally, there is a lack of information on the feasibility of the time/temperature equivalence principle at large deformation for polymer with different molar masses and crosslinking degree. This is a main aspect for characterizing and understanding the molecular mobility at large deformation. All these factors may enhance the processing modelling of polymers in the rubbery state.

The aim of the study presented in this Chapter, is to explore the ability of equivalent strain rate at reference temperature to be a convenient parameter to account for temperature and strain rate effects for characterizing PMMAs of different architectures. More especially, we target:

- To extrapolate the time/temperature equivalence from small to large deformation from the onset of the viscoelastic region to the onset of the flow region. This topic will be first studied for unloading-unloading tensile tests.
- To verify if this equivalence may be used at finite strain in another stress state than tensile loading. For this case, shear loading will be examined.
- To prove if this methodology also works for polymer systems of different architectures. The superposition principle will be tested at large deformation level for five PMMAs with different entanglements and cross-links densities.

- To compare the mechanical behaviour at large deformation between polymer systems that are physically entangled and chemically crosslinked.

Before presenting the results, we will present bibliographic aspects related to the factors to be considered for characterizing the mechanical behaviour of polymers at large deformation. Indeed, we will first introduce the importance of performing non-monotonic mechanical tests. Then, the influence of the temperature and strain rate will be investigated. Later, we will present the first attempts to couple strain rate and temperature dependencies into one parameter. At last, we will introduce the role of the molar mass and crosslinking degree in the mechanical response.

4.1 Importance of non-monotonic mechanical tests

Very often, monotonic tensile loading is used to describe the mechanical response of polymers. However, this does not allow fully discriminating the mechanical behaviour as such loading does not allow characterizing the reversible and irreversible behaviour of the polymer. For doing such discrimination, it is necessary to perform non-monotonic tests and apply cyclic loading for verifying the energy dissipation [11], [21], [25], [68]–[70].

Figure 4.1 shows an example of three possible mechanical responses of an amorphous polymer above its glass transition temperature after being submitted to an uploading-unloading test. The case 1 shows that the stress during the load and unload path is the same, which means that there is no energy dissipation. This behaviour is hyperelastic and is related to non-linear elasticity. The case 2 displays energy dissipation related to an increase in hysteresis with some residual strain after unloading. Thus, the material has features regrouping hyperelasticity, viscoelasticity and plasticity. Finally the case 3 shows a material which exhibits hyperelastic behaviour during uploading but, displays during unloading, an important residual strain and hysteresis, related to plasticity. These are some of the many possible mechanical responses that a polymer can exhibit.

Therefore, cyclic tests are more reliable for characterizing the material since they illustrate the non-reversible contributions to stress, which are related to evolutions of the material internal variables under deformation. This is fundamental for discriminating the reversible from the irreversible part of the strain, which is needed for modelling the mechanical response of the polymer. Thus, uploading-unloading tests will be used for fully characterizing the different PMMAs.

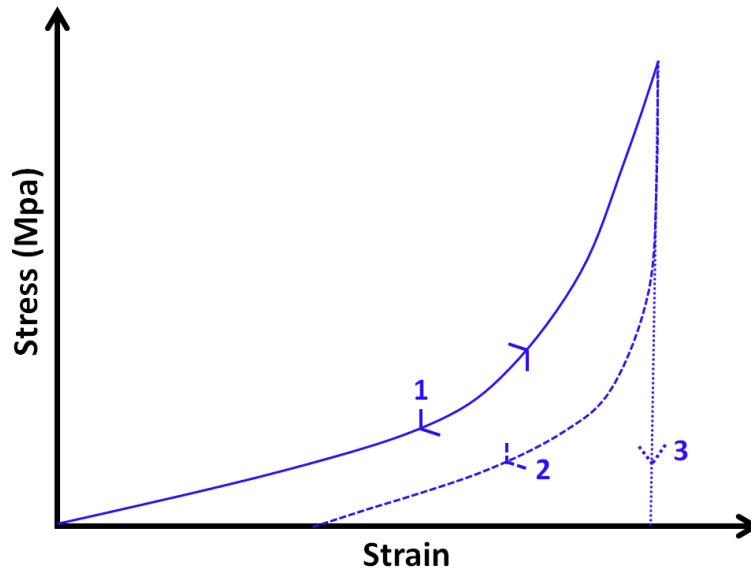


Figure 4.1: Schematization of three possible mechanical responses of a polymer for uploading-unloading test.

4.2 Effect of the temperature and strain rate on the mechanical behaviour of polymers

4.2.1 Temperature effect

Arruda et al. [12] and Richeton et al. [14] studied the effect of the temperature on the mechanical response of different amorphous polymers: PC, PMMA and PAI. This is depicted in Figure 4.2. It can be seen that initial modulus and yield decreases with an increase of temperature. Strain hardening considerably decreases with the temperature. In general, higher temperatures increase the molecular mobility and decrease the mechanical stiffness of the polymer. Additionally, they also suggested that the behaviour tends to be hyperelastic above T_g . This has been also proposed by G'Sell and Haudin [13] by observing that the polymer behaviour tends to be more rubbery above the glass transition temperature.

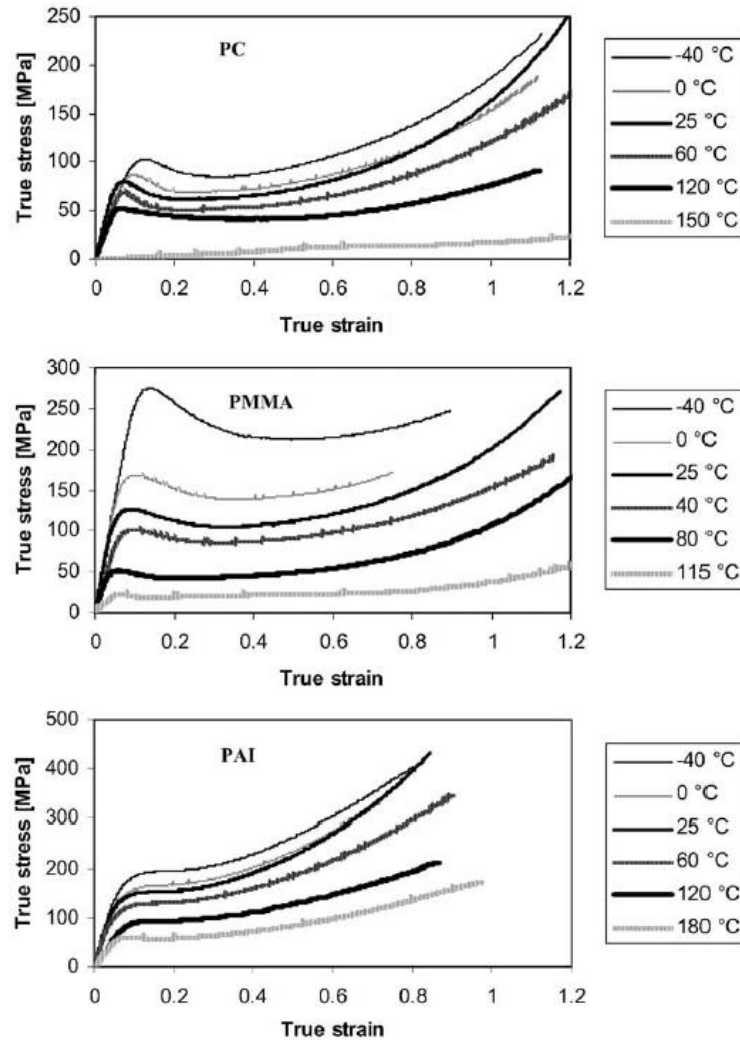


Figure 4.2: Experimental uniaxial compression stress-strain curves for PC, PMMA and PAI at the strain rate of 0.01 s^{-1} over a wide range of temperatures. [14]

4.2.2 Strain rate effect

Richeton et al. [14] also analysed the effect of the strain rate on the stress-strain curves for amorphous polymers. This is depicted in Figure 4.3. Observations showed that the modulus and yield increase when increasing the strain rate. Many authors (Xiao et al [71]; Chen et al [72]; Brulé et al [73]; Rana et al [74]; Richeton et al.[75]) suggested that an increase of the strain rate will decrease the time necessary for the polymer chains to rearrange, decreasing molecular mobility and making the chains stiffer. In parallel, the increase of strain rate promotes an adiabatic heating effect. In general, this thermal effect becomes relevant at strain rates above 0.01 s^{-1} .

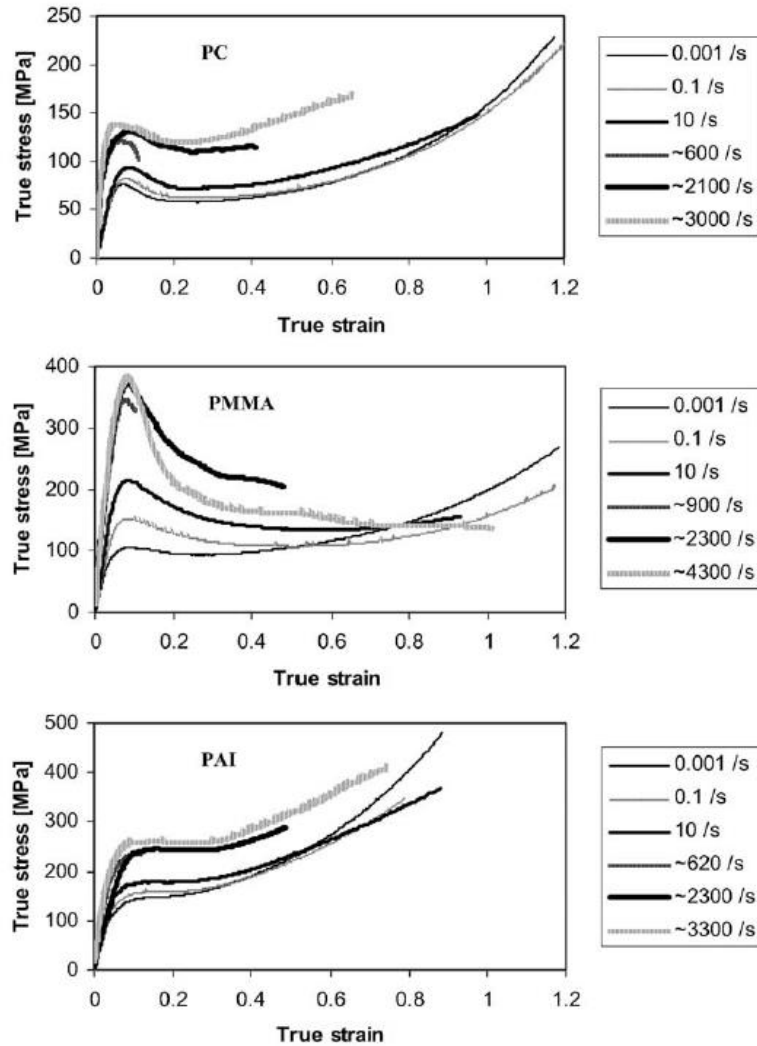


Figure 4.3: Experimental uniaxial compression stress-strain curves for PC, PMMA and PAI at the temperature 25°C, over a wide range of strain rates. [14]

At this point, it can be confirmed that polymers are highly sensitive to temperature and strain rate at large deformation levels. However, most of the analyses in the glassy region rely on a vision of viscoelastoplastic framework. However this framework is not relevant in our case as drastic changes in behaviour can be experienced above T_g .

4.3 First approaches on extrapolating the time/temperature superposition temperature at large deformation

So far, it has been observed that polymers are highly sensitive to the temperature and strain rate in the linear and non-linear domains. The characterization of such dependence may require an incredible number of experimental tests for building a representative material database and also

a vast number of parameters for constitutive equations. From an industrial point of view, this is expensive and highly time-consuming.

Roughly speaking, mechanical properties in the linear viscoelastic region and non-linear domain depend in a similar fashion on the strain rate and the temperature [2], [12], [76]. Therefore, for simplifying the number of tests and parameters required for describing the mechanical response of polymers, previous studies by Billon et al. [11], [21] suggested that constitutive parameters could be defined as depending on the so-called “equivalent strain rate at reference temperature” by taking advantage of the well-known time-temperature superposition principle in the linear domain [22]. Such principle may allow to couple dependencies on strain rate and temperature when classical material databases are built based on the separation of these two conditions.

Only few attempts were made to use similar approaches for simplifying the mechanical characterization on polymers. Neviere [63] used an extension of the time/temperature superposition principle to study the tensile response of non-linear viscoelastic solids such as filled elastomers. By first determining the shift factors in the linear domain, he was able to obtain two independent normalization factors that were applied to strain and stress. Figure 4.4 a) shows the tensile response of the filled elastomer at different temperatures. Figure 4.4 b) shows the superposition of the previous curves into a unique master curve using normalization depending on the maximum stress and modulus at each temperature condition. He also experimentally validated this principle for volumetric and biaxial behaviour.

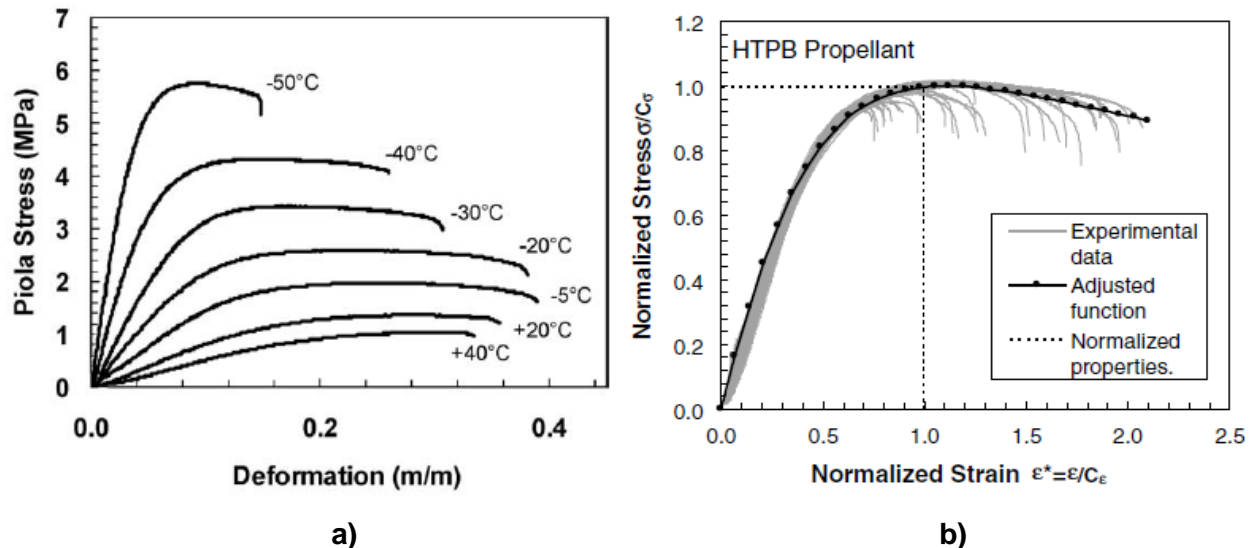


Figure 4.4: a) Uniaxial tensile test results for a filled elastomer at different temperatures. b) Superposition of the sets of tensile stress – strain response into a unique curve. [63]

Similarly, attempts to link the time/temperature superposition principle in the non-linear domain have been investigated for reproducing the mechanical response of polymers at high strain rates [65], [77], [78]. More precisely, Siviour et al. [66] and Furmanski et al. [64] proposed experimental methods to reproduce the mechanical response of a polymer deformed at high strain rates level performing testing at low strain rates with appropriate temperature profiles. They also accounted the effects of adiabatic heating.

They first proposed to map the dependence of the yield stress with temperature at constant strain rate as suggested by other authors [14], [64], [75], [78]–[80]. This mapping is illustrated in Figure 4.5 and can be described empirically as:

$$T_{Eq} = T_{Test} + A[\log_{10}(\dot{\epsilon}_{Eq}) - \log_{10}(\dot{\epsilon}_{Test})], \quad 4.1$$

where $\dot{\epsilon}_{Eq}$ is an equivalent strain rate and $\dot{\epsilon}_{Test}$ is the actual test strain rate. These two strain rates correspond to the temperatures T_{Eq} and T_{Test} . A is an experimentally identified parameter that relates the temperature and strain rate sensitivity of the mechanical response. For instance, HDPE and UHMWPE materials showed temperature/strain rate sensitivity higher than pPVC. Siviour et al. [66] used this mapping to determine the initial temperature of testing at low strain rates and then to simulate the modulus and yield stress response at higher strain rates.

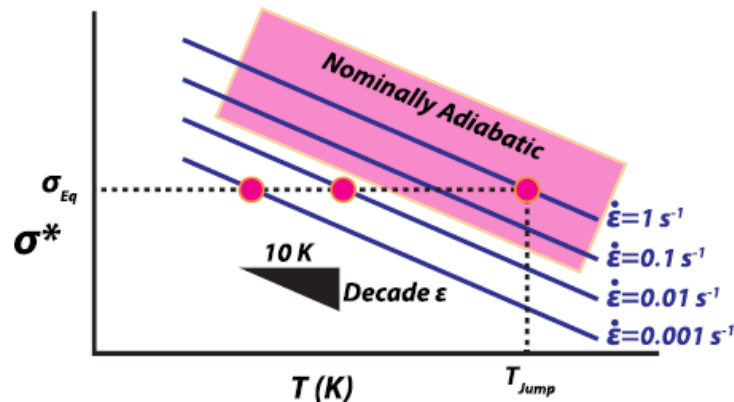


Figure 4.5: Yield stress dependence on temperature for multiple strain rates at fixed deformation. [64]

The authors also accounted for the adiabatic condition when simulating the mechanical response at high strain rate from low strain rate data by assuming that the temperature increase was induced by the onset of plastic work. The following equation was used:

$$\Delta T_{(\varepsilon)} = \frac{1}{\rho C_p} \int_{\varepsilon_y}^{\varepsilon} \beta_{(\varepsilon, \dot{\varepsilon})} \sigma d\varepsilon,$$

where C_p is the heat capacity of the polymer and β is the fraction of plastic work converted to heat. Some authors found that for large tensile deformation (in HDPE), plastic work was nearly totally converted into heat, i.e., $\beta \sim 1$ [81]. Other works [82], [83] found that, at moderate strain level, the conversion into heat is lower due to viscoelastic recovery. Siviour et al. [66] chose to use $\beta = 1$ for their computations.

Figure 4.6 a) illustrates the methodology to reproduce adiabatic heating obtained at high strain rates from tests performed at low strain rates. Figure 4.6 b) shows experimental results on pPVC where a mechanical behaviour was simulated at 15 s^{-1} and 20°C from a test performed at 10^{-3} s^{-1} and 0°C .

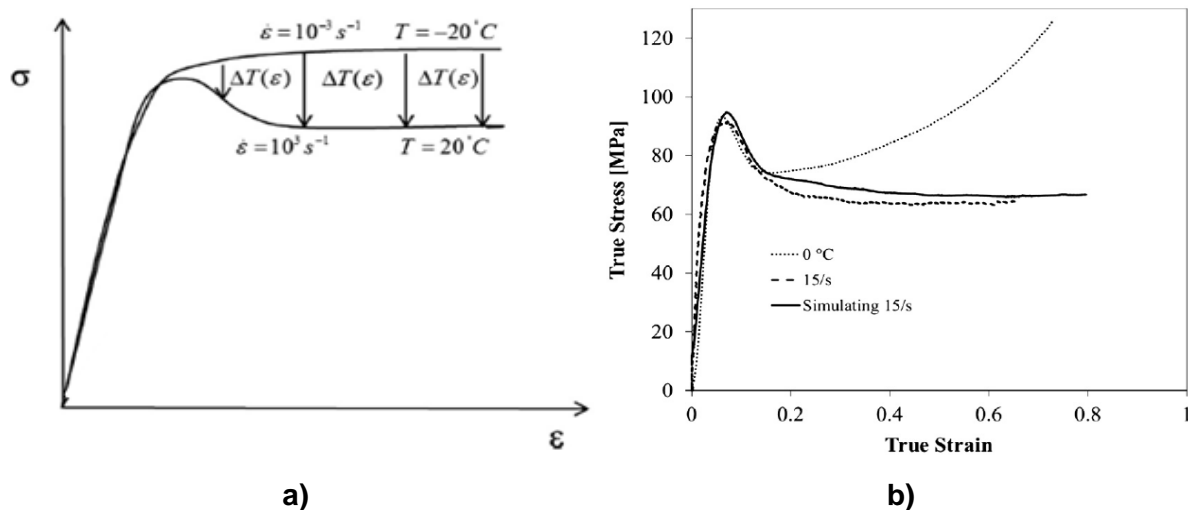


Figure 4.6: a) Methodology to reproduce adiabatic heating obtained at high strain rates from tests performed at low strain rates. b) Experimental and simulated curves obtained for tests performed at 15 s^{-1} and 20°C on pPVC.[66]

Works of Furmanski et al. [64] also targeted to extrapolate the time/temperature equivalence at large strain for compression tests performed on UHMWPE. The authors used strain rate jumps to account for adiabatic heating.

Figure 4.7 illustrates this technique. In Figure 4.7 a), the strain evolution with time (solid) and strain rate jumps at different strain levels are shown. Figure 4.7 b) displays the ideal isothermal viscoplastic response expected after using the strain jumps. Figure 4.7 c) shows the real mechanical response where adiabatic heating appears and increases progressively with the

accumulation of plastic work. Their approach successfully described the mechanical response of semicrystalline polymer at high strain rates (above 0.1 s^{-1}) accounting for adiabatic heating.

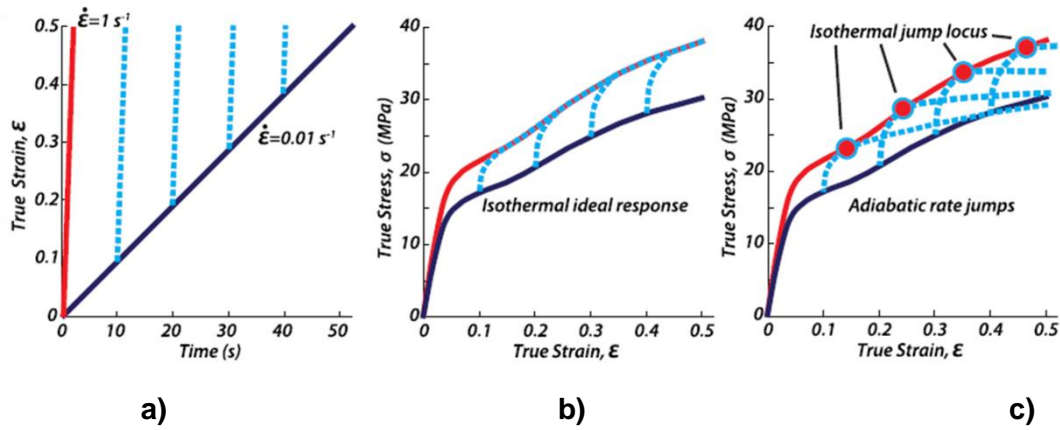


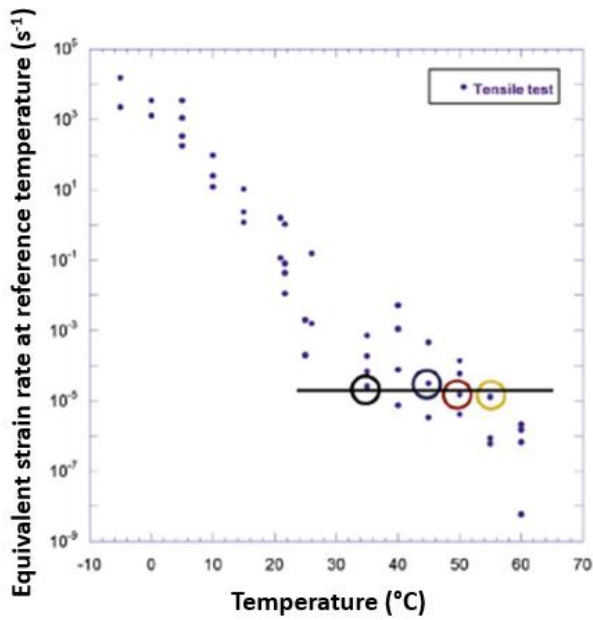
Figure 4.7: Strain jump technique for accounting adiabatic heating. [64]

Additionally, work of Billon et al. [11] on PMMA and Maurel-Pantel et al. [21] on PA66, was able to extrapolate the time/temperature superposition principle for non-monotonic loading. Their idea was to obtain the shift factors from infinitesimal strain tests performed on DMTA and extrapolate those conditions at large deformation. This was done through an “equivalent strain rate at reference temperature” using a similar expression as presented in Chapter III, Equation 3.1:

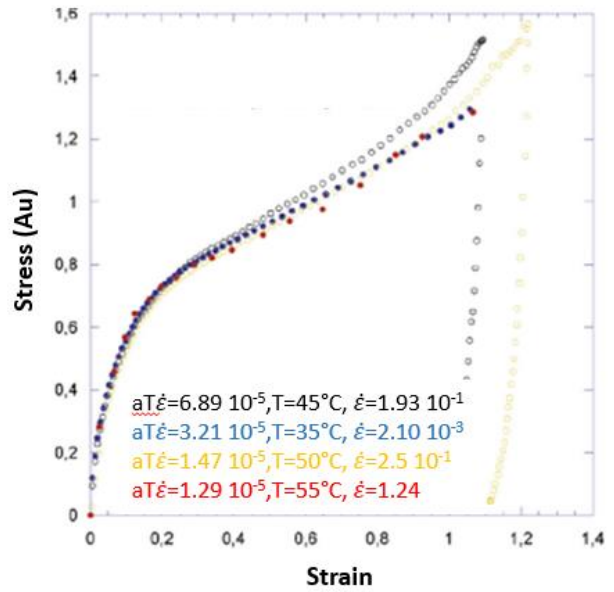
$$\dot{\varepsilon}_{eq} = a_{T_2/T_0} \dot{\varepsilon}, \quad 4.3$$

where $\dot{\varepsilon}$ is the experimental applied strain. Figure 4.8 a) shows the 46 conditions of strain rate/temperature coupled with Equation 4.3. Taking $\dot{\varepsilon}_{eq} \approx 10^{-5} \text{ s}^{-1}$, it can be seen on Figure 4.8 b) that the mechanical response is similar at large deformation for the different couples. This methodology is a way of reducing the number of experimental tests needed to capture the polymer mechanical response under tensile loading.

Additionally, Diani et al. [67] used shift factor determined from infinitesimal uniaxial tensile and torsional tests for applying the time/temperature superposition principle for uniaxial tensile tests until failure. The study was performed on an acrylate copolymer. Figure 4.9 a) and b) show the stress-strain curves obtained for different sets of temperature and strain rates leading to the same equivalent strain rate. By using the same definition of “equivalent strain rate at reference temperature” as Billon et al. [11], experimental evidence was obtained on the validity of the time/temperature equivalence at infinitesimal strain and finite strain.

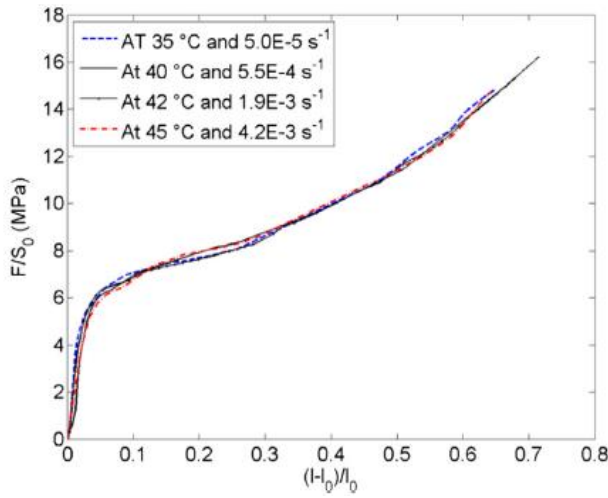


a)

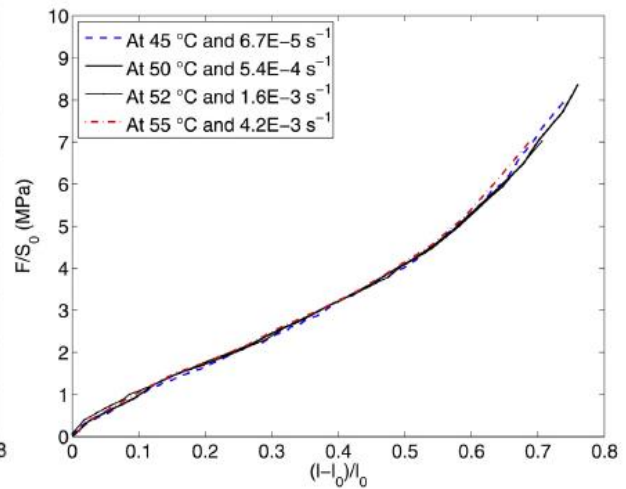


b)

Figure 4.8: Experimental time/temperature equivalence validation: a) Experimental coupled testing conditions. b) Tensile stress-strain curves at $\dot{\epsilon}_{eq} \approx 10^{-5} s^{-1}$. [21]



b)



b)

Figure 4.9: Experimental evidence of the time/temperature equivalence at finite strain. Uniaxial tensile stress-strain curves. a) Visco-elasto-plastic behaviour, b) Visco-hyperelastic behaviour.

[67]

4.4 Topological effects on the mechanical behaviour of polymers

Besides the effect of temperature and strain rate on the mechanical response of polymers, the molecular weight and crosslinking may also affect the polymer mechanical behaviour at large deformation levels.

4.4.1.1 *Molecular weight effect*

The increase of the molecular weight promotes entanglements which affect the mechanical behaviour of the polymer at large deformations [84]–[87]. Indeed, there are three main aspects of entanglements to be considered: influence on the deformability, effect on the mechanical stiffness and sensitivity to time/temperature effects.

Regarding to the deformability, Prentice et al. [88] and Nunes et al. [15] found that amorphous polymer tested at constant temperature and strain rate with higher molecular weight, stand higher elongation before fracture. According to Harward et al. [89] and Tomita [90] regarding amorphous polymers under deformation, molecular alignment occurs with inelastic deformation, involving disentanglement process that allows sustaining higher strain levels.

Concerning the mechanical stiffness, some authors [91]–[93] have reported that as the molecular weight increased, the tensile strength to fracture increased sharply until reaching a plateau. These observations suggest that entanglements allow transferring the load in the polymer network and strengthen the material at large deformation. Additionally, the work of van Melick et al. [17] revealed that strain hardening intensifies with the density of entanglements. Studies of Bartczak [94] showed that polymers with high number of entanglement displayed more molecular orientation when deformed than those with low entanglement density, promoting a more pronounced strain hardening. Consequently, polymers with a high entanglement density have a network that behaves stiffer in the plastic region with an earlier apparition of the strain hardening compared to polymer with lower entanglement density.

The last aspect to be considered is the entanglements sensitivity to time/temperature effects. Entanglements are considered as transitory since chain slippage is highly sensitive to strain rate, temperature and deformation [1]. Indeed, Hossain et al. [95] performed molecular dynamic simulations of an amorphous PE to address the evolution of entanglement parameter with the true strain at different strain rates and constant temperature. They observed that, at large deformation, the entanglement parameter was decreasing faster when strain rate was lower. This was attributed to the capacity of polymer chains to accommodate deformation trough disentanglement when more time was granted. Additionally, Shepherd et al. [96] stated that the evolution of entanglements may be influenced by two opposite mechanisms:

1. When stretched, loose knot-like entanglements may be tightened, forming additional topological constraints.
2. Time/temperature effects increase relative chain slippage when the polymer is deformed, reducing the number of entanglements.

4.4.1.2 Crosslinking effect

Chemical crosslinks are permanent topological constraints that affect the mechanical response of polymers. Indeed, when an amorphous polymer is stretched above its glass transition, chain segments uncoil until crosslinks hinder further chain alignment, leading to hyperelastic behaviour [4], [51], [59].

Figure 4.10 shows a general summary of the effect of crosslink density on the polymer properties for temperatures higher than the glass transition temperature. The elastic modulus increases with the crosslink density since molecular mobility is more constrained. Additionally, the energy dissipation or hysteresis decreases with the crosslink density. In parallel, the toughness initially increases but after reaching a maximum value, it reduces with the crosslinking density. These observations can be attributed to an embrittlement of the polymer by a reduction of the chain mobility.

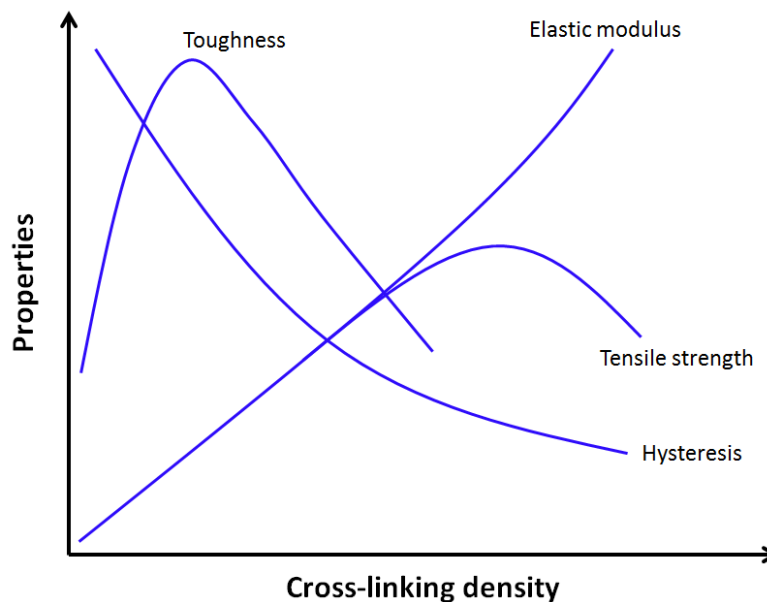


Figure 4.10: Polymer properties dependence on the cross-linking density [4].

Additionally, Bensason et al. [18] studied the influence of the crosslink density on the mechanical behaviour of elastomers when deformed above their glass transition. Results

revealed that mechanical stiffness and strain hardening increased with the crosslinking density while the deformability decreased. This is depicted in Figure 4.11.

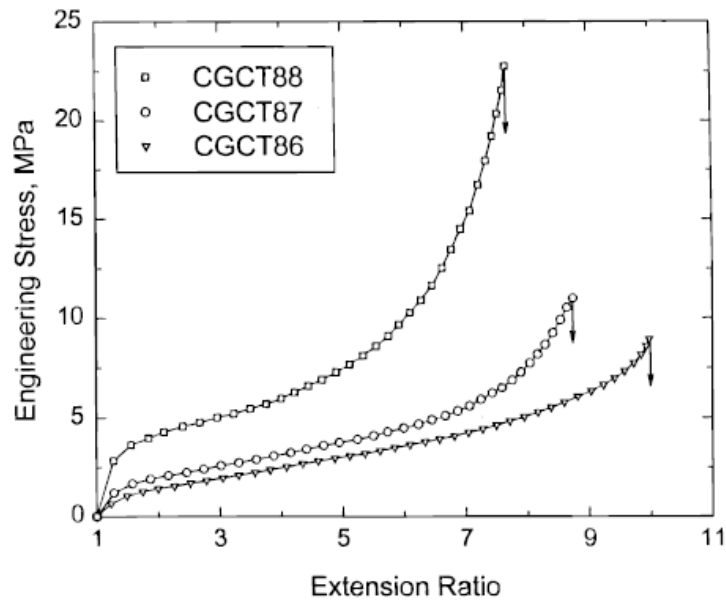


Figure 4.11: Stress-stretch curves of three elastomeric copolymers at room temperature. [18]

4.5 Results and Discussions

In this Section, the results obtained from mechanical testing at large deformation will be presented. As a reminder, the analysis was restrained to strain rates lower than 10^{-2} s^{-1} to avoid any effect related to adiabatic heating or thermomechanical coupling. Moreover, the analysis will be focus on the true stress and true strain as defined in Equations 2.11 and 2.14.

4.5.1 Global mechanical response

Before going further in this study, it is important to verify if the PMMA panels did not present any anisotropy induced by the processing. In Section 3.1, this was validated in the linear domain of deformation. To verify the reliability of these results, isotropy was checked also in the domain of large deformation by performing uniaxial uploading-unloading tensile test for samples oriented parallel and perpendicular to the injection/extrusion flow direction. Figure 4.12 shows the true stress-true strain curves of PMMA 120 for different orientations. Results show that the mechanical response does not vary with material orientation during the uploading-unloading along the tested range of deformation. This means that no particular molecular orientation was promoted during processing. Therefore the mechanical behaviour is isotropic, as it was also observed in the linear domain.

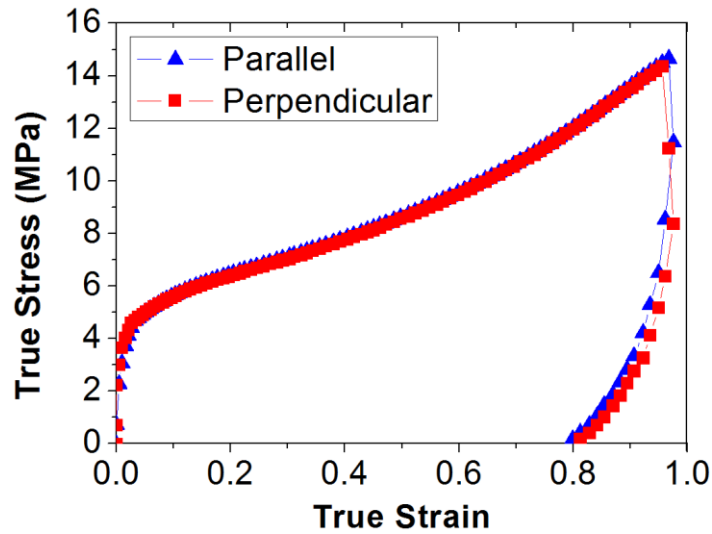


Figure 4.12: True stress-true strain tensile curves for PMMA 120 oriented perpendicularly and parallel to the processing flow direction at $100^{\circ}\text{C} - 0.0015 \text{ s}^{-1}$.

Figure 4.13 a) and b) present the true stress – true strain curves for PMMA 3500 below and above its α -transition temperature (around 130°C), at constant strain rate. These curves give a first glimpse of the mechanical response of PMMA at large deformation levels.

Below the α -transition temperature, the material initially displays a viscoelastic response that becomes less linear with the increase of the strain. A softening starts to appear around 7% of true strain and develops up to 25% of strain. At higher deformation, strain hardening can be observed up to the maximum strain. The unloading reveals a strong irreversible response which may be related to a partial viscoelastic recovery and a permanent residual strain associated to a viscoplastic response. Therefore, below the α -transition temperature, PMMA displays trends related to viscoelastoplastic and hyperelastic behaviours. Above the α -transition temperature, PMMA 3500 displays a more rubbery behaviour, with a no-linear evolution of the stress-strain curves and almost no hysteresis, i.e. no energy dissipation. Thus, above the transition temperature the material behaves mainly as a hyperelastic solid.

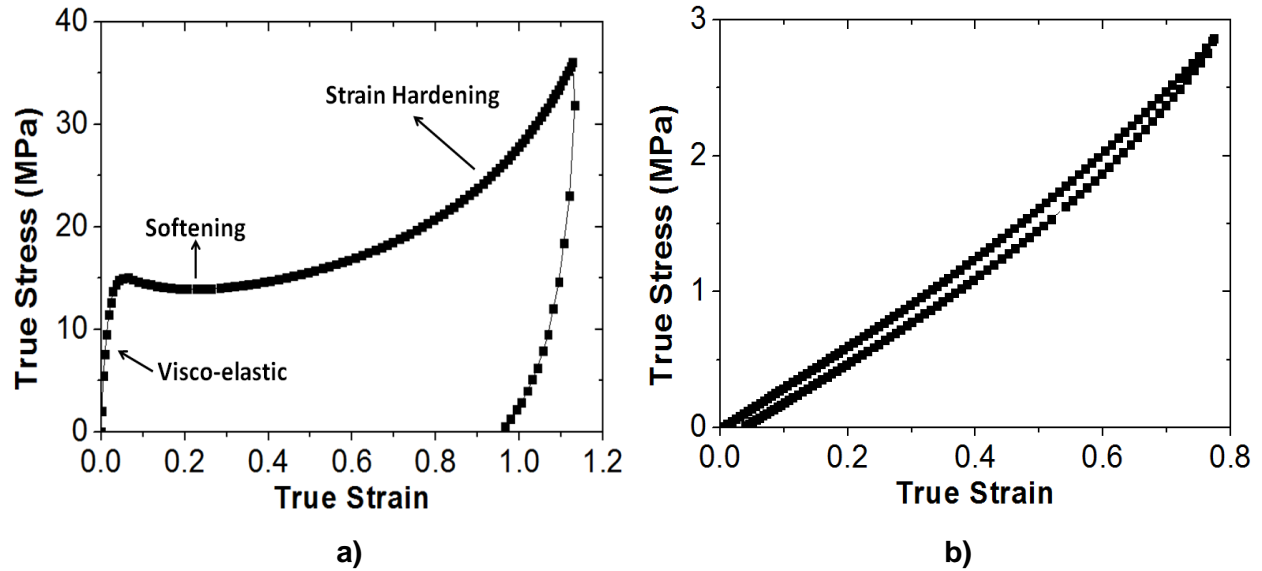


Figure 4.13: True stress-true strain tensile curves for PMMA 3500 at 0.0015 s^{-1} for temperatures of a) 110°C and b) 150°C .

4.5.2 Effect of the temperature on PMMA

As displayed in previous Section, the mechanical behaviour of PMMA is highly sensitive to the temperature. Therefore, a deeper study of the temperature effect on the mechanical response of PMMA will be examined in this Section.

For this study, results presented in Chapter III regarding the evolution of the storage and loss moduli will be used as reference to better understand the macroscopic behaviour. To properly link the strain rate obtained in the tensile tests (TT) at large deformation level to the sinusoidal strain period imposed in DMTA in the linear domain, several authors have proposed to account one-quarter of the sinusoidal loading cycle: [2], [71], [75], [97]

$$\dot{\varepsilon}^{TT} = 4f^{DMTA}\varepsilon_{\varepsilon_{max}}^{DMTA}, \quad 4.4$$

where $\dot{\varepsilon}^{TT}$ is the strain rate of the tensile test, f^{DMTA} is the frequency of the DMTA test and $\varepsilon_{\varepsilon_{max}}^{DMTA}$ corresponds to the maximum strain value of oscillatory deformation. For instance, a tensile test performed at a strain rate of 0.015 s^{-1} as shown in Figure 4.13, would be equivalent to a frequency of 3.75 Hz on the DMTA when imposing a maximum strain of 0.1%.

Figure 4.14 a) displays the temperature scans of PMMA 3500 for the moduli and $\tan \delta$ obtained from DMTA tests at 3.75 Hz. Figure 4.14 b) presents the true stress-true strain curves of PMMA 3500 obtained from unloading-unloading tensile tests at 0.015 s^{-1} . Figure 4.14 c)

shows a zoom of the curves obtained at higher temperatures whose stress were too low to be appreciated in Figure 4.14 b). A decrease of the mechanical stiffness is observed when the temperature is higher. This agrees with the evolution of the storage modulus with the temperature. Indeed, at the onset of the viscoelastic region around 110°C, the storage modulus is around 1000 MPa and by just increasing the temperature of 10°C, the modulus decreases up to 500 MPa. With further temperature increases up to 200°C (i.e. in the rubbery plateau), the modulus drastically reaches a value in the order of 2 MPa.

Additionally, Figure 4.14 b) and c) also reveal a variation of the hysteresis loop when changing the temperature, meaning that the energy dissipation changes with the tests conditions. More precisely, at 110°C an important hysteresis is observed, followed by a gradual decrease when increasing the temperature and reaching a value close to zero at 150°C and finally an increase in the loop area at 220°C. Figure 4.14 a) shows that the hysteresis observed in the stress-strain curve at 110°C is related to a high loss modulus in the onset of the viscoelastic region. Between 120°C and 130°C hysteresis is still present but is lower than before. At this level, the material is in its viscoelastic region. At 150°C, the material behaves as a hyperelastic solid, where hysteresis and residual plastic strain are almost zero. At higher temperatures (220°C), disentanglements are likely promoted, reducing the capacity of the material to act as an entropic spring. Thus, more energy is dissipated during the deformation turning the material more viscohyperelastic.

These observations are in agreement with previous studies and enrich the comprehension on the effect of the temperature on the mechanical response of amorphous polymers. However, this was done for only one strain rate. The next step is to address the relevance of the strain rate on the mechanical response of PMMA.

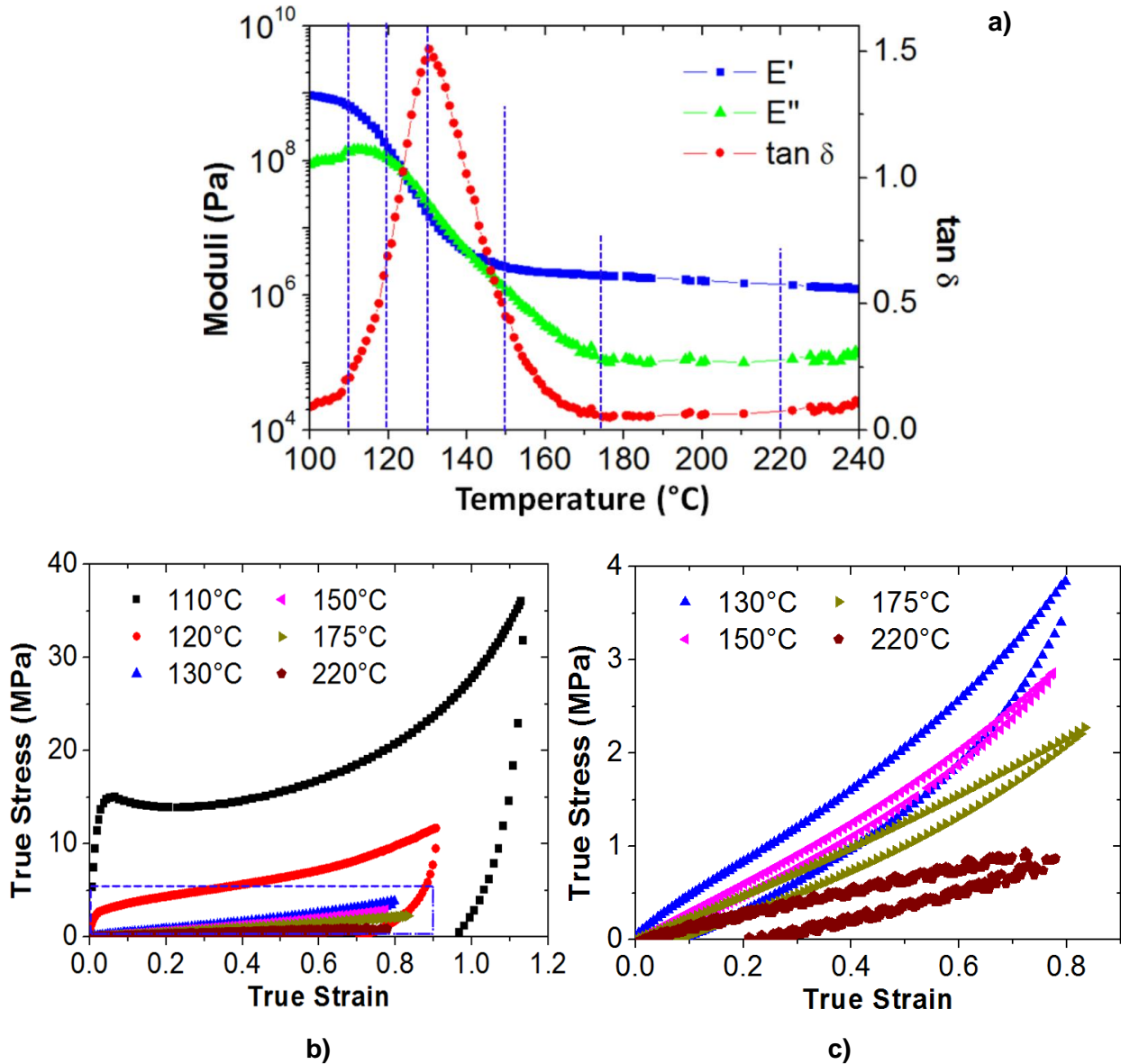


Figure 4.14: a) Temperature scans for PMMA 3500 at 3.75 Hz. b) True stress-true strain curves for PMMA 3500 at 0.015 s^{-1} for different temperatures. c) Zoom area of curve b) indicating the results obtained at higher temperatures.

4.5.3 Effect of the strain rate on PMMA

As it was mentioned, strain rate also have a strong effect on the mechanical response on PMMA. This is addressed in this Section thanks to mechanical tests performed at different strain rates. Figure 4.15 a) shows the true stress-true strain curve for PMMA 3500 when submitted at different strain rates at 130 $^{\circ}\text{C}$ and at 150 $^{\circ}\text{C}$ (Figure 4.15 b)).

At 130°C, the apparent elastic modulus, the material stiffness and hysteresis gradually decrease when reducing the strain rate. These results reveal that the material goes from a viscoelastoplastic state to hyperelastic state. At 150°C, the material presents almost no hysteresis but the mechanical stiffness decreases with the strain rate, suggesting that the material behaves as a viscohyperelastic solid. In general, results reveal an increase of the stresses when the strain rate is increased.

It is clear that the material stiffness of PMMA increases with the strain rate. However, the sensitivity to the strain rate also evolves with the temperature. Indeed, the macroscopic response was more sensitive to the strain rate near the viscoelastic region (at 130°C) than in the rubbery plateau (at 150°C). This was also illustrated in Section 3.3.2. Contrary, when the material behaves hyper-elastically or rubbery, large strain inelastic processes are constrained by the active entanglements points which are less time dependent.

Therefore, a complete characterization of the polymer dependence on the temperature and on the strain rate would require a huge amount of experimental data accounting for all the possible couples of temperature/strain rate that covers the onset of the viscoelastic region up to the rubbery plateau. In the next Section, a novel methodology will be introduced to overcome this issue.

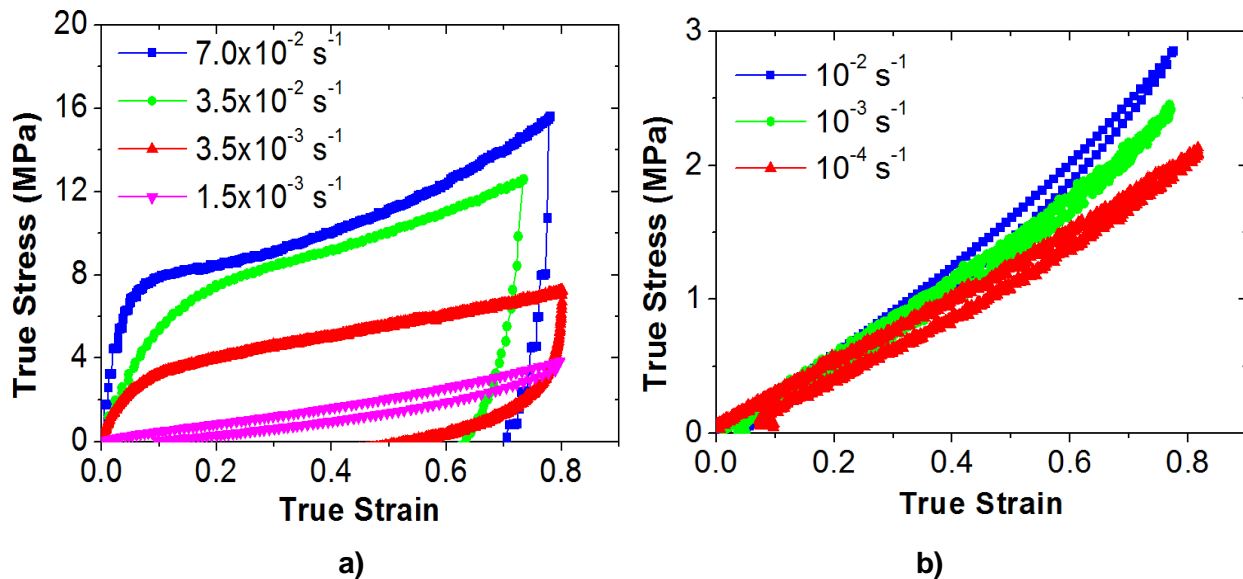


Figure 4.15: True stress-true strain curves for PMMA 3500 at different strain rates at a) 130°C and b) 150°C.

4.5.4 Coupling the temperature/strain rate effect at large deformations: Equivalent strain rate at reference temperature

As introduced in Section 4.3, many authors have studied ways to simplify the mechanical characterization of polymers by extrapolating the time/temperature equivalence from the linear domain of deformations, to large deformation levels. In this work, we will take the observations made by [11], [14], [21], [67], [75] as a starting point to experimentally validate that the shift factors, determined from DMTA, can be used to couple the effect of strain rate and temperature during uploading-unloading mechanical tests at large deformation. This concept consists on:

1. Firstly, an approach (similar to Cox Merz rule [98]) was postulated: the steady state modulus at a given strain rate is equal to the dynamic modulus at the same frequency. So the Young's modulus of the material should evolve as a function of strain rate as complex modulus evolves as a function of frequency.
2. Secondly, master curves determined from frequency scans on DMTA were used as a reference to define some equivalent strain rates at a reference temperature, 130°C, that would promote different behaviours: close to glassy state, viscoelastic, rubbery or fluid state.
3. Thirdly, for each of the equivalent strain rates, two experimental conditions (in term of temperature and strain rate) were chosen accordingly to the protocol presented previously. Actual experimental conditions were chosen to avoid any self-heating (strain rate not too high) and creeping (strain rate not too low). The couples of temperature/strain rate were defined thanks to Equation 4.3, which links the equivalent and experimental strain rates through the shift factors determined from DMTA. As a reminder, these shift factors are dependent on the temperature. Therefore, this is why the equivalent strain rate at reference temperature considers the temperature/strain rate effect. Additionally, by means of Equation 4.4, it can be proven that shift factors should remain the same either by determining them through strain rate or frequency:

$$a_{T_2/T_0} = \frac{f_{eq}}{f} = \frac{\dot{\epsilon}_{eq}}{\dot{\epsilon}} \quad 4.5$$

Using this protocol, tests were performed for different conditions of temperature and strain rate, giving one unique equivalent strain rate at a reference temperature of 130°C. Typical conditions of temperature and imposed local strain rate are given in Table 4.1 for all the PMMAs of this study. These conditions were determined using experimental results from DMTA on tensile loadings. For instance, performing the test on PMMA 80 at 130°C/0.017s⁻¹ should be equivalent to a test at 119°C/0.002s⁻¹.

Table 4.1: Equivalent strain rates at 130 °C for PMMAs as a function of temperature and actual strain rate for tensile loadings.

| Equivalent strain rate (s ⁻¹) | PMMA 80 | PMMA 93 | PMMA 120 | PMMA 3500 | PMMA CL |
|-------------------------------------------|-------------------------------------------------------|------------------------|------------------------|------------------------|------------------------|
| | Couples Temperature/Strain rate (°C/s ⁻¹) | | | | |
| 10³ | 93/0.021 90/0.002 | 106/0.026 103/0.002 | 102/0.027 100/0.002 | - | - |
| 10² | 97/0.017 93/0.002 | 108/0.021 106/0.002 | 106/0.020 101/0.002 | 109/0.021 107/0.002 | 109/0.026 106/0.002 |
| 10¹ | 103/0.017 97/0.002 | 113/0.017 109/0.002 | 110/0.018 106/0.002 | - | - |
| 10⁰ | 110/0.017 103/0.002 | 117/0.019 113/0.002 | 115/0.018 107/0.002 | 118/0.019 114/0.002 | 118/0.017 113/0.002 |
| 10⁻¹ | 119/0.017 110/0.002 | 123/0.018 117/0.002 | 120/0.017 115/0.002 | - | 123/0.017 118/0.002 |
| 10⁻² | 130/0.017 119/0.002 | 130/0.017 123/0.002 | 130/0.017 120/0.002 | 130/0.019 124/0.002 | 130/0.016 122/0.002 |
| 10⁻⁴ | - | 150/0.017 140/0.002 | 157/0.017 140/0.002 | 150/0.017 140/0.002 | 147/0.016 138/0.002 |
| 10⁻⁶ | - | - | - | 177/0.018 170/0.002 | 173/0.016 160/0.002 |
| 10⁻⁸ | - | - | - | 196/0.019 185/0.002 | - |

4.5.4.1 Tensile loading

The experimental conditions of temperature and strain rate were tested under tensile unloading-unloading conditions, and then compared experimentally to validate the concept of equivalent strain rate at reference temperature at the macroscopic level. To quantify the accuracy of the methodology, an absolute relative error (ARE) is calculated between the curves:

$$ARE = \left| \frac{\sigma_{EXP1} - \sigma_{EXP2}}{\sigma_{EXP1}} \right| \times 100, \quad 4.6$$

where σ_{EXP1} is the true stress obtained at one strain rate and temperature condition and σ_{EXP2} is the true stress obtained for the other test condition. Figure 4.16, Figure 4.18 and Figure 4.20 show the master curve associated to PMMA 80, 3500 and CL respectively. Vertical dotted lines indicate the equivalent strain rate that was targeted at the macroscopic level. Additionally, Figure 4.17, Figure 4.19 and Figure 4.21 show the true stress-true strain curves for PMMAs 80, 3500 and CL, obtained with different couples of strain rate/temperature (indicated in Table 4.1). giving the same equivalent strain rate (displayed in the legends)

Comparing the different experimental conditions displayed in Figure 4.17, Figure 4.19 and Figure 4.21, it is possible to conclude that using two experimental temperature/strain rate setups leading to the same equivalent strain rate, promotes the same type of behaviour. Indeed, this is confirmed when observing that the absolute relative error between the stress vs strain curves at similar equivalent rate stays lower than 10% for all the different conditions. However, there are two aspects that need special attention regarding this methodology:

1. High equivalent strain rates: Figure 4.17 a) and Figure 4.19 a) show the stress-strain curves for PMMA 80 at 10^3 s^{-1} and PMMA 3500 at 10^2 s^{-1} , respectively. We can observe that, even if the overall behaviour is similar, the strain hardening of one condition is higher for a true strain of 60%. This may be related to thermo-mechanical coupling that leads to some self-heating inducing softening. Nevertheless results are still satisfactory. These results reveal that for higher equivalent strain rates corresponding to applications such as impact (10^5 s^{-1}), a fully coupled thermo-mechanical approach will be needed. For the purpose of this work, the domain of high strain rate is not of main interest. Thus, further research on this topic will remain as a perspective.
2. Viscoelastic region: When the material goes through its viscoelastic region, the storage and loss moduli drops sharply. Therefore, the material is highly sensitive to temperature and strain rate when using the equivalent strain rate in this region. For instance, varying a test by 2°C may lead to important differences. As a consequence, if the experimental conditions are not well controlled, the superposition may fail. This drawback was overcome by pre-heating the sample until reaching the thermal equilibrium and also by carefully choosing cross-head velocities to impose the appropriate local strain rates.

These previous drawbacks can be easily solved, which makes the equivalent strain rate at reference temperature a useful and relevant parameter for material testing. Indeed, thanks to its accuracy, it is possible to considerably reduce the number of experimental tests needed to fully characterize the polymer. Additionally, this methodology may help us to avoid complex

experimental conditions. For instance, as depicted in Figure 4.17 f) and also in Appendix 8.5 some stress-strain curves are obtained near the viscous region of the polymer at high temperature ($\dot{\epsilon}_{eq} = 10^{-2} \text{ s}^{-1}$ - $\dot{\epsilon}_{eq} = 10^{-4} \text{ s}^{-1}$). At these temperatures, the material is quasi-liquid, making the tensile tests highly challenging. Using the time/temperature superposition, we can overcome this obstacle by choosing conditions with a lower temperature but lower strain rate for determining low equivalent strain rate.

PMMA 80

Figure 4.17 presents the evolution of the mechanical response with the equivalent strain rate (indicated in the legends of the figures) for PMMA 80. We can notice that when the material is in the onset of the viscoelastic region (at 10^3 s^{-1} and at 10^2 s^{-1}), it displays an apparent elastic zone followed by some strain hardening, high hysteresis and residual strain. This suggests viscoelastoplastic behaviour. At lower equivalent strain rate when the material goes through its viscoelastic region (10^1 s^{-1} and 10^0 s^{-1}), the initial apparent linear zone disappears. The stresses are lower and the hysteresis decreases. Here, the polymer behaves as a viscoelastic solid.

When the polymer goes to the rubbery state, at 10^{-1} s^{-1} , the hysteresis and mechanical stiffness decrease significantly. However, a residual strain and hysteresis are still present, indicating that, in the rubbery plateau of PMMA 80, there is not a fully hyperelastic behaviour but more a non-linear viscohyperelastic behaviour. This suggests that the molecular rearrangements and disentanglement processes co-exist with entropic elasticity, which may be the source of the dissipation of energy when the polymer is deformed. Finally, near the flowing state, at 10^{-2} s^{-1} , the stresses decrease and hysteresis rises again. This is likely attributed to the increase of the disentanglements process. The material behaviour is closer to that of a viscous material.

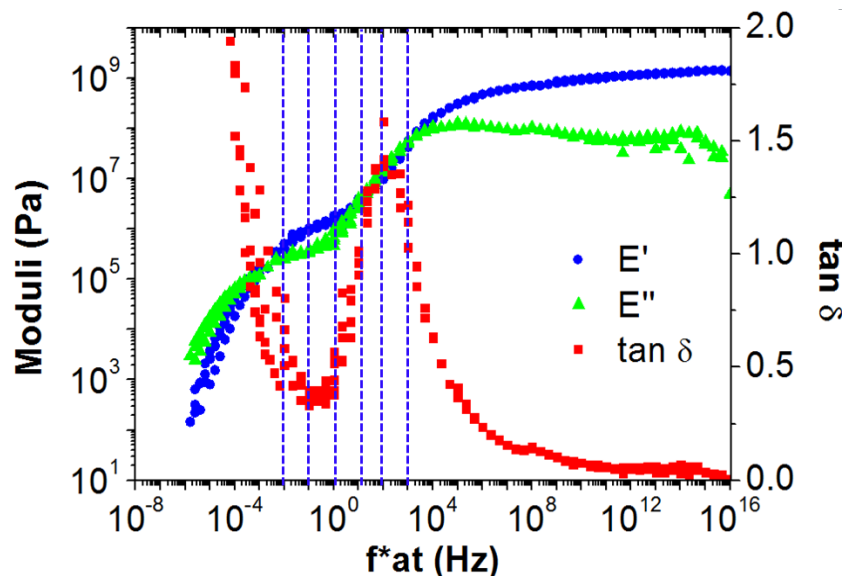


Figure 4.16: E' , E'' and $\text{Tan } \delta$ master curves for PMMA 80.

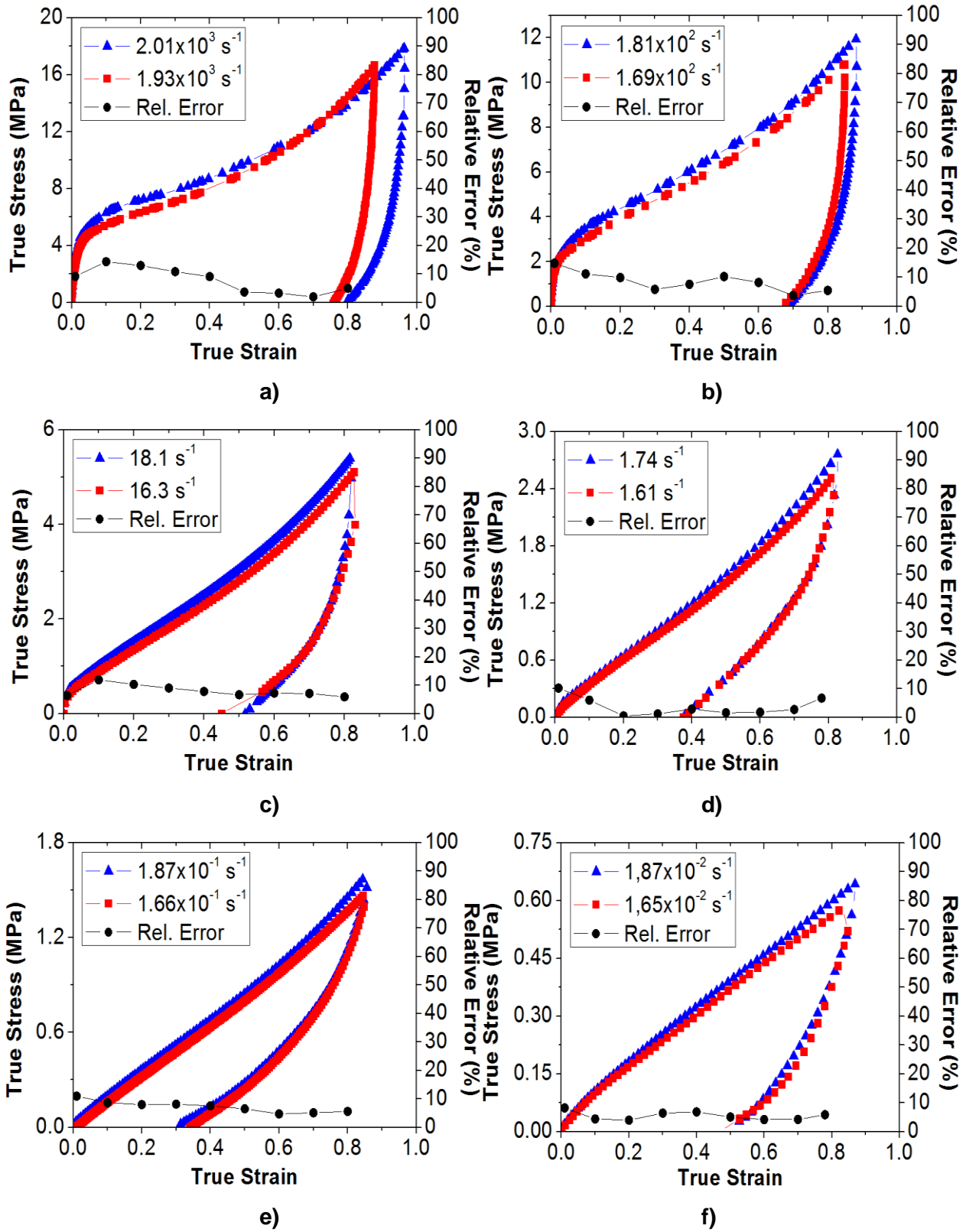


Figure 4.17: Macroscopic tensile curves for PMMA 80 at a reference temperature of 130 °C. a) $\dot{\epsilon}_{eq} \approx 10^3 \text{ s}^{-1}$ b) $\dot{\epsilon}_{eq} \approx 10^2 \text{ s}^{-1}$. c) $\dot{\epsilon}_{eq} \approx 10^1$ d) $\dot{\epsilon}_{eq} \approx 10^0$. e) $\dot{\epsilon}_{eq} \approx 10^{-1}$ f) $\dot{\epsilon}_{eq} \approx 10^{-2} \text{ s}^{-1}$.

PMMA 3500

Figure 4.19 displays the evolution of the true stress with the true strain for different equivalent strain rates on PMMA 3500. We observe that similar values of equivalent strain rate lead to an equivalent mechanical behaviour. For PMMA 3500, the tested couples (T ; $\dot{\epsilon}_{eq}$) relative to the same equivalent strain rate lead to similar mechanical responses when the material passed through the different viscoelastic regions. Additionally, using the equivalent strain rates, we captured the energy dissipation evolution previously mentioned (showed through loss modulus and $\text{Tan } \delta$ in Figure 4.18). In general, the following behaviours are addressed:

- A viscoelastoplastic behaviour (at $\dot{\epsilon}_{eq}=10^2 \text{ s}^{-1}$), with a relevant apparent linear zone, stress softening, strain hardening and high residual plastic strain after unloading. The energy dissipation is likely related to permanent plastic-like processes.
- A viscoelastic response (at $\dot{\epsilon}_{eq}=10^0 \text{ s}^{-1}$), with a decrease in the apparent modulus, stress and strain hardening. Energy dissipation may be produced by the polymer conformation changes.
- A hyperelastic behaviour in the rubbery plateau (at $\dot{\epsilon}_{eq}=10^{-4} \text{ s}^{-1}$) with non-linear behaviour, lower mechanical stiffness and almost no hysteresis and residual stresses. Entropic elasticity is available due to mobility of chains and to entanglements whose life-time is long enough compared to strain rate.
- A viscohyperelastic state (at $\dot{\epsilon}_{eq}=10^{-6} \text{ s}^{-1}$ and $\dot{\epsilon}_{eq}=10^{-8} \text{ s}^{-1}$), where some disentanglement is promoted due to the low equivalent strain rate, leading to a viscous component of the behaviour with partial energy dissipation.

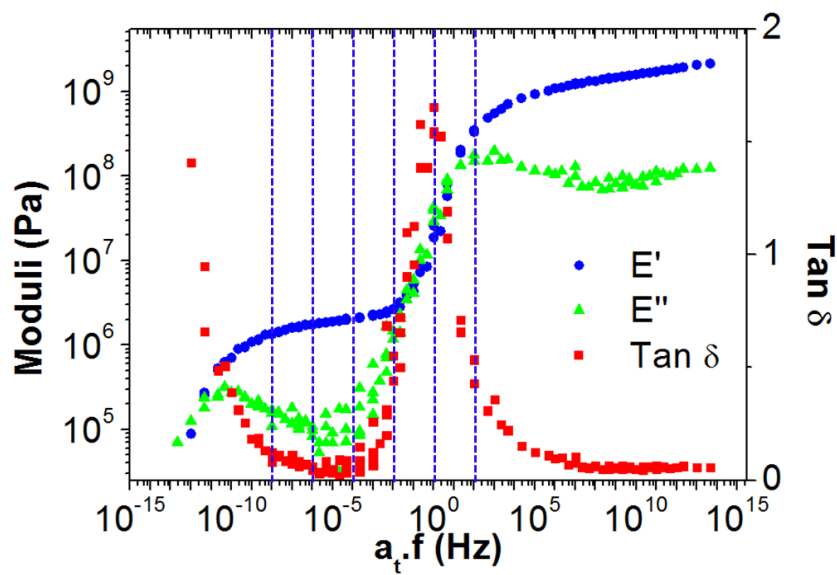


Figure 4.18: E' , E'' and $\text{Tan } \delta$ master curves for PMMA 3500.

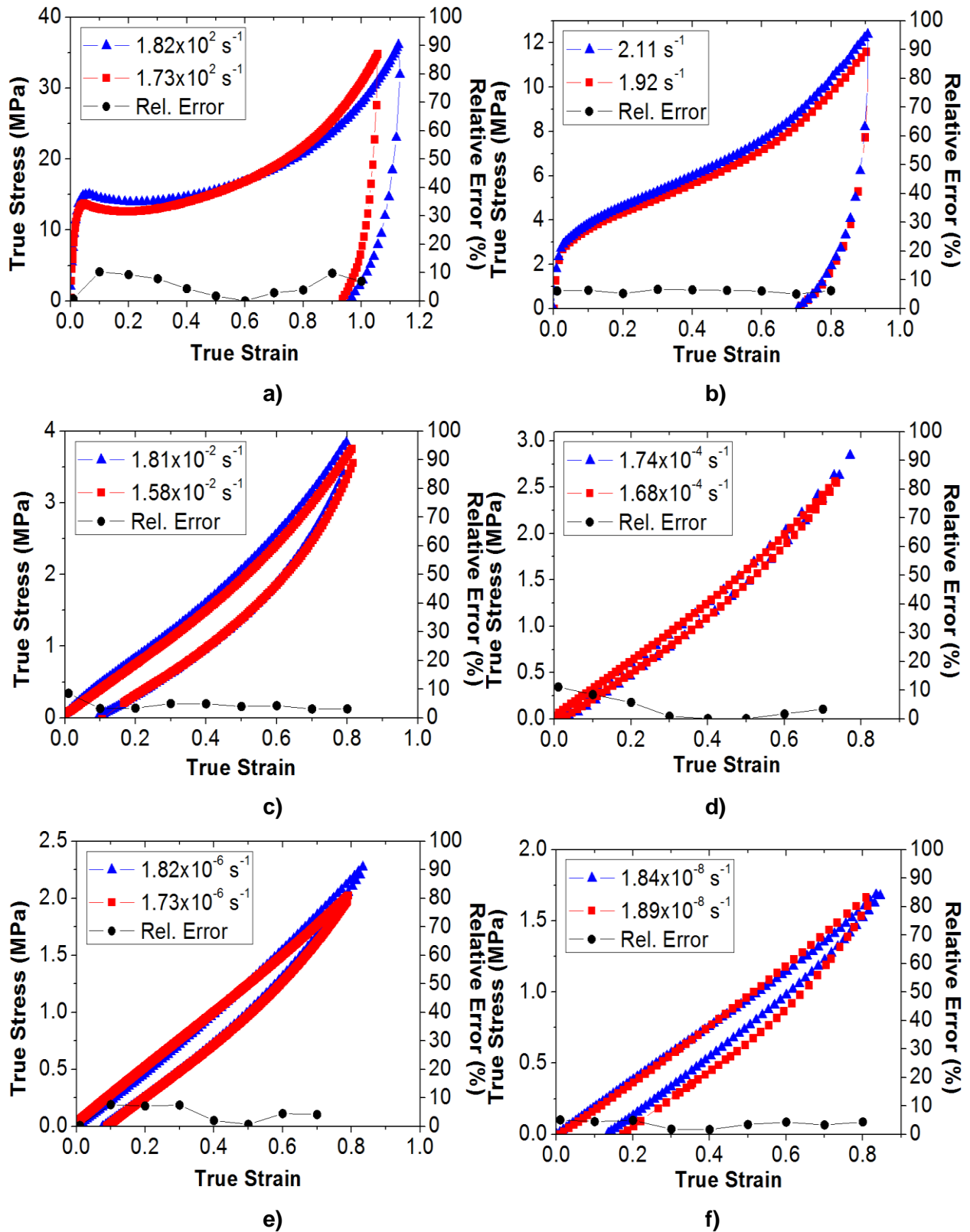


Figure 4.19: Macroscopic tensile curves for PMMA 3500 at a reference temperature of 130 °C. a) $\dot{\epsilon}_{eq} \approx 10^2 \text{ s}^{-1}$ b) $\dot{\epsilon}_{eq} \approx 10^0 \text{ s}^{-1}$. c) $\dot{\epsilon}_{eq} \approx 10^{-2}$ d) $\dot{\epsilon}_{eq} \approx 10^{-4}$. e) $\dot{\epsilon}_{eq} \approx 10^{-6}$ f) $\dot{\epsilon}_{eq} \approx 10^{-8} \text{ s}^{-1}$.

PMMA CL

Figure 4.21 presents the true stress - true strain curves for different equivalent strain rates on PMMA CL. As shown in previous PMMAs, the time/temperature equivalence allows displaying the material properties from viscoelastic to hyperelastic regime. In general, the following behaviours were addressed:

- A viscoelastoplastic behaviour (at $\dot{\epsilon}_{eq} = 10^2 \text{ s}^{-1}$), with a pertinent apparent linear zone, strain hardening and relevant residual plastic strain after unloading. The energy dissipation is likely related to plastic processes. No stress softening was observed as in PMMA 3500.
- At $\dot{\epsilon}_{eq} = 10^0 \text{ s}^{-1}$, a viscoelastic response is observed, with a lower apparent modulus, stress and strain hardening. Energy dissipation may be due to energy dissipation while initiating conformation changes associated to the α -transition.
- A hyperelastic behaviour is also observed when the material is in its rubbery plateau (at $\dot{\epsilon}_{eq} = 10^{-4} \text{ s}^{-1}$) with almost no hysteresis and residual stresses. For PMMA CL, the topological factors that govern the mechanical behaviour are the crosslinks. They constrain the molecular motions when the material is deformed, reducing the energy dissipation and allowing an entropic elasticity.
- At lower equivalent strain rates (at $\dot{\epsilon}_{eq} = 10^{-6} \text{ s}^{-1}$), the material remains hyperelastic with the same mechanical stiffness observed at 10^{-4} s^{-1} . This suggests that crosslinks are still active and they do not evolve in the rubbery plateau, confirming their “permanent” nature as displayed in the DMTA results in Section III.

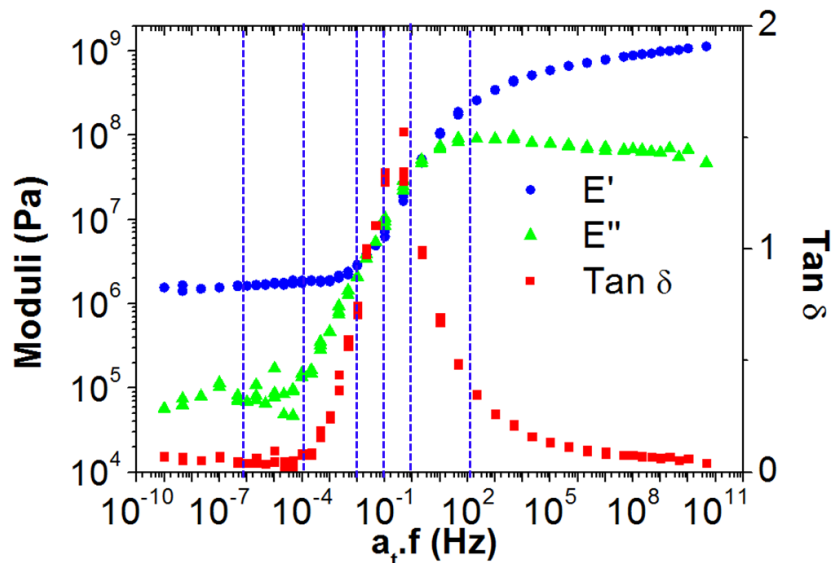


Figure 4.20: E' , E'' and $\text{Tan } \delta$ master curves for PMMA CL.

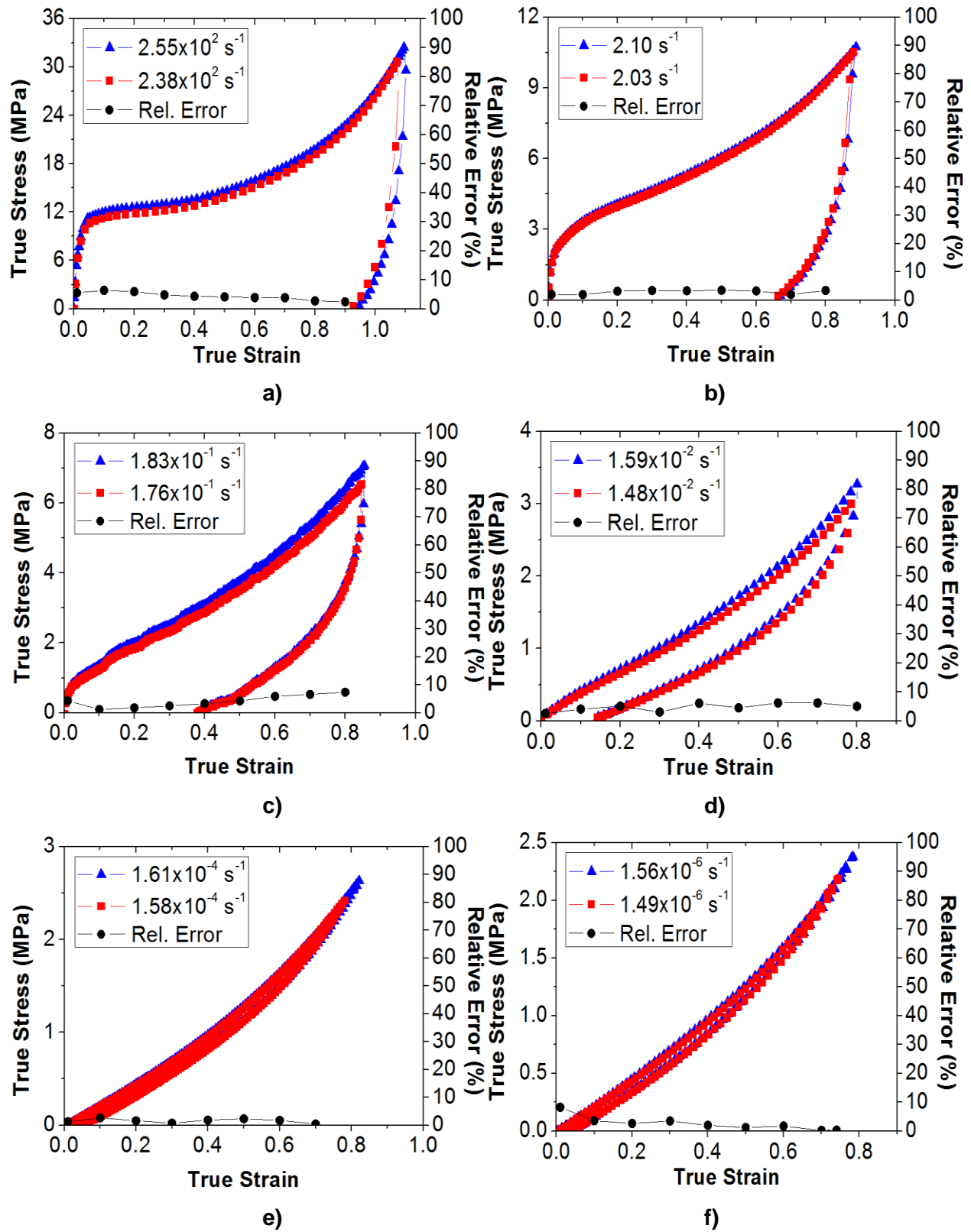


Figure 4.21: Macroscopic tensile curves for PMMA CL at a reference temperature of 130 °C. a) $\dot{\epsilon}_{eq} \approx 10^2 \text{ s}^{-1}$ b) $\dot{\epsilon}_{eq} \approx 10^0 \text{ s}^{-1}$. c) $\dot{\epsilon}_{eq} \approx 10^{-1}$ d) $\dot{\epsilon}_{eq} \approx 10^{-2}$. e) $\dot{\epsilon}_{eq} \approx 10^{-4}$ f) $\dot{\epsilon}_{eq} \approx 10^{-6} \text{ s}^{-1}$.

In consequence, observing the tensile test results of the different PMMAs, we verified that similar equivalent strain rates at reference temperature of 130°C lead to an equivalent macroscopic mechanical response. This was valid from the onset of the viscoelastic region, passing through the rubbery plateau, up to the onset of the flowing region. Therefore, it can be stated that $\dot{\epsilon}_{eq}$ obtained from low strain domain is a relevant parameter at large deformation, coupling temperature and strain rate effects successfully for amorphous PMMAs with different molecular weights under cycling tests. The following general conclusions can be drawn:

- Firstly, there is a clear correlation between the equivalent strain rate that is targeted and the overall behaviour of the material. This behaviour will be close to viscoelastoplastic when equivalent strain rate is close to the glassy plateau, viscoelastic in the so-called viscoelastic zone, hyperelastic on the rubbery plateau and more viscous close to the fluid zone. So targeting an equivalent strain rate allows a quick characterization of the kind of tensile behaviour exhibited by the material.
- Secondly, two experimental temperature/strain rate conditions giving the same equivalent strain rate will lead not only to the same type of behaviour but also to the same stress vs strain curve. Modelling with the equivalent strain rate as parameter will allow accounting for temperature and strain rate at the same moment. The relative error stayed lower than 10% for the different equivalent strain rates.
- Finally, as shown in Figure 4.17 f) and also in Appendix 8.5, we can notice that mechanical behaviour close to the viscous region of the polymer ($\dot{\epsilon}_{eq} = 10^{-2} \text{ s}^{-1}$ - $\dot{\epsilon}_{eq} = 10^{-4} \text{ s}^{-1}$) can be characterized. At such temperatures, the material is quasi-liquid, making the tensile tests highly challenging. Using the time/temperature superposition, we can overcome this obstacle by choosing conditions with lower temperatures and lower strain rates for determining low equivalent strain rates.

After validating the methodology for uploading-unloading tensile test, we aim at verifying the accuracy of the equivalent strain rate for more than one cycle. Figure 4.22 shows two cycling tests for PMMA 80, a), and PMMA CL, b), at a targeted equivalent strain rate (displayed in the legend of the figures). Same observation than previously can be made. Therefore, these figures suggest that the methodology may also be used for predicting the mechanical behaviour under several cycles. Further work will try to extend such approach to fatigue testing.

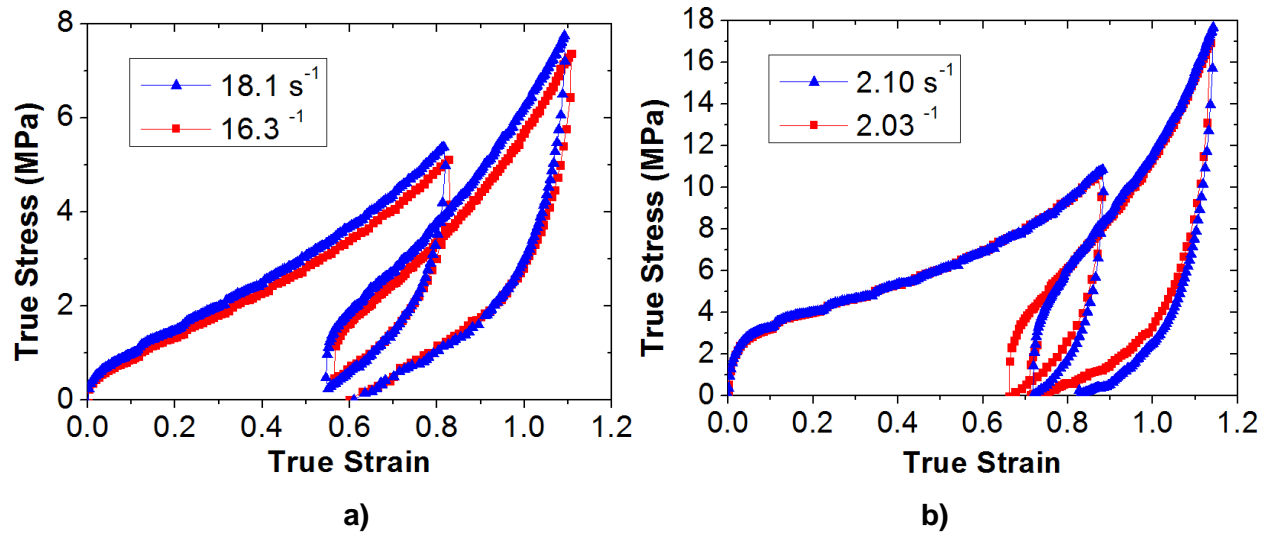


Figure 4.22: Two cycling load-unload tests for a) PMMA 80 and b) PMMA CL.

So far, we successfully extrapolated the time/temperature equivalence from small to large deformation for a wide range of conditions. The next step is to validate this approach when a different stress state is applied.

4.5.4.2 Shear loading

This Section is devoted to the validation of the method for tests performed under shear cycling loading as described in Section 2.2.2.

The methodology was the same as explained for tensile loading: by means of Equation 4.3, temperature and strain rate were coupled through the equivalent strain rate at reference temperature (130°C). In a first attempt, shift factors were taken from experimental tensile DMTA data, which means that the studied conditions were the same as than the ones displayed in Table 4.1. However, results were not satisfactory when comparing the true shear stress – true shear strain on PMMA 80 (as displayed in Figure 4.23). It can be seen that the conditions used did not promote the same mechanical response even if the equivalent strain rate was similar.

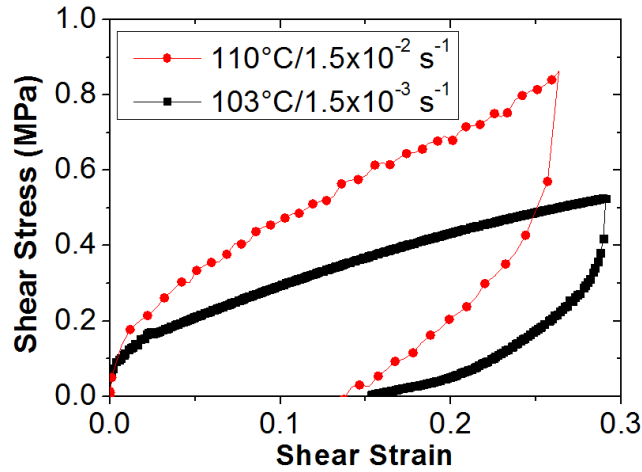


Figure 4.23: Shear stress-strain curves for PMMA 80 obtained using conditions of Table 4.1 for a theoretical equivalent strain rate of 10^0 s^{-1} .

Recalling the results presented in Section 3.2.4 in Figure 3.14, shift factors obtained from tensile loading (DMTA) and shear loading (Rheology) were different. Therefore, using the shift factors determined under shear loading will lead to different equivalent strain rates that may improve the superposition at the macroscopic level. However, this needs to be experimentally validated. The new experimental conditions are presented in Table 4.2 for all the PMMAs.

Table 4.2: Equivalent strain rates at 130 °C for PMMAs as a function of temperature and actual strain rate for shear loading.

| Equivalent strain rate in shear (s^{-1}) | PMMA 80 | PMMA 93 | PMMA 120 | PMMA 3500 | PMMA CL |
|-----------------------------------------------------|----------------------------------------------------------------------|-----------------------------|------------------------|------------------------|------------------------|
| | Couples Temperature/Strain rate ($^{\circ}\text{C}/\text{s}^{-1}$) | | | | |
| 10^2 | 97/0.027 93/0.002 | - | - | - | - |
| 10^0 | 112/0.021 103/0.002 | 116/0.021 111/0.002 | 115/0.019 110/0.002 | 117/0.018 114/0.002 | 118/0.019 113/0.002 |
| 10^{-2} | 130/0.019 117/0.002 | 130/0.018 125/0.002 | 130/0.018 120/0.002 | 130/0.018 126/0.002 | 130/0.018 124/0.002 |
| 10^{-4} | - | 149/ 10^{-2} 137/0.002 | 154/0.017 140/0.002 | 150/0.017 140/0.002 | 148/0.017 138/0.002 |
| 10^{-6} | - | - | - | 177/0.017 170/0.002 | 173/0.017 160/0.002 |

Using the values presented in Table 4.2, we can compare once again the true shear stress – true shear strain curves. This is depicted in Figure 4.24 for PMMAs 80 and CL for different equivalent strain rates. These results reveal that the same equivalent strain rate will lead to the same mechanical behaviour. This is highlighted with the relative errors that are also lower than 10%. These results show the validity of the equivalent strain rate for shear loading, which opens new ways for characterizing and modelling the mechanical response in polymers.

Similar to tensile tests, we observed viscoelastoplastic behaviour for sets of temperature/strain rate giving an equivalent strain rate close to the glassy region, viscoelastic behaviour in the transition zone and hyperelastic behaviour in the rubbery plateau. Using this shear test, we will be able to target specific equivalent strain rate related to a specific mechanical response without the need of performing large range of tests.

Regarding the mechanical behaviour, we can observe that the mechanical response of PMMA 80 under shear loading evolves in a similar way with the equivalent strain rate than the one observed under tensile loading. At 10^2 s^{-1} , a linear and non-linear viscoelastic zone is observed for low strain level, followed by a plastic regime where the stress seems remaining constant. We finally observe an important residual strain and hysteresis after unloading. At 10^0 s^{-1} , the apparent elastic zone, mechanical stiffness and hysteresis decrease. In the rubbery plateau (at 10^{-2} s^{-1}), a hyperelastic behaviour less pronounced than the one reported in tensile loading was observed.

Under shear loading, PMMA CL also displayed similar features than the ones observed under tensile loading. At 10^2 s^{-1} materials behaves as a viscoelastoplastic solid, with a decrease of mechanical stiffness when reducing the equivalent strain rate at 10^0 s^{-1} . Finally at 10^{-4} s^{-1} , PMMA CL displays hyperelastic behaviour, suggesting that crosslinks promote an entropic behaviour under shear loading.

In this Section we verified that, all the couples strain rate/temperature leading to equivalent strain rate, we will obtain same mechanical response under shear loading. These couples need to be determined from shear tests performed in the linear domain. Additionally, we observed that the mechanical behaviour depends on the same way to the equivalent strain and more especially, to the molecular mobility, as it did under tensile loading. A comparison of the stress-strain curves under tensile and shear loading may be fruitful for improving the physical understanding of the stress state impact on the polymer chains motion. This will be presented in next Section.

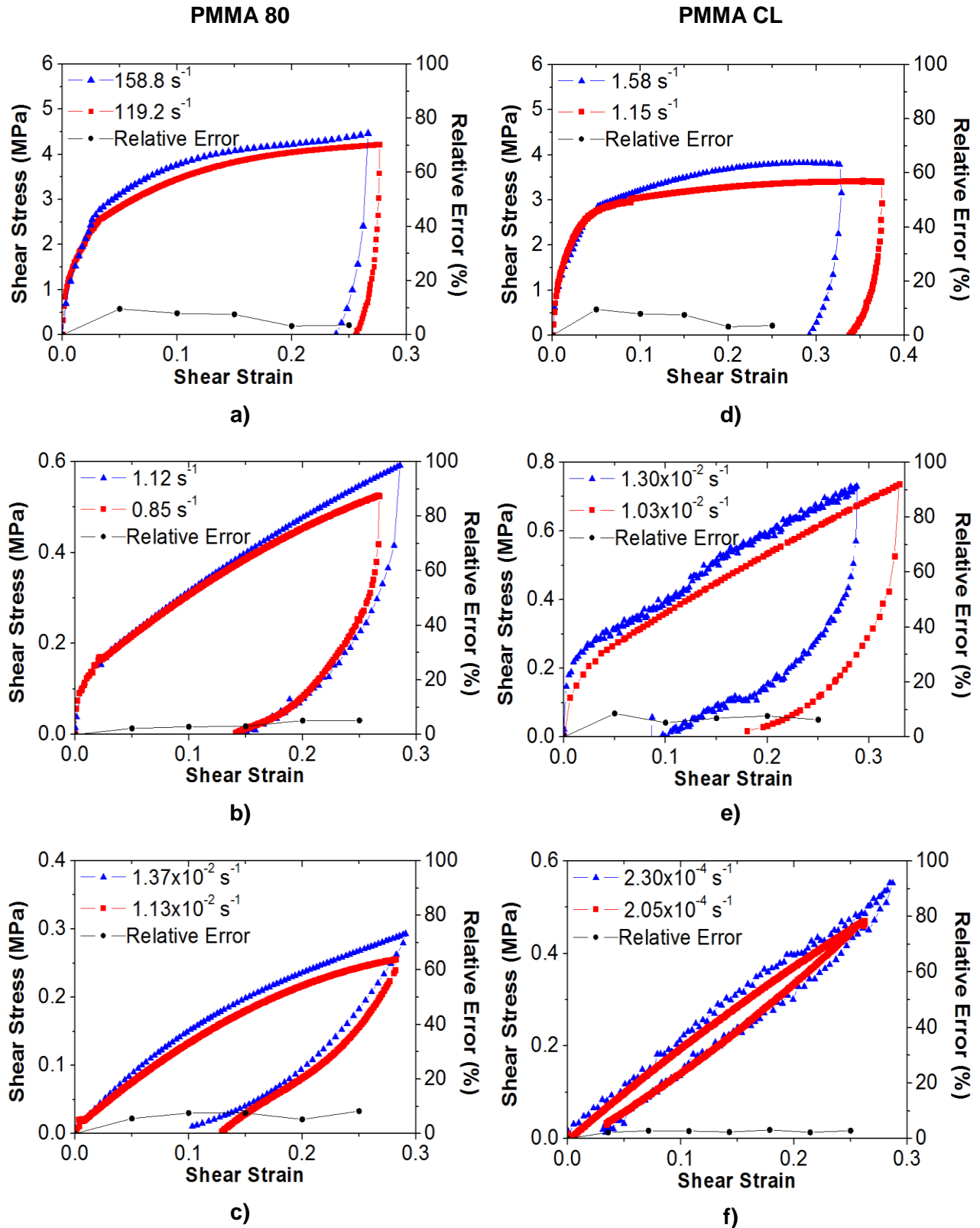


Figure 4.24: Macroscopic shear stress-strain curves for PMMA 80: a), b), c); and PMMA CL: d), e), f) at reference temperature of 130 °C. Equivalent strain rates are indicated in the legends.

4.5.5 Stress state effect on the mechanical response

After showing the validity of the equivalent strain rate at reference temperature for large deformation level under tensile and shear loading, we can now compare the mechanical response of the polymer at a specific equivalent strain rate for different stress states. However, as the stress states are different, a straightforward comparison is not possible. Instead, we can compute the von Mises stress, $\bar{\sigma}$, and strain, $\bar{\epsilon}$. These terms are defined as:

Tensile loading:

$$\bar{\sigma} = |\sigma_{yy}|, \quad 4.7$$

“Pure” shear loading:

$$\bar{\sigma} = \sqrt{3}|\sigma_{xy}^c|, \quad 4.8$$

$$\bar{\epsilon} = \sqrt{\frac{2}{3}[\epsilon_1^2 + \epsilon_2^2 + \epsilon_3^2]}, \quad 4.9$$

where σ_{yy} is the true stress under tensile loading (Equation 2.11), σ_{xy}^c is the corrected shear stress (Equation 2.14) and ϵ_i with $i=[1,3]$, are strain components in the principal reference frame (extracted from VIC 3D). Figure 4.25 displays the von Mises stress-strain curves obtained through tensile and shear tests at similar equivalent strain rates for PMMA 80. Conditions are indicated in the legend of the figures.

Comparing the mechanical response of the PMMA when tested near the glassy region, Figure 4.25 a), it can be noticed that the mechanical behaviour is quite similar up to 15% of strain. At higher deformation level, the hardening appears to be negligible under shearing, which is usual in polymers [99]–[101]. This suggests that chain alignment to the stretch direction may be less pronounced in the case of shear loading, leading to a more plastic-like response.

In the viscoelastic region, Figure 4.25 b), both loading modes seem to promote similar viscoelastic behaviour. Once again the plastic components could be more pronounced in the case of shear loading, when looking the existence of an apparent yield during loading.

On the rubbery plateau, Figure 4.25 c), both behaviours are viscoelastic and rather equivalent. The other PMMAs with low molar mass (93 and 120) also displayed similar relationship between their mechanical responses when tested under tensile and shear loading.

It could be concluded that the type of loading does not affect much the initial viscoelastic components through the studied temperature and strain rate. However, at higher strain level, the viscoelasticity and or plastic-like processes could depend on the loading stress state.

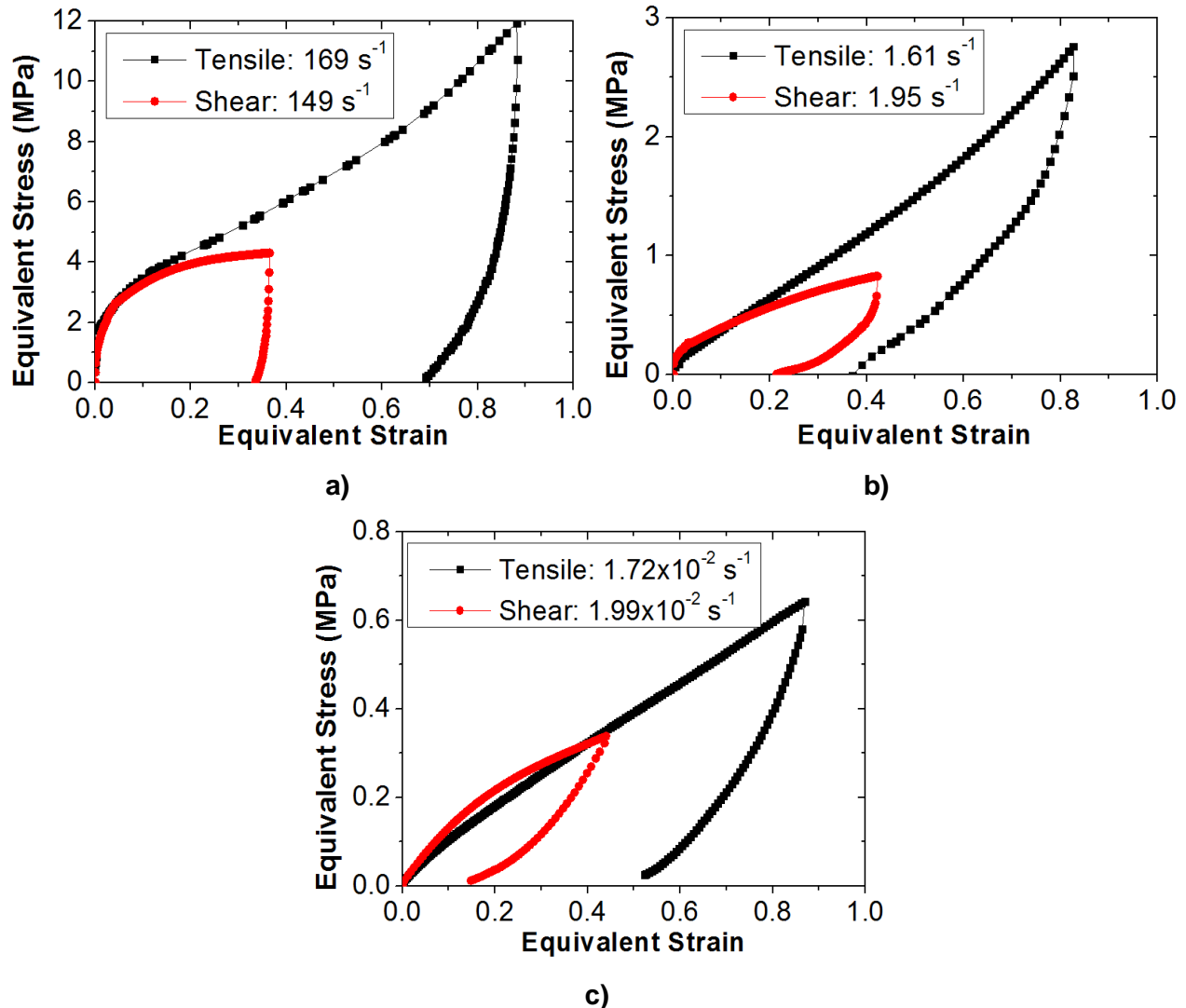


Figure 4.25: Comparison of the equivalent stress-strain curves of PMMA 80 under uniaxial tensile and shear loading: a) near the glassy region, b) viscoelastic region and c) rubbery plateau.

By comparing the von Mises stress-strain curves obtained at similar equivalent strain rates for shear and tensile tests on PMMA CL (Figure 4.26), we can notice that the mechanical behaviour

is similar for the different material states (Figure 4.26 a), b) and c)). However, the strain hardening and mechanical stiffness are higher for tensile loading compared to shear loading. The same tendency was found on PMMA 3500. Treolar [102] also reported such differences between the tensile and shear mechanical response for hyperelastic rubbers.

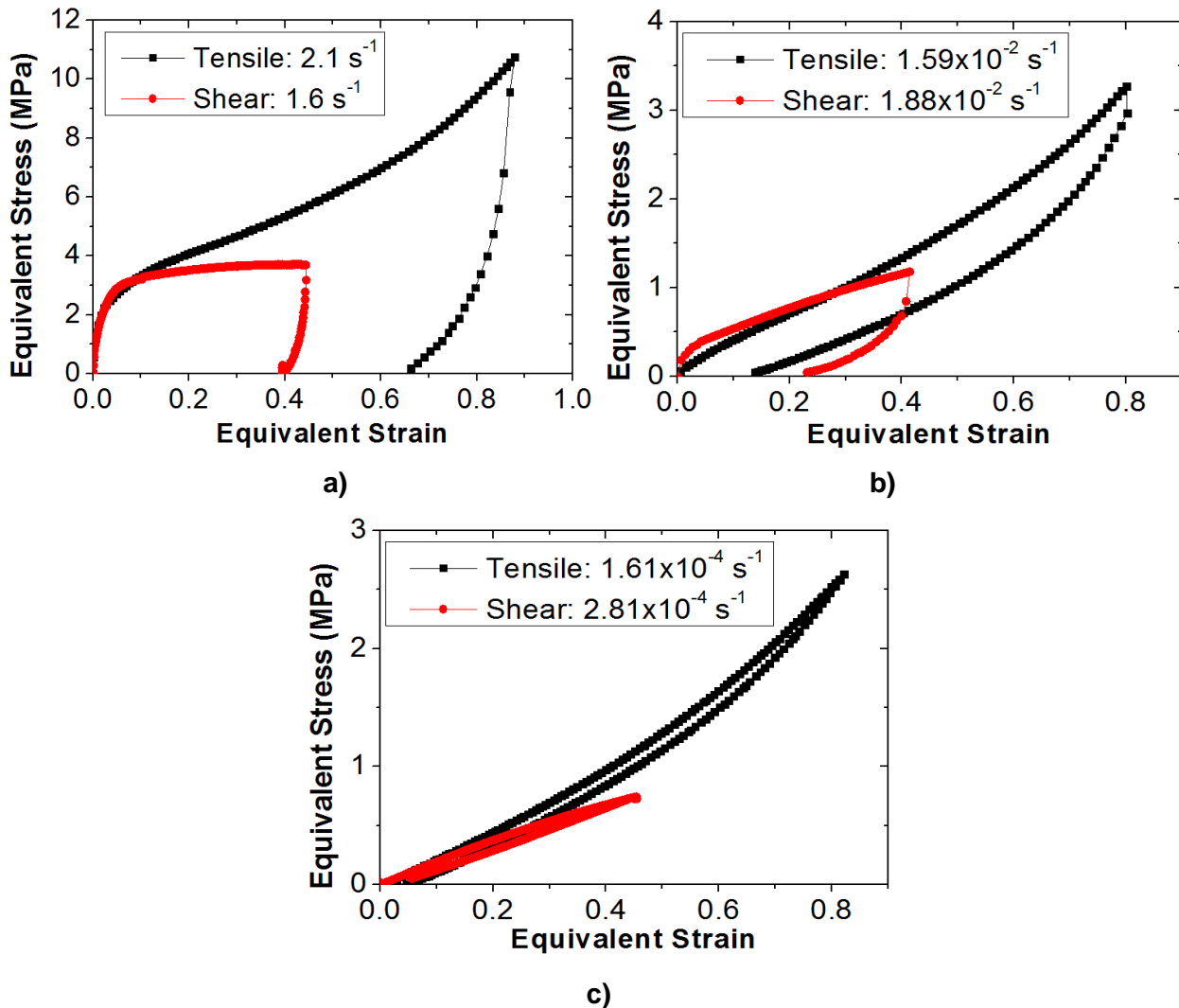


Figure 4.26: Comparison of the equivalent stress-strain curves of PMMA CL under uniaxial tensile and shear loading: a) near the glassy region, b) viscoelastic region and c) rubbery plateau.

These results showed a difference between the mechanical behaviours of the PMMAs under tensile and shear loading. G'Sell et al. [99], [100] studied the polycarbonate when plastically deformed under shear loading using birefringence and X-ray diffraction measurements. Their work revealed that, with the increase of deformation, there is a gradual rotation of the mean orientation axis of the polymer molecules towards the shear principal direction. Indeed, we can imagine a polymer coil submitted to shear load (as displayed in Figure 4.27): at zero strain, the

mean orientation axis of the polymer (dotted red line) will be unaffected. When the deformation starts, the molecules will progressively orient themselves along a mean direction parallel to the macroscopic strain direction, which may promote a further chain stretching. Contrary to this under tensile loading, chains are extended parallel to the loading which induces more hardening.

Further research is proposed to explore different experimental configurations that will promote a shear state up to higher deformations. Additionally, birefringence analysis would be useful to quantify the molecular orientation of the PMMAs when deformed. Moreover, other mechanical tests as compression and biaxial tests are recommended to explore the molecular mobility dependence on the stress state.

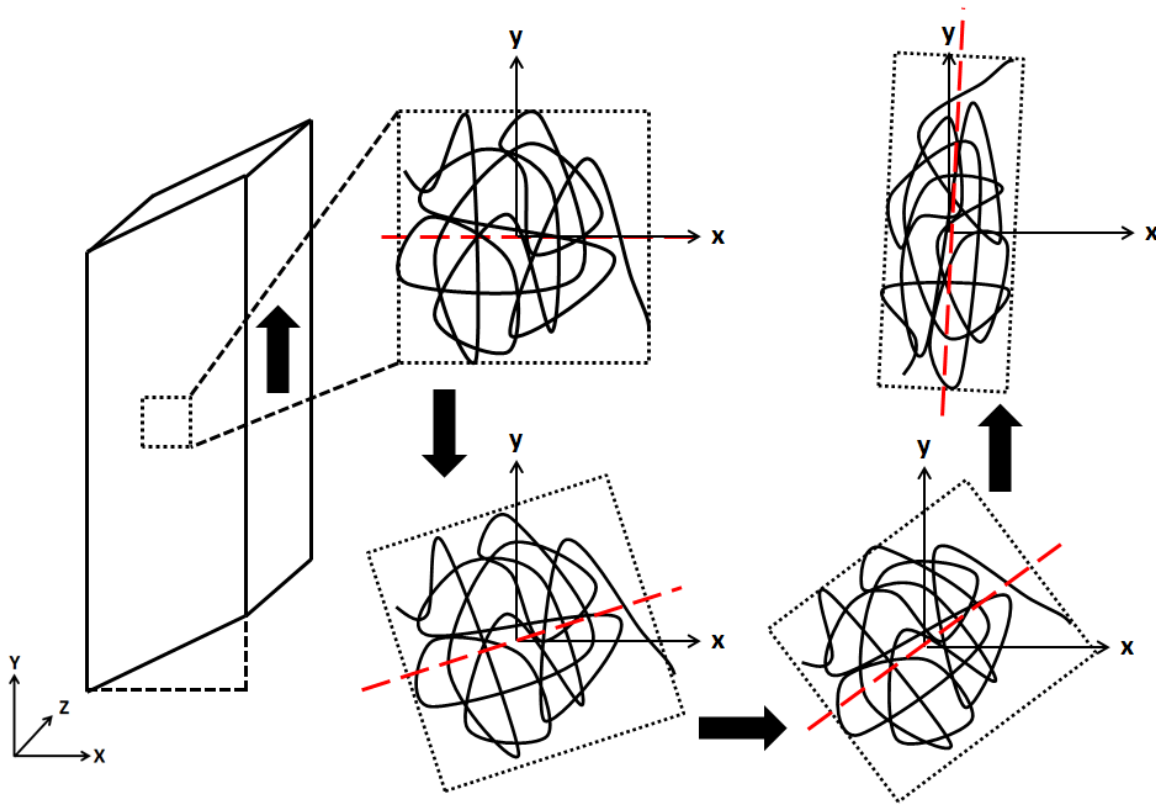


Figure 4.27: Schematization of a polymer coil submitted to a shear loading.

It was mentioned that the hysteresis varied with the equivalent strain rate. However this has not been quantified yet. In a tensile or shear cycling test, the hysteresis, ϕ , may be computed through the area inside the loop. This can be written as:

$$\phi = \frac{1}{\varepsilon_f} \int_0^{\varepsilon_f} \sigma d\varepsilon, \quad 4.10$$

where ε_f is the final true strain of the test. The first term of the Equation is used to normalize the hysteresis, since this value increases with the final strain [103]. Figure 4.28 shows the hysteresis evolution with the equivalent strain rate for PMMA 80 and PMMA CL when submitted to tensile and shear loading.

The hysteresis of both PMMAs is considerably lower under shear loading. The most striking data correspond to PMMA CL at 10^{-4} s^{-1} where even if the mechanical behaviour for both loading modes was hyperelastic, the hysteresis was remarkably lower when the material was under shear loading. These differences could be explained for the higher mechanical stiffness that the material displays under tensile loading.

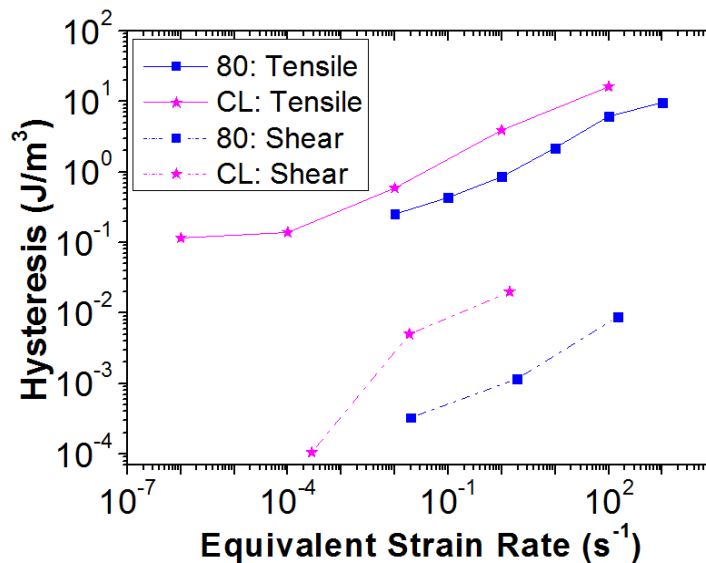


Figure 4.28: Normalized hysteresis evolution with the equivalent strain rate for PMMA 80 and PMMA CL under tensile and shear loads.

4.5.6 Molecular Weight and Cross-linking Effect on the Mechanical Response at Large Deformation

After verifying that the equivalent strain rate is a relevant parameter for addressing the mechanical behaviour of the material at large deformation, we propose to compare the mechanical response of the five PMMAs under tensile loading at a constant equivalent strain rate.

4.5.6.1 Molecular weight effect

Figure 4.29 a) - d) display the effect of the molecular weight on the mechanical response (true stress – true strain curves) of PMMAs for different equivalent strain rates (indicated in the title of the figure). Figure 4.29 e) shows their respective storage modulus master curves for reference. We observe that for a given equivalent strain rate, the mechanical behaviour of the polymer changes considerably.

At equivalent strain rates of 10^2 s^{-1} and 10^0 s^{-1} , Figure 4.29 a) and b) reveals that PMMAs 3500 and 93 present a more glassy mechanical response with an apparent viscoelastic behaviour, followed by a softening and a strain hardening with an important hysteresis. At these conditions, PMMAs 120 and 80 show a viscoelastic and rubbery-like behaviour with smaller hysteresis. This results could be related with the master curves, where at 10^2 s^{-1} PMMAs 3500 and 93 are near the glassy region, while PMMAs 120 and 80 are closer to the viscoelastic region.

At 10^{-2} s^{-1} , Figure 4.29 c) shows that PMMAs 3500, 120 and 93 display a non-linear response with a decreasing hysteresis while PMMA 80 already behaves as a liquid viscoelastic material. Such behaviour is confirmed by Figure 4.29 e) where the storage modulus of PMMAs 3500, 120 and 93 is closer to the rubbery plateau. In this regime, entanglements partially constrain molecular motions, leading to viscohyperelastic behaviour. Regarding PMMA 80, the storage modulus is near from the flowing region, meaning that the number of entanglements is lower.

Figure 4.29 d) displays that PMMA 3500 exhibits hyperelastic behaviour (almost zero hysteresis) while PMMAs 120 and 93 show a liquid viscoelastic response. PMMA 80 could not be characterized at this equivalent strain rate since the material entered in its flowing region. This is highlighted by the storage modulus master curve where PMMA is in the rubbery region at $\dot{\epsilon}_{\text{eq}} \approx 10^{-4} \text{ s}^{-1}$. Entanglements act as “tied” points that promote an entropic elastic behaviour while PMMAs 120, 93 are on the onset of the flowing region and PMMA 80 in the flowing region. In this region, the entanglements density has considerably decreased and become ineffective.

Results suggest that both in low and large deformation domain, the increase of the molecular weight promotes a higher density of entanglements which act as junction points and govern the material mechanical response. When decreasing the equivalent strain rate, a progressive disentanglement of the junction points is allowed. Such disentanglement will allow molecular motions leading to an evolution of the elastic and inelastic responses, the tendencies of which being predicted by the master curves determined from DMTA.

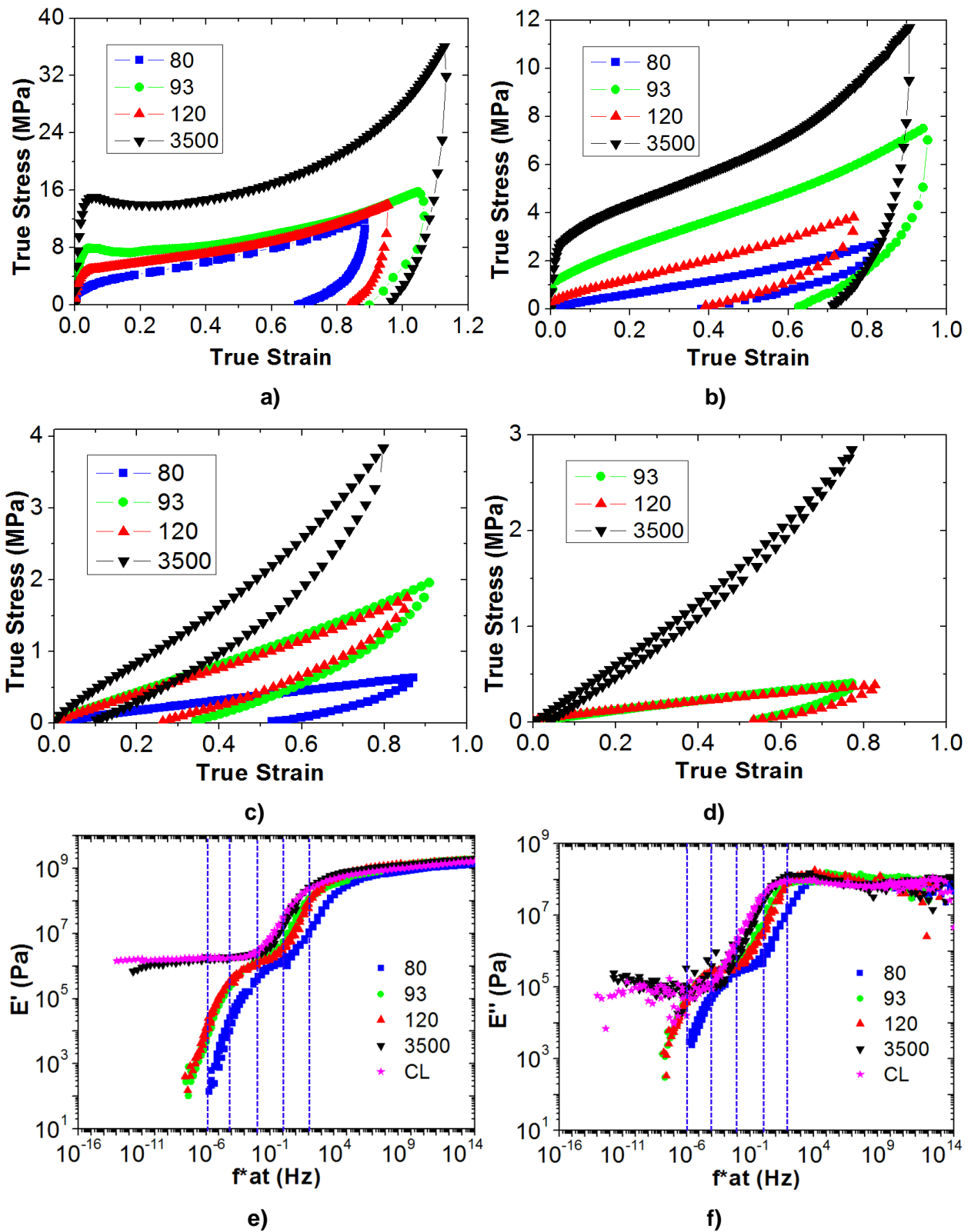


Figure 4.29: Macroscopic tensile curves for PMMAs with different molar masses at different equivalent strain rates: a) 10^2 s^{-1} , b) 10^0 s^{-1} , c) 10^{-2} s^{-1} and d) 10^{-4} s^{-1} . e) Storage Modulus and f) loss modulus master curves at reference temperature of $130 \text{ }^\circ\text{C}$.

For a better understanding of the role of entanglements on the energy dissipation, we can use Equation 4.10 to quantify the hysteresis evolution with the equivalent strain rate of the different PMMAs. Results are presented in Figure 4.30 where the variation of the normalized hysteresis with the equivalent strain rate is highlighted for the PMMAs of different molar masses. These data suggest that the hysteresis drastically decreases for all PMMAs when the equivalent strain rate decreases, i.e. when moving from the surrounding of the glassy region to the viscoelastic state and then to the rubbery regime. These observations were also reported by other authors on epoxy [70] and silicone rubbers [103].

In conclusion, we showed qualitatively and quantitatively that the hysteresis evolution displayed by the different PMMAs under large deformation, is in agreement with the loss modulus evolution displayed in Figure 4.29 f) using DMTA.

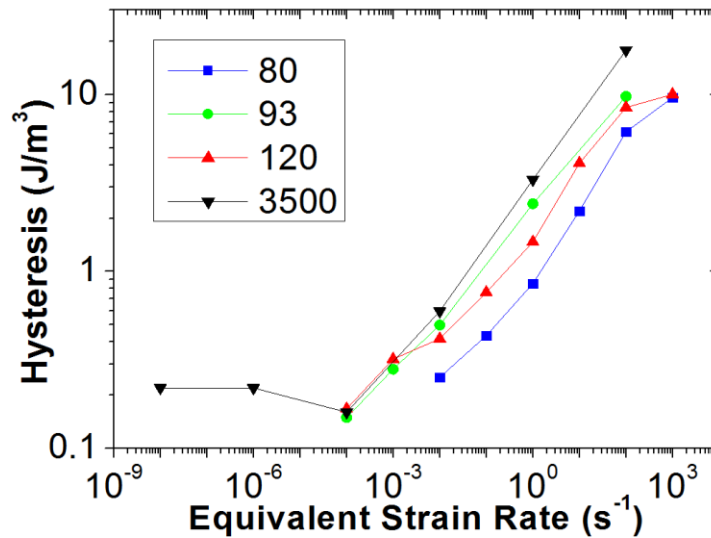


Figure 4.30: Normalized hysteresis evolution with the equivalent strain rate for the different molecular weight PMMAs.

4.5.6.2 Crosslinking effect

Regarding the influence of the crosslinks density at large deformation, Figure 4.31 a) - e) displays the true stress – true strain curves of the crosslinked PMMA and the PMMA 3500 for different equivalent strain rates. This comparison was chosen to understand the differences between a polymer network highly entangled and a crosslinked one. The tested conditions are illustrated in Figure 4.29 e) and f) on the storage and loss moduli master curves.

Figure 4.31 a) shows the mechanical response near the glassy region, at 10² s⁻¹. Both materials display viscoelastoplastic behaviour, with an initial viscoelastic region, a strain hardening and an important residual plastic strain. Unlike PMMA 3500, the crosslinked PMMA

does not display stress softening. Despite this difference, the mechanical response of both PMMAs is quite similar.

In the viscoelastic region at 10^0 s^{-1} , we can observe on Figure 4.31 b) that both materials have viscoelastoplastic behaviour with reduced mechanical stiffness compared to the behaviour at 10^2 s^{-1} . Additionally, both PMMAs display a similar material stiffness and hysteresis, meaning that the entanglements and crosslinks have an equivalent impact at the viscoelastic region, as it was seen previously.

Figure 4.31 c) presents the mechanical response near the rubbery plateau, at 10^{-2} s^{-1} . Both materials show a mix between viscoelasticity and hyperelasticity. Indeed, a non-linear response is observed, with some residual strain and hysteresis after unloading. PMMA CL shows a lower mechanical stiffness than PMMA 3500, which indicates that the molecular constraining promoted from the crosslinks may be less effective than the one established from the physical entanglements.

Figure 4.31 d) shows the mechanical response at 10^{-4} s^{-1} when the materials are in their rubbery plateau. The PMMAs exhibit hyperelastic behaviour with almost no hysteresis. This hyperelasticity may be explained by the lack of chain slippage in the polymer network induced by high amount of physical entanglements regarding PMMA 3500 and chemical crosslinks regarding PMMA CL. Additionally, even though the storage modulus of both PMMAs seems to be similar (Figure 4.29 e)), PMMA 3500 presents higher stresses at large deformation, suggesting that physical entanglement still burdens the chain motions more effectively than crosslinks.

Figure 4.31 e) reveals that both materials show a hyperelastic behaviour at 10^{-6} s^{-1} with a slight increase of the dissipated energy for PMMA 3500. Moreover, at a deformation of 0.6, the strain hardening in the PMMA CL is more relevant than in the PMMA 3500. This difference can be attributed to disentanglement process activated for these test conditions for the high molecular weight PMMA. The polymer may present a reduction of its physical junction points while, for PMMA CL, the chemical crosslinks are still present and effective for promoting strain hardening mechanisms. Therefore the material resistance and amount of hysteresis remain the same as for $\dot{\epsilon}_{\text{eq}} \approx 10^{-4} \text{ s}^{-1}$.

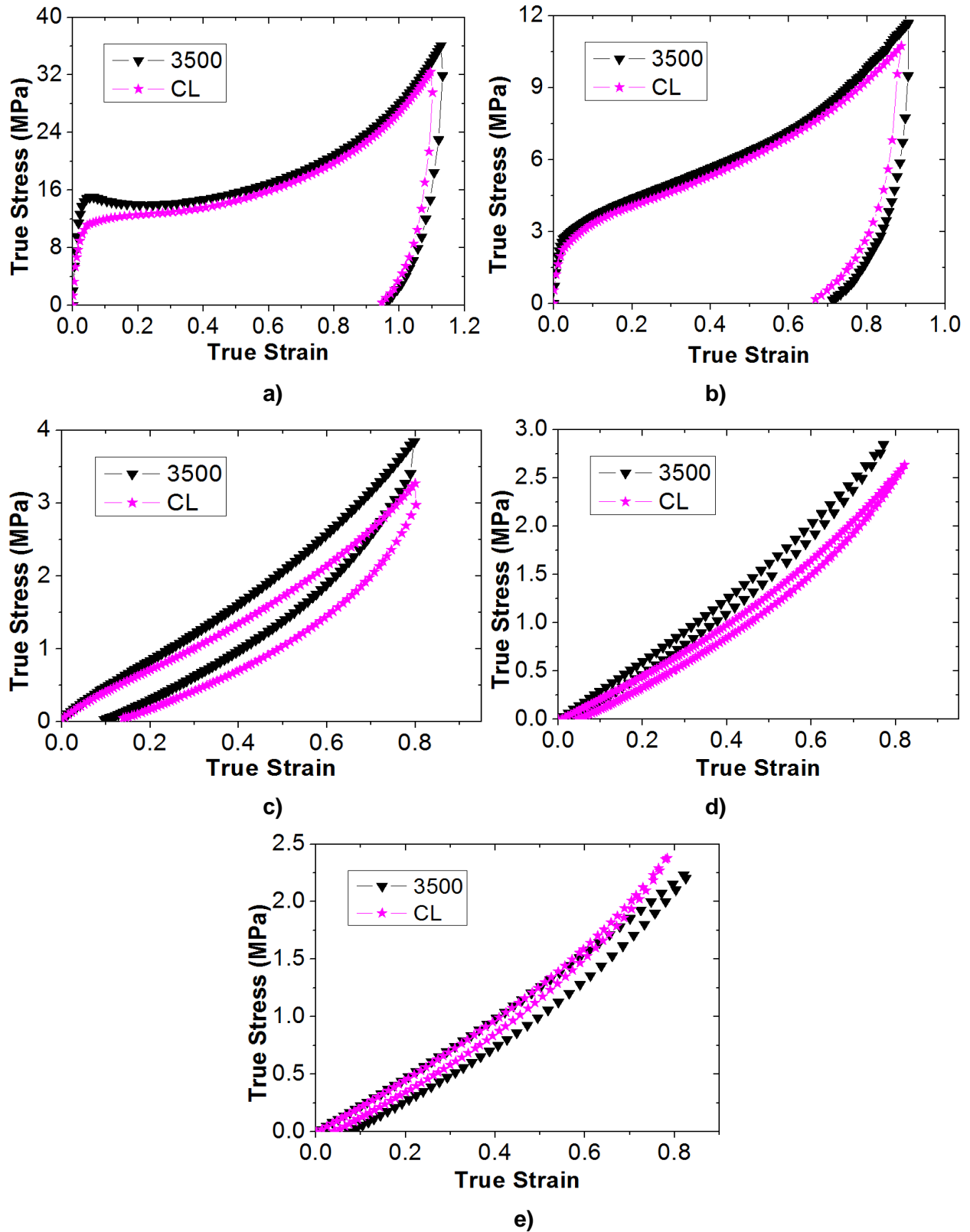


Figure 4.31: Macroscopic tensile curves for PMMA 3500 and PMMA CL at equivalent strain rates of a) 10^2 , b) 10^0 s⁻¹, c) 10^{-2} s⁻¹, d) 10^{-4} s⁻¹ and e) 10^{-6} s⁻¹.

By means of Equation 4.10, we can also quantify evolution of hysteresis with the equivalent strain rate. This is depicted in Figure 4.32. Once again, results seem to be coherent with master curves from Figure 4.29 f), showing that the hysteresis decrease along the viscoelastic region is almost the same for both PMMAs. At this point, we can infer that crosslinks and entanglements constrain the polymer network in a similar manner. In the rubbery plateau, results confirm that unlike PMMA 3500, the hysteresis remains nearly constant for PMMA CL when decreasing the equivalent strain rate, suggesting that crosslinks density may remain constant in these conditions. In parallel, PMMA 3500 experiences an increase in dissipation, which is an image of new inelastic process we have named viscous flow.

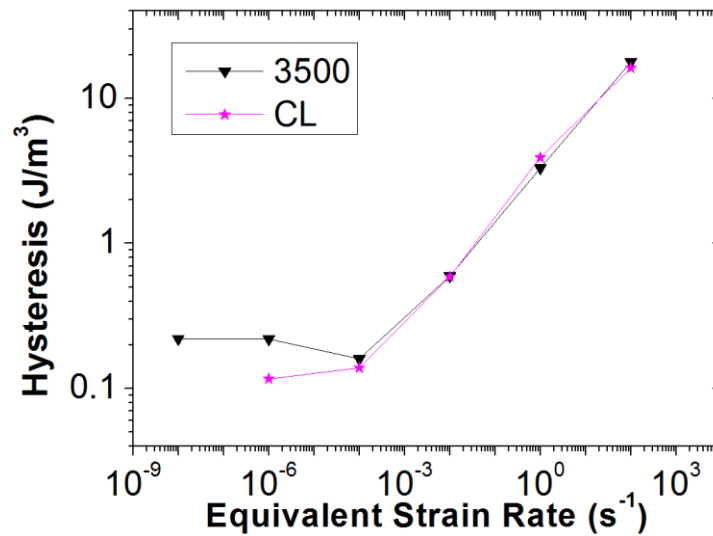


Figure 4.32: Normalized hysteresis evolution with the equivalent strain rate for PMMA 3500 and PMMA CL.

4.6 Summary

In this Chapter, the mechanical behaviour of five PMMAs characterized by different molecular weights and the presence or not of crosslinking was investigated at large deformation levels by performing uploading-unloading tensile and shear tests.

The shift factors determined from the linear domain were validated to the range of large deformation, which allowed building a test matrix using, as main parameter, the equivalent strain rate at a reference temperature (chosen at 130 °C). This parameter allows coupling the effects of temperature and of strain rate. This opens new doors for characterizing the temperature/strain rate dependence of polymers and may also help to simplify the modelling of mechanical behaviour. Further works will focus on validating this methodology for other stress states like compression and biaxial conditions. Additionally, future effort may focus on exploring the applicability of the equivalent strain rate for high strain rate applications such as impact by also accounting for thermomechanical coupling.

Then, by fixing an equivalent strain rate, we compared the influence of the stress state on the mechanical behaviour of the PMMAs. It was observed that the global mechanical response was similar; however the strain hardening, mechanical stiffness and hysteresis were higher for tensile loading compared to shear loading.

Besides the validity of the equivalent strain rate for different stress states, it was also showed that this concept was successfully applied for PMMAs with different entanglements and crosslinks densities. By choosing an equivalent strain rate, it was observed that the molecular weight, and more seemingly the entanglements density, governs the mechanical response at large deformation levels in the viscoelastic region and rubbery plateau. Additionally, crosslinks seemed to have an equivalent mechanical behaviour to PMMA 3500 in the viscoelastic region. However, differences were found in the rubbery plateau were PMMA CL remained hyperelastic with unaffected mechanical resistance. This illustrates the permanent nature of chemical crosslinks along this plateau.

These experimental results provides a relevant material database which accounts for the effects of the temperature, strain rate, stress state, molecular weight and crosslinking degree. This overall data will be used as reference for modelling the mechanical behaviour of amorphous polymers at large deformation. This will be presented in next Chapter.

CHAPTER V

MODELLING OF THE MECHANICAL BEHAVIOUR OF AMOPHOUS POLYMERS WITH DIFFERENT ARCHITECTURES

This Chapter addressed the modelling of the mechanical behaviour of amorphous PMMAs accounting for inelastic mechanisms coming from the evolution of internal state variables under deformation. The theoretical results were compared with the experimental observations showed in previous Chapters.

The first part focused on the different approaches available in the literature to describe the mechanical response of polymers. Additionally, the model formalisms are then summarized. Such aspect includes the hypothesis of the internal state variables. The second part of this Chapter corresponds to the comparison between the experimental stress-strain curves obtained previously and the theoretical curves given by the model. This comparison is performed at constant equivalent strain rate. Thanks to this approach, empirical equations were then proposed to describe the time/temperature dependence of model parameters. Then, these results were used to enhance the comprehension of the polymer chain motions when the material was deformed.

Ce chapitre a porté sur la modélisation du comportement mécanique des PMMA amorphes en tenant compte des mécanismes inélastiques. Les résultats théoriques ont été comparés aux observations expérimentales présentées dans les chapitres précédents.

La première partie a porté sur les différentes approches disponibles dans la littérature pour décrire la réponse mécanique des polymères. De plus, les formalismes des modèles sont ensuite résumés. La deuxième partie de ce chapitre correspond à la comparaison entre les courbes de contrainte-déformation expérimentales obtenues précédemment et les courbes théoriques données par le modèle. Cette comparaison est effectuée à vitesse de déformation équivalente constante. Grâce à cette approche, des équations empiriques ont ensuite été proposées pour décrire la dépendance temps/température des paramètres du modèle. Ensuite, ces résultats ont été utilisés pour améliorer la compréhension des mouvements de la chaîne polymère lorsque le matériau était déformé.

CONTENT

| | | |
|-------|-------------------------------------------------------------------------------------------------------|-----|
| 5 | Modelling of the Mechanical Behaviour of PMMA with Different Molar Mass and Crosslinking Degree | 99 |
| 5.1 | Literature review on the modelling of mechanical response of polymers | 100 |
| 5.1.1 | Phenomenological models | 100 |
| 5.1.2 | Physically based models | 100 |
| 5.1.3 | Combining phenomenological and physical approaches | 102 |
| 5.1.4 | Summary..... | 107 |
| 5.2 | Viscohyperelastic modelling | 107 |
| 5.2.1 | Model definition | 107 |
| 5.2.2 | Internal state variables evolution | 111 |
| 5.2.3 | Model summary..... | 113 |
| 5.2.4 | 1D Case: Incompressible visco-hyperelastic model..... | 113 |
| 5.3 | Results and Discussions | 115 |
| 5.3.1 | Relevance of the model..... | 116 |
| 5.3.2 | Physical contribution of each branch on the overall mechanical response..... | 124 |
| 5.3.3 | Role of the branches when varying the equivalent strain rate..... | 126 |
| 5.3.4 | Dependence of the EV's parameters with the equivalent strain rate..... | 131 |
| 5.3.5 | Sensitivity to the material parameters..... | 135 |
| 5.4 | Summary..... | 137 |

5 Modelling of the Mechanical Behaviour of PMMA with Different Molar Mass and Crosslinking Degree

The experimental results presented in the previous Chapter confirmed that the mechanical response on amorphous PMMA is not trivial to predict. Indeed, there are several factors that will affect the mechanical behaviour: strain level, stress state, temperature, strain rate and factors such as the entanglements and crosslinks density. Depending on these factors, polymers may display a nonlinear behaviour that combines viscoelasticity, viscoplasticity, softening and strain hardening without any clear threshold, making difficult the modelling of their mechanical response.

In the literature, it is possible to find many works devoted to describe the mechanical behaviour of amorphous polymers. In this work, we chose the approach proposed by Billon [11] and then extended by Gehring et al. [25] which has proven satisfactory results in the past for amorphous PMMA and PET. However, there are still some questions that need to be answered. Indeed, the model used in [25] was tested just at moderate strain levels, around 30%. Therefore the domain of large deformations is still unexplored. Additionally, the use of the “equivalent strain rate” is still not included in this way of modelling. Also, this model has not yet been verified for a wide range of condition, corresponding to near-liquid, rubbery state, viscoelastic and near glassy state. Moreover, there is not enough information on how the internal state variables evolution (such as the entanglements or weak bond interactions) depends with the strain rate, temperature, molar mass and crosslinking degree.

Therefore, we aim to verify the versatility of the model when tested for a large number of experimental conditions, accounting for the concept of equivalent strain rate for PMMAs of different molecular weights and crosslinking degree. More especially, the specific goals of this Chapter can be listed as next:

- To successfully model the mechanical response under tensile cyclic loading at different equivalent strain rates for all the PMMAs.
- To understand the effect of the different parameters regarding the Edward and Vilgis strain energy function.
- To propose empirical relationships between the internal state variables and the equivalent strain rate.
- To physically describe and understand the evolution of the internal state variables during the deformation process, and relate them to the macroscopic mechanical response.

In the next Section, we will list different work used in the literature to describe the mechanical response of polymers, highlighting their advantages but also pointing aspects that may be improved. Then, the approach used in this work, proposed by Billon [11] and Gehring et al. [25], will be introduced. Later, results and discussions will be presented.

5.1 Literature review on the modelling of mechanical response of polymers

In the literature, we can find several constitutive behaviours used to model the mechanical behaviour of polymers (See Bouvard et al. [104] for a review). These models can be classified in two main families: phenomenological based models and physically based models.

5.1.1 Phenomenological models

The phenomenological models aim to describe the mechanical behaviour of the polymer by determining empirical parameters from experimental observations. These models are normally easier to implement than the physically-based ones. However, most of them do not consider the influence of material microstructural characteristics as well as their evolutions, which may lead to some limitations.

Many of these phenomenological models consist on differential equations combining linear and nonlinear springs with dashpots [105]–[107]. For instance and among others, G'Sell and Jonas [108], [109], Billon [110] and more recently Wang et al. [97] employed a phenomenological approach characterized by the next form:

$$\sigma = K \exp\left(\frac{a}{T}\right) (1 - \exp(-W\bar{\varepsilon})) \exp(h\varepsilon^n) \dot{\varepsilon}^m, \quad 5.1$$

where K is linked to the elastic modulus, a , W , h , n and m are material parameters. The term $\exp(a/T)$ accounts for the temperature dependency, $(1 - \exp(-W\bar{\varepsilon}))$ considers the initial non-linear behaviour, $\exp(h\varepsilon^n)$ describes the strain hardening and $\dot{\varepsilon}^m$ introduces the time dependency [110]. This model was satisfactory used for describing the behaviour of PVC, HDPE and PC under tensile and compression loading, but lacked in predicting the mechanical response over a wide range of temperature/strain rate conditions and also in describing cyclic loading.

5.1.2 Physically based models

The physically based models aim to account for the internal microstructure of the polymer. Haward and Trackary [111] were some of the first ones to model the mechanical response of

glassy polymers by combining yield/flow physical models [112]–[117] and rubbery elasticity. Other authors like Boyce et al. [118] and Dupaix et al. [119] have also used this idea for describing the mechanical response near the glass transition temperature by means of hyperelastic models.

5.1.2.1 Hyperelasticity

In general, hyperelasticity is defined through strain energy functions, ψ_v , that can be linked to the stress through:

$$\sigma = 2 \left(\lambda_i^2 \frac{\partial \psi_v}{\partial I_1} - \frac{1}{\lambda_i^2} \frac{\partial \psi_v}{\partial I_2} \right) - p, \quad i = 1, 3 \quad 5.2$$

where I_1 and I_2 are the invariants of the left Cauchy-Green strain tensor, $(\lambda_i)_{i=1,3}$ are the principal stretch ratios and p is the pressure which can be determined from the boundary conditions.

Several energy functions can be found in the literature. (see Marckmann and Verron [120] for a review). Similar to the viscoelastic/viscoplastic modelling, hyperelasticity can be classified through phenomenological and physical based models.

Phenomenological models derive from mathematical developments, as polynomial functions that depends on the strain invariants (Mooney-Rivlin [121], [122] and Yeoh [123]) or on the principal stretch ratios (Ogden [124]–[126]). Material parameters are determined at specific conditions of deformation, temperature and strain rate.

Physically based strain energy functions are classically obtained through statistical methods that quantify the probabilities for the polymer network to adopt certain conformations. One of the first approaches was the Neo-Hookean model proposed by Treloar [127] whose energy function consisted in a Gaussian statistical distribution. Then, Ball et al. [128] developed a slip-link model to account the chain slippage during the deformation. Later, Arruda and Boyce [129] proposed a 8-chain model which includes number of rigid links between entanglements. After this, Kaliske and Heinrich [130] worked on an extended tube model which used a non-Gaussian distribution and introduced an inextensibility parameter.

In conclusion, phenomenological and physically based models have different positive aspects and drawbacks. Phenomenological approaches are easier to implement and may have less parameters. However they exhibit some lack on describing microstructural changes. Physical

models do consider internal changes in the microstructure of the material, but they may be more complex. Regardless their differences, both approaches are often found in constitutive modelling [131]–[134].

5.1.3 Combining phenomenological and physical approaches

Studies devoted to describe the complex mechanical behaviour of amorphous polymers under large deformation combine phenomenological and physical approaches to take advantage of their virtues. Examples can be found in constitutive modelling proposed by Hasan et al. [135], Muliana et al. [136], Guo et al. [137], Yu et al. [138], Li et al. [139], Gu et al. [140] and Praud et al. [141] which display satisfactory result for monotonic and non-monotonic loading. However, these examples were successfully employed up to 20% of true strain, leaving the domain of larger strain level unexplored. We will present next, some models from the literature that have shown promising results in modelling the mechanical response of polymers at high deformation levels.

5.1.3.1 Dooling et al. 2002 [142]

Using the constitutive model proposed by Buckley et al. [143], [144] on PET, Dooling et al. modelled the hot drawing of high molecular weight PMMA. Two main sources of stored energy were considered: i) bond stretching and ii) perturbations in the configurational entropy. Thus, the model used linear elasticity, Eyring viscous flow and the Edward-Vilgis energy function [23], respectively. For PMMA, they proposed to incorporate two slippage viscosities: one above the glass transition temperature and another one below. Figure 5.1 displays the comparison of the model with the experimental data for a PMMA at 0.4 min^{-1} at various temperatures under monotonic loading. It can be seen that the model properly describes the change in shape of the stress-strain curves with the increase in temperature. However, this model was not developed for reproducing the response during unloading stage.

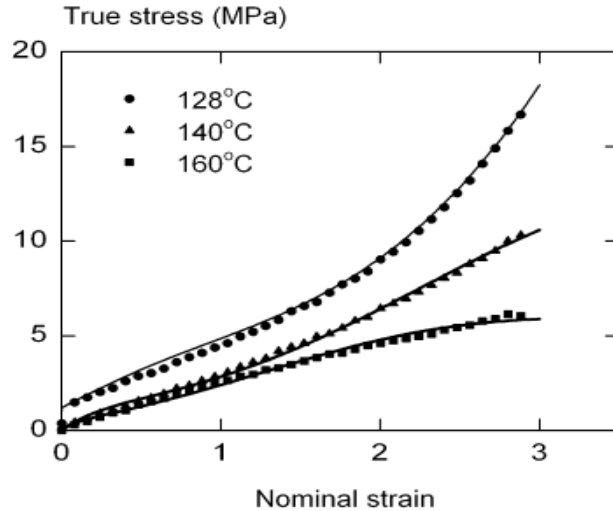


Figure 5.1: Drawing of a PMMA at nominal strain rate of 0.4min^{-1} and various temperatures. Experimental data (points) and model (lines) [142].

5.1.3.2 *Dupaix and Boyce 2006* [119]

This constitutive model aimed to capture the rate-dependent behaviour of an amorphous PETG at temperatures near the glass transition. In this work, the mechanical response was assumed to be a combination of the resistance originated from intermolecular interactions and from the network resistance produced when the material is stretched. A representation of the rheological components is depicted in Figure 5.2 a).

Intermolecular interactions were described as a combination of linear elasticity and viscous strain rate as proposed by Argon et al. [114] and Boyce et al. [115]. The network resistance was considered as a non-linear elastic component (using the 8-Chain Model [129]) and non-linear viscous element which includes chain reptation [145] and cessation of molecular relaxation [146]. Figure 5.2 a) and b) show a comparison between the experimental and theoretical data on PETG. The model shows promising results in capturing the strain rate and temperature dependence up to deformation of around 80%. However similar to the previous model, it is not used for reproducing an unloading path.

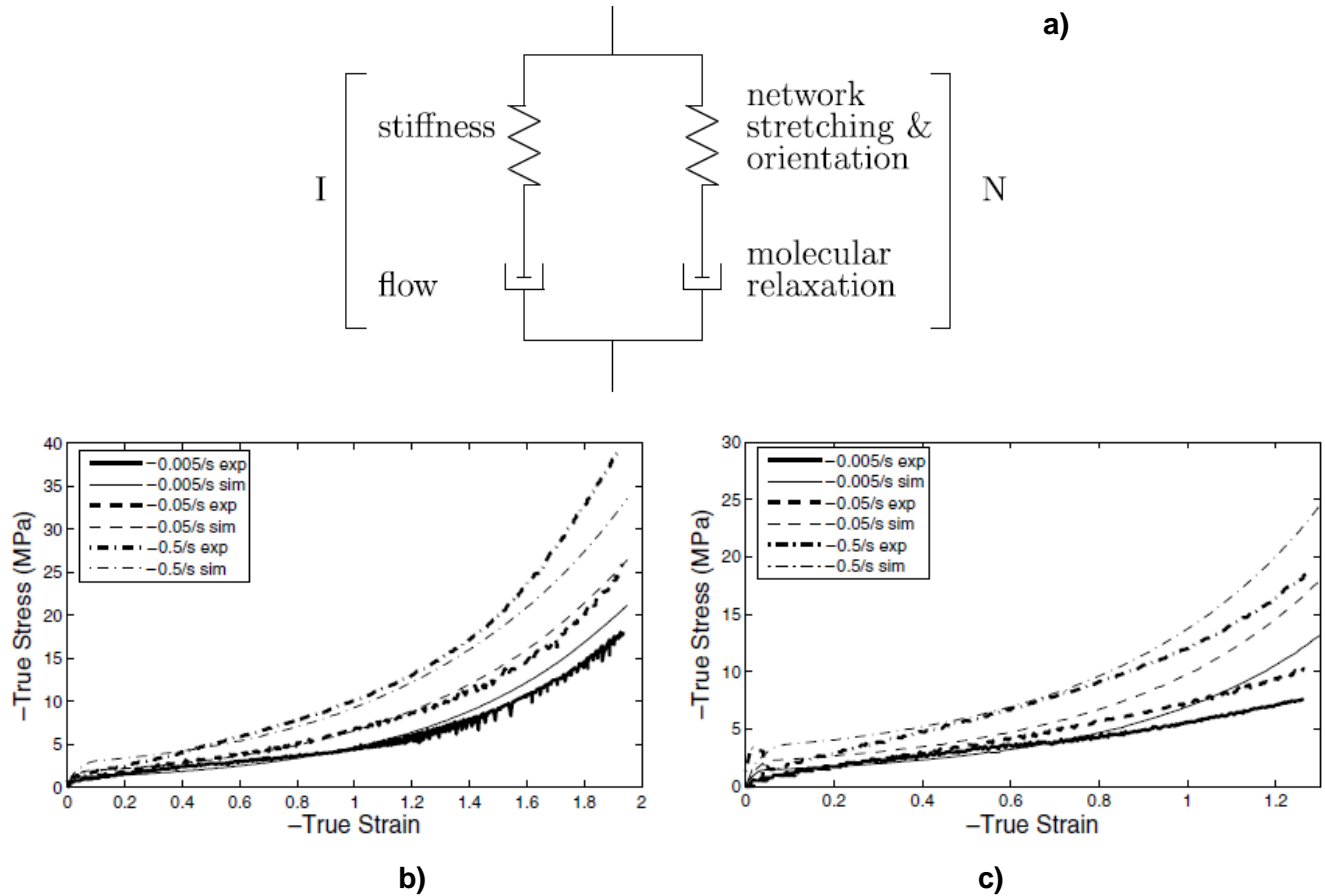


Figure 5.2: a) Schematic representation of the model. Comparison between experimental and numerical results on compression loading on PETG at 90°C: b) uniaxial and c) plane strain [119].

5.1.3.3 *Sweeney et al. 2009* [147]

The constitutive model proposed by Sweeney et al. is based on a rate dependent component described with an Eyring viscous process and two hyperelastic Edward-Vilgis equivalent networks, as depicted in Figure 5.3 a). This model showed good agreement with experimental data performed under monotonic biaxial testing of PP at 135°C (see Figure 5.3 b) and c)). The initial apparent modulus and yielding are well described. The model is therefore able to capture the mechanical behaviour of polymers at large deformation for biaxial loading. But once again, this approach was not verified for cyclic loading.

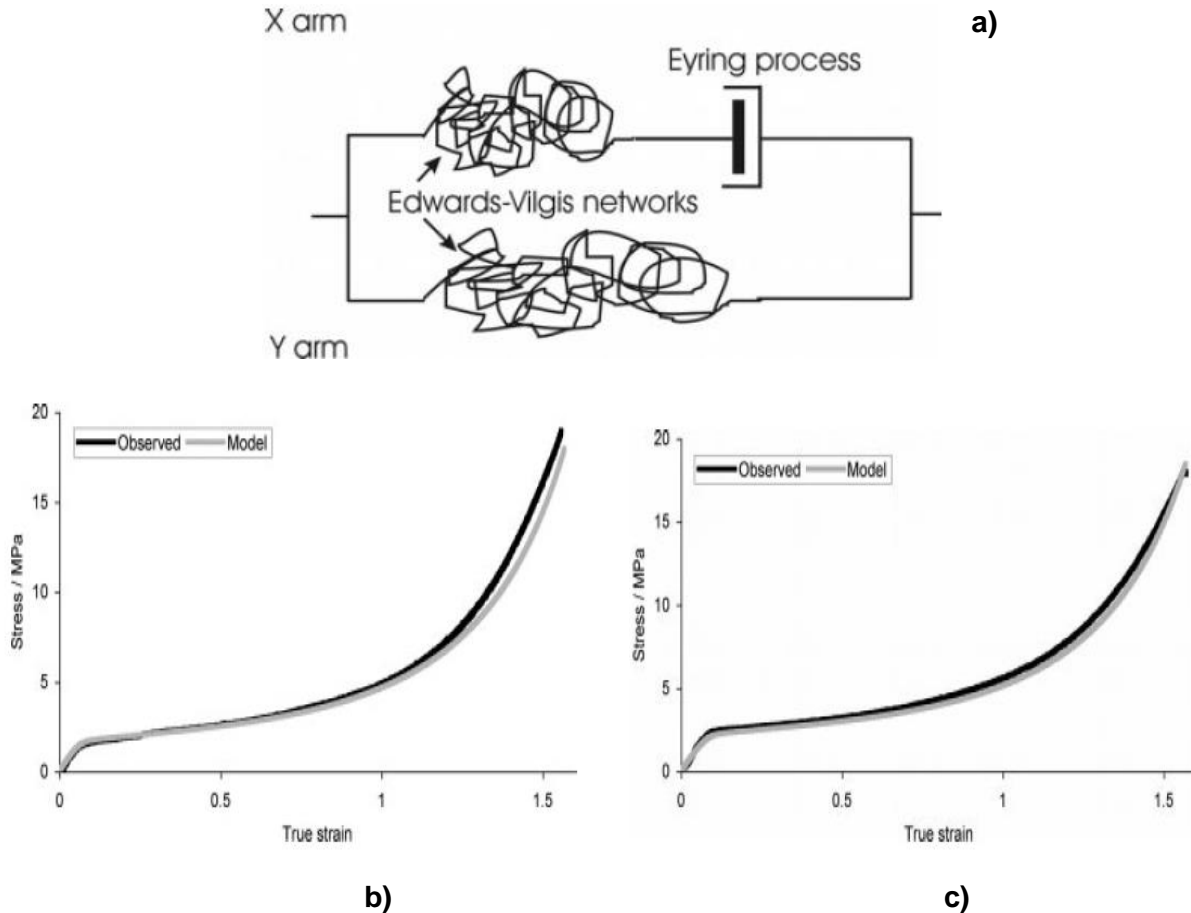


Figure 5.3: a) Schematic representation of the constitutive model. Simultaneous biaxial stretching at 135°C for strain rate of: b) 0.37 s^{-1} and c) 2.3 s^{-1} [147].

5.1.3.4 *Srivastava, Anand, Ames et al. 2010* [148]–[150]

This constitutive theory was developed to describe the thermomechanical behaviour of amorphous polymers at large deformation levels from room temperature to approximately 50°C above the glass transition temperature. This approach introduced macroscopic internal state variables to represent important features of the microstructure resistance to plastic flow and strain hardening. Intermolecular resistance was described by nonlinear springs and thermally-activated dashpots in parallel with another nonlinear spring. The molecular network resistance was described using a phenomenological form of the free energy function (see Gent [151]) and the viscous part was included by using evolution equation for internal state variables.

Figure 5.4 shows a comparison of the experimental unloading-unloading compression tests on PMMA with the constitutive modelling. The model is in good agreement with the experimental results. Despite of the model accuracy, the number of parameters is quite high which makes the identification of the model parameter more exhaustive.

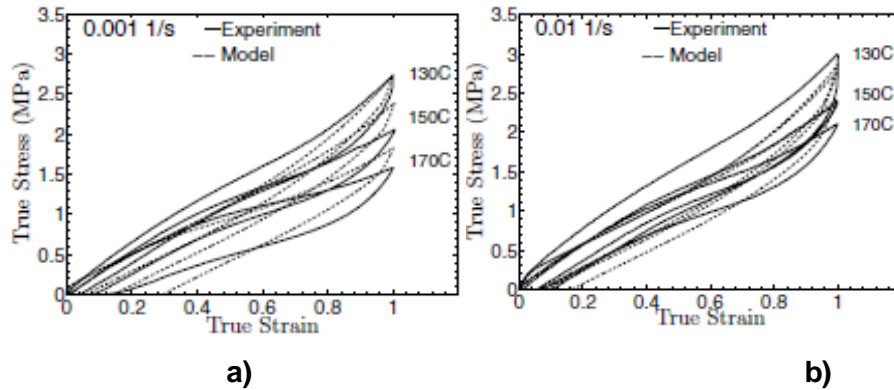


Figure 5.4: Comparison between the constitutive model and the experimental stress-strain curves for PMMA at various temperatures and strain rates of: a) 0.001 s^{-1} and b) 0.01 s^{-1} [150].

5.1.3.5 Ayoub et al. 2010 [152]

In this work, a physically-based inelastic model was developed for describing uploading-unloading large deformation tests on HDPE. The inelastic mechanisms were described using two parallel elements: a viscohyperelastic network resistance and a viscoelastic-viscoplastic intermolecular resistance. The network resistance was constituted by the eight-chain rubber model [129] and an inelastic shear strain rate given by Bergstrom and Boyce [153], [154]. The intermolecular resistance was composed by an initial elastic response followed by a non-linear transition to the inelastic flow (Colak [155]).

Figure 5.5 compares the simulated and experimental results of the stress-strain curves during load-unload tests at various strain levels. The nonlinear unloading behaviour was well described by this model, which is a remarkable achievement. However, the stress during the uploading stage was underestimated up to a strain of 90% and beyond this deformation stresses were highly overestimated.

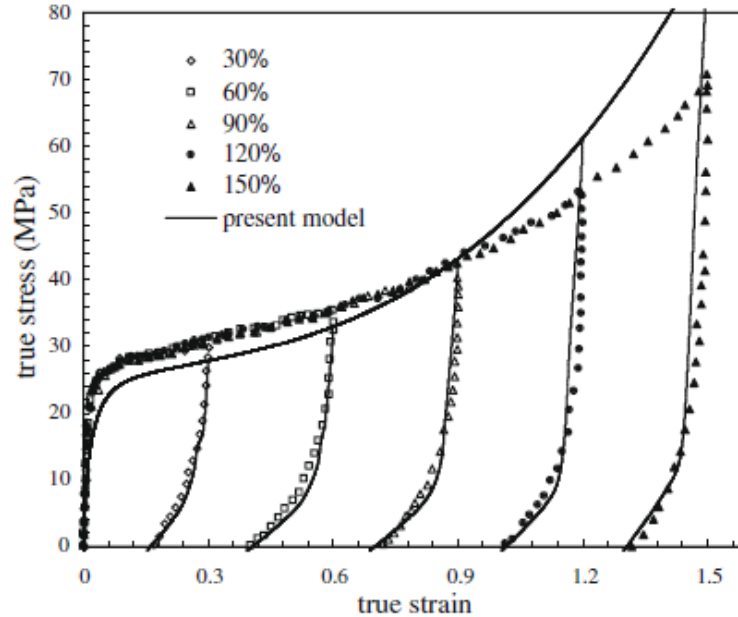


Figure 5.5: Result for load-unload tensile tests on HDPE at 10^{-3} s^{-1} . Experiment vs model [152].

5.1.4 Summary

Despite some promising results regarding the constitutive models available in the literature, we have noticed that these models still display some drawbacks. First, they do not fully capture the unloading part of the material response under cycling loading. Then, the models display some difficulties to capture the material response over a wide range of temperature and strain rates and when they do, the number of required parameters is quite large. This makes numerical modelling and parameters identification difficult. Additionally, there is not always a clear relationship between the state variables used in constitutive model and the main microstructural characteristics of amorphous polymers such as entanglements and crosslinks. Therefore, we will present next section an alternative in term of constitutive modelling to overcome these downsides.

5.2 Viscohyperelastic modelling

5.2.1 Model definition

The model used in this project was inspired by previous research performed at CEMEF on the viscohyperelastic nature of polymers [11], [20], [21], [25]. The first approach came from Billon [11] who proposed to consider polymers as a homogeneous equivalent statistical network that experiences some sources of inelasticity. So, mechanical behaviour will combine hyperelasticity due to the network and inelasticity which lead to viscohyperelasticity and viscoplasticity. Indeed, when the material undergoes deformation the arrangement of the polymer chains is altered, leading to some variation of the microstructure. Thermodynamically, these changes have to be compensated in order to obey thermodynamic principles. Basic assumption is that energy

changes, related to the microstructure evolution, are compensated by elastic energy stored in the polymer network. Therefore, the energy dissipation comes from the energy balance needed due to the changes in the microstructure and/or topology when the material is deformed.

Most recent works [25] suggested that amorphous polymers may present three main topological factors that will be affected when applying a certain deformation level: entanglements, crosslinks and weak bonds (van der Waals, hydrogen bonds). Permanent nodes (as crosslinks) will enable chain extensibility in a “constant” manner. This contribution will be of entropic and elastic nature. Entanglements have more conformational freedom than crosslinks. Ball [156] proposed to see the entanglements as slip links (see Figure 5.6) which allow the chains to slide among them before they are stopped by crosslink node. Thus, entanglements slippage will contribute to elastic mechanisms by adding a source of entropy. In Billon’s approach, their “mobility” (associated to length of slippage) can increase as the elastic energy increases. This will introduce some inelasticity in the material. Finally, inter-chain interactions as van der Waal interaction or hydrogen bonds will act as temporary nodes. Such interaction will be equivalent to crosslinks, as no slippage can be associated to them, but can disappear when stretching (elastic energy) is high enough on the branch of the associated network. This is a second source of inelasticity. Therefore, we will assume that the kinetics of these three variables when deformed will be the source of inelasticity of the polymer network.

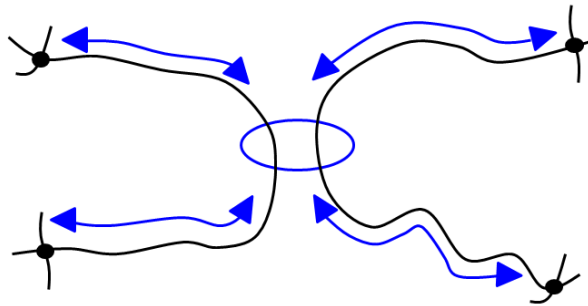


Figure 5.6: Slip-link model proposed by Ball [128].

For accounting all these factors, Billon [11] proposed to use the non-Gaussian hyperelastic model proposed by Edward and Vilgis (EV) [23] which considers that the storage energy contribution in the polymer network is associated to the entanglements and to the crosslinks. Other authors like Sweeney et al. [147], [157], Buckley et al. [143], [144], Adams et al. [146] Dooling et al. [142], Wu et al. [85], Lew et al. [158] and Gorlier et al. [159] have used the Edward and Vilgis strain energy to reproduce the mechanical response under tensile and compression loading for amorphous and semicrystalline polymers.

This potential is found in the literature in terms of the principal stretch ratios (see Appendix 8.6). In this work, we decided to use a modified version of this model which is written in function of the invariant of the stretch tensor:

$$\psi_v^k(I_1^k, I_2^k, I_3^k, \eta_k, \alpha_k^2) = (1/2)\kappa\theta \left[\begin{array}{l} N_c^k \left(\frac{(1 - \alpha_k^2)I_1^k}{(1 - \alpha_k^2 I_1^k)} + \ln(1 - \alpha_k^2 I_1^k) \right) + \\ N_s^k \left(\frac{(1 + \eta_k)(1 - \alpha_k^2)I_1^k}{(1 - \alpha_k^2 I_1^k)} \frac{(I_1^k + 2\eta_k I_2^k + 3\eta_k I_3^k)}{(1 + \eta_k I_1^k + \eta_k^2 I_2^k + \eta_k^3 I_3^k)} \right) \\ + \ln[(1 - \alpha_k^2 I_1^k)(1 + \eta_k I_1^k + \eta_k^2 I_2^k + \eta_k^3 I_3^k)] \end{array} \right] \quad 5.3$$

where I_1 , I_2 and I_3 are the invariant of the strain tensor, κ is the Boltzmann's constant, θ is the absolute temperature, N_c is the density of crosslinks per unit volume, N_s is the density of entanglements per unit volume, α is the chain extensibility (being 0 in the case of a Gaussian chain) and η is related to the degree of mobility of the slip links, i.e. the distance related to chain slippage. A zero value of η corresponds to a permanent node (crosslink). Previous works [11], [21], [25], [26] showed that disentanglement occurs when the polymer is deformed, which leads to an increase of η .

The three different contributions (entanglements, crosslinks and weak bonds) are set into two parallel networks for convenience, each one considering the stored energy based on Edward and Vilgis model. This is depicted in Figure 5.7 where red dots correspond to crosslinks and dotted blue lines represent the weak interactions. The "Branch 1" combines the effect of the entanglements, N_s^1 , and crosslinks, N_c^1 . Inelasticity comes from the release of stored energy in the branch to compensate the evolution of η , associated to disentanglement. The "Branch 2" accounts for the density of weak interactions, N_s^2 . Those interactions can disappear or be restored depending on the elastic energy in the branch, leading to inelasticity. Finally, chain extensibility is assigned to each branch. In Branch 1, the chain extensibility is assumed to be constant, while in Branch 2 the chain extensibility is linked to the level of connectivity in the network, which means that α_2^2 is proportional to N_s^2 .

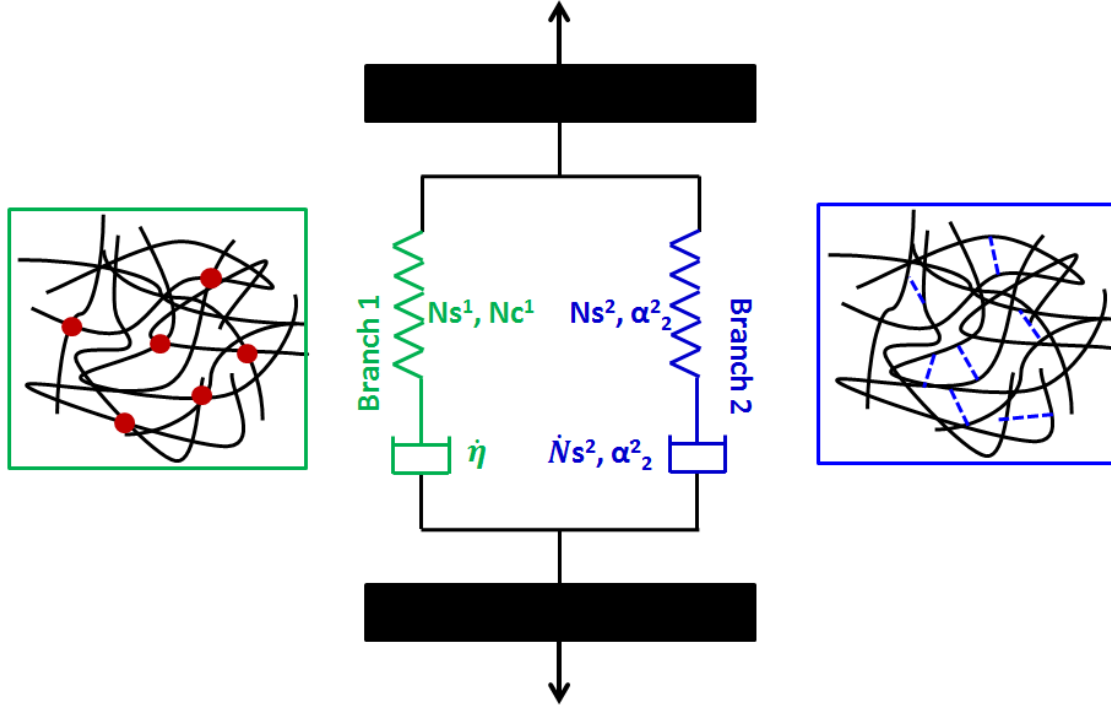


Figure 5.7: Schematic representation of topological interactions responsible of changes in the microstructure when the polymer is deformed.

To complete the constitutive material description, we need to define the material viscous flow and the Cauchy stress. The description of the 3D constitutive model [21], [25] is reminded in Appendix 8.7.

The material viscous flow describes the kinetic of the inelastic mechanisms which will allow addressing the kinematics (see Appendix 8.7) during the deformation of the polymer. The rate of inelastic deformation stand as follow [68]:

$$\bar{\mathbf{D}}_k^v = \frac{3}{2} \frac{1}{(1 - \beta_k)} \frac{1}{\|dev(\bar{\mathbf{M}}_k)\|} \left(\frac{\partial \psi_v^k}{\partial \bar{\eta}_k} \dot{\bar{\eta}}_k + \frac{\partial \psi_v^k}{\partial N_s^k} \dot{N}_s^k + \frac{\partial \psi_v^k}{\partial \alpha_k^2} \dot{\alpha}_k^2 \right) \left(\frac{dev(\bar{\mathbf{M}}_k)}{\|dev(\bar{\mathbf{M}}_k)\|} \right), k = [1,2] \quad 5.4$$

where β_k is associated to the coefficient of Taylor-Quinney and $\bar{\mathbf{M}}_k$ is the Mandel stress.

At this point, we need to define the kinetic laws for the evolution of internal state variables ($\dot{\bar{\eta}}_k$, \dot{N}_s^k and $\dot{\alpha}_k^2$) which will be dependent on stored elastic energy and will rule the inelasticity of the equivalent network.

5.2.2 Internal state variables evolution

As described by Billon [11], the evolution of the chain arrangements or microstructure with the deformation will depend on the elastic energy stored in the equivalent network. Physically, this means that having more elastic stored energy in the polymer network will promote chains arrangement and microstructural evolution. Therefore, we will use this stored energy as a driven force to describe the kinematic evolution of the internal state variables.

To quantify the elastic stored energy, we define $\Delta\psi$ as the difference between the energy of the deformed polymer and the no deformed:

$$\Delta\psi = \bar{\psi}_v^k(\bar{I}_1^k, \bar{I}_2^k, \bar{I}_3^k, \bar{\eta}_k, \bar{\alpha}_k) - \bar{\psi}_v^k(3, 3, 1, \bar{\eta}_k, \bar{\alpha}_k) \quad 5.5$$

All the kinetic laws for the internal state variables that will be presented next, are phenomenological formulations used to describe how the topology of the polymer evolves under deformation.

5.2.2.1 Chain slippage kinetics, $\bar{\eta}$

The evolution of the degree of mobility of the slip links, $\bar{\eta}$, is related to the chain slippage that occurs when the polymer is deformed. Indeed, an increase of this variable may be linked to the disentanglement of the polymer chains when an external load is applied. The evolution kinetics is assumed to follow the next forms:

For k=1,

$$\dot{\bar{\eta}} = Z \cdot \Delta\psi^{p_1} \quad \text{and} \quad \eta_0 = 0.2343 \quad 5.6$$

For k=2,

$$\dot{\bar{\eta}} = 0 \quad \text{and} \quad \eta_0 = 0, \quad 5.7$$

where Z and p_1 are material parameters. In Branch 1, the parameter $\bar{\eta}$ was chosen to evolve from the initial theoretical value $\eta_0 = 0.2343$ as proposed elsewhere [23], [156]. Additionally, since chain slippage are just accounted in the Branch 1, no kinetics will be used in the Branch 2 for this variable.

5.2.2.2 Weak bond density evolution, N_{s2}

The evolution equation of the state variable N_{s2} is associated to the variation of the weak bonds density when the polymer is deformed. Since this kinetic is just accounted for the Branch 2, we have:

For k=1,

$$\dot{N}_{s2} = 0 \quad 5.8$$

As proposed by Gehring et al. [25], we will state that an equilibrium value exists (N_s^{lim}) depending on the amount of available energy. Therefore, the rate of this kinetic will depend on the energy needed to reach this equilibrium:

For k=2,

$$N_s^{lim} = \frac{N_{s2}}{1 + (\tau_s \Delta \psi)^\xi} \quad 5.9$$

$$\begin{cases} N_s^{lim} - N_{s2} > 0 \text{ then } \dot{N}_{s2} = v |N_s^{lim} - N_{s2}|^p \\ N_s^{lim} - N_{s2} \leq 0 \text{ then } \dot{N}_{s2} = -v' |N_s^{lim} - N_{s2}|^p \end{cases}$$

where v , v' and p are material parameters.

5.2.2.3 Chain extensibility evolution, $\bar{\alpha}_k$

At certain level of deformation, polymer chains are fully stretched and cannot longer be extended. This is defined by the chain extensibility. This variable will depend on the number of chain interactions that will act as junction points. For convenience, we consider the topological constrain that will affect the extensibility as the number of weak bonds (Branch 2) [25]. Thus, we assume that the kinetics of evolution of $\bar{\alpha}_k$ is proportional to the kinetic of evolution of N_{s2}

$$\text{For k=1, } \dot{\bar{\alpha}}_k = 0 \quad 5.10$$

$$\text{For k=2, } \dot{\bar{\alpha}}_k = \frac{\bar{\alpha}_k^2}{N_{s2}} \dot{N}_{s2}$$

5.2.3 Model summary

Parameters of the model are summarized in Table 5.1

Table 5.1: Model parameters for each branch

| | | |
|---------------|-------------------|-------------------------|
| Branch k=1 | N_s^* (MPa) | To identify |
| | N_c^* (MPa) | To identify |
| | α^2 (-) | 1×10^{-6} [25] |
| | Z (-) | To identify |
| | p_1 (-) | To identify |
| Branch k=2 | N_s^* (MPa) | To identify |
| | N_c^* (MPa) | 0 [25] |
| | $\alpha^2(\cdot)$ | To identify |
| | $\tau_s(\cdot)$ | To identify |
| | $\xi(\cdot)$ | To identify |
| | $v(\cdot)$ | To identify |
| | $v'(\cdot)$ | To identify |
| | $p^*(\cdot)$ | 2 [25] |

(N_s^* and N_c^* for each branch correspond to N_{skT} and N_{ckt} respectively).

5.2.4 1D Case: Incompressible visco-hyperelastic model

To study the model capabilities, we will restrain for now our study to the description of the model in 1D assuming incompressibility. The Cauchy stress for uniaxial loading on incompressible material can be defined as:

$$\sigma = 2 \left(\lambda^2 - \frac{1}{\lambda} \right) \left(\frac{\partial \bar{\Psi}_v^k}{\partial \bar{I}_1^k} + \frac{1}{\lambda} \frac{\partial \bar{\Psi}_v^k}{\partial \bar{I}_2^k} \right)$$

The terms $\frac{\partial \bar{\Psi}_v^k}{\partial \bar{I}_1^k}$ and $\frac{\partial \bar{\Psi}_v^k}{\partial \bar{I}_2^k}$ are defined in Appendix 8.8 and the invariants are defined by:

$$I_1 = 2\lambda^{-1} + \lambda^2 \text{ and } I_2 = \lambda^{-2} + 2\lambda.$$

Inverse analysis for parameters identification

As explained in Chapter II, the inverse analysis for the parameters identification was carried out by minimizing a cost function (Equation 2.19) thanks to the simplex algorithm of the “fminsearch” MATLAB[®] function. The initial set of parameters were taken from previous works of Billon [11] on PMMA and Gehring et al. [25] on amorphous PET. In parallel, some parameters were initially chosen by either physical and/or mathematical reasons. For instance:

- Equation 5.3 demands that the extensibility limit goes in the range of $0 < \alpha^2 < 1/3$.
- Rubber elasticity theories stand that, at low strain, the storage modulus and the density of entanglements can be related as $E \approx 3kT(N_{s1} + N_{s2} + N_{c1})$. Thus, we can roughly approximate these values to the storage modulus determined from the DMTA tests.
- We assumed that mobility degree, η , should not be higher than 1 since higher values could be interpreted as entanglements no longer exist. Thus, we aimed to use values of Z and p_1 (see Equation 5.6) to keep the mobility degree, η , in the range of 0 and 1.

Figure 5.8 shows the evolution of the cost function with the number of iterations used for the simplex algorithm of the “fminsearch” function. Convergence to the minimum value of the cost function is reached after 170 iterations.

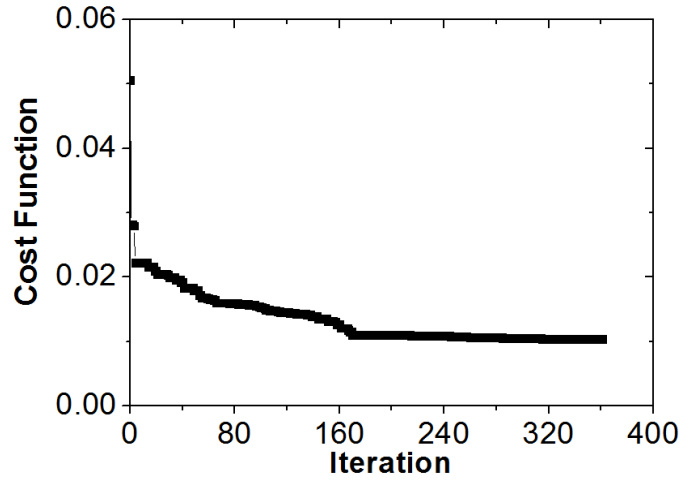


Figure 5.8: Cost function vs number of iterations from the Nelder-Mead simplex algorithm.

To quantify the accuracy of the model with the respect to the experimental results, we used the adjusted coefficient of determination, \bar{R}^2 , presented in Equation 5.12 [160]. An accurate result is obtained if the adjusted coefficient of determination is close or equal (ideally) to 1.

$$\bar{R}^2 = 1 - \frac{n-1}{n-p-1} \frac{\sum_{i=1}^n (Y_i - \hat{Y}_i)^2}{\sum_{i=1}^n (Y_i - \bar{Y}_i)^2} \quad 5.12$$

where n is the number of data, p is the number of parameters in the model, Y_i is the measured value, \hat{Y}_i is the model obtained from the model and \bar{Y}_i is the average of the measured values.

5.3 Results and Discussions

In this Section, the results obtained from the theoretical model presented in Chapter 5.2 will be compared to the uniaxial tensile tests displayed in Chapter IV. Experimental results were chosen for targeted equivalent strain rates to address the temperature/strain rate influence on the internal state variables.

5.3.1 Relevance of the model

5.3.1.1 Relevance at large deformation

Parameters were identified, as mentioned in Section 2.2.3, using the tensile tests at reference temperature 130°C one by one. The identified set of parameters for PMMA 80 is presented in Table 5.2. The calibrated set of parameters for the other PMMAs can be found in Appendix 8.9.

Table 5.2: Parameters for PMMA 80.

| | | | | | | |
|-----------------------------------------------|-----------------------------|-----------------------------|-----------------------|-----------------------|-----------------------|-----------------------|
| $\dot{\epsilon}_{eq} \text{ (s}^{-1}\text{)}$ | 1.87x10⁻² | 1.66x10⁻¹ | 1.61 | 18.1 | 169 | 1930 |
| Ns₁* (MPa) | 7.42x10 ⁻¹ | 1.02 | 2.92 | 21.55 | 105 | 120 |
| Nc₁* (MPa) | 2.83x10 ⁻⁴ | 1.69x10 ⁻³ | 9.53x10 ⁻³ | 2.51x10 ⁻² | 2.27x10 ⁻² | 2.27x10 ⁻² |
| Z (-) | 9.58x10 ⁻³ | 8.58x10 ⁻² | 1.10x10 ⁻¹ | 1.70x10 ⁻¹ | 9.13x10 ⁻¹ | 1.89 |
| p1 (-) | 7.45x10 ⁻¹ | 7.58x10 ⁻¹ | 7.29x10 ⁻¹ | 9.92x10 ⁻¹ | 9.18x10 ⁻¹ | 1.07 |
| Ns₂* (MPa) | 1.32x10 ⁻¹ | 2.98x10 ⁻¹ | 5.19x10 ⁻¹ | 4.78x10 ⁻¹ | 1.80 | 1.97 |
| α_2^2 (·) | 2.85x10 ⁻³ | 1.03x10 ⁻² | 4.28x10 ⁻² | 1.50x10 ⁻¹ | 4.81x10 ⁻² | 7.08x10 ⁻² |
| τ_s (·) | 3.32x10 ⁻¹ | 7.75x10 ⁻² | 9.17x10 ⁻² | 2.12x10 ⁻¹ | 1.77x10 ⁻² | 5.12x10 ⁻⁵ |
| ξ (·) | 6.39x10 ⁻¹ | 4.59x10 ⁻¹ | 4.28x10 ⁻¹ | 7.17x10 ⁻¹ | 3.88x10 ⁻⁵ | 1.99x10 ⁻⁵ |
| ν (·) | 1.67 | 2.33 | 6.86 | 1.41x10 ⁻¹ | 8.55x10 ⁻² | 1.80x10 ⁻¹ |
| ν' (·) | 2.47x10 ⁻¹ | 1.63x10 ⁻² | 7.27x10 ⁻⁴ | 7.69x10 ⁻⁵ | 9.08x10 ⁻⁶ | 2.21x10 ⁻⁵ |

Figure 5.9 and Figure 5.10 show the comparison between the experimental (dots) and theoretical results from the model (lines) for PMMA 80 and PMMA 120, respectively. The accuracy of the results is quantified with the adjusted coefficient of determination, \bar{R}^2 , which can be found in the figures legend. Results suggest that the model proposed in this work has enough degree of freedom to reproduce the experimental curve with a good agreement using ten parameters per condition. Indeed, the model is able to capture the different features of the mechanical curves during uploading to large strain levels (between 80% and 100%) and also during the unloading. Additionally, mechanical response of the PMMAs is highly different in the experimental range investigated in this study, with material behaviours close to viscous fluids to a glassy solids. Regardless such strong difference, the model was able to well reproduce all these changes, proving its adaptability and efficiency.

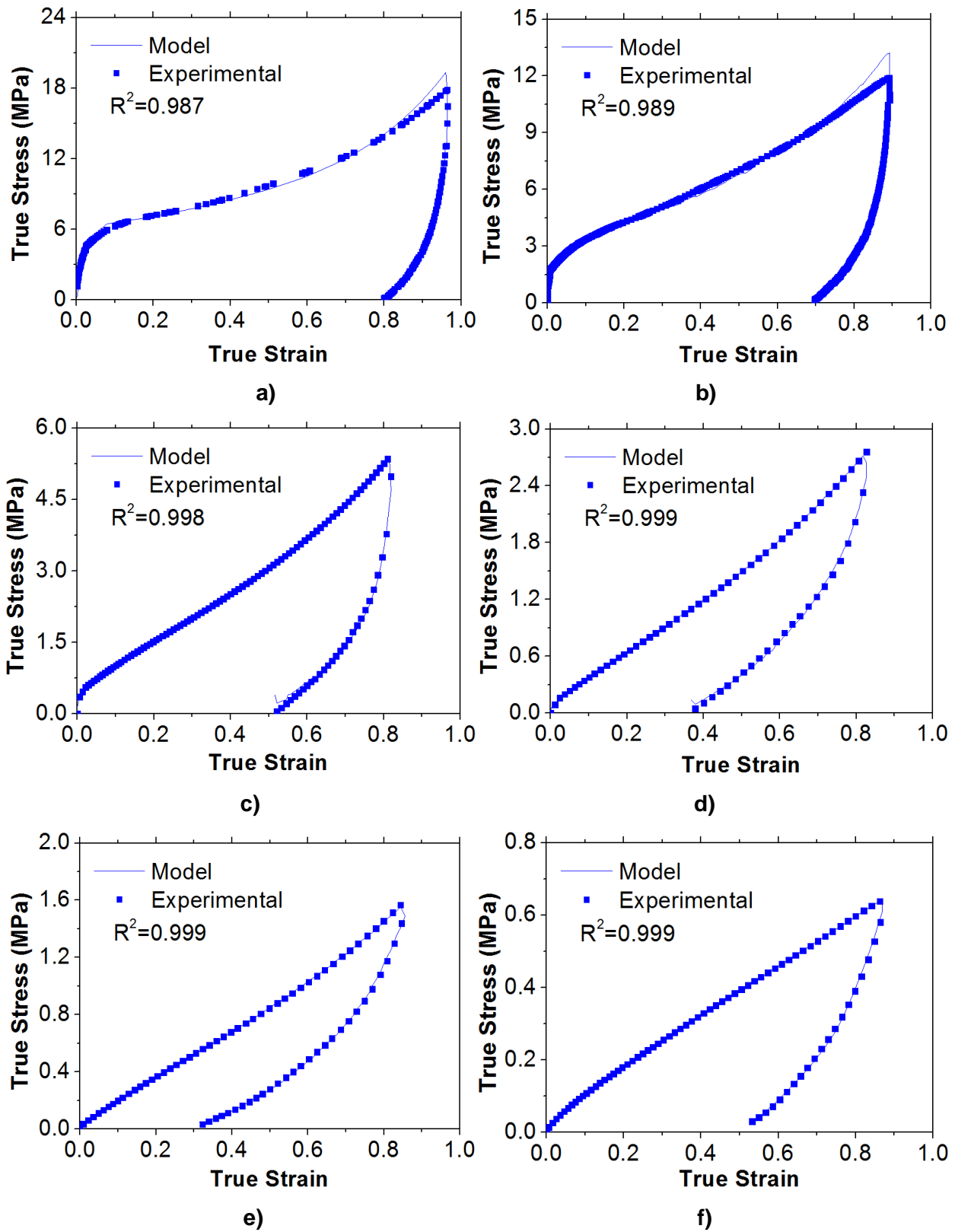


Figure 5.9: Comparison between experiments (dots) and model (lines) on load-unload tensile tests on PMMA 80 at $\dot{\epsilon}_{eq}$: a) 10^3 s^{-1} b) 10^2 s^{-1} c) 10^1 s^{-1} d) 10^0 s^{-1} , e) 10^{-1} s^{-1} , f) 10^{-2} s^{-1} .

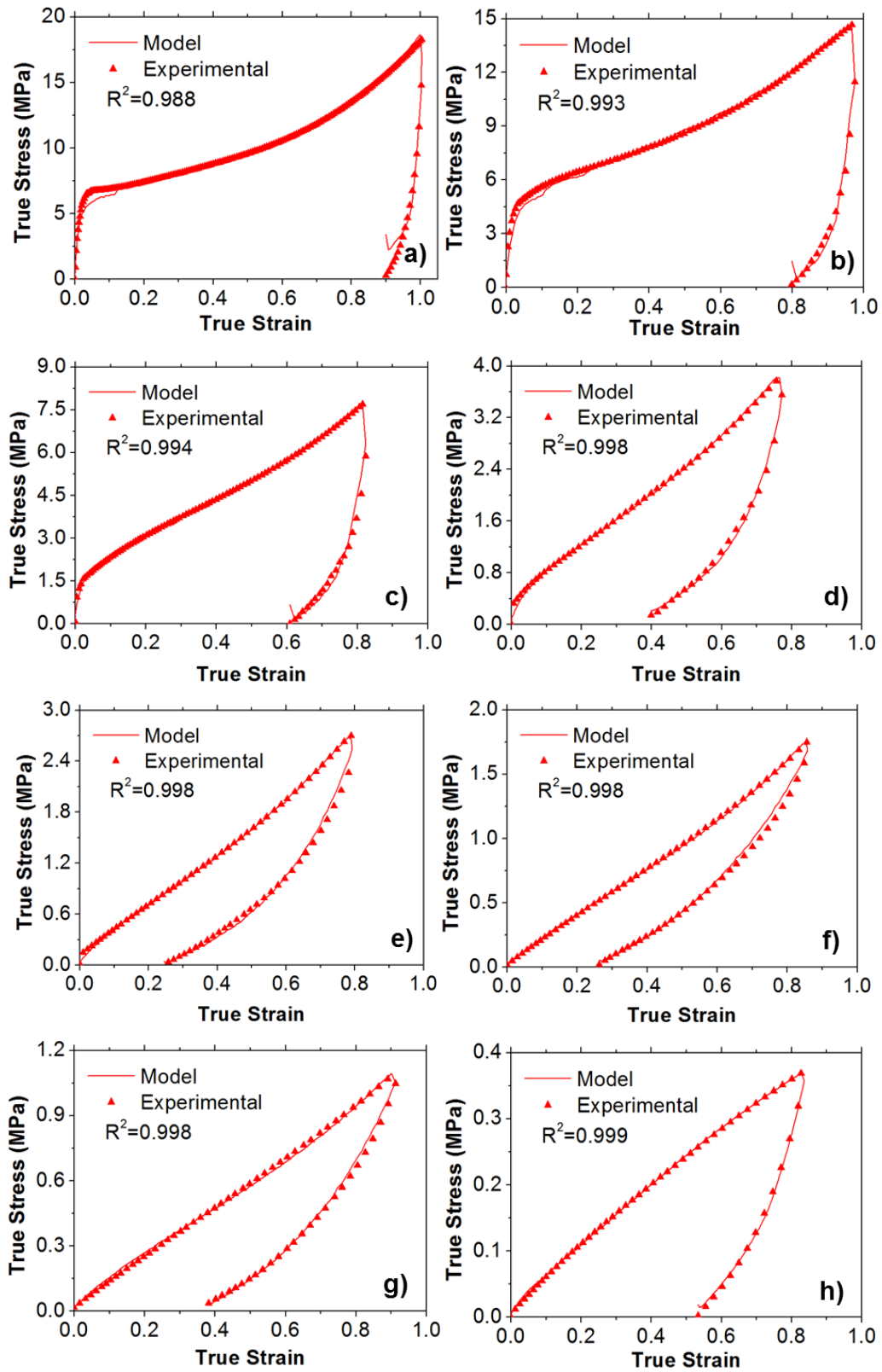


Figure 5.10: Comparison between experiments (dots) and model (lines) on load-unload tensile tests on PMMA 120 at $\dot{\epsilon}_{eq}$: a) 10^3 s^{-1} a) 10^2 s^{-1} a) 10^1 s^{-1} b) 10^0 s^{-1} c) 10^{-1} s^{-1} d) 10^{-2} s^{-1} , e) 10^{-3} s^{-1} , f) 10^{-4} s^{-1} .

Figure 5.11 and Figure 5.12 shows the comparison between the experimental (dots) and theoretical results from the model (lines) for PMMA 3500 and PMMA CL, respectively.

Results reveal that the constitutive model was in good agreement with the experimental data from both PMMAs, even when behaviours exhibit drastic changes since they passed from a hyperelastic state (10^{-6} s^{-1}) to a more viscoelastic/viscoplastic (10^0 s^{-1}). However near the glassy region (10^2 s^{-1}), the model showed to be less efficient, especially for PMMA 3500. For this condition the apparent elastic regime was slightly underestimated and the apparent yield and softening were not described for the model. Nevertheless, at higher strains (above 20%) the behaviour in the plastic region/strain hardening was well reproduced, as well as the unloading. As softening is often related to physical aging during which polymer densified, we suggest modifying the kinetic form of the variable of Branch 2 for including the softening in a further step.

In parallel, the model accuracy was quantified using the adjusted coefficient of determination. Rigorously speaking, if the adjusted coefficient of determination is in the range of $0.990 < \bar{R}^2 < 1$, the accuracy of the constitutive model can be considered as really good.

Figure 5.13 shows the values of these coefficients for different equivalent strain rates. Results reveal that \bar{R}^2 remained above 0.99 for most of the tested equivalent strain rates, more especially up to values of 10^1 s^{-1} . At higher equivalent strain rates, \bar{R}^2 is below the minimum imposed value. Recalling the master curves presented in Section 3.2.4, we can see that equivalent strain rates above 10^1 s^{-1} correspond to material near the glassy region. Therefore, we can conclude that the constitutive model used in this work present a good accuracy when the material is near the flowing region, in the rubbery state and in its viscoelastic region, but may lead to more discrepancies when the material is near the glassy region.

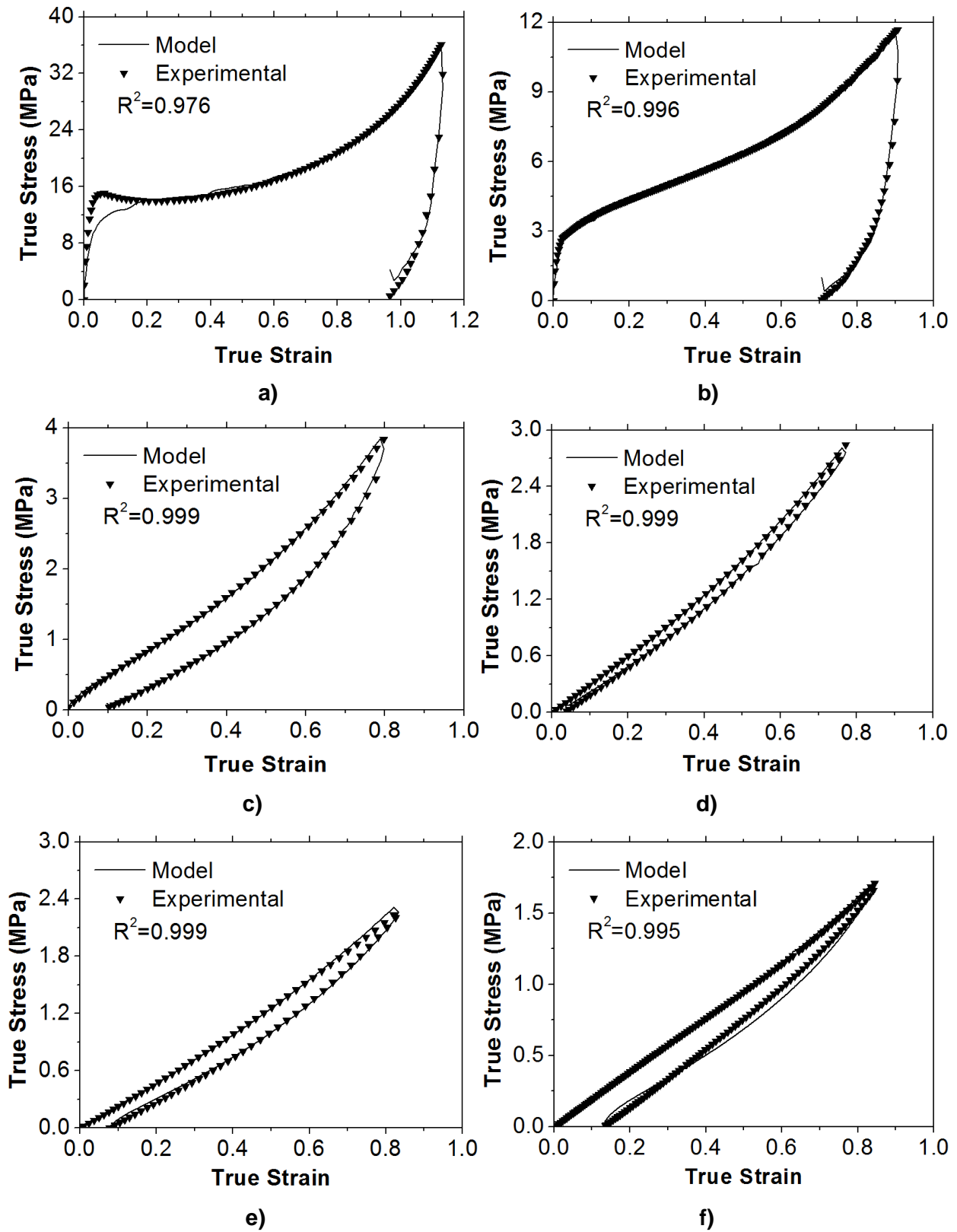


Figure 5.11: Comparison between experiments (squares) and model (lines) on load-unload tensile tests on PMMA 3500 at $\dot{\epsilon}_{eq}$: a) 10^2 s^{-1} b) 10^0 s^{-1} c) 10^{-2} s^{-1} d) 10^{-4} s^{-1} , e) 10^{-6} s^{-1} , f) 10^{-8} s^{-1} .

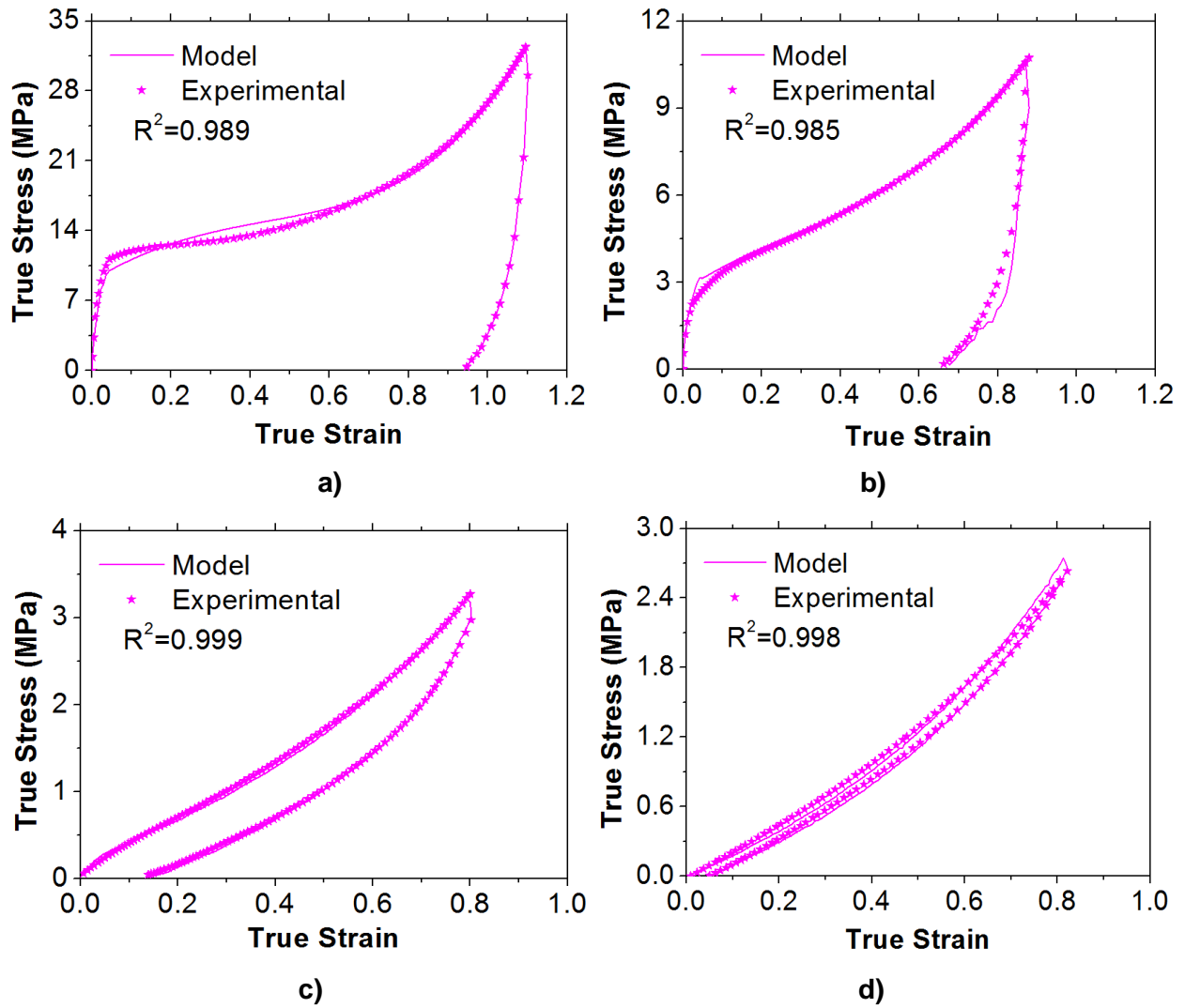


Figure 5.12: Comparison between experiments (squares) and model (lines) on load-unload tensile tests on PMMA CL at $\dot{\epsilon}_{eq}$: a) 10^2 s^{-1} b) 10^0 s^{-1} d) 10^{-2} s^{-1} , e) 10^{-4} s^{-1} .

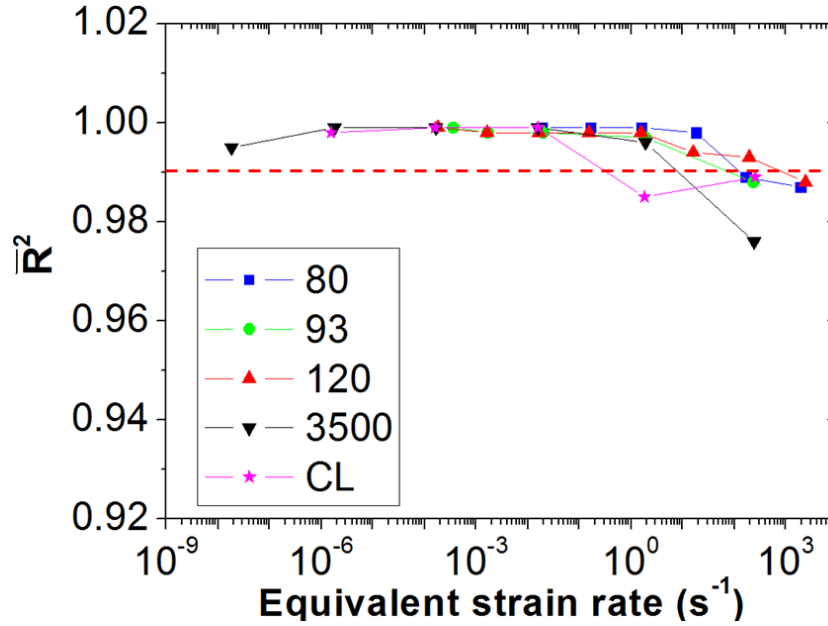


Figure 5.13: Adjusted coefficient of determination vs equivalent strain rate for all the PMMAs.

5.3.1.2 Relevance in the linear domain

Parameters identified for each PMMA can be used to compute the apparent Young's modulus, E , by using the EV's energy as:

$$E = 3kT \left[\frac{N_s^k \left\{ (1 - \alpha_k^2 - 2\eta\alpha_k^2)(1 - 3\alpha_k^2) + 2\alpha_k^2(1 + \eta)^2 \right\}}{(1 + \eta)^2(1 - 3\alpha_k^2)^2} + \frac{N_c^k \left\{ (1 - \alpha_k^2)(1 - 3\alpha_k^2) + 2\alpha_k^2 \right\}}{(1 - 3\alpha_k^2)^2} \right], \quad k = 1, 2 \quad 5.13$$

Then, we can compare this modulus with the master curves of the storage modulus presented in Chapter III. This is depicted in Figure 5.14 for PMMA 120 and PMMA CL. Results are in good agreement between the values calculated through Equation 5.13 and those determined experimentally through DMTA. The discrepancies are expected since we are comparing two different properties: E and E' . Moreover, we can notice that Young's modulus determined from Branch 1, E_1 , exhibits a bigger contribution to the total stiffness than the one of Branch 2.

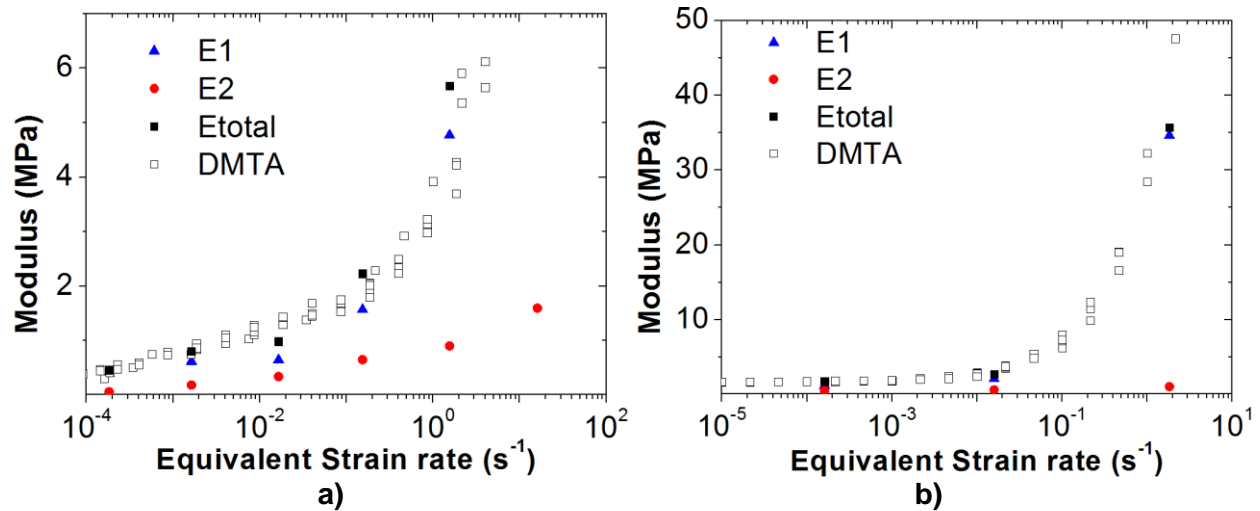


Figure 5.14: Comparison between elastic modulus determined from DMTA tests and those identified through EV's strain energy function: a) PMMA 120, b) PMMA CL.

Next, we will focus on presenting which topological constrain (physical entanglements, crosslinks and weak bonds) is more important for the model. Figure 5.15 shows evolution of Ns_1^* , Nc_1^* and Ns_2^* with the equivalent strain rate for a) PMMA 120 and b) PMMA CL. We can see that the contribution of Nc_1^* is quite low. Indeed, $Ns_1^* > 100.Nc_1^*$ and $Ns_2^* > 10.Nc_1^*$. Therefore, we will consider that crosslinks are negligible. Moreover, at high equivalent strain rates, the parameter Ns_1^* is the main topological factor accounted for the model. However, when decreasing the equivalent strain rate, the gap between Ns_1^* and Ns_2^* reduces, suggesting that the model considers Ns_1^* more sensitive to the equivalent strain rate than Ns_2^* . Thanks to the model used in this work, we are able to identify the real nature and contribution of the topological constrains.

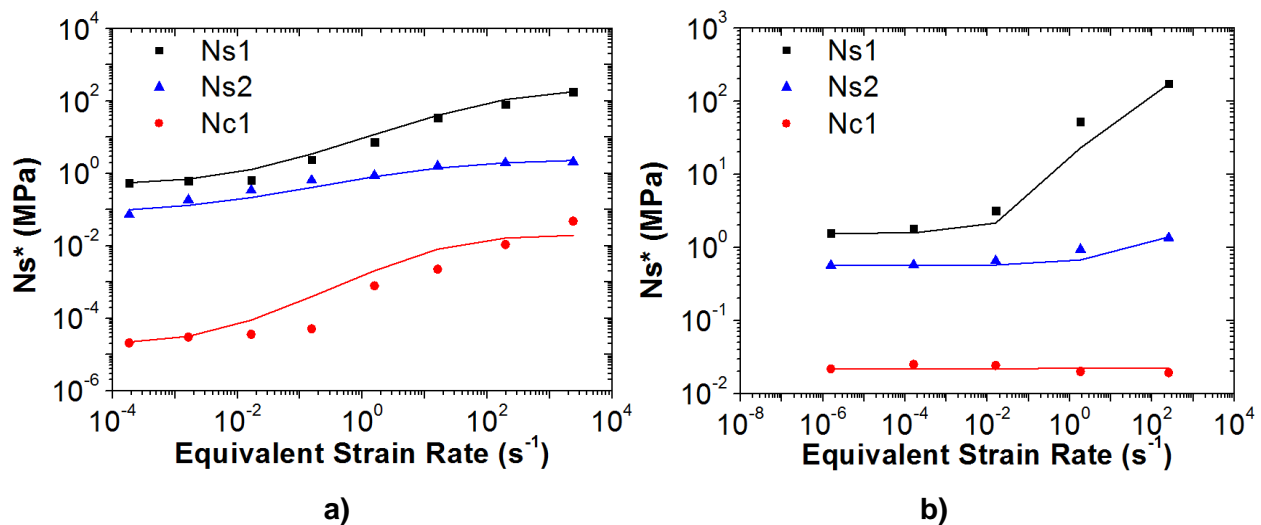


Figure 5.15: Evolution of Ns_1^* , Nc_1^* and Ns_2^* with the equivalent strain rate for a) PMMA 120 and b) PMMA CL.

5.3.2 Physical contribution of each branch on the overall mechanical response

The model is decomposed in two branches: one branch accounts for the entanglements, crosslinking and disentanglements, while the second one considers the weak bonds density contribution to elasticity and inelasticity. In this section, we aim to illustrate the contribution of each branch to the global mechanical response, as the evolution of the internal state variables with time.

Figure 5.16 displays the contribution of the different branches to the total stress. This figure suggests that the Branch 1 has a mechanical behaviour similar to a viscoplastic material while the Branch 2 displays viscoelastic behaviour. Thus, the disentanglement process accounted for the Branch 1, considered here as an irreversible process, is the main source of plasticity. The amount of plasticity will be related to the evolution of η . In Branch 2, weak bonds act as crosslinks at small energy and tend to disappear as the energy increases, which is the source of energy dissipation in this branch.

Additionally, we can see that the Branch 1 pass to a compressive state around 75% of true strain during unloading while the Branch 2 does not reach zero stress after unloading. Indeed, stress represents the increment of energy related to an increment of strain. In this model, each branch represents a decomposition of energy of the polymer network depending on internal processes. Some of these processes may evolve such that energy increases when increasing the strain and some others may behave such that energy decreases, leading to “compressive” or “tensile” states as showed in Figure 5.16.

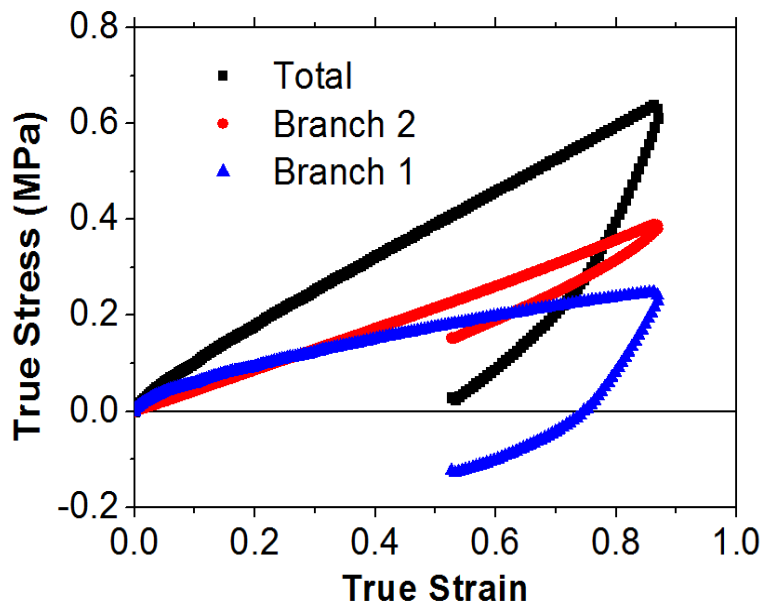


Figure 5.16: Contribution of each branch to the total stress-strain curves for PMMA 80 at equivalent strain rate of 10^{-2} s^{-1} .

It has been said that the evolution of the internal state variables will rule the inelastic behaviour of the material. Therefore, it is important to address how they do evolve with time. The first variable that will be studied is the degree of mobility of entanglements, η . The evolution of this parameter with time is depicted in Figure 5.17 for PMMA 80 at equivalent strain rate of $1.87 \times 10^{-2} \text{ s}^{-1}$. At the beginning of the loading, this variable seems to remain approximately constant at 0.2343 (which is the imposed theoretical value) up to 50 seconds (strain level of 2%). Then, η increases up to (around) 0.36 during the loading stage. When the unloading starts, one can observe, once again, that η is first nearly constant. This may correspond to the apparent elastic regime during unloading. Later, η increases again when the unloading continues.

These observations show that the model is able to describe the increase of η when the polymer is deformed. This increase is related to an increase of the distance between molecular nodes. Indeed, during uploading, elastic energy in the statistical branch is high enough for promoting a change in the internal arrangement, corresponding to chain slippage. During the unloading, the increase of η matches with the onset of the compressive regime showed in Figure 5.16. Thus, this means that the chain slippage during the unloading balances the internal energy of the polymer network.

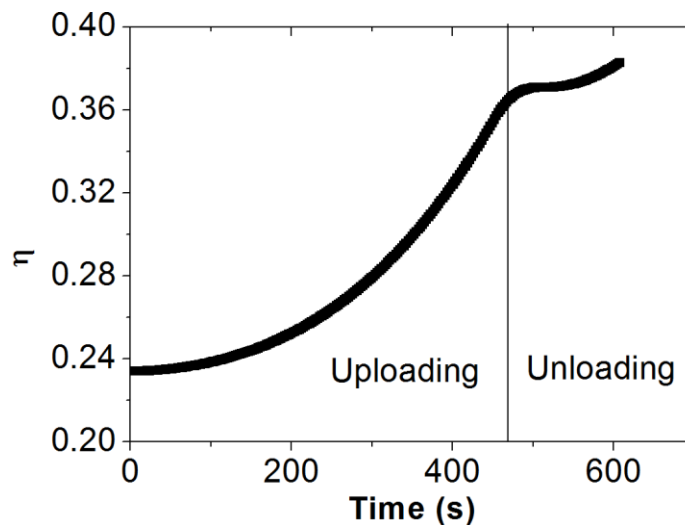


Figure 5.17: Evolution of the state variable η with time during the load-unload tensile test on PMMA 80 at $1.87 \times 10^{-2} \text{ s}^{-1}$.

Regarding Branch 2, Figure 5.18 a) and b) show the kinetic of the variables Ns_2^* and α_2^2 with time. Figure 5.18 a) exhibits that Ns_2^* initially remains constant. As the load increases, the density of active weak bond decreases. This means that during the stretching process, not just disentanglement may occur but also van der Waals interactions may disappear. During the unloading, Ns_2^* initially remains constant and then slightly increases. This increase in the van der Waals bonds density may be attributed to the fact that polymer chains are getting more mobile as unstretched during the unloading, promoting the reappearance of inter-chain

interactions. Moreover, the evolution of α^2_2 is directly linked to the density of weak bonds (see Equation 5.10). Thus, as shown in Figure 5.18 b), the trend of its kinetic is the same as the one for Ns_2^* .

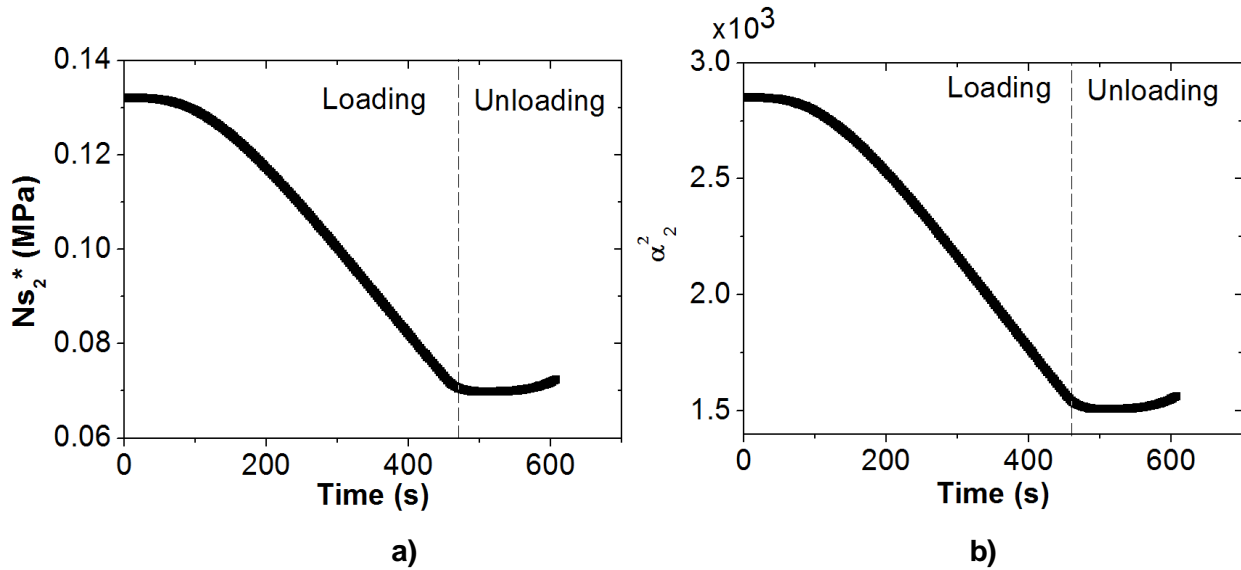


Figure 5.18: Evolution of the state variable Ns_2^* , a), and α^2_2 , b), with time during the load-unload tensile test on PMMA 80 at $1.87 \times 10^{-2} \text{ s}^{-1}$.

5.3.3 Role of the branches when varying the equivalent strain rate

In this section, we aim to address the mechanical response of each branch when varying the equivalent strain rate. To do this, we present the contribution of the different branches to the total stress at equivalent strain rates below the α -transition, viscoelastic region and rubbery plateau.

5.3.3.1 Below α -transition

Figure 5.19 shows the contribution of each branch to the total stress for PMMA 120 at equivalent strain rate of 10^3 s^{-1} . This condition corresponds to the glassy region of this PMMA.

Branch 1 describes the initial elastic regime and contributes to most of the mechanical stiffness up to strain of 80%. Additionally, this branch also accounts for most of the energy dissipation. This branch describes the material viscoelastoplasticity. Branch 2 contributes to the nonlinear mechanical stiffness, which becomes more relevant above 80% of deformation, adding strain hardening at large strain. Moreover, Branch 2 displays almost no hysteresis. This branch accounts for the hyperelasticity of the material. These trends were also observed for all PMMAs.

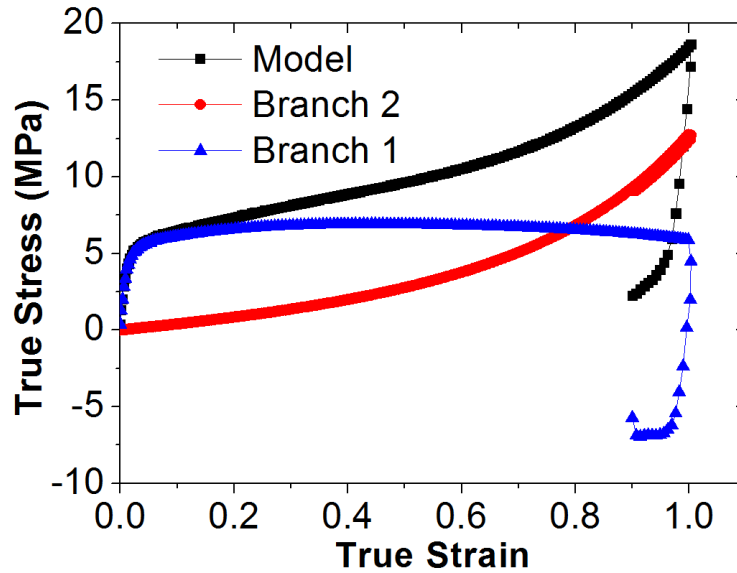


Figure 5.19: Contribution of each branch to the total stress-strain curves for PMMA 120 at equivalent strain rate of 10^3 s^{-1} .

5.3.3.2 Viscoelastic region

Figure 5.20 displays the contribution of each branch to the total stress for PMMA 120 at equivalent strain rate of 10^0 s^{-1} . This condition corresponds to the viscoelastic region of this PMMA.

Branch 1 still captures most of the initial elasticity but its contribution to the mechanical stiffness is more significant up to 20% of deformation. Additionally, energy dissipation is lower than in the glassy region. Thus, this branch acts as a viscoelastic network. Branch 2 represents the main source of strain hardening large deformation (above 20%). Regarding its contribution to inelasticity, we can see that energy dissipation is slightly higher than in the glassy region. Therefore, this branch acts now as visochyperelastic network. These conclusions were also drawn for all PMMAs.

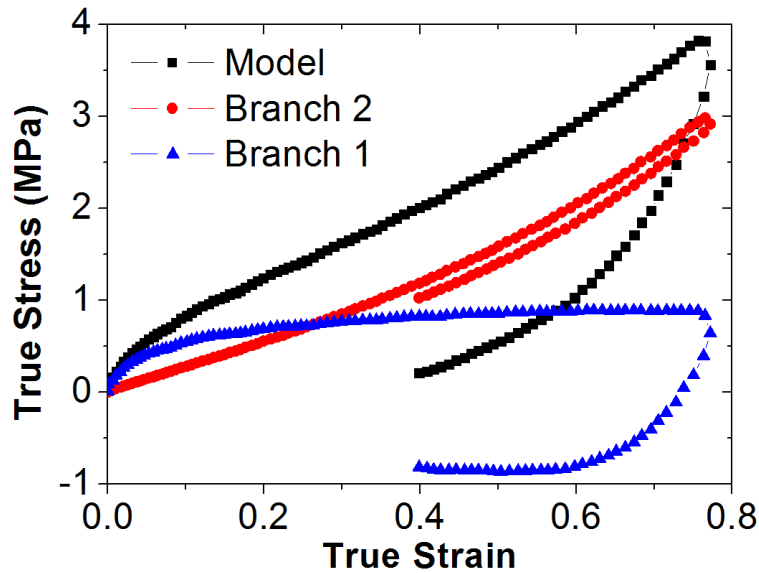


Figure 5.20: Contribution of each branch to the total stress-strain curves for PMMA 120 at equivalent strain rate of 10^0 s^{-1} .

5.3.3.3 Rubbery plateau

In Chapter IV, we observed that the mechanical behaviour in the rubbery plateau varied with the PMMAs. For accounting these differences, we present three PMMAs:

PMMA 120

Figure 5.21 shows the contribution of each branch to the total stress for PMMA 120 at equivalent strain rate of a) 10^{-2} s^{-1} (rubbery plateau) and b) 10^{-4} s^{-1} (near the flow region) of this PMMA.

For both equivalent strain rates, Branch 1 describes the initial elastic regime and contributes to a relevant fraction of energy dissipation. This branch behaves as a viscoelastic material. Moreover at 10^{-2} s^{-1} Branch 2 adds viscohyperelasticity and then turns into a viscoelastic network when reaching the flowing at 10^{-4} s^{-1} .

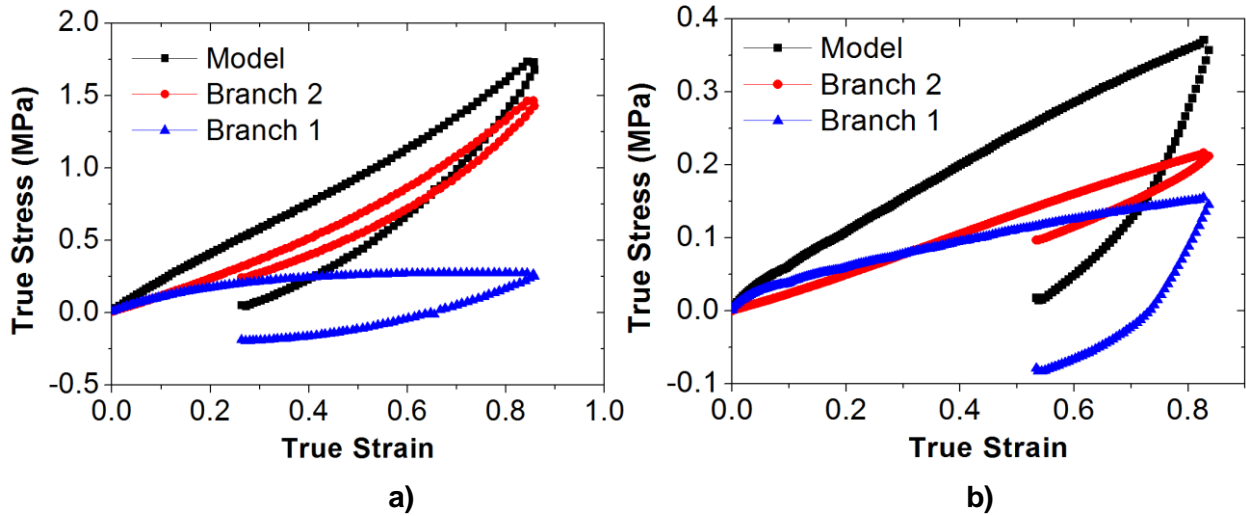


Figure 5.21: Contribution of each branch to the total stress-strain curves for PMMA 120 at equivalent strain rate of a) 10^{-2} s^{-1} and b) 10^{-4} s^{-1} .

PMMA 3500

Figure 5.22 displays the contribution of each branch to the total stress for PMMA 3500 at equivalent strain rate of a) 10^{-2} s^{-1} and b) 10^{-8} s^{-1} . This condition corresponds to the rubbery plateau of this PMMA. At 10^{-2} s^{-1} , Branch 1 contributes to viscoelasticity by describing the initial elasticity and exhibiting energy dissipation. At 10^{-8} s^{-1} , the contribution of this branch becomes almost negligible. Additionally, Branch 2 exhibits a viscohyperelastic (with no much hysteresis) behaviour at 10^{-2} s^{-1} . Then, at 10^{-8} s^{-1} , the elastic and inelastic components of the mechanical response are described by Branch 2 which displays viscohyperelastic behaviour with more hysteresis than at 10^{-2} s^{-1} . At this point, the mechanical behaviour could be just described with this branch.

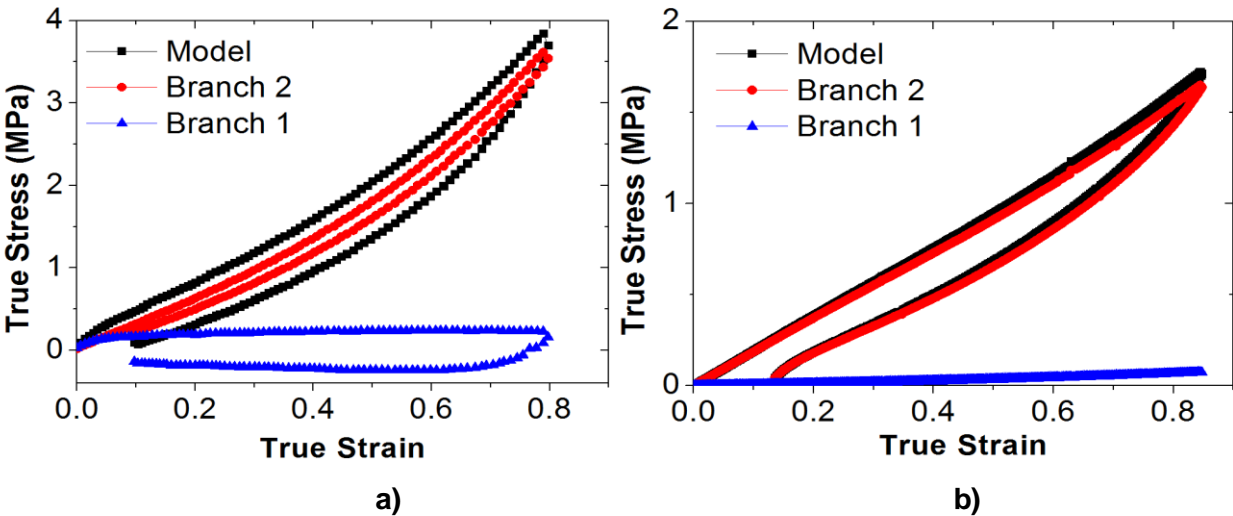


Figure 5.22: Contribution of each branch to the total stress-strain curves for PMMA 3500 at equivalent strain rate of a) 10^{-2} s^{-1} and b) 10^{-8} s^{-1} .

PMMA CL

Figure 5.23 displays the contribution of each branch to the total stress for PMMA CL at equivalent strain rate of a) 10^{-2} s^{-1} and b) 10^{-6} s^{-1} . At 10^{-2} s^{-1} , Branch 1 contributes to viscoelasticity in the network, accounting for the initial elasticity and the overall hysteresis while at 10^{-6} s^{-1} , its contribution becomes negligible. Branch 2 behaves as a hyperelastic network for both equivalent strain rate and its contribution is high enough for describing the total mechanical response at 10^{-6} s^{-1} .

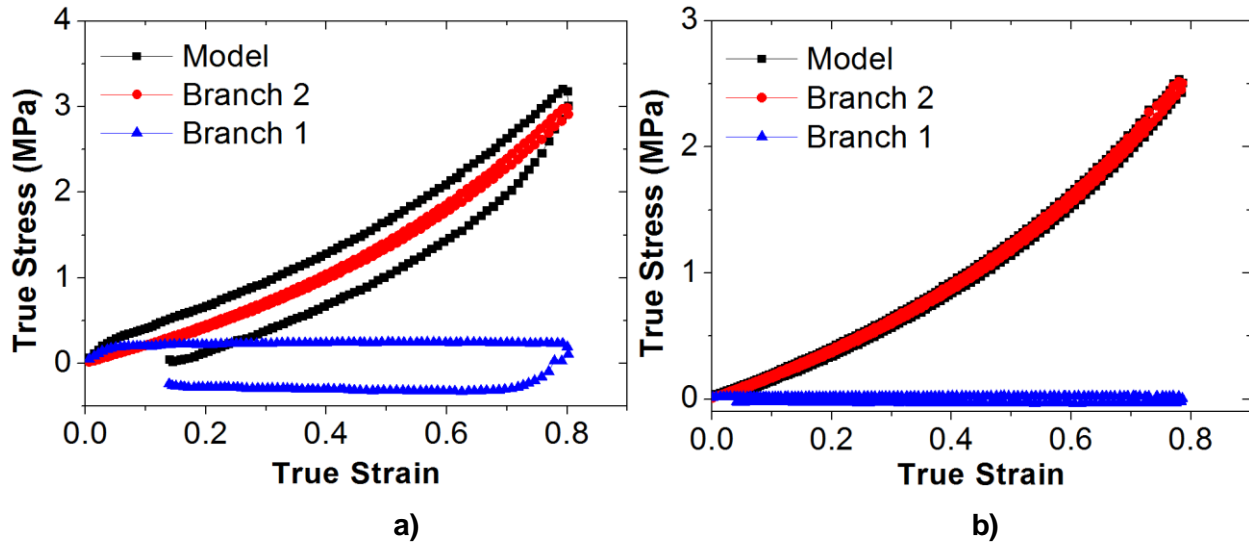


Figure 5.23: Contribution of each branch to the total stress-strain curves for PMMA CL at equivalent strain rate of a) 10^{-2} s^{-1} and b) 10^{-6} s^{-1} .

5.3.3.4 Summary

Branch 1 plays a significant role in describing the initial elasticity regardless the equivalent strain rate. Below the α -transition, this branch contributes greatly to the mechanical stiffness and energy dissipation. When moving through the viscoelastic region, these contributions decrease, passing from viscoelastoplastic behaviour to viscoelastic behaviour. In the rubbery plateau, the contribution of this branch becomes less relevant when moving to lower equivalent strain rates.

Branch 2 describes the strain hardening of the polymer network for all the equivalent strain rates. Below the α -transition, this branch has no hysteresis, acting as a hyperelastic network. In the viscoelastic region, the energy dissipation increases, turning into viscohyperelastic. In the rubbery plateau, the features of this branch will depend on the polymer architecture. For PMMAs of low molar mass, the branch behaved as a viscohyperelastic network and then turned into a viscoelastic network when reaching the flowing state. For PMMA 3500 and PMMA CL the elasticity and inelasticity was fully accounted by this branch. Therefore, its behaviour was hyperelastic and viscohyperelastic depending on the tested conditions.

Therefore, using two parallel branches that account for viscoelastoplastic/viscoelastic and hyperelastic/viscohyperelastic behaviours results into a versatile approach that allows capturing the mechanical response of amorphous PMMAs when near and above the α -transition. Also, this approach requires few parameters which may enrich the modelling for predicting the material behaviour when studied in the viscoelastic and rubbery state.

5.3.4 Dependence of the EV's parameters with the equivalent strain rate

So far, we addressed that the physical entanglements contribute to viscoelastoplastic behaviour and van der Waals interaction adds viscoelastic or hyperelastic behaviour. However, entanglements and van der Waals interactions are likely dependent on the strain rate, temperature, molecular weight and crosslink.

Indeed in Table 5.2 we can see an important variation of the model parameters, increasing with the equivalent strain rate at reference temperature. Other authors have also found effect of the strain rate and temperature on the parameters of the EVs' strain energy function. For instance, Brereton and Klein [161] studied a crosslinked polyethylene observing that the entanglement density was decreasing with a reduction of the strain rate. Then, Sweeney et al. [162], [163] worked on PVC and PP proposing that Ns^* varied with the strain rate through an Eyring equation as follows:

$$Ns^* = A + B \ln \left(\frac{\dot{\gamma}}{\dot{\gamma}_0} \right) \quad 5.14$$

where A and B are material parameters, $\dot{\gamma}$ is the shear strain rate, $\dot{\gamma}_0$ is a reference shear strain rate, with $\dot{\gamma} \geq \dot{\gamma}_0$. This relationship was then verified with good agreement on PET by Matthews et al. [164], Gorlier [24] and Yann Marco [165]. Additionally, Gorlier [24] also showed that the entanglement density was decreasing with the increase of temperature

In other works, Billon [11] and Baquet et al. [20], [21] observed a similar dependence of the EVs parameters with the equivalent strain rate as showed in Table 5.2 and Appendix 8.10. Indeed they found that these parameters had a similar trend to those exhibited by the storage modulus (Chapter III). Therefore, they proposed to relate these parameters to the equivalent strain rate at reference temperature by using a phenomenological sigmoid formulation:

$$P = P_0 + P_1 \left(\frac{2}{1 + (\tau_r \dot{\epsilon}_{eq})^{-2m}} \right) \quad 5.15$$

where, P is the desired parameter, P_0 , P_1 , τ_r and m are material parameters.

Therefore, a second step will be to verify such dependence on our current material database. A first comparison was done between the phenomenological function proposed by Sweeney et al. [162], [163] (Equation 5.14) and Billon [11], Baquet et al. [20], [21] (Equation 5.15) to describe the evolution of Ns_1^* . This is depicted in Figure 5.24 for PMMA 120.

Results reveal that Ns_1^* remains approximately constant at low equivalent strain rates (up to 10^0 s^{-1}), which correspond to the rubbery plateau of the material. Then a sharp increase of Ns_1^* is observed in the viscoelastic region. Thus, the entanglement density seems to follow the same evolution than the storage modulus. Regarding to phenomenological models, the equation proposed by Sweeney describes properly the behaviour in the rubbery plateau. However, it cannot capture the behaviour in the viscoelastic region. On the other hand, the model of Billon describes properly the values of Ns_1^* in the rubbery plateau as well as their evolution in the viscoelastic region, making it more suitable for a wide range of equivalent strain rates.

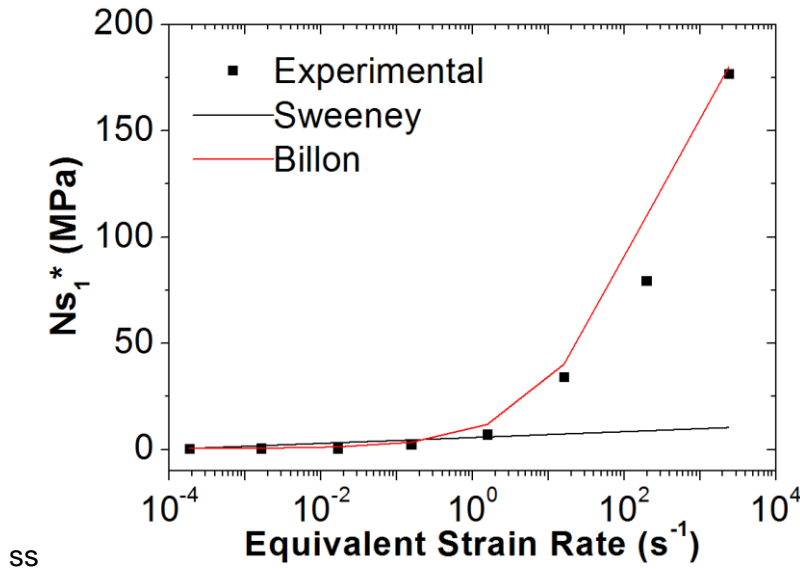


Figure 5.24: Entanglement density evolution with the equivalent strain rate for PMMA 120.

After verifying that the approach proposed by Billon [11] and Baquet et al. [20], [21] is able to capture the evolution of the parameters with the equivalent strain rate, we use such function to describe the evolution of Ns_1^* , Nc_1^* , z , $p1$, Ns_2^* and α_2^2 with the equivalent strain rate as follows:

$$\begin{pmatrix} N_s^{1*} \\ N_c^{1*} \\ z \\ p_1 \\ N_s^{2*} \\ \alpha_2^2 \end{pmatrix} = \begin{pmatrix} N_{s0}^{1*} \\ N_{c0}^{1*} \\ z_0 \\ p_{10} \\ N_{s0}^{2*} \\ \alpha_{20}^2 \end{pmatrix} + \begin{pmatrix} N_{s1}^{1*} \\ N_{c1}^{1*} \\ z_1 \\ p_{11} \\ N_{s1}^{2*} \\ \alpha_{21}^2 \end{pmatrix} \left(\frac{2}{1 + (\tau_r \dot{\epsilon}_{eq})^{-2m}} \right) \quad 5.16$$

Thus, we will present next the evolution of the different parameters with the equivalent strain rate for PMMA 120. This is depicted in Figure 5.25. Results for the other PMMAs can be found in Appendix 8.10. All the parameters were well described for all the different PMMAs by using $\tau_r = 0.037s^{-1}$ and $m=0.375$. The other values, for fulfilling Equation 5.16, are shown in Table 5.3. A good agreement between the experimental and theoretical values is displayed in Figure 5.25. Indeed, we showed that a sigmoid function is able to capture the evolution of the parameters over a wide range of equivalent strain rates. This was also true for the other PMMAs, as shown in Appendix 8.10.

Figure 5.25 also displays that parameters sharply increase with the equivalent strain rate when passing through α -transition and, more especially, N_{s1}^* , z , p_1 and N_{s2}^* . First, at short time scale or low temperature, the density of entanglement and van der Waals interaction (N_{s1}^* and N_{s2}^*) seems to be more effective [161]. Then, disentanglement parameters (z and p_1), which rule the part of the energy dissipated by the polymer network under deformation, increase when the equivalent strain rate is higher. This is consistent with experimental observations from Chapter IV, Section 4.5.6. Therefore, these results show that the model accounts for a polymer network more rigid and dissipating more energy at high strain rate or low temperature. As a perspective, we recommend to couple the constitutive model with the sigmoid evolution of the parameters for accounting the strain rate/temperature effect on the mechanical response.

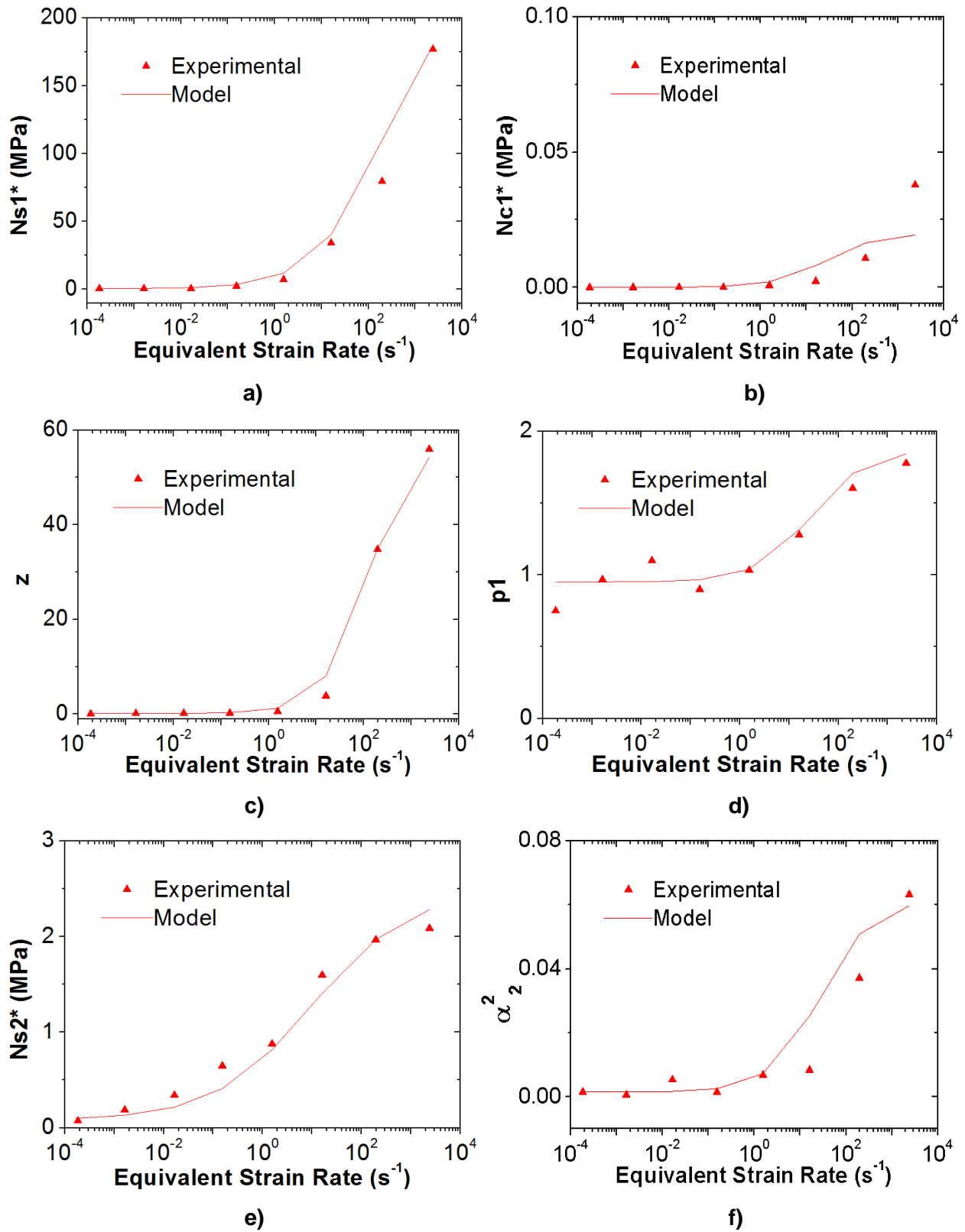


Figure 5.25: Parameters evolution with the equivalent strain rate for PMMA 120: a) Ns_1^* , b) Nc_1^* , c) z , d) p_1 , e) Ns_2^* and f) α_2^2 .

Table 5.3: Phenomenological parameters identification for the different PMMAs.

| | PMMA 80 | PMMA 93 | PMMA 120 | PMMA 3500 | PMMA CL |
|-----------------|--------------------|--------------------|--------------------|--------------------|--------------------|
| N_{s0}^1 * | 0.300 | 0.400 | 0.500 | 0.015 | 1.560 |
| N_{s1}^1 * | 60 | 56 | 75 | 140 | 100 |
| N_{c0}^1 * | 2×10^{-4} | 1×10^{-5} | 2×10^{-5} | 0.013 | 0.022 |
| N_{c1}^1 * | 0.014 | 0.014 | 0.010 | 0.007 | 2×10^{-4} |
| Z_0 | 0.070 | 0.090 | 0.120 | 1×10^{-8} | 12 |
| Z_1 | 0.770 | 23 | 29 | 3000 | 950 |
| P_{10} | 0.750 | 0.750 | 0.950 | 0.002 | 1.200 |
| P_{11} | 0.155 | 0.500 | 0.460 | 2.2 | 0.620 |
| α_{20}^2 | 0.003 | 0.001 | 0.002 | 8×10^{-5} | 0.001 |
| α_{21}^2 | 0.045 | 0.010 | 0.030 | 0.049 | 0.030 |
| N_{s0}^2 * | 0.125 | 0.080 | 0.080 | 0.610 | 0.570 |
| N_{s1}^2 * | 1 | 1.500 | 1.200 | 0.600 | 0.480 |

5.3.5 Sensitivity to the material parameters

In the results showed in Section 5.3.1.1, we could notice some disagreement with the experimental results for high equivalent strain rates. For the particular case of PMMA 80 at equivalent strain rate of 10^3 s^{-1} and 10^2 s^{-1} , higher differences were found between model and experiments performed at large strain level. To understand such difference, we have performed a sensitivity analysis of the Edward-Vilgis strain energy function. Similar, to Ogden et al. [166], we will compute the derivative of the stress with respect to the parameter to be evaluated in term of model sensitivity. For the case of tensile loading, the stress can be expressed as defined in Equation 5.11. To obtain the derivative, we will apply numerical differentiation as next:

$$\left| \frac{\partial \sigma}{\partial P} \right| = \left| \frac{\sigma_{(P+h)} - \sigma_{(P)}}{h} \right| \quad 5.17$$

where P is the parameter to be studied and h is a small change in the parameter value. h was chosen equal to 10^{-5} to be small enough to guarantee accurate values of the derivative. The investigated parameters of Branch 1 are: N_{s1}^* , N_{c1}^* , α_1^2 and η ; while for Branch 2: N_{s2}^* and α_2^2 . For this study, we took the optimal parameters of PMMA 120 at 1.56 s^{-1} (see in Appendix 8.9) as reference values. Figure 5.26 shows the derivatives as a function of the parameter of interest and the true strain.

Figure 5.26 shows that α_1^2 and α_2^2 (related to the chain extensibility) and η (linked to the chain slippage), are the most sensitive parameters. Indeed, they display abrupt changes in the derivative when passing from low deformation to high deformation level. In parallel, Ns_1^* , Nc_1^* and Ns_2^* (related to the density of entanglement, crosslinks and weak bonds) act as scaling factors regardless the deformation level.

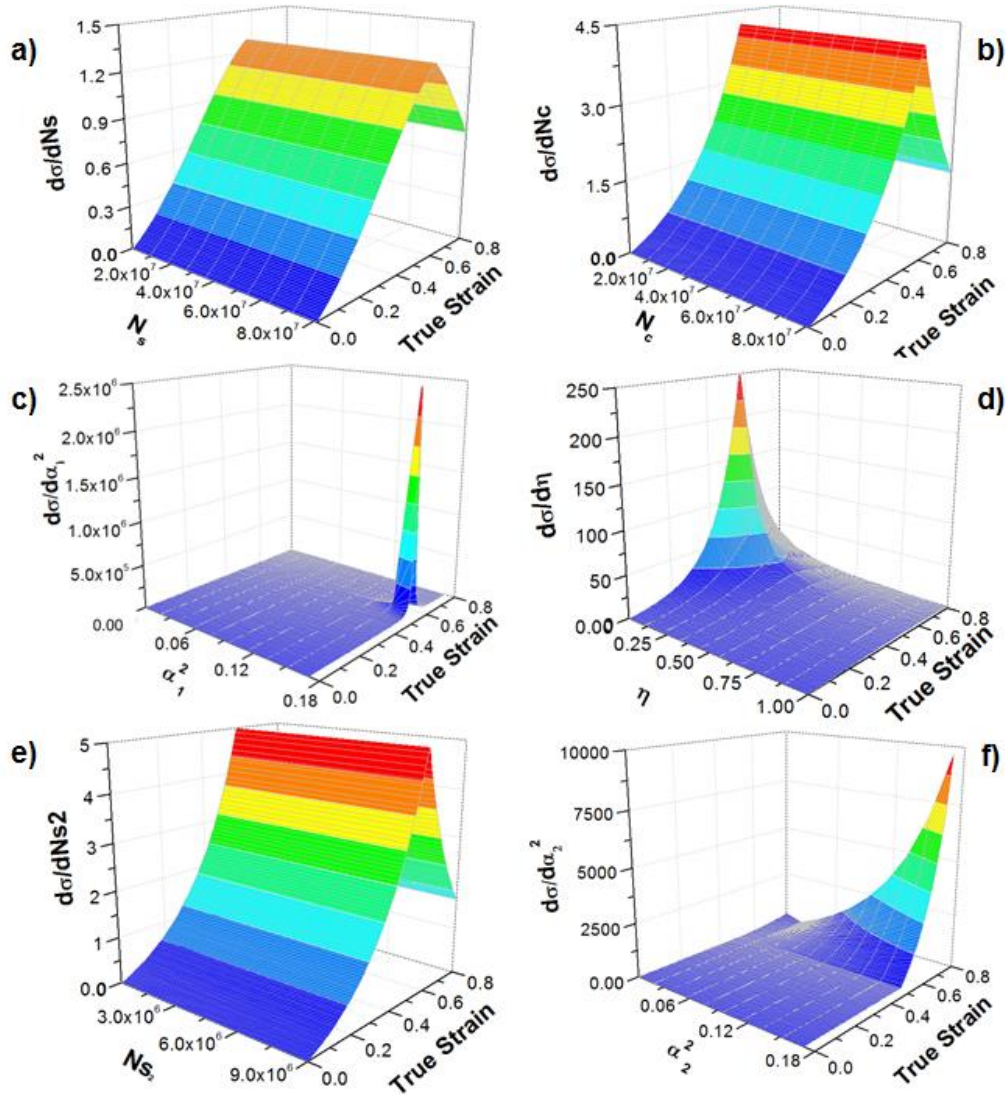


Figure 5.26: Relative sensitivity of the Edward-Vilgis parameters on PMMA 120 at 1.56 s^{-1} : a) Ns_1 , b) Nc_1 , c) α_1^2 , d) η e) Ns_2 and f) α_2^2 .

Moreover, Figure 5.27 displays the effect of Ns_1^* , η and α_2^2 on the stress for PMMA 120 at 1.56 s^{-1} . Results show that stresses are higher when Ns_1^* increases; increasing η leads to a reduction of the strain hardening; and while increasing α_2^2 promotes a sharp increase of the strain hardening. These observations show that EVs parameters are more sensitive at high

strain levels, more especially α_1^2 , α_2^2 and η . However, their influence occurs at very narrow conditions, while Ns_1^* , Nc_1^* and Ns_2^* affect the behaviour in the whole range of deformations.

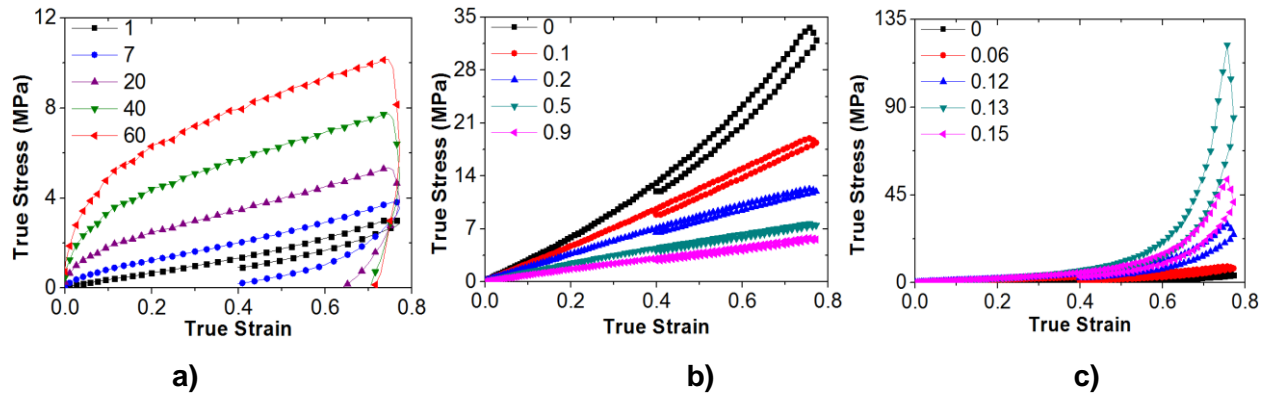


Figure 5.27: Sensitivity of the true stress with the Edward and Vilgis parameters on PMMA 120 at 1.56 s^{-1} : a) Effect of Ns_1^* , b) effect of η and c) effect of α_2^2 .

5.4 Summary

In this Chapter, the mechanical behaviour of the different PMMAs was modelled for cyclic uniaxial tensile loading. Additionally, we included the concept of “equivalent strain rate at reference temperature” into the constitutive model proposed by Billon et al. [11], [21], [25].

From a practical point of view, this approach reduces the number of constitutive parameters to be considered in the modelling, which simplify the inverse analysis for predicting the mechanical response of amorphous polymers. Thus, this methodology may enhance the numerical computations for predicting the material behaviour when studied in the viscoelastic and rubbery state.

The versatility of the model reproducing different mechanical behaviours shows the efficiency of including the evolution of parameters in Edward-Vilgis strain energy function. Indeed, the model showed some capabilities to account for different physical and topological aspects of the polymer network under deformation.

The model considered the elastic contribution of the active physical entanglements, crosslinks and van der Waals interactions, and also the inelastic mechanisms induced by disentanglements, evolution in the secondary bond density and chain extensibility.

6 Conclusions and Perspectives

6.1 General Conclusions

The main goal of this study was to characterize and model in a simplified and accurate manner, the mechanical behaviour of amorphous polymers with different architectures from the quasi-fluid state up to the solid state. Therefore, we worked with five PMMAs of different molar masses and crosslinking degree. The study consisted into three stages:

- First, we addressed the mechanical behaviour in the linear domain of deformation through DMTA and rheological tests. This gave a glimpse of the effect of molar mass and crosslinking on the linear viscoelastic properties (elastic and loss moduli), the α -transition and the time/temperature dependency.
- Then, we characterized the mechanical response at large strain while coupling the strain rate/temperature by means of the “equivalent strain rate at reference temperature” extracted from observations in the linear domain. This was possible by performing unloading-unloading tensile and shear tests using DIC techniques.
- Finally, we modelled based on the work from [11], [21] the mechanical response at large deformation while accounting the evolution of internal state variables when the polymer was deformed. For this, we used the experimental material database from Chapter IV as input.

Linear viscoelastic behaviour

In Chapter III we observed that the α -transition temperature, the storage and loss moduli (as their extension over the frequency range) increased with the molar mass and crosslinking. This was likely due to the increase of entanglement and crosslinks density. In parallel, crosslinks were more effective at low equivalent frequencies since E' remained constant for PMMA CL up to low frequencies without exhibiting a fluid behaviour, while moduli on PMMA 3500, gradually decreased when reducing the equivalent frequency.

Moreover, time/temperature equivalence was successfully applied for all the different PMMAs, identifying shift factors for tensile and shear loading. This study revealed that time/temperature dependence was sensitive to the stress state and polymer architecture. These results were essential for characterization at large deformation.

Mechanical behaviour at large deformation

In Chapter IV, we observed that true stress-strain curves obtained at different temperature/strain rate conditions were the same for a given the same equivalent strain rate, more especially when near the flowing region, rubbery plateau and viscoelastic region. Such observations were validated for tensile and shear loading on amorphous PMMAs of different molar masses and crosslinking degree. In parallel, this equivalence was also validated for two cycles of uploading-unloading tensile tests, which is a promising observation for future fatigue analysis. Experimental evidence on validating the equivalent strain rate at large deformation is not abundant in the literature and is mainly focused on monotonic loading.

Moreover, it was observed that the material behaviour at large deformation was in good agreement with the storage and loss moduli observed from the linear domain. For instance when the material was near the glassy region, it displayed a viscoelastoplastic behaviour while in the rubbery plateau, polymer presented hyperelastic behaviour. Therefore, the use of master curves obtained in the linear domain enhance the understanding on the effect of the molar mass and crosslinking in the mechanical response at large deformation.

These results open new possibilities in characterizing the mechanical response of polymers since targeting an equivalent strain rate (derived from the linear domain) allows reducing the number of experimental testing needed to characterize the material behaviour at large deformation level.

Modelling the mechanical response

In Chapter V, we observed that the constitutive model used in this work presented a good agreement with the experimental results in the linear domain (apparent Young's modulus) and large deformations (stress-strain curves) when the material was deformed under non-monotonic tensile tests near the flowing region, in the rubbery state and in its viscoelastic region.

It was shown that the versatility of the model comes from its capability to adapt the behaviour of each branch while obeying to thermodynamical framework. Indeed, the model accounts for two parallel contributions: one branch considers entanglements, crosslinks and chain slippage, adding viscoelastoplasticity (below α -transition) and viscoelasticity (above α -transition), while the second branch accounts for weak bond interactions, limit of chain extensibility and destruction/reappearance of these factors, adding hyperelasticity and viscohyperelasticity (near flowing). These results demonstrated that the model accounts for the physics of the polymer network under deformation.

In parallel, we determined that a sigmoid function was able to describe the evolution of the Edward-Vilgis parameters with the equivalent strain rate. This confirms the coherence of the

model by accounting that at low temperatures or high strain rates, the polymer network is stiffer and dissipates more energy. These results allow coupling the constitutive parameter proposed in this work, with the thermodynamic model proposed by Billon [11], [21]. This reduces also the number of parameters needed to model the mechanical behaviour of polymers.

In the literature, only few models are capable of capturing the different mechanical responses of amorphous polymers when tested under non-monotonic conditions and when they do, the number of parameters is large. The approach presented in this work allows describing many features of the polymer behaviour (viscoelastoplasticity, viscoelasticity, hyperelasticity and viscohyperelasticity) with few numbers of parameters while accounting for the physics and thermodynamics, i.e. the evolution of internal states variables. This work showed the capabilities of such modelling approach and settled the basis for enhancing the prediction of the mechanical behaviour in the viscoelastic and rubbery state.

In conclusion, this work proposed and validated a strategy to reduce the number of experimental tests needed to characterize the mechanical behaviour at large deformation by means of the “equivalent strain rate at reference temperature”. Additionally, experimental results served as input to calibrate the parameters of constitutive model, which also allowed proposing empirical relationship between these parameters and the equivalent strain rate. Results proved that we are able to simplify the characterization and modelling of the mechanical behaviour of amorphous polymers while keeping accuracy and accounting for physical aspects.

6.2 Perspectives

As we observed along this work, molar mass and crosslinking degree have a striking effect on the mechanical behaviour. To have a deeper understanding of the effect of these factors, we recommend to study more PMMAs of different molecular weights (300 Kg/mol, 700 Kg/mol, 1000 Kg/mol and 2000 Kg/mol) and different percentage of crosslinking agent.

We presented in this study that the use of the equivalent strain rate at reference was a relevant parameter for the PMMAs in the viscoelastic and rubbery region. However, the validity of this methodology in the glassy region is still unclear. Therefore, we encourage future efforts in studying this aspect, which will likely require thermo-mechanical coupling and, therefore, temperature field measurements (either by infrared cameras or pyrometer). This could be a relevant research for high strain rate applications such as impact.

Additionally, the validity of the equivalent strain rate was studied in this work for non-monotonic tensile and shear tests. However, other loading conditions such as compression, creep, fatigue and stress relaxations are still unexplored. As it was shown in Chapter IV, the equivalence principle worked for two cyclic tensile loading. It may be a promising way of investigating fatigue

condition. In parallel, preliminary studies on stress relaxation were done at different deformation level while using different set of temperature/strain rate and targeting the same equivalent strain rates. Results were quite promising, showing also that this parameter may be used in this field.

Regarding the modelling, we observed overall a good agreement between the experimental and theoretical results. However, when PMMA 3500 was near the glassy region, stress-strain curves displayed a softening regime that was not captured by the current model. We advise to include this in the model for describing accurately the mechanical response at low temperatures or high strain rates.

Additionally, the model was proved to work for non-monotonic tensile loading. However, different stress states as shearing, compression, stress relaxation and creep were not studied. This could be including by modifying the kinetics of internal state variables or by adding a triaxiality term in the model. This is an important aspect to be studied in the future since it would add some robustness to this model.

Finally, the model was verified for 1D conditions. Thus, we recommend including the model in a finite element code for validating its relevance in more complex geometries. Preliminary studies were already performed in one element (a cube) under cyclic tensile loading (boundaries conditions were selected from experimental results). Results displayed a good agreement with the 1D results from MATLAB[®] computations. Such results are promising and should encourage future efforts in completing this research.

7 BIBLIOGRAPHY

- [1] J.-L. Halary, F. Lauprêtre, and L. Monnerie, *Polymer Materials: Macroscopic Properties and Molecular Interpretations*. France, 2011.
- [2] M. Nasraoui, P. Forquin, L. Siad, and A. Rusinek, "Influence of strain rate, temperature and adiabatic heating on the mechanical behaviour of poly-methyl-methacrylate: Experimental and modelling analyses," *Mater. Des.*, vol. 37, pp. 500–509, May 2012.
- [3] K. Schmidt-Rohr, A. S. Kulik, H. W. Beckham, A. Ohlemacher, U. Pawelzik, C. Boeffel, and H. W. Spiess, "Molecular Nature of the β Relaxation in Poly(methyl methacrylate) Investigated by Multidimensional NMR," *Macromolecules*, vol. 27, pp. 4733–4745, 1994.
- [4] I. M. Ward and J. Sweeney, *An Introduction to the Mechanical Properties of Solid Polymers*, vol. 17. 2004.
- [5] P. Lomellini, "Effect of chain length on the network modulus and entanglement," *Polymer*, vol. 33, no. 6, pp. 1255–1260, 1992.
- [6] L. H. Sperling, *Introduction to Physical Polymer Science*, Fourth Edi. Wiley.
- [7] N. Alves, G. Ribelles, G. Tejedor, and J. Mano, "Viscoelastic behavior of poly (methyl methacrylate) networks with different cross-linking degrees," *Macromolecules*, pp. 3735–3744, 2004.
- [8] I. M. Neyelov, A. A. Darinskii, Y. Ya, and N. K. Balabayev, "Molecular dynamics of a polymer chain with a crosslink," *Polym. Sci. U.S.S.R.*, vol. 22, no. 8, pp. 1929–1939, 1980.
- [9] T. J. Fox and S. Loshaek, "Influence of molecular weight and degree of crosslinking on the specific volume and glass temperature of polymers," *J. Polym. Sci.*, vol. 15, pp. 371–390, 1955.
- [10] M. Krumova, D. Lopez, R. Benavente, C. Mijangos, and J. M. Peren, "Effect of crosslinking on the mechanical and thermal properties of poly (vinyl alcohol)," *Polymer*, vol. 41, pp. 9265–9272, 2000.
- [11] N. Billon, "New Constitutive Modeling for Time-Dependent Mechanical Behavior of Polymers Close to Glass Transition : Fundamentals and Experimental Validation," *J. Appl. Polym. Sci.*, 2012.
- [12] E. M. Arruda, M. C. Boyce, and R. Jayachandran, "Effects of strain rate, temperature and thermomechanical coupling on the finite strain deformation of glassy polymers," *Mech. Mater.*, vol. 19, pp. 193–212, 1995.
- [13] C. G'Sell and J. M. Haudin, *Lois de comportement mécanique des polymères solides. Introduction à la mécanique des polymères*. 1995.
- [14] J. Richeton, S. Ahzi, K. S. Vecchio, F. C. Jiang, and R. R. Adharapurapu, "Influence of temperature and strain rate on the mechanical behavior of three amorphous polymers: Characterization and modeling of the compressive yield stress," *Int. J. Solids Struct.*, vol. 43, no. 7–8, pp. 2318–2335, Apr. 2006.
- [15] R. W. Nunes, J. R. Martin, and J. F. Johnson, "Influence of Molecular Weight and Molecular Weight Distribution on Mechanical Properties of Polymers," *Polym. Eng. Sci.*, vol. 22, no. 4, pp. 205–228, 1982.
- [16] L. Song, L. Ren, M. Zhang, S. Sun, G. Gao, Y. Gui, L. Zhang, and H. Zhang, "Effect of

- Entanglement Density on Mechanical Properties and Deformation Behavior of Rubber-Modified PVC/ α -MSAN Blends,” *Ind. Eng. Chem. Res.*, vol. 52, pp. 12567–12573, 2013.
- [17] H. G. H. van Melick, L. E. Govaert, and H. E. H. Meijer, “On the origin of strain hardening in glassy polymers,” *Polymer*, vol. 44, pp. 2493–2502, 2003.
- [18] S. Bensason, E. V Stepanov, S. Chum, A. Hiltner, and E. Baer, “Deformation of Elastomeric Ethylene - Octene Copolymers,” *Macromolecules*, vol. 9297, no. 96, pp. 2436–2444, 1997.
- [19] M. A. Sutton, J.-J. Orteu, and H. W. Schreier, *Image Correlation for Shape, Motion and Deformation Measurements: Basic Concepts, Theory and Applications*. Springer.
- [20] E. Baquet, “Modélisation thermomécanique visco-hyperélastique du comportement d’un polymère semi-cristallin : application au cas d’une matrice polyamide 6.6,” Ecole Nationale Supérieure des Mines de Paris, 2011.
- [21] A. Maurel-Pantel, E. Baquet, J. Bikard, J. L. Bouvard, and N. Billon, “A thermo-mechanical large deformation constitutive model for polymers based on material network description: Application to a semi-crystalline polyamide 66,” *Int. J. Plast.*, vol. 67, pp. 102–126, Apr. 2015.
- [22] J. D. Ferry, *Viscoelastic Properties of Polymers*, 3rd ed. New York: John Wiley & Sons, 1980.
- [23] S. F. Edwards and T. Vilgis, “The effect of entanglements in rubber elasticity,” *Polymer*, vol. 27, pp. 483–492, 1986.
- [24] E. Gorlier, “Caractérisation rhéologique et structurale d’un PET. Application au procédé de bi-étirage soufflage de bouteilles,” Ecole Nationale Supérieure des Mines de Paris, 2001.
- [25] F. Gehring, J.-L. Bouvard, and N. Billon, “Modeling of time dependent mechanical behavior of polymers: Comparison between amorphous and semicrystalline polyethylene terephthalate,” *J. Appl. Polym. Sci.*, vol. 133, no. 35, pp. 1–17, Sep. 2016.
- [26] G. Quandalle, “Etude et modélisation mécanique de la cristallisation induite par la déformation des polymères: caoutchouc naturel réticulé et PET,” MINES ParisTech, 2017.
- [27] J. Brydson, “Acrylic Plastics,” in *Plastics Materials (7th Edition)*, 1999, pp. 398–424.
- [28] J. Brandup, E. Immergut, and E. Grulke, *Polymer handbook*. Poymer International, 1999.
- [29] R. J. Young and C. I. Chung, “Introduction to Polymers,” *Journal of Engineering Materials and Technology*, vol. 104. p. 297, 1982.
- [30] N. G. McCrum, C. P. Buckley, and C. B. Bucknall, *Principles of polymer engineering*. USA: Oxford University Press, 1997.
- [31] J. D. Menczel and R. B. Prime, *Thermal Analysis of Polymers: Fundamentals and Applications*. Wiley, 2008.
- [32] T. G. Fox Jr and P. J. Flory, “Second-order transition temperatures and related properties of polystyrene. I. Influence of molecular weight,” *Appl. Phys.*, vol. 21, no. 6, pp. 581–591, 1950.
- [33] L. P. Blanchard, J. Hesse, and S. L. Malhotra, “Effect of Molecular Weight on Glass Transition by Differential Scanning Calorimetry,” *Can. J. Chem.*, vol. 52, no. 18, pp. 3170–3175, 1974.
- [34] H. Stutz, K. Illers, and J. Mertes, “A Generalized Theory for the Glass Transition Temperature of Crosslinked and Uncrosslinked Polymers,” *J. Polym. Sci. Part B*, vol. 28,

pp. 1483–1498, 1990.

- [35] K. P. Menard, “Dynamic mechanical analysis,” *En. Polym. Sci. Tech.*, vol. 9, pp. 563–590, 2004.
- [36] O. Starkova and A. Aniskevich, “Poisson’s ratio and the incompressibility relation for various strain measures with the example of a silica-filled SBR rubber in uniaxial tension tests,” *Polym. Test.*, vol. 29, pp. 310–318, 2010.
- [37] C. G. Sell, J. M. Hiver, and A. Dahoun, “Experimental characterization of deformation damage in solid polymers under tension, and its interrelation with necking,” *Int. J. Solids Struct.*, vol. 39, pp. 3857–3872, 2002.
- [38] S. I. Naqui and I. M. Robinson, “Review Tensile dilatometric studies of deformation in polymeric materials and their composites,” *J. Mater. Sci.*, vol. 28, pp. 1421–1429, 1993.
- [39] P. Bhargava and A. T. Zehnder, “High Temperature Shear Strength of T650-35 / HFPE-II-52 Polyimide Matrix Unidirectional Composite,” *Exp. Mech.*, vol. 46, pp. 245–255, 2006.
- [40] ASTM Standard D 5379/D 5379M-98, “Standard Test Method for Shear Properties of Composite Materials by the V-Notched.”
- [41] F. Pierron and A. Vautrin, “MEASUREMENT OF THE IN-PLANE SHEAR STRENGTHS OF UNIDIRECTIONAL COMPOSITES WITH THE IOSIPESCU TEST,” *Compos. Sci. Technol.*, vol. 3538, no. 97, 1998.
- [42] N. Melin, “The modified Iosipescu shear test for orthotropic materials,” KTH Engineering Sciences, 2008.
- [43] J. Morton, H. Ho, M. Y. Tsai, and G. L. Farley, “An Evaluation of the Iosipescu Specimen for Composite Materials Shear Property Measurement,” *J. Compos. Mater.*, vol. 26, pp. 708–750, 1992.
- [44] H. Ho, M. Y. Tsai, J. Morton, and G. L. Farley, “Numerical Analysis of the Iosipescu Specimen for Composite Materials,” *Compos. Sci. Technol.*, vol. 46, pp. 115–128, 1993.
- [45] F. Pierron, A. Vautrin, and B. Harris, “The Iosipescu in-plane Shear Test: Validation on an Isotropic Material,” *Exp. Mech.*, vol. 35, pp. 130–136, 1995.
- [46] J. P. Norton, *An introduction to identification*. London: Academic Press, 1985.
- [47] A. Tarantola, *Inverse Problem Theory*. ELSEVIER, 1987.
- [48] H. D. Bui and P. Germain, *Introduction aux problèmes inverses en mécanique des matériaux*. Paris: EYROLLES, 1993.
- [49] J. A. Nelder and R. Mead, “A simplex method for function minimization,” *Comput. J.*, vol. 7, pp. 308–313, 1965.
- [50] J. C. Lagarias, J. A. Reeds, M. H. Wright, and P. E. Wright, “Convergence properties of the nelder–mead simplex method in low dimensions,” *SIAM J. Optim.*, vol. 9, no. 1, 1998.
- [51] L. Monnerie, L. Jean, L. Halary, D. Recherche, and H. Dunant, “Investigation of Solid-State Transitions in Linear and Crosslinked Amorphous Polymers,” *Adv. Polym. Sci.*, no. October, pp. 35–213, 2005.
- [52] N. M. Alves, J. F. Mano, J. L. Gómez Ribelles, and J. A. Gómez Tejedor, “Departure from the Vogel behaviour in the glass transition—thermally stimulated recovery, creep and dynamic mechanical analysis studies,” *Polymer*, vol. 45, no. 3, pp. 1007–1017, Feb. 2004.
- [53] A. Schönhals, “Dielectric spectroscopy on the dynamics of amorphous polymeric

- systems,” *Sta*, no. i, pp. 1–17, 1998.
- [54] A. D. Mulliken and M. C. Boyce, “Mechanics of the rate-dependent elastic–plastic deformation of glassy polymers from low to high strain rates,” *Int. J. Solids Struct.*, vol. 43, no. 5, pp. 1331–1356, Mar. 2006.
- [55] B. Zuo, W. Liu, H. Fan, Y. Zhang, T. He, and X. Wang, “Suppressed surface dynamics of poly(methyl methacrylate) chains in the corona of collapsed dry micelles tethered by a fluorinated block core,” *Soft Matter*, vol. 9, pp. 5428–5437, 2013.
- [56] R. Casalini and C. M. Roland, “Effect of crosslinking on the secondary relaxation in polyvinylethylene,” *J. Polym. Sci. Part B Polym. Phys.*, vol. 48, no. 5, pp. 582–587, Mar. 2010.
- [57] M. T. Shaw and W. J. MacKnight, *Introduction to Polymer Viscoelasticity: Third Edition*. 2005.
- [58] J. L. Halary, A. K. Outlache, J. F. Louyot, B. Jasse, T. Sarraf, and R. Muller, “Viscoelastic Properties of Styrene-co-Methyl Methacrylate Random Copolymers,” *J. Polym. Sci. Part B Polym. Phys.*, vol. 29, pp. 933–943, 1991.
- [59] O. Kramer, “Contribution of entanglements to rubber elasticity,” *Polymer*, vol. 20, no. July, pp. 1336–1342, 1979.
- [60] W. W. Graessley and S. F. Edwards, “Entanglement interactions in polymers and the chain contour concentration,” *Polymer*, vol. 22, no. 10, pp. 1329–1334, 1981.
- [61] S. Wu, “Chain Structure and Entanglement,” *J. Polym. Sci. Part B Polym. Phys.*, vol. 27, pp. 723–741, 1989.
- [62] L. J. Fetters, D. J. Lohse, and R. H. Colby, *Chain Dimensions and Entanglement Spacings: Physical Properties of Polymers Handbook*. Springer Science+Business Media, LLC, 1996.
- [63] R. Neviere, “An extension of the time–temperature superposition principle to non-linear viscoelastic solids,” *Int. J. Solids Struct.*, vol. 43, pp. 5295–5306, 2006.
- [64] J. Furmanski, C. M. Cady, and E. N. Brown, “Time - temperature equivalence and adiabatic heating at large strains in high density polyethylene and ultrahigh molecular weight polyethylene,” *Polymer*, vol. 54, no. 1, pp. 381–390, 2013.
- [65] J. Furmanski, E. N. Brown, B. Clements, C. M. Cady, and G. T. Gray, “Large-strain time-temperature equivalence in high density polyethylene for prediction of extreme deformation and damage,” *EPJ Web Conf.*, vol. 26, 2012.
- [66] M. J. Kendall and C. R. Siviour, “Experimentally simulating adiabatic conditions: Approximating high rate polymer behavior using low rate experiments with temperature profiles,” *Polymer*, vol. 54, no. 18, pp. 5058–5063, 2013.
- [67] J. Diani, P. Gilormini, and J. S. Arrieta, “Direct experimental evidence of time-temperature superposition at finite strain for an amorphous polymer network,” *Polymer*, vol. 58, pp. 107–112, 2015.
- [68] J. L. Bouvard, D. K. Francis, M. A. Tschopp, E. B. Marin, D. J. Bammann, and M. F. Horstemeyer, “An internal state variable material model for predicting the time, thermomechanical, and stress state dependence of amorphous glassy polymers under large deformation,” *Int. J. Plast.*, vol. 42, pp. 168–193, 2013.
- [69] A. Chrysochoos, “Thermomechanical Analysis of the Cyclic Behavior of Materials,” *Procedia IUTAM*, vol. 4, pp. 15–26, 2012.

- [70] J. W. Kim, G. A. Medvedev, and J. M. Caruthers, "The response of a glassy polymer in a loading/unloading deformation: The stress memory experiment," *Polymer*, vol. 54, no. 21, pp. 5993–6002, 2013.
- [71] C. Xiao, J. Y. Jho, and A. F. Yee, "Correlation between the shear yielding behaviour and secondary relaxations of bisphenol A polycarbonate and related copolymers," *Macromolecules*, vol. 27, pp. 2761–2768, 1994.
- [72] L. P. Chen, A. F. Yee, and E. J. Moskala, "The molecular basis for the relationship between the secondary and mechanical properties of a series of polyester copolymer glasses," *Macromolecules*, vol. 32, pp. 5944–5955, 1999.
- [73] B. Brulé, J. L. Halary, and L. Monnerie, "Molecular analysis of the plastic deformation of amorphous semi-aromatic polyamides," *Polymer*, vol. 42, pp. 9073–9083, 2001.
- [74] D. Rana, V. Sauvant, and J. L. Halary, "Molecular analysis of yielding in pure and antiplasticized epoxy-amine thermosets," *J. Mater. Sci.*, vol. 37, pp. 5267–5274, 2002.
- [75] J. Richeton, S. Ahzi, L. Daridon, and Y. Rémond, "A formulation of the cooperative model for the yield stress of amorphous polymers for a wide range of strain rates and temperatures," *Polymer*, vol. 46, no. 16, pp. 6035–6043, Jul. 2005.
- [76] J. Richeton, S. Ahzi, K. S. Vecchio, F. C. Jiang, and A. Makradi, "Modeling and validation of the large deformation inelastic response of amorphous polymers over a wide range of temperatures and strain rates," *Int. J. Struct.*, vol. 44, pp. 7938–7954, 2007.
- [77] C. M. Cady, W. Blumenthal, I. G. Gray, and D. Idar, "Determining the constitutive response of polymeric materials as a function of temperature and strain rate," *J. Phys. IV*, vol. 110, pp. 27–32, 2003.
- [78] J. L. Jordan, C. R. Siviour, J. R. Foley, and E. N. Brown, "Compressive properties of extruded polytetrafluoroethylene," *Polymer*, vol. 48, pp. 4184–4195, 2007.
- [79] C. R. Siviour, S. M. Walley, W. G. Proud, and J. E. Field, "The high strain rate compressive behavior of polycarbonate and polyvinylidene difluoride," *Polymer*, vol. 46, pp. 12546–12555, 2005.
- [80] J. L. Jordan, J. R. Foley, and C. R. Siviour, "Mechanical properties of Epon 826/DEA epoxy," *Mech. Time-Dependent Mater.*, vol. 31, pp. 523–544, 2008.
- [81] S. Hillmansen and R. N. Haward, "Adiabatic failure in polyethylene," *Polymer*, vol. 42, pp. 9301–9312, 2001.
- [82] S. V. Shenogin, G. W. H. Hohne, and E. F. Oleinik, "Thermodynamics of the pre-yield deformation behavior of glassy polymers: measurements with new deformation calorimeter," *Thermochim. Acta*, vol. 391, pp. 13–23, 2002.
- [83] O. B. Salamatina, S. N. Rudnev, Z. Bartczk, A. Galeski, and E. F. Oleinik, "Thermodynamics of inelastic deformation of amorphous and crystalline phases in linear polyethylene," *Polym. Sci. Ser. A*, vol. 53, pp. 775–786, 2011.
- [84] D. N. Theodorou and U. V. Suter, "Local structure and the mechanism of response to elastic deformation in a glassy polymer," *Macromolecules*, vol. 19, pp. 379–387, 1986.
- [85] J. . Wu and C. P. Buckley, "Plastic deformation of glassy polystyrene: a unified model of yield and the role of chain length," *J. Polym. Sci. Part B*, vol. 42, pp. 2027–2040, 2004.
- [86] E. T. . Klompen, T. A. . Engels, L. E. Goavert, and H. E. H. Meijer, "Modelling of the post-yield response of glassy polymers: influence of thermomechanical history," *Macromolecules*, vol. 38, pp. 6997–7008, 2005.

- [87] H. E. H. Meijer and L. E. Govaert, "Mechanical performance of polymer systems : The relation between structure and properties," *Prog. Polym. Sci.*, vol. 30, pp. 915–938, 2005.
- [88] P. Prentice, "Influence of molecular weight on the fracture of poly (methyl methacrylate) (P M M A)," *Polymer*, vol. 24, 1982.
- [89] R. N. Harward and G. Thackray, "The use of a mathematical model to describe isothermal stress-strain curves in glassy thermoplastics," *Proc. R. Soc. London*, vol. A302, pp. 453–472, 1968.
- [90] Y. Tomita, "Constitutive modelling of deformation behavior of glassy polymers and applications," *Int. J. Mech. Sci.*, vol. 42, pp. 1455–1469, 2000.
- [91] G. Capaccio and I. M. Ward, "Preparation of ultra-high modulus linear polyethylenes; effect of molecular weight and molecular weight distribution on drawing behaviour and mechanical properties," *Polymer*, vol. 15, 1974.
- [92] R. P. Wool, *Polymer Interfaces: Structure and Strength*. Munich: Hanser, 1995.
- [93] L. E. Nielsen and R. F. Landel, *Mechanical Properties of Polymers*. New York: Reinhold, 1994.
- [94] Z. Bartczak, "Effect of Chain Entanglements on Plastic Deformation Behavior of Linear Polyethylene," *Macromolecules*, vol. 38, pp. 7702–7713, 2005.
- [95] D. Hossain, M. A. Tschopp, D. K. Ward, J. L. Bouvard, P. Wang, and M. F. Horstemeyer, "Molecular dynamics simulations of deformation mechanisms of amorphous polyethylene," *Polymer*, vol. 51, no. 25, pp. 6071–6083, 2017.
- [96] J. E. Shepherd, D. L. Mcdowell, and K. I. Jacob, "Modeling morphology evolution and mechanical behavior during thermo-mechanical processing of semi-crystalline polymers," *J. Mech. Phys. Solids*, vol. 54, pp. 467–489, 2006.
- [97] H. Wang, H. Zhou, Z. Huang, Y. Zhang, and X. Zhao, "Constitutive modeling of polycarbonate over a wide range of strain rates and temperatures," *Mech. Time-Dependent Mater.*, vol. 21, pp. 97–117, 2017.
- [98] W. P. Cox and E. H. Merz, "Correlation of dynamic and steady flow viscosities," *J. Polym. Sci.*, vol. 28, pp. 619–622, 1958.
- [99] C. G'Sell and S. Boni, "Application of the plane simple shear test for determination of the plastic behaviour of solid polymers at large strains," *J. Mater. Sci.*, vol. 18, pp. 903–918, 1983.
- [100] C. G'Sell and A. J. Gopez, "Plastic banding in glassy polycarbonate under plane simple shear," *J. Mater. Sci.*, vol. 20, pp. 3462–3478, 1985.
- [101] M. C. Boyce, E. M. Arruda, and R. Jayachandran, "The Large Strain Compression, Tension, and Simple Shear of Polycarbonate," *Polym. Eng. Sci.*, vol. 34, pp. 716–725, 1994.
- [102] L. R. G. Treloar, "THE PHOTO-ELASTIC PROPERTIES OF RUBBER. PART I : THEORY OF THE OPTICAL PROPERTIES OF STRAINED RUBBER," *Trans. Faraday Soc.*, vol. 43, pp. 277–284, 1946.
- [103] T. Rey, G. Chagnon, J. Le Cam, and D. Favier, "Influence of the temperature on the mechanical behaviour of filled and unfilled silicone rubbers," *Polym. Test.*, vol. 32, pp. 492–501, 2013.
- [104] J. L. Bouvard, D. K. Ward, D. Hossain, S. Nouranian, E. B. Marin, and M. F. Horstemeyer, "Review of Hierarchical Multiscale Modeling to Describe the Mechanical Behavior of

Amorphous Polymers," *J. Eng. Mater. Technol.*, vol. 131, 2009.

- [105] S. G. Bardenhagen, M. G. Stout, and G. T. Gray, "Three-Dimensional Finite Deformation Viscoplastic Constitutive Models for Polymeric Materials," *Mech. Mater.*, vol. 25, pp. 235–253, 1997.
- [106] V. A. Lubarda, D. J. Benson, and M. A. Meyers, "Strain-Rate Effects in Rheological Models of Inelastic Response," *Int. J. Plast.*, vol. 19, pp. 1097–118, 2003.
- [107] A. S. Khan, O. Lopez-Pamies, and R. Kasmi, "Thermo-mechanical large deformation response and constitutive modeling of viscoelastic polymers over a wide range of strain rates and temperatures," *Int. J. Plast.*, vol. 22, pp. 581–601, 2006.
- [108] C. G'Sell and J. J. Jonas, "Determination of the plastic behavior of solid polymers at constant true strain rate," *J. Mater. Sci.*, vol. 14, pp. 583–591, 1979.
- [109] C. G'Sell, N. A. Aly-Helal, and J. J. Jonas, "Effect of stress triaxiality on neck propagation during the tensile stretching of solid polymers," *J. Mater. Sci.*, vol. 18, pp. 1731–1742, 1983.
- [110] N. Billon, "Effet de couplage thermomécanique dans la caractérisation du comportement de polymères solides," *Mécanique Ind.*, vol. 4, pp. 357–364, 2003.
- [111] R. N. Haward and G. Thackray, "The Use of a Mathematical Model to Describe Isothermal Stress-Strain Curves in Glassy Thermoplastics," *Proc. R. Soc. London*, vol. 302, pp. 453–472, 1968.
- [112] H. Eyring, "Viscosity, plasticity and diffusion as examples of absolute reaction rates," *J. Chem.*, vol. 4, 1936.
- [113] R. E. Robertson, "Theory for the Plasticity of Glassy Polymers," *J. Chem. Phys.*, vol. 44, pp. 3950–3956, 1966.
- [114] A. S. Argon, "A Theory for the Low Temperature Plastic Deformation of Glassy Polymers," *Philos. Mag.*, vol. 28, pp. 839–865, 1973.
- [115] M. C. Boyce, D. M. Parks, and A. S. Argon, "Large enelastic deformation of glassy polymers, part I rate dependent constitutive model," *Mech. Mater.*, vol. 7, pp. 15–33, 1988.
- [116] T. Ree and H. Eyring, "Theory of Non-Newtonian Flow. I. Solid Plastic System," *J. Appl. Phys.*, vol. 26, pp. 793–800, 1955.
- [117] T. Ree and H. Eyring, *Rheology: Theory and Applications*, Volume III. New York: Academic Press, 1958.
- [118] M. C. Boyce, E. L. Montagut, and A. S. Argon, "The effect of thermomechanical coupling on the cold drawing process of glassy polymersNo Title," *Polym. Eng. Sci.*, vol. 32, pp. 1073–1085, 1992.
- [119] R. Dupaix and M. C. Boyce, "Constitutive modeling of the finite strain behavior of amorphous polymers in and above the glass transition," *Mech. Mater.*, vol. 39, pp. 39–52, 2007.
- [120] G. Marckmann and E. Verron, "COMPARISON OF HYPERELASTIC MODELS FOR RUBBER-LIKE MATERIALS," *RUBBER Chem. Technol.*, vol. 79, pp. 835–858, 2006.
- [121] M. Mooney, "A theory of large elastic deformation," *J. Appl. Phys.*, vol. 11, pp. 582–592, 1940.
- [122] R. S. Rivlin, "Large elastic deformations of isotropic materials. IV. Further developments of the general theory," *Philos. Trans. R. Soc. London. Ser. A, Math. Phys. Sci.*, vol. 241,

pp. 379–397, 1948.

- [123] O. H. Yeoh, “Some Forms of the Strain Energy Function for Rubber,” *Rubber Chem. Technol.*, vol. 66, pp. 754–771, 1993.
- [124] R. W. Ogden, “Large deformation isotropic elasticity – on the correlation of theory and experiment for incompressible rubberlike solids,” *Proc. R. Soc. London*, vol. 326, 1972.
- [125] R. W. Ogden, *Elastic deformations of rubberlike solids*. Pergamon Press, 1982.
- [126] R. W. Ogden, *Non-Linear elastic deformations*. Dover Publications, 1997.
- [127] L. R. G. Treloar, “THE ELASTICITY OF A NETWORK OF LONG CHAIN MOLECULES I,” *Trans. Faraday Soc.*, vol. 39, pp. 36–41, 1942.
- [128] R. Ball, M. Doi, S. F. Edwards, and M. Warner, “Elasticity of entangled networks,” *Polymer*, vol. 22, 1981.
- [129] E. M. Arruda and M. C. Boyce, “A three-dimensional constitutive model for the large stretch behavior of rubber elastic materials,” *J. Mech. Phys. Solids*, vol. 41, pp. 389–412, 1993.
- [130] M. Kaliske and G. Heinrich, “An Extended Tube-Model for Rubber Elasticity: Statistical-Mechanical Theory and Finite Element Implementation,” *Rubber Chem. Technol.*, vol. 72, pp. 602–632, 1999.
- [131] M. Pyrz and F. Zairi, “Identification of viscoplastic parameters of phenomenological constitutive equations for polymers by deterministic and evolutionary approach,” *Model. Simul. Mater. Sci. Eng.*, vol. 15, pp. 85–103, 2007.
- [132] F. Zairi, M. Nait-Abdelaziz, K. Woznica, and J. Gloaguen, “Elasto-viscoplastic constitutive equations for the description of glassy polymers behavior at constant strain rate,” *J. Eng. Mater. Technol.*, vol. 129, pp. 29–35, 2007.
- [133] S. M. Mirkhalaf, F. M. Andrade Pires, and R. Simoes, “An elasto-viscoplastic constitutive model for polymers at finite strains: Formulation and computational aspects,” *Comput. Struct.*, vol. 166, pp. 60–74, 2016.
- [134] S. M. Mirkhalaf, F. M. Andrade Pires, and R. Simoes, “Modelling of the post yield response of amorphous polymers under different stress states,” *Int. J. Plast.*, vol. 88, pp. 159–187, 2017.
- [135] O. A. Hasan and M. C. Boyce, “A Constitutive Model for the Nonlinear Viscoelastic Viscoplastic Behavior of Glassy-Polymers,” *Polym. Eng. Sci.*, vol. 35, no. 4, pp. 331–344, 1995.
- [136] A. Muliana, K. R. Rajagopal, D. Tscharnuter, and G. Pinter, “A nonlinear viscoelastic constitutive model for polymeric solids based on multiple natural configuration theory,” *Int. J. Solids Struct.*, vol. 100–101, pp. 95–110, 2016.
- [137] J. Guo, J. Liu, Z. Wang, X. He, L. Hu, L. Tong, and X. Tang, “A thermodynamics viscoelastic constitutive model for shape memory polymers,” *J. Alloys Compd.*, vol. 705, pp. 146–155, 2017.
- [138] C. Yu, G. Kang, K. Chen, and F. Lu, “A thermo-mechanically coupled nonlinear viscoelastic–viscoplastic cyclic constitutive model for polymeric materials,” *Mech. Mater.*, vol. 105, pp. 1–15, 2017.
- [139] Y. Li, Y. He, and Z. Liu, “A viscoelastic constitutive model for shape memory polymers based on multiplicative decompositions of the deformation gradient,” *Int. J. Plast.*, vol. 91, pp. 300–317, 2017.

- [140] J. Gu, J. Leng, and H. Sun, "A constitutive model for amorphous shape memory polymers based on thermodynamics with internal state variables," *Mech. Mater.*, vol. 111, pp. 1–14, 2017.
- [141] F. Praud, G. Chatzigeorgiou, J. Bikard, and F. Meraghni, "Phenomenological multi-mechanisms constitutive modelling for thermoplastic polymers, implicit implementation and experimental validation," *Mech. Mater.*, vol. 114, pp. 9–29, 2017.
- [142] P. J. Dooling, C. P. Buckley, S. Rostami, and N. Zahlan, "Hot-drawing of poly(methyl methacrylate) and simulation using a glass - Rubber constitutive model," *Polymer*, vol. 43, pp. 2451–2465, 2002.
- [143] C. P. Buckley and D. C. Jonest, "Glass-rubber constitutive model for amorphous polymers near the glass transition," *Polymer*, vol. 36, pp. 3301–3312, 1995.
- [144] C. P. Buckley and D. C. Jonest, "Hot-drawing of poly (ethylene terephthalate) under biaxial stress: application of a three-dimensional glass-rubber constitutive model," *Polymer*, vol. 37, pp. 2403–2414, 1996.
- [145] P. G. Gennes, *Scaling Concepts in Polymer Physics*, First Edit. Ithaca: Cornell University Press, 1979.
- [146] A. M. Adams, C. P. Buckley, and D. P. Jones, "Biaxial hot drawing of poly(ethylene terephthalate): Measurements and modelling of strain-stiffening," *Polymer*, vol. 41, pp. 771–786, 2000.
- [147] J. Sweeney, R. Spares, and M. Woodhead, "A Constitutive Model for Large Multiaxial Deformations of Solid Polypropylene at High Temperature," *Polym. Eng. Sci.*, vol. 49, pp. 1902–1908, 2009.
- [148] L. Anand, N. M. Ames, V. Srivastava, and S. A. Chester, "A thermomechanically coupled theory for large deformations of amorphous polymers. part I: Formulation," *Int. J. Plast.*, vol. 25, pp. 1474–1494, 2009.
- [149] N. M. Ames, V. Srivastava, S. A. Chester, and L. Anand, "A thermomechanically coupled theory for large deformations of amorphous polymers. part II: Applications," *Int. J. Plast.*, vol. 25, pp. 1495–1539, 2009.
- [150] V. Srivastava, S. A. Chester, N. M. Ames, and L. Anand, "A thermo-mechanically-coupled large-deformation theory for amorphous polymers in a temperature range which spans their glass transition," *Int. J. Plast.*, vol. 26, no. 8, pp. 1138–1182, 2010.
- [151] A. N. Gent, "A new constitutive relation for rubber," *Rubber Chem. Technol.*, vol. 69, pp. 59–61, 1996.
- [152] G. Ayoub, F. Zaïri, M. Naït-Abdelaziz, and J. M. Gloaguen, "Modelling large deformation behaviour under loading-unloading of semicrystalline polymers: Application to a high density polyethylene," *Int. J. Plast.*, vol. 26, no. 3, pp. 329–347, 2010.
- [153] J. S. Bergstrom and M. C. Boyce, "Constitutive modeling of the large strain time-dependent behavior of elastomers," *J. Mech. Phys. Solids*, vol. 46, pp. 931–954, 1998.
- [154] M. C. Boyce, S. Socrate, and P. G. Llana, "Constitutive model for the finite deformation stress–strain behavior of poly(ethylene terephthalate) above the glass transition," *Polymer*, vol. 41, pp. 2183–2201, 2000.
- [155] O. U. Colak, "Modeling deformation behavior of polymers with viscoplasticity theory based on overstress," *Int. J. Plast.*, vol. 21, pp. 145–160, 2005.
- [156] R. Ball, "Elasticity of entangled networks," *Polymer*, vol. 22, pp. 1010–1018, 1981.

- [157] J. Sweeney, "A constitutive law for large deformations of polymers at high temperatures," *J. Mech. Phys. Solids*, vol. 44, pp. 1033–1049, 1996.
- [158] A. C.-Y. Lew and C. P. Buckley, "Biaxial constitutive response of PET during hot drawing: Experimental study and new implications for constitutive modelling," *Annual Technical Conference - ANTEC, Conference Proceedings*, vol. 4, Pages. pp. 2294–2298, 2007.
- [159] E. Gorlier, J. F. Agassant, J. M. Haudin, and N. Billon, "Experimental and theoretical study of uniaxial deformation of amorphous poly(ethylene terephthalate) above glass transition temperature," *Plast. Rubber Compos.*, vol. 30, 2001.
- [160] L. Fahrmeir, T. Kneib, and S. Lang, *Regression: Modelle, Methoden und Anwendungen*, 2nd ed. Berlin and Heidelberg: Springer, 2009.
- [161] M. G. Brereton and P. G. Klein, "Analysis of the rubber elasticity of polyethylene networks based on the slip link model of S. F. Edwards et al.," *Polymer*, vol. 29, pp. 970–974, 1988.
- [162] J. Sweeney and I. M. Ward, "Rate dependent and network phenomena in the multiaxial drawing of poly(vinyl chloride)," *Polymer*, vol. 36, pp. 299–308, 1995.
- [163] J. Sweeney, T. L. D. Collins, P. D. Coates, and I. M. Ward, "Application of an elastic model to the large deformation, high temperature stretching of polypropylene," *Polymer*, vol. 38, pp. 5991–5999, 1997.
- [164] R. G. Matthews, R. A. Duckett, I. M. Ward, and D. P. Jones, "The biaxial drawing behaviour of poly(ethylene terephthalate)," *Polymer*, vol. 38, no. 19, pp. 4795–4802, 1997.
- [165] Y. Marco, "Caractérisation multi-axiale du comportement et de la micro-structure d'un semi-cristallin : Application au cas du PET," Ecole Normale Supérieure de Cachan, 2003.
- [166] R. W. Ogden, G. Saccomandi, and I. Sgura, "Fitting hyperelastic models to experimental data," *Comput. Mech.*, vol. 34, no. 6, pp. 484–502, 2004.
- [167] C. Dessi, G. D. Tsibidis, D. Vlassopoulos, M. De Corato, M. Trofa, G. D'Avino, P. L. Maffettone, and S. Coppola, "Analysis of dynamic mechanical response in torsion," *J. Rheol. (N. Y. N. Y.)*, vol. 60, no. 2, pp. 275–287, 2016.
- [168] C. A. Schneider, W. S. Rasband, and K. W. Eliceiri, "NIH Image to ImageJ: 25 years of image analysis," *Nat. Methods*, vol. 9, pp. 671–675, 2012.
- [169] F. Grytten, H. Daiyan, M. Polanco-Loria, and S. Dumoulin, "Use of digital image correlation to measure large-strain tensile properties of ductile thermoplastics," *Polym. Test.*, vol. 28, no. 6, pp. 653–660, Sep. 2009.
- [170] N. Candau, C. Pradille, J. L. Bouvard, and N. Billon, "On the use of a four-cameras stereovision system to characterize large 3D deformation in elastomers," *Polym. Test.*, vol. 56, no. October, pp. 314–320, 2016.
- [171] H. Schreier, J. Braasch, and M. Sutton, "Systematic errors in digital image correlation caused by intensity interpolation," *Opt. Eng.*, vol. 39, no. 11, 2000.
- [172] V. P. Zok, M. N. Rajan, and W. F. Rossol, "Optimization of Digital Image Correlation for High-Resolution Strain Mapping of Ceramic Composites," *Exp. Mech.*, pp. 1407–1421, 2012.
- [173] I. Eshraghi, M. R. Y. Dehnavi, and N. Soltani, "Effect of Subset Parameters Selection on the Estimation of Mode-I Stress Intensity Factor in a Cracked PMMA Specimen using Digital Image Correlation," *Polym. Test.*, no. August, 2014.

- [174] M. Ashrafi and M. E. Tuttle, "High Strain Gradient Measurements in Notched Laminated Composite Panels by Digital Image Correlation," *Compos. Hybrid, Multifunct. Mater.*, vol. 4, pp. 75–81, 2015.
- [175] P. J. Flory, "Thermodynamics Relation for High Elastic Materials," *Trans. Faraday Soc.*, vol. 57, pp. 829–838, 1961.
- [176] J. C. Simo, R. L. Taylor, and K. S. Pister, "Variational and Projection Methods for the Volume Constraint in Finite Deformation Elastoplasticity," *Comput. Methods Vol. Constraints Finite Deform. Elastoplast.*, vol. 51, pp. 177–208, 1985.
- [177] E. H. Lee, "Elastic Plastic Deformation at Finite Strain," *ASME J. Appl. Mech.*, vol. 36, pp. 1–6, 1969.
- [178] F. Sidoroff, "Nonlinear Viscoelastic Model with Intermediate Configuration," *J. Mech.*, vol. 13, pp. 679–713, 1974.
- [179] J. Lubliner, "A Model of Rubber Viscoelasticity," *Mech. Res. Commun.*, vol. 12, pp. 93–99, 1985.
- [180] A. Andriyana, L. Silva, and N. Billon, "Viscoelastic Characterization of Short Fibres Reinforced Thermoplastic in Tension and Shearing," *Appl. Mech. Mater.*, vol. 24–25, pp. 419–423, 2010.
- [181] G. A. Holzapfel, *Nonlinear Solid Mechanics. A Continuum Approach for Engineering*. Chichester: John Wiley & Sons, 2000.
- [182] J. C. Simo and T. R. J. Hughes, *Computational Inelasticity*. New York: Springer-Verlag, 1998.
- [183] S. Reese and S. Govindjee, "A THEORY OF FINITE VISCOELASTICITY AND NUMERICAL ASPECTS," *Int. J. Solids Struct.*, vol. 35, pp. 3455–3481, 1998.

8 APPENDIX

8.1 Modulus and stress computation from rheology tests

For linking the material parameters (stress, σ , and strain, γ) to the rheometer data (torque, M , and rotation angle, θ), two geometry constants are used: the stress constant, K_σ , and the strain constant, K_γ . These constants depend on the geometry sample [167]. For parallel plates, they can be written as:

$$K_\sigma = \frac{\sigma}{M} = \frac{2}{\pi R^3} \quad 8.1$$

$$K_\gamma = \frac{\gamma}{\theta} = \frac{R}{h} \quad 8.2$$

where R and h are the radius and the thickness of the sample. On the torsion configuration, the geometry constants are defined as:

$$K_\sigma = \frac{\sigma}{M} = \frac{3 + 1.8\left(\frac{t}{w}\right)}{wt^2} 1000g_c \quad 8.3$$

$$K_\gamma = \frac{\gamma}{\theta} = \frac{t}{l} \left[1 - 0.378\left(\frac{t}{w}\right)^2 \right] \quad 8.4$$

where t and w are the thickness of the sample respectively, l is the tested length and g_c is the gravity constant.

Then, the complex shear modulus can be computed as:

$$G^* = \frac{\sigma}{\gamma} = \frac{K_\sigma M}{K_\gamma \theta} \quad 8.5$$

8.2 Digital Image Correlation

The tracking of the displacement field on the front face of the sample was possible by recording pictures of random speckle patterns (Figure 8.1 a)). Two cameras in stereo-correlation were used to account for out of plane displacement during testing. Pattern was generated by

spraying a black and white paint. The speckle size was quantified using ImageJ software [168] by assuming that the speckles had a circular shape. Figure 8.1 b) displays the statistical analysis of initial size distribution of the speckle patterns for both tensile and shear tests. The distribution of the speckle average size was similar for both geometries.

Digital Image Correlation (DIC) [19], [169] was carried out using VIC-3D version 7 for post-processing the strain fields. An “area of interest” (AOI) was defined on the visible face and then “meshed” with square elements (Figure 8.2 a)). The meshing allows tracking the changes in grey value pattern during the test. The displacement field was then post-processed to compute the strain field.

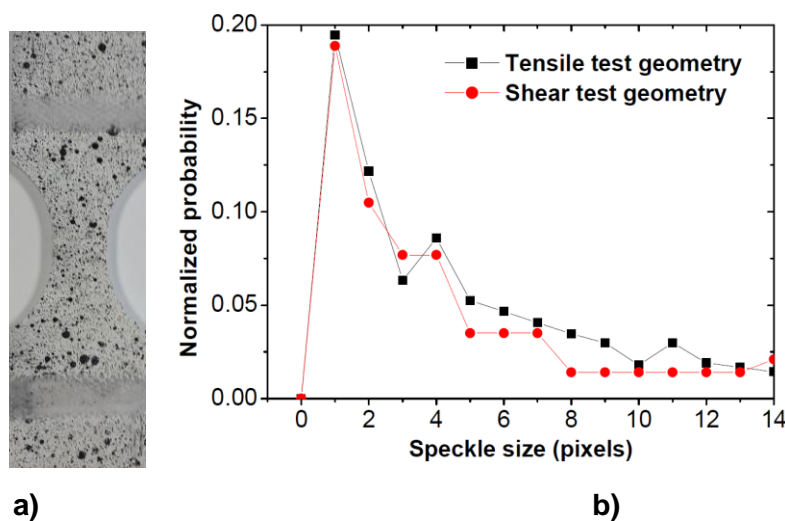


Figure 8.1: a) Tensile test specimen painted with speckle pattern and b) probability of the number of speckles as a function of their size for the tensile test samples (square symbols) and shear test samples (circle symbols).

The main parameters of the mesh are the subset size, the subset step and the filter size. The subset size defines the size of the area being used for pixel motion detection. The step size is related to the calculation periodicity. For instance, working with a subset size of 21 pixels and a step size of 3 pixels, leads to compute a 21x21 pixel area for every 3 pixels, obtaining data points for every 3 pixels. Additionally, VIC-3D uses the displacement field for post-processing the data to obtain true strain. The number of measurement is defined by the filter size. More precisely, the filter size, n , and the step size, m , define a smoothing area in $n*m$ pixels, where the deformation gradient is interpolated before being derived. The displacement data is then used to compute the true strain. We define ε_{yy} as the true strain in the loading direction and ε_{xx} as the true strain in the lateral direction. Figure 8.2 b) shows an example of the strain field in the loading direction.

To have a good compromise between accuracy and computational time, a mesh sensitivity study was performed by changing values of the correlation parameters (subset, step and filter size) in a similar manner as proposed by other authors [170]–[173]. The analysis was performed from the pictures recorded at the maximum strain in the exact same region, indicated by a square in Figure 8.2 b).

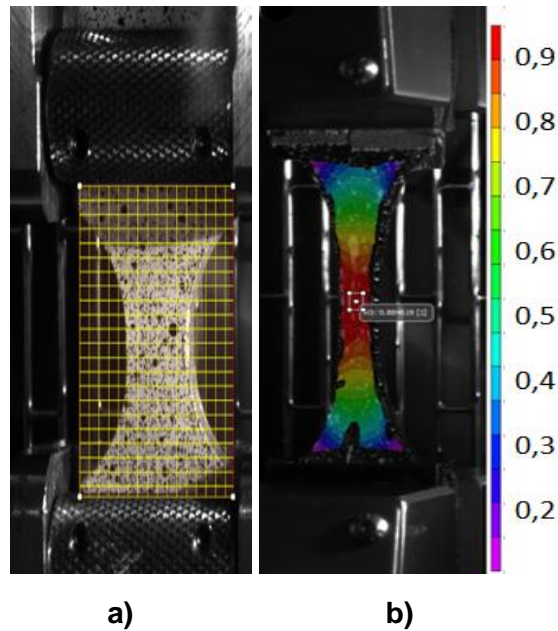


Figure 8.2: (a) Mesh on a speckle sample for the Digital Image Correlation (b) True strain field in the loading direction obtained by post-processing the displacement field.

The values of the longitudinal strain as a function of the subset for different step size are presented in Figure 8.3 a). These results suggest that true strain remains mainly constant, especially up to 35 pixels. However, the strain level starts to be underestimated when the step size is higher than three pixels. The effect of the step size for different subset is showed in Figure 8.3 b). This indicates that strain remains nearly constant up to a step size of 3 pixels, and then decreases, which is related to a loss of accuracy. In the following, a subset size of 21 pixels will be used.

The effect of the filter size is displayed in Figure 8.3 c) for different step sizes. The strain decreases by increasing the filter size, which is consistent with other studies [170], [174]. When plotted as a function of the smoothing size (filter size*step size), all the data merge into a master curve (Figure 8.3 d)). Thus, the combination of large step size with small filter size or small step size with large strain filter leads to an equivalent estimation of the strain. In a reasonable range of smoothing size, the strain remains constant. However, about a critical value of 100 pixels, the strain value reduces drastically. This reveals that, independently of the step and filter size, the smoothing size is the most influential parameter. A low filter size could generate noise during the

computing of the strain field. Thus, an intermediate value of 15 has been chosen. Regarding the step size, its value should not be too low as the analysis time would increase. The step size chosen was 2 pixels giving a smoothing size of 30 pixels. The sensitivity of the lateral strain on the VIC analysis parameters has also been studied leading to equivalent results to those presented in Figure 8.3.

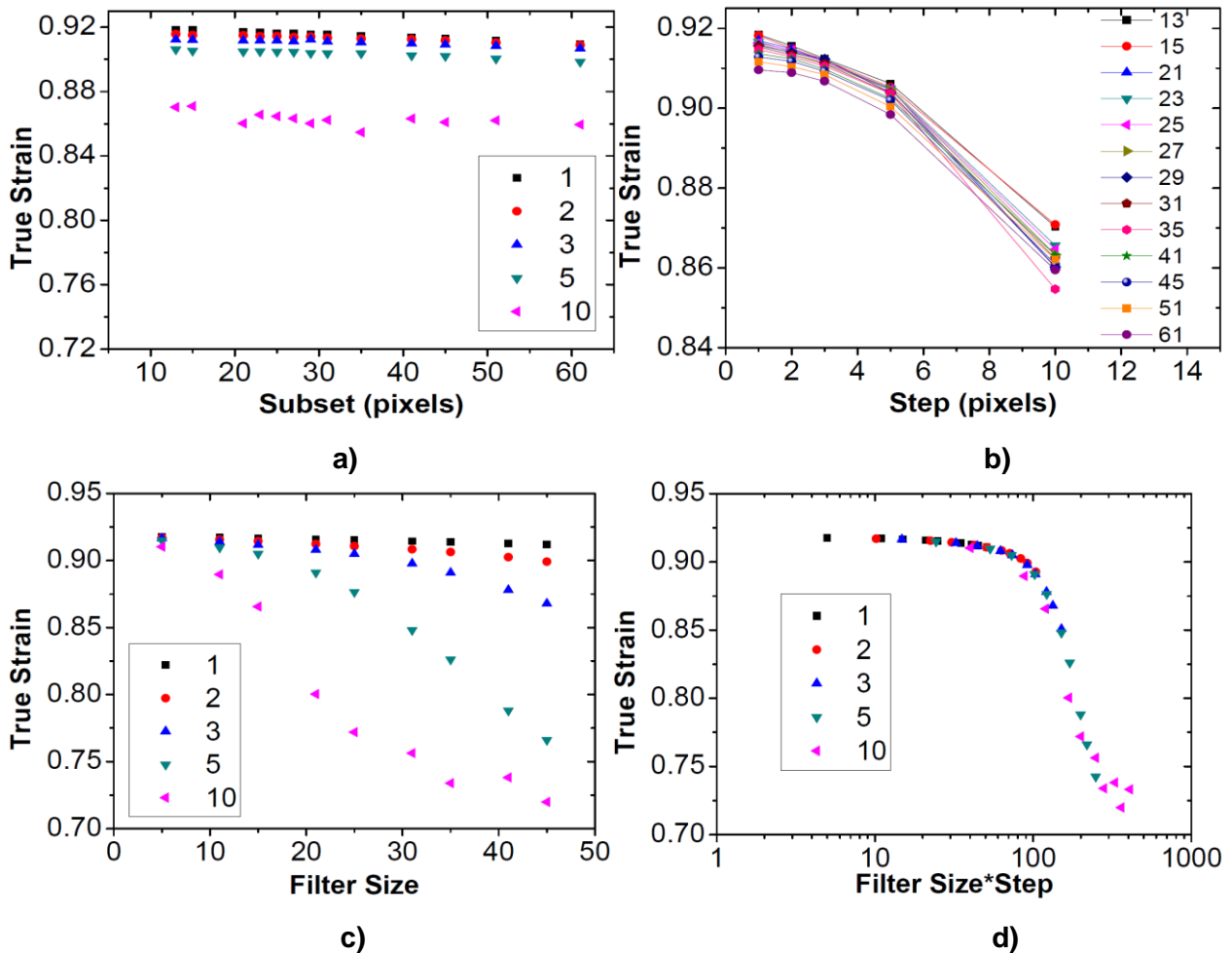


Figure 8.3: a) True strain as a function of the subset size for different steps at maximum displacement. Filter size value is equal to 15. b) True strain as a function of the step size for different subsets at maximum displacement. Filter size value is equal to 15. c) True strain versus filter size for different steps. Subset size value is equal to 21 pixels. d) True strain as a function of the smoothing size for different steps at maximum displacement. Subset size value is equal to 21 pixels.

8.3 Estimation of the stress correction factor, C_s

For estimating the correction stress factor on Iosipescu tests, finite element calculations were carried out on ABAQUS 6.14-1. Figure 8.4 displays the mesh and boundary conditions used to simulate the shear tests. The sample is modelled using a 10-node quadratic tetrahedron with hybrid formulation and constant pressure elements (ABAQUS C3D10H). This choice was based on the interest of simulating the incompressibility of the material when deformed. All the nodes along the left side are fixed in all three directions, while an exponential displacement profile is

applied to all the nodes along the right side of the sample. A mesh sensitivity study was performed to determine the optimal mesh size. For doing this, the local shear stress was addressed for different mesh sizes. This is depicted in Figure 8.5. An element of dimension “1.5 mm” was chosen since it was the best compromise between accuracy and computational time.

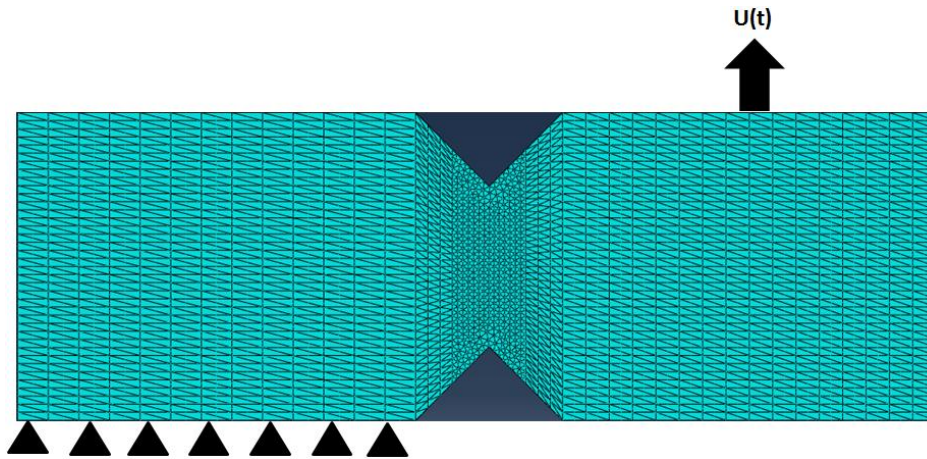


Figure 8.4: Mesh and boundary conditions of Iosipescu shear tests simulations.

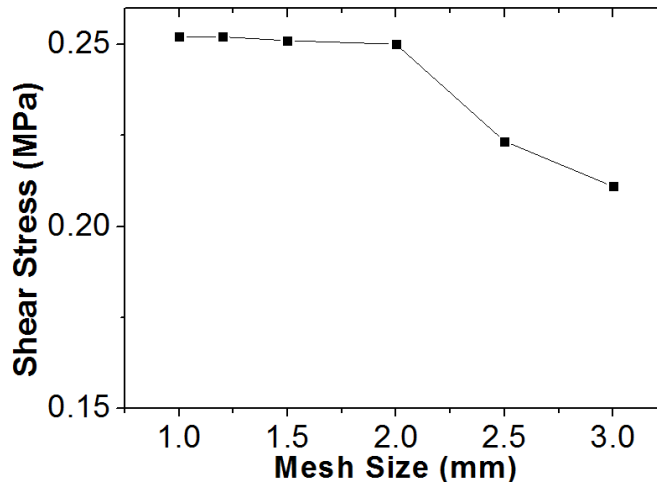


Figure 8.5: Mesh sensitivity study.

For the hyperelastic material, we employed the Mooney-Rivlin model [121], [122] considering the material constants as: $C_1=0.188$ MPa, $C_2=0.157$ MPa and $D_1=1 \times 10^{-5}$. The first two parameters were empirically determined from experimental results, and D_1 was almost zero since we assumed incompressibility. For the elastoplastic material, we considered a Young Modulus of 22.1 MPa, a Poisson modulus of 0.499 and the plastic part was identified experimentally. A comparison between the experimental results and the finite element computations is shown in Figure 8.6.

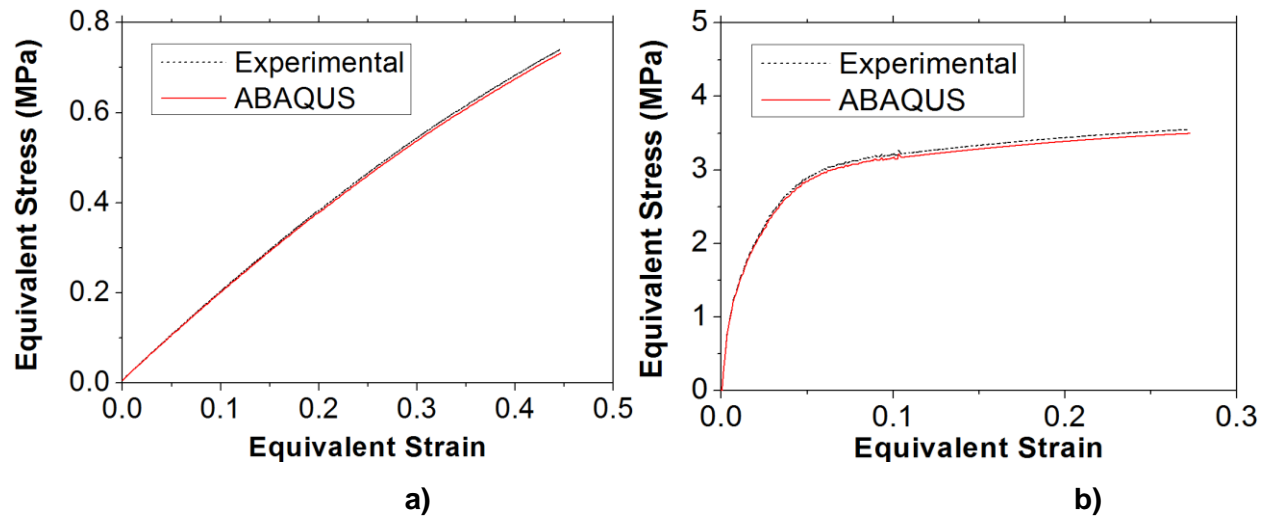


Figure 8.6: Stress-strain curves for a hyperelastic PMMA, a), and a elastoplastic PMMA, b).

Result for the hyperelastic material is shown in Figure 8.7. A gradient of stress can be observed, with a stress concentration in the midsection of the sample between the notches. As displayed in the Figure, a local element is extracted to obtain the local shear stress, τ_{xy} . Additionally, an average value of the stress is computed by determining the mean value of each element indicated in the dotted line. Finally, using the definition of the correction stress factor (Equation 2.13), it was possible to estimate this value. The same protocol was used for the elastoplastic material.

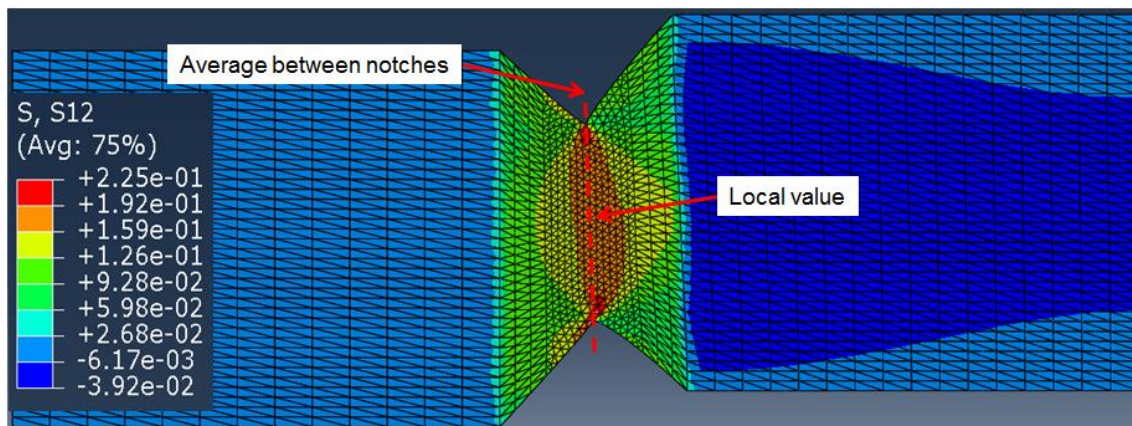


Figure 8.7: Equivalent stress contour of the deformed hyperelastic specimen.

8.4 Piecewise function for describing shift factors on PMMA 3500

$$a_{T_j/T_0} = \begin{cases} \frac{-C_1(T-T_0)}{C_2+(T-T_0)} & T \in [100;170] \\ -0.122T + 17.449 & \text{if } T \in [170;190] \\ \exp\left(\frac{Q_{plateau}}{R}\left(\frac{1}{T} - \frac{1}{T_0}\right)\right) & T \in [190;240] \end{cases} \quad 8.6$$

8.5 Experimental validation of the equivalent strain rate for macroscopic load-unload tensile tests on PMMA 93 and PMMA 120

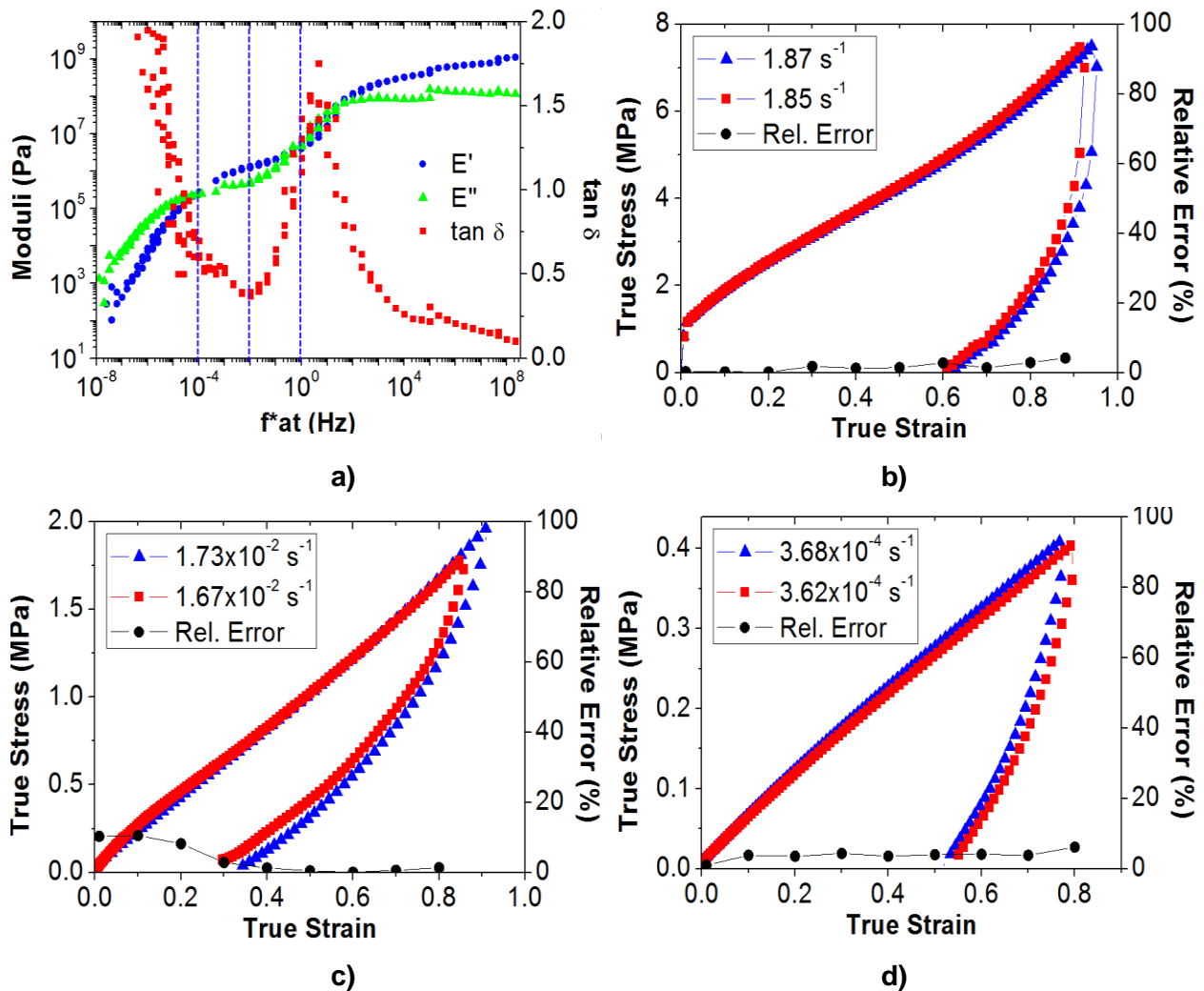


Figure 8.8: Master curve and macroscopic true tensile curves for PMMA 93 at a reference temperature of 130 °C. a) E' , E'' and $\tan \delta$ master curves. b) $\dot{\epsilon}_{eq} \approx 10^0 \text{ s}^{-1}$. c) $\dot{\epsilon}_{eq} \approx 10^{-2} \text{ s}^{-1}$. d) $\dot{\epsilon}_{eq} \approx 10^{-4} \text{ s}^{-1}$.

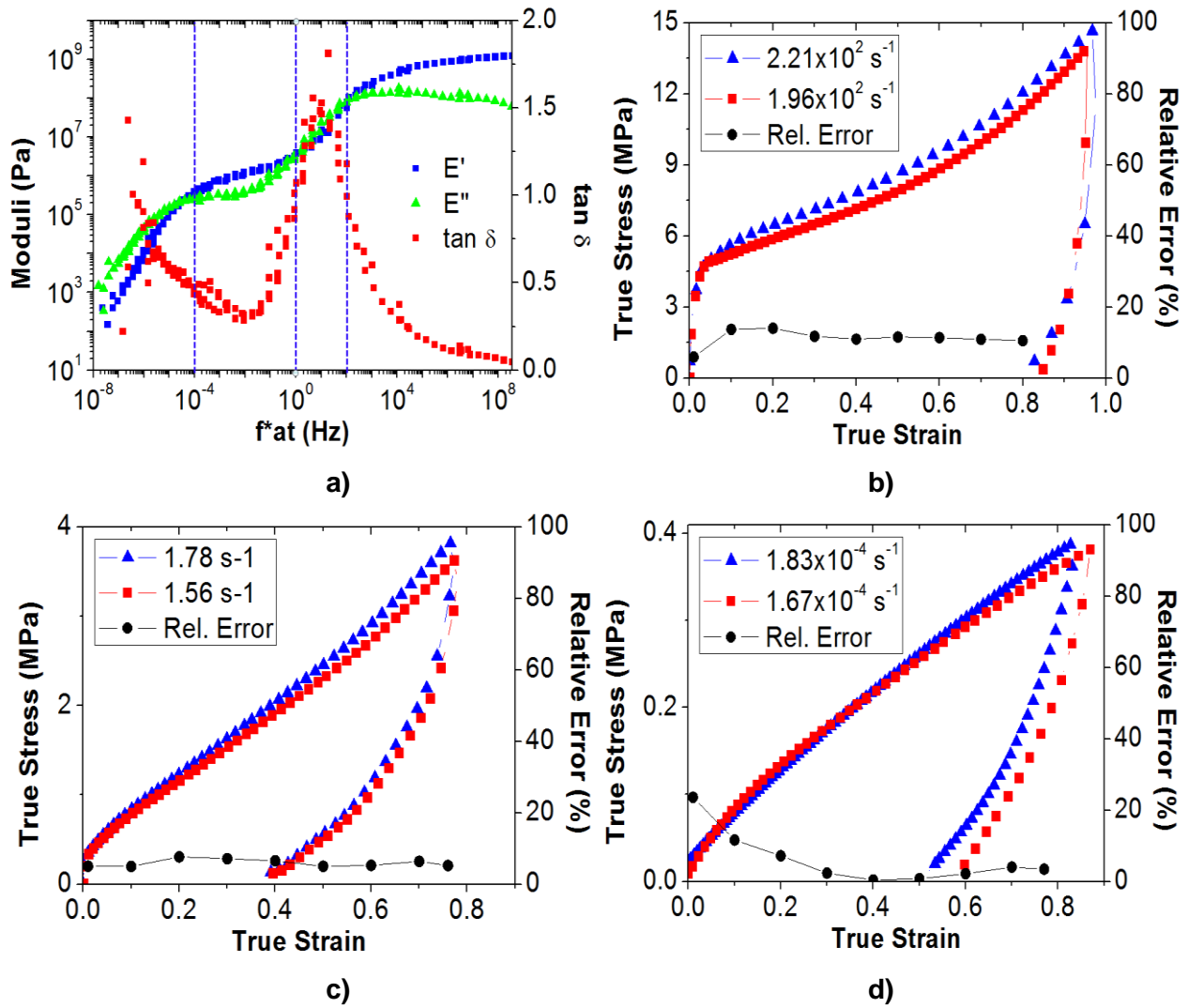


Figure 8.9: Master curve and macroscopic true tensile curves for PMMA 120 at a reference temperature of 130 °C. a) E' , E'' and $\tan \delta$ master curves. b) $\dot{\epsilon}_{eq} \approx 10^2 \text{ s}^{-1}$. c) $\dot{\epsilon}_{eq} \approx 10^0 \text{ s}^{-1}$. d) $\dot{\epsilon}_{eq} \approx 10^{-4} \text{ s}^{-1}$.

8.6 Edward-Vilgis model in function of the principal stretch ratios

$$\psi_v^k \left(\lambda_1, \lambda_2, \lambda_3, N_c, N_s, \eta, \alpha^2 \right) = (1/2)k\theta \left[\begin{array}{l} N_c \underbrace{\left(\ln(1 - \alpha^2) + \frac{\sum_{i=1}^3 (1 - \alpha^2) \lambda_i^2}{(1 - \alpha^2 \sum_{i=1}^3 \lambda_i^2)} \right)}_{w_c} \\ + N_s \underbrace{\left(\sum_{i=1}^3 \left(\frac{\lambda_i^2 (1 + \eta)(1 - \alpha^2)}{(1 + \eta \lambda_i^2)(1 - \alpha^2 \sum_{i=1}^3 \lambda_i^2)} + \ln(1 + \eta \lambda_i^2) \right) - \ln(1 - \alpha^2 \sum_{i=1}^3 \lambda_i^2) \right)}_{w_s} \end{array} \right] \quad 8.7$$

where $\lambda_{i, i=\{1,3\}}$ are the principal extension, κ is the Boltzmann's constant, θ is the absolute temperature, N_c is the density of crosslinks per unit volume, N_s is the density of entanglements per unit volume, α is the chain extensibility and η is related to the degree of mobility of the slip links.

8.7 3D Constitutive modelling

The 3D constitutive modelling described next is a summary of the work presented by Gehring et al. [25]

Kinematics

In standard continuum mechanics, we can consider “ X ” an arbitrary material point in a body in a reference configuration, B_0 . The motion of B is described through the mapping $x=y(X,t)$ via a deformation gradient, F , velocity, v , and velocity gradient, l , defined by:

$$\begin{aligned} \mathbf{F} &= \nabla \mathbf{y}, \\ \mathbf{v} &= \dot{\mathbf{y}}, \\ \mathbf{l} &= \text{grad } \mathbf{v} = \dot{\mathbf{F}}\mathbf{F}^{-1}. \end{aligned} \quad 8.8$$

The total deformation gradient can be decomposed into uncoupled volumetric and deviatoric parts [175], [176]. For this purpose, we introduce a volumetric and deviatoric (volume-preserving) multiplicative split of \mathbf{F} :

$$\mathbf{F} = J^{1/3} \bar{\mathbf{F}}, \det \bar{\mathbf{F}} = 1, \det \mathbf{F} = J (J > 0) \quad 8.9$$

Similar to Lee [177], Sidoroff [178], Lubliner [179], Boyce et al. [118], Arruda et al. [129], Dupaix et al. [119] and more recently Andriyana et al. [180], we assumed that the kinematics of the problem are based on a multiplicative decomposition of the volume preserving deformation gradient, $\bar{\mathbf{F}}$, into elastic and inelastic components for each branch:

$$\bar{\mathbf{F}} = \bar{\mathbf{F}}_1^e \bar{\mathbf{F}}_1^v = \bar{\mathbf{F}}_2^e \bar{\mathbf{F}}_2^v, \quad 8.10$$

where $(\bar{\mathbf{F}}_k^e)_{k=\{1,2\}}$ represents the elastic part due to reversible elastic mechanisms, such as conformational changes due to polymer chain rotations. On the other hand, $(\bar{\mathbf{F}}_k^v)_{k=\{1,2\}}$ is related to the inelastic part due to irreversible mechanisms such as chain slippage. The decomposition described in Equations 8.9 and 8.10 is summarized in Figure 8.10

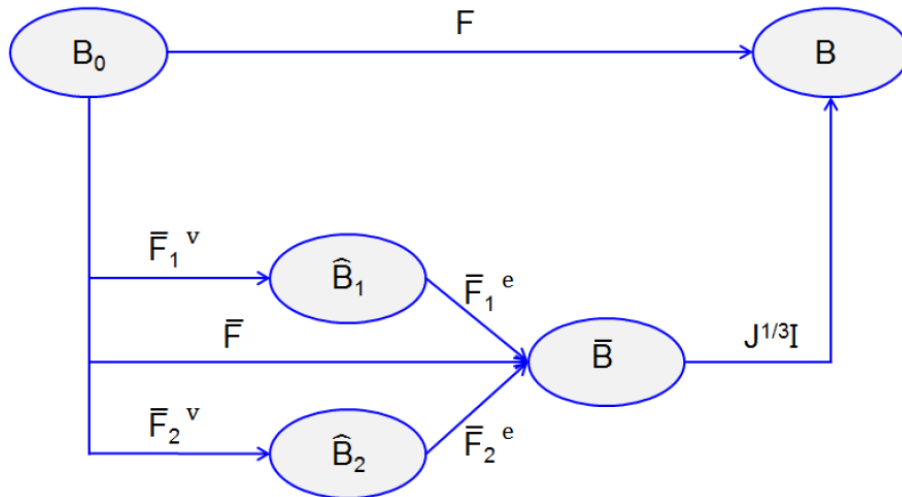


Figure 8.10: Schematic representation of the deformation gradient decomposition.

Strain notion can be introduced as the right Cauchy Green tensor, \mathbf{C} , and left Cauchy Green tensor, \mathbf{b} , which is defined as:

$$\mathbf{C} = \mathbf{F}^T \mathbf{F} = J^{2/3} \bar{\mathbf{C}} \quad 8.11$$

$$\mathbf{b} = \mathbf{F} \mathbf{F}^T = J^{2/3} \bar{\mathbf{b}} \quad 8.12$$

Combining Equations 8.10 and 8.11, the right Cauchy Green tensor can be written as:

$$\bar{\mathbf{C}}_k^e = \bar{\mathbf{F}}_k^{eT} \bar{\mathbf{F}}_k^e = (\bar{\mathbf{F}}_k^v)^{-T} \bar{\mathbf{C}} (\bar{\mathbf{F}}_k^v)^{-1}, \quad k = \{1,2\} \quad 8.13$$

Additionally, the velocity gradient defined in Equation 8.8 can be rewritten as:

$$\bar{\mathbf{L}} = \bar{\mathbf{L}}_k^e + \bar{\mathbf{F}}_k^e \bar{\mathbf{L}}_k^v \bar{\mathbf{F}}_k^{e-1}, \quad k = \{1,2\} \quad 8.14$$

where:

$$\bar{\mathbf{L}}_k^v = \dot{\bar{\mathbf{F}}}_k^v \bar{\mathbf{F}}_k^{v-1}, \quad k = \{1,2\} \quad 8.15$$

The velocity gradient, l , can be also decomposed into its symmetric part, d , corresponding to the rate of deformation tensor, and its antisymmetric part (skew), w , which is related to the rate of rotation tensor: The deviatoric velocity gradient, \bar{L} , can be then defined as:

$$\bar{\mathbf{L}} = \bar{\mathbf{D}} + \bar{\mathbf{W}} \quad 8.16$$

Assuming that the flow is irrotational in the two branches, $\bar{\mathbf{W}}_1^v = \bar{\mathbf{W}}_2^v = 0$, we can say that the velocity gradients defined in Equation 8.14 can be expressed as:

$$\begin{aligned} \bar{\mathbf{L}}_1^v &= \bar{\mathbf{D}}_1^v \\ \bar{\mathbf{L}}_2^v &= \bar{\mathbf{D}}_2^v \end{aligned} \quad 8.17$$

Thermodynamics and stress definition

After presenting the kinematic framework, we will precise the stresses. The Cauchy or true stress tensor, σ , can be written as [181]:

$$\boldsymbol{\sigma} = \mathbf{J}^{-1} \boldsymbol{\tau} = \mathbf{J}^{-1} \mathbf{F} \mathbf{S} \mathbf{F}^T \quad 8.18$$

where $\boldsymbol{\tau}$ is the Kirchhoff stress and \mathbf{S} is the second Piola-Kirchhoff stress in the configuration B_0 . \mathbf{S} will be determined from the thermodynamic framework described in the next Section

Using the second law of thermodynamic, we can obtain the internal dissipation inequality given by:

$$\mathbf{S} : \frac{1}{2} \dot{\mathbf{C}} - \dot{\psi} \geq 0 \quad 8.19$$

where ψ is the Helmholtz free energy per unit volume and can be also referred as the strain energy function.

The Helmholtz free energy function is assumed to be a function of a number of state variables: the right elastic Cauchy-Green Tensor, $(\bar{\mathbf{C}}_k^e)_{k=\{1,2\}}$, and a set internal state variables (ISVs), $\bar{\Pi}$:

$$\psi_v = \psi_v \left((\bar{\mathbf{C}}_k^e)_{k=\{1,2\}}, \bar{\Pi} \right) \quad 8.20$$

As it was mentioned before, the non-Gaussian statistic approach of Edward and Vilgis [23] (see Equation 5.3) is chosen in this study. Let's remember that the free energy is decomposed into the contribution coming from the crosslinks networks and the entangled ones:

$$\psi(\bar{\mathbf{C}}^e, \eta, \theta) = \frac{1}{2} k\theta (N_c \psi_c(\bar{\mathbf{C}}^e, \alpha) + N_s \psi_s(\bar{\mathbf{C}}^e, \eta)) \quad 8.21$$

Then, we decomposed the free energy into volumetric and deviatoric parts:

$$\psi_v = \sum_{k=1}^2 \bar{\psi}_v^k(\bar{\mathbf{C}}_k^e, \bar{\eta}_k, N_s^k, \bar{\alpha}_k) + \hat{\psi}_J(J) \quad 8.22$$

where $\bar{\psi}_v^k$ is the isochoric contribution of the branch k to the free energy ψ_v^k and $\hat{\psi}_J(J)$ represents the volumetric part [182].

Thus, the time derivative of ψ_v , needed to solve the inequality on 8.19 can be computed as:

$$\dot{\Psi}_v = \sum_{k=1}^2 \left(\frac{\partial \bar{\Psi}_v^k}{\partial \bar{\mathbf{C}}_k^e} : \dot{\bar{\mathbf{C}}}_k^e + \frac{\partial \bar{\Psi}_v^k}{\partial \bar{\eta}_k} \dot{\bar{\eta}}_k + \frac{\partial \bar{\Psi}_v^k}{\partial \bar{N}_s^k} \dot{\bar{N}}_s^k + \frac{\partial \bar{\Psi}_v^k}{\partial \bar{\alpha}_k} \dot{\bar{\alpha}}_k \right) + \frac{\partial \hat{\Psi}_J(J)}{\partial J} \dot{J} \quad 8.23$$

Based on [181]–[183], we can use Equation 8.13 and accounts also for the symmetry of $\bar{\mathbf{C}}_k^e$, $\frac{\partial \bar{\Psi}_v^k}{\partial \bar{\mathbf{C}}_k^e}$ and $\bar{\mathbf{D}}_k^v$ to develop the first term of Equation 8.23:

$$\frac{\partial \bar{\Psi}_v^k}{\partial \bar{\mathbf{C}}_k^e} : \dot{\bar{\mathbf{C}}}_k^e = (\mathbf{F}_k^v)^{-1} \left(\frac{\partial \bar{\Psi}_v^k}{\partial \bar{\mathbf{C}}_k^e} \right) (\mathbf{F}_k^v)^{-T} : \dot{\bar{\mathbf{C}}}_k^e - \bar{\mathbf{C}}_k^e \left(2 \frac{\partial \bar{\Psi}_v^k}{\partial \bar{\mathbf{C}}_k^e} \right) : \bar{\mathbf{D}}_k^v \quad 8.24$$

Then, we can obtain from the inequality in Equation 8.19 that:

$$\dot{\bar{\mathbf{C}}} = 2 \left(\frac{\partial \bar{\mathbf{C}}}{\partial \mathbf{C}} \right) : \dot{\mathbf{C}} = 2J^{-2/3} \mathbf{P}^T : \dot{\mathbf{C}}, \quad \dot{J} = J\mathbf{C}^{-1} : \dot{\mathbf{C}} \quad 8.25$$

$$\mathbf{P}^T = \mathbf{I} - \frac{1}{3} \mathbf{C} \otimes \mathbf{C}^{-1} \quad 8.26$$

Replacing Equations 8.23, 8.24 and 8.25 into the dissipation inequality in Equation 8.19, we can obtain:

$$\begin{aligned} & \left(\mathbf{S} - J^{-2/3} \mathbf{DEV} \left[\sum_{k=1}^2 (\mathbf{F}_k^v)^{-1} \left(2 \frac{\partial \bar{\Psi}_v^k}{\partial \bar{\mathbf{C}}_k^e} \right) (\mathbf{F}_k^v)^{-T} \right] - \frac{\partial \hat{\Psi}_J(J)}{\partial J} J\mathbf{C}^{-1} \right) : \frac{1}{2} \dot{\mathbf{C}} \\ & + \sum_{k=1}^2 \left[\bar{\mathbf{C}}_k^e \sum \left(2 \frac{\partial \bar{\Psi}_v^k}{\partial \bar{\mathbf{C}}_k^e} \right) : \bar{\mathbf{D}}_k^v - \left(\frac{\partial \bar{\Psi}_v^k}{\partial \bar{\eta}_k} \dot{\bar{\eta}}_k \right) - \left(\frac{\partial \bar{\Psi}_v^k}{\partial \bar{N}_s^k} \dot{\bar{N}}_s^k \right) - \left(\frac{\partial \bar{\Psi}_v^k}{\partial \bar{\alpha}_k} \dot{\bar{\alpha}}_k \right) \right] \geq 0 \end{aligned} \quad 8.27$$

with:

$$\mathbf{DEV}(\bullet) = (\bullet) - \frac{1}{3} [(\bullet) : \mathbf{C}] \mathbf{C}^{-1} \quad 8.28$$

For guaranteeing that the process respects the thermodynamic framework, we can obtain from the inequality in Equation 8.27 that the constitutive equation of the second Piola-Kirchhoff stress is:

$$\mathbf{S} = J^{-2/3} \mathbf{DEV}(\bar{\mathbf{S}}) + pJ\mathbf{C}^{-1} \quad 8.29$$

with:

$$\bar{\mathbf{S}} = \sum_{k=1}^2 (\mathbf{F}_k^v)^{-1} \left(2 \frac{\partial \bar{\Psi}_v^k}{\partial \bar{\mathbf{C}}_k^e} \right) (\mathbf{F}_k^v)^{-T}, \quad p = \frac{\partial \hat{\Psi}_J(J)}{\partial J} \quad 8.30$$

Then, the dissipation inequality stands as:

$$\sum_{k=1}^2 \left[\bar{\mathbf{C}}_k^e \sum \left(2 \frac{\partial \bar{\Psi}_v^k}{\partial \bar{\mathbf{C}}_k^e} \right) : \bar{\mathbf{D}}_k^v - \left(\frac{\partial \bar{\Psi}_v^k}{\partial \bar{\eta}_k} \dot{\bar{\eta}}_k \right) - \left(\frac{\partial \bar{\Psi}_v^k}{\partial N_s^k} \dot{N}_s^k \right) - \left(\frac{\partial \bar{\Psi}_v^k}{\partial \bar{\alpha}_k} \dot{\bar{\alpha}}_k \right) \right] \geq 0 \quad 8.31$$

By introducing the Mandel stress, $\bar{\mathbf{M}}_k = \bar{\mathbf{C}}_k^e \left(2 \frac{\partial \bar{\Psi}_v^k}{\partial \bar{\mathbf{C}}_k^e} \right)$, on each branch:

$$\underbrace{\bar{\mathbf{M}}_k : \bar{\mathbf{D}}_k^v}_{\text{plastic dissipation}} - \underbrace{\left(\frac{\partial \bar{\Psi}_v^k}{\partial \bar{\eta}_k} \dot{\bar{\eta}}_k + \frac{\partial \bar{\Psi}_v^k}{\partial N_s^k} \dot{N}_s^k + \frac{\partial \bar{\Psi}_v^k}{\partial \bar{\alpha}_k} \dot{\bar{\alpha}}_k \right)}_{\text{internal work}} \geq 0, \quad k = \{1, 2\} \quad 8.32$$

The first term represents the plastic work dissipated from irreversible mechanisms during the plastic flow. The second term concerns to the internal work associated with the polymer network reorganization, which is related to topological or microstructural evolutions.

Use of the constitutive model for defining the stress

To compute the Cauchy stress tensor, we need to express the additive strain energy function showed in Equation 8.23. For the deviatoric part, an Edward and Vilgis energy depending on invariant (see Equation 5.3) was chosen:

$$\begin{cases} \bar{I}_1^k = \text{tr}(\bar{\mathbf{C}}_k^e) \\ \bar{I}_2^k = \frac{1}{2} \left[\bar{I}_1^{k2} - \text{trace}(\bar{\mathbf{C}}_k^{e2}) \right] \\ \bar{I}_3^k = \det(\bar{\mathbf{C}}_k^e) \end{cases} \quad 8.33$$

For an incompressible material, $\bar{I}_3^k = \det(\bar{\mathbf{C}}_k^e) = 1$, the free energy function would be just a function of $(\bar{I}_1^k, \bar{I}_2^k)$.

On the other hand, the volumetric term of the free energy is chosen to be as proposed by Simo and Hughes [182]:

$$\hat{\Psi}_{J^e} = \frac{1}{2} K_B \left[\frac{1}{2} (J^{e2} - 1) - \ln J^e \right], \quad 8.34$$

where K_B is the elastic bulk modulus.

Then, the stress $\bar{\mathbf{S}}$ in Equation 8.30 can be written as:

$$\begin{aligned} \bar{\mathbf{S}} &= \sum_{k=1}^2 (\mathbf{F}_k^v)^{-1} \left(2 \frac{\partial \bar{\Psi}_v^k}{\partial \bar{\mathbf{C}}_k^e} \right) (\mathbf{F}_k^v)^{-T} \\ &= \sum_{k=1}^2 (\mathbf{F}_k^v)^{-1} \left(2 \sum_{i=1}^2 \frac{\partial \bar{\Psi}_v^k(\bar{\mathbf{I}}_i^k)}{\partial \bar{\mathbf{I}}_i^k} \frac{\partial \bar{\mathbf{I}}_i^k}{\partial \bar{\mathbf{C}}_k^e} \right) (\mathbf{F}_k^v)^{-T} \end{aligned} \quad 8.35$$

with:

$$\begin{cases} \frac{\partial \bar{\mathbf{I}}_1^k}{\partial \bar{\mathbf{C}}_k^e} = \mathbf{I} \\ \frac{\partial \bar{\mathbf{I}}_2^k}{\partial \bar{\mathbf{C}}_k^e} = \bar{\mathbf{I}}_1^k \mathbf{I} - \bar{\mathbf{C}}_k^e \end{cases}, \quad 8.36$$

and:

$$p = \frac{1}{2} K_B (J - 1/J), \quad 8.37$$

By substituting Equations 8.35, 8.37 into 8.29 and then in Equation 8.18, we can express the Cauchy stress as:

$$\begin{aligned} \boldsymbol{\sigma} &= J^{-1} \mathbf{F} \mathbf{S} \mathbf{F}^T = J^{-1} \left(\text{dev}(\bar{\mathbf{F}} \bar{\mathbf{S}} \bar{\mathbf{F}}^T) + p \mathbf{I} \right) \\ &= J^{-1} (\boldsymbol{\tau}_{\text{dev}} + \boldsymbol{\tau}_{\text{vol}}), \end{aligned} \quad 8.38$$

with:

$$\boldsymbol{\tau}_{\text{dev}} = \sum_{k=1}^2 2 \text{dev} \left(\left(\frac{\partial \bar{\Psi}_v^k}{\partial \bar{\mathbf{I}}_1^k} + \frac{\partial \bar{\Psi}_v^k}{\partial \bar{\mathbf{I}}_2^k} \bar{\mathbf{I}}_1^k \right) \bar{\mathbf{b}}_k^e - \frac{\partial \bar{\Psi}_v^k}{\partial \bar{\mathbf{I}}_2^k} \bar{\mathbf{b}}_k^{e2} \right), \quad 8.39$$

$$\boldsymbol{\tau}_{\text{vol}} = \frac{1}{2} K_B (J^2 - 1) \mathbf{I}, \quad 8.40$$

and:

$$\text{dev}(\bullet) = (\bullet) - \frac{1}{3} [(\bullet) : \mathbf{I}] \mathbf{I}, \quad 8.41$$

The terms $\frac{\partial \bar{\Psi}_v^k}{\partial \bar{I}_1^k}$ and $\frac{\partial \bar{\Psi}_v^k}{\partial \bar{I}_2^k}$ are defined in Appendix 8.8.

Inelastic flow rules

To complete the description of the constitutive equations, we need to define the material viscous flow in order to describe the kinetic of the inelastic mechanisms. This will allow addressing and updating the kinematics (see Equations 8.13-8.15) during the deformation of the polymer.

The velocity gradient from the inelastic part can be deduced from the energy inequality (Equation 8.32):

$$\phi_{\text{int}} = \bar{\mathbf{M}}_k : \bar{\mathbf{D}}_k^v - \left(\frac{\partial \bar{\Psi}_v^k}{\partial \bar{\eta}_k} \dot{\bar{\eta}}_k + \frac{\partial \bar{\Psi}_v^k}{\partial \bar{N}_s^k} \dot{\bar{N}}_s^k + \frac{\partial \bar{\Psi}_v^k}{\partial \bar{\alpha}_k} \dot{\bar{\alpha}}_k \right) \geq 0, \quad k = \{1,2\} \quad 8.42$$

Assuming that the internal work related to the polymer molecular arrangement is proportional to the inelastic work:

$$\left(\frac{\partial \bar{\Psi}_v^k}{\partial \bar{\eta}_k} \dot{\bar{\eta}}_k + \frac{\partial \bar{\Psi}_v^k}{\partial \bar{N}_s^k} \dot{\bar{N}}_s^k + \frac{\partial \bar{\Psi}_v^k}{\partial \bar{\alpha}_k} \dot{\bar{\alpha}}_k \right) = (1 - \beta_k) \bar{\mathbf{M}}_k : \bar{\mathbf{D}}_k^v, \quad k = \{1,2\} \quad 8.43$$

where β_k is associated to the coefficient of Taylor-Quinney. Equation 8.42 is then defined as:

$$\phi_{\text{int}} = \beta_k \bar{\mathbf{M}}_k : \bar{\mathbf{D}}_k^v, \quad k = \{1,2\} \quad 8.44$$

Therefore, the rate of inelastic deformation can be deduced from Equations 8.42 and 8.44 [68] as:

$$\bar{\mathbf{D}}_k^v = \frac{3}{2} \frac{1}{(1 - \beta_k)} \frac{1}{\|dev(\bar{\mathbf{M}}_k)\|} \left(\frac{\partial \psi_v^k}{\partial \bar{\eta}_k} \dot{\bar{\eta}}_k + \frac{\partial \psi_v^k}{\partial N_s^k} \dot{N}_s^k + \frac{\partial \psi_v^k}{\partial \alpha_k^2} \dot{\alpha}_k^2 \right) \left(\frac{dev(\bar{\mathbf{M}}_k)}{\|dev(\bar{\mathbf{M}}_k)\|} \right), k = [1,2] \quad 8.45$$

Then, the evolution for \mathbf{F}_k^v can be described by:

$$\dot{\mathbf{F}}_k^v = \bar{\mathbf{D}}_k^v \mathbf{F}_k^v, \quad \bar{\mathbf{D}}_k^v = \dot{\bar{\gamma}}_k^v \bar{\mathbf{N}}_k^v, \quad k = \{1,2\} \quad 8.46$$

where $\bar{\mathbf{N}}_k^v = dev(\bar{\mathbf{M}}_k) / \|dev(\bar{\mathbf{M}}_k)\|$ is the direction of viscous flow, and $\dot{\bar{\gamma}}_k^v$ is the viscous shear strain rate. The terms $\frac{\partial \bar{\psi}_v^k}{\partial \bar{\eta}_k}$, $\frac{\partial \bar{\psi}_v^k}{\partial N_s^k}$ and $\frac{\partial \bar{\psi}_v^k}{\partial \alpha_k^2}$ are defined in Appendix 8.8.

8.8 Strain energy function derivatives

$$\frac{\partial \bar{\psi}_v^k}{\partial \bar{I}_1^k} = \frac{1}{2} \left[N_c^k \left(\frac{1 - 2\alpha_k^2 - \alpha_k^4 \bar{I}_1^k}{(1 - \alpha_k^2 \bar{I}_1^k)^2} \right) + N_s^k \left(- \frac{\alpha_k^2 (1 + \bar{\eta}_k) (1 - \alpha_k^2)}{(1 - \alpha_k^2 \bar{I}_1^k)^2} \frac{\bar{I}_1^k + 2\bar{\eta}_k \bar{I}_2^k + 3\bar{\eta}_k^2 \bar{I}_3^k}{1 + \bar{\eta}_k \bar{I}_1^k + \bar{\eta}_k^2 \bar{I}_2^k + \bar{\eta}_k^3 \bar{I}_3^k} + \frac{(1 + \bar{\eta}_k) (1 - \alpha_k^2)}{(1 - \alpha_k^2 \bar{I}_1^k)} \left(\frac{1 - \bar{\eta}_k^2 \bar{I}_2^k - 2\bar{\eta}_k^3 \bar{I}_3^k}{(1 + \bar{\eta}_k \bar{I}_1^k + \bar{\eta}_k^2 \bar{I}_2^k + \bar{\eta}_k^3 \bar{I}_3^k)^2} \right) + \frac{-\alpha_k^2}{1 - \alpha_k^2 \bar{I}_1^k} + \frac{\bar{\eta}_k}{1 + \bar{\eta}_k \bar{I}_1^k + \bar{\eta}_k^2 \bar{I}_2^k + \bar{\eta}_k^3 \bar{I}_3^k} \right) \right], \quad 8.47$$

$$\frac{\partial \bar{\psi}_v^k}{\partial \bar{I}_2^k} = \frac{1}{2} N_s^k \left(\frac{(1 + \bar{\eta}_k) (1 - \alpha_k^2)}{(1 - \alpha_k^2 \bar{I}_1^k)} \left(\frac{2\bar{\eta}_k (1 + \bar{\eta}_k \bar{I}_1^k + \bar{\eta}_k^2 \bar{I}_2^k + \bar{\eta}_k^3 \bar{I}_3^k) - \bar{\eta}_k^2}{(1 + \bar{\eta}_k \bar{I}_1^k + \bar{\eta}_k^2 \bar{I}_2^k + \bar{\eta}_k^3 \bar{I}_3^k)^2} \right) + \frac{\bar{\eta}_k^2}{(1 + \bar{\eta}_k \bar{I}_1^k + \bar{\eta}_k^2 \bar{I}_2^k + \bar{\eta}_k^3 \bar{I}_3^k)} \right), \quad 8.48$$

$$\frac{\partial \bar{\psi}_v^k}{\partial \bar{\eta}_k} = \frac{1}{2} N_s^k \left[\begin{aligned} & \left(\frac{(1-\alpha_k^2) \left((\bar{I}_1^k + 2\bar{\eta}_k \bar{I}_2^k + 3\bar{\eta}_k^2 \bar{I}_3^k) + 2(1+\bar{\eta}_k) (\bar{I}_2^k + 3\bar{\eta}_k \bar{I}_3^k) \right)}{(1-\alpha_k^2 \bar{I}_1^k) (1+\bar{\eta}_k \bar{I}_1^k + \bar{\eta}_k^2 \bar{I}_2^k + \bar{\eta}_k^3 \bar{I}_3^k)} \right) \\ & - \frac{(1-\alpha_k^2) (1+\bar{\eta}_k) (\bar{I}_1^k + 2\bar{\eta}_k \bar{I}_2^k + 3\bar{\eta}_k^2 \bar{I}_3^k)^2}{(1-\alpha_k^2 \bar{I}_1^k) (1+\bar{\eta}_k \bar{I}_1^k + \bar{\eta}_k^2 \bar{I}_2^k + \bar{\eta}_k^3 \bar{I}_3^k)^2} \\ & + \frac{(\bar{I}_1^k + 2\bar{\eta}_k \bar{I}_2^k + 3\bar{\eta}_k^2 \bar{I}_3^k)}{(1+\bar{\eta}_k \bar{I}_1^k + \bar{\eta}_k^2 \bar{I}_2^k + \bar{\eta}_k^3 \bar{I}_3^k)} \end{aligned} \right], \quad 8.49$$

$$\frac{\partial \bar{\psi}_v^k}{\partial N_s^k} = \frac{1}{2} \left(\frac{(1-\alpha_k^2) (1+\bar{\eta}_k) (\bar{I}_1^k + 2\bar{\eta}_k \bar{I}_2^k + 3\bar{\eta}_k^2 \bar{I}_3^k)}{(1-\alpha_k^2 \bar{I}_1^k) (1+\bar{\eta}_k \bar{I}_1^k + \bar{\eta}_k^2 \bar{I}_2^k + \bar{\eta}_k^3 \bar{I}_3^k)} + \log \left((1-\alpha_k^2 \bar{I}_1^k) (1+\bar{\eta}_k \bar{I}_1^k + \bar{\eta}_k^2 \bar{I}_2^k + \bar{\eta}_k^3 \bar{I}_3^k) \right) \right), \quad 8.50$$

$$\frac{\partial \bar{\psi}_v^k}{\partial \alpha_k} = \frac{1}{2} \left[\begin{aligned} & N_c^k \left(\bar{I}_1^k \frac{(\bar{I}_1^k - 1)}{(1-\alpha_k^2 \bar{I}_1^k)^2} - \frac{\bar{I}_1^k}{(1-\alpha_k^2 \bar{I}_1^k)} \right) \\ & + N_s^k \left(\frac{(1+\bar{\eta}_k) (\bar{I}_1^k + 2\bar{\eta}_k \bar{I}_2^k + 3\bar{\eta}_k^2 \bar{I}_3^k)}{(1+\bar{\eta}_k \bar{I}_1^k + \bar{\eta}_k^2 \bar{I}_2^k + \bar{\eta}_k^3 \bar{I}_3^k)} \frac{(\bar{I}_1^k - 1)}{(1-\alpha_k^2 \bar{I}_1^k)^2} - \frac{\bar{I}_1^k}{(1-\alpha_k^2 \bar{I}_1^k)} \right) \end{aligned} \right], \quad 8.51$$

8.9 Model parameters for uniaxial tensile loading

Table 8.1: Parameters for PMMA 93.

| | | | | | |
|--------------------------------------------------|-----------------------|-----------------------|-----------------------|-----------------------|------------------------|
| $\dot{\varepsilon}_{eq} \text{ (s}^{-1}\text{)}$ | 3.62×10^{-4} | 1.68×10^{-3} | 2.00×10^{-2} | 1.87 | 305 |
| $Ns_1^* \text{ (MPa/mm}^3\text{)}$ | 5.43×10^{-1} | 6.17×10^{-1} | 6.49×10^{-1} | 7.32 | 83.26 |
| $Nc_1^* \text{ (MPa/mm}^3\text{)}$ | 2.00×10^{-5} | 2.95×10^{-5} | 2.61×10^{-5} | 7.98×10^{-4} | 1.28×10^{-2} |
| Z (-) | 1.01×10^{-2} | 1.22×10^{-1} | 1.41×10^{-1} | 5.41×10^{-1} | 41.21 |
| p1 (-) | 7.25×10^{-1} | 9.45×10^{-1} | 1.13 | 1.05 | 1.55 |
| $Ns_2^* \text{ (MPa/mm}^3\text{)}$ | 7.11×10^{-2} | 1.81×10^{-1} | 3.42×10^{-1} | 8.92×10^{-1} | 2.25 |
| $\alpha_2^2 (\cdot)$ | 1.47×10^{-3} | 6.33×10^{-4} | 5.38×10^{-3} | 6.39×10^{-3} | 1.75×10^{-2} |
| $\tau_s (\cdot)$ | 2.94×10^{-1} | 1.11×10^{-1} | 7.70×10^{-2} | 2.45×10^{-6} | 2.96×10^{-10} |
| $\xi (\cdot)$ | 9.09×10^{-1} | 3.04×10^{-1} | 3.44×10^{-1} | 3.91×10^{-2} | 1.93×10^{-2} |

| | | | | | |
|--------------|-----------------------|-----------------------|-----------------------|------------------------|------------------------|
| $v (\cdot)$ | 3.08 | 5.54×10^{-1} | 3.31×10^{-1} | 8.32×10^{-1} | 3.43×10^{-1} |
| $v' (\cdot)$ | 1.01×10^{-1} | 2.01×10^{-4} | 1.40×10^{-2} | 2.41×10^{-12} | 7.52×10^{-12} |

Table 8.2: Parameters for PMMA 120.

| | | | | | | |
|-----------------------------------------------------|-----------------------------------------|-----------------------------------------|-----------------------|------------------------|------------------------|------------------------|
| $\dot{\varepsilon}_{eq} (s^{-1})$ | 1.83×10^{-4} | 1.65×10^{-2} | 1.56 | 16.1 | 196 | 2390 |
| Ns_1^* (MPa/mm³) | 5.41×10^{-1} | 6.45×10^{-1} | 7.27 | 34.18 | 79.58 | 176.88 |
| Nc_1^* (MPa/mm³) | 2.08×10^{-5} | 2.60×10^{-5} | 7.87×10^{-4} | 2.27×10^{-3} | 1.08×10^{-2} | 7.79×10^{-2} |
| Z (-) | 1.07×10^{-2} | 1.39×10^{-1} | 5.43×10^{-1} | 3.82 | 34.78 | 55.96 |
| p1 (-) | 7.50×10^{-1} | 1.10 | 1.03×10^{-1} | 1.28 | 1.60 | 1.78 |
| Ns_2^* (MPa/mm³) | 7.22×10^{-2} | 3.41×10^{-1} | 8.77×10^{-1} | 1.60 | 1.97 | 2.09 |
| $\alpha_2^2 (\cdot)$ | 1.51×10^{-3} | 5.35×10^{-3} | 6.79×10^{-3} | 7.39×10^{-3} | 1.71×10^{-2} | 6.33×10^{-2} |
| $\tau_s (\cdot)$ | 2.94×10^{-1} | 7.72×10^{-2} | 6.82×10^{-4} | 2.40×10^{-6} | 2.76×10^{-10} | 3.28×10^{-13} |
| $\xi (\cdot)$ | 9.79×10^{-1} | 3.04×10^{-1} | 1.44×10^{-1} | 3.95×10^{-2} | 1.81×10^{-2} | 1.83×10^{-4} |
| v (\cdot) | 3.18 | 3.54×10^{-1} | 8.31×10^{-1} | 8.28×10^{-1} | 3.12×10^{-1} | 1.17 |
| v' (\cdot) | 1.12×10^{-1} | 1.44×10^{-2} | 4.92×10^{-8} | 2.64×10^{-12} | 7.20×10^{-12} | 6.13×10^{-12} |

Table 8.3: Parameters for PMMA 3500.

| | | | | | | |
|-----------------------------------------------------|-----------------------------------------|-----------------------------------------|-----------------------------------------|-----------------------------------------|-----------------------|-----------------------|
| $\dot{\varepsilon}_{eq} (s^{-1})$ | 1.84×10^{-8} | 1.82×10^{-6} | 1.68×10^{-4} | 1.58×10^{-2} | 1.92 | 244 |
| Ns_1^* (MPa/mm³) | 1.56×10^{-2} | 1.21×10^{-1} | 4.33×10^{-1} | 2.40 | 65.81 | 189.04 |
| Nc_1^* (MPa/mm³) | 1.34×10^{-2} | 1.34×10^{-2} | 1.34×10^{-2} | 1.34×10^{-2} | 3.34×10^{-2} | 3.34×10^{-2} |
| Z (-) | 1.07×10^{-3} | 3.58×10^{-7} | 5.19×10^{-4} | 7.33×10^{-1} | 1.55 | 6584.89 |
| p1 (-) | 5.34×10^{-1} | 2.02×10^{-2} | 3.19×10^{-1} | 1.05^1 | 1.39^1 | 2.37 |
| Ns_2^* (MPa/mm³) | 5.93×10^{-1} | 5.96×10^{-1} | 6.02×10^{-1} | 1.00 | 1.10 | 1.55 |
| $\alpha_2^2 (\cdot)$ | 8.49×10^{-5} | 8.93×10^{-4} | 8.93×10^{-4} | 5.34×10^{-3} | 3.43×10^{-2} | 4.71×10^{-2} |

| | | | | | | |
|------------------|-----------------------|-----------------------|-----------------------|-----------------------|-----------------------|-----------------------|
| $\tau_s (\cdot)$ | 5.21×10^{-1} | 1.01×10^{-1} | 3.46×10^{-4} | 2.24×10^{-4} | 2.17×10^{-5} | 2.58×10^{-4} |
| $\xi (\cdot)$ | 5.24×10^{-1} | 6.13×10^{-1} | 1.87×10^{-1} | 1.32×10^{-1} | 1.68×10^{-1} | 8.83×10^{-7} |
| $\nu (\cdot)$ | 1.21×10^{-1} | 6.90 | 6.55×10^{-1} | 7.60×10^{-1} | 1.22×10^{-1} | 1.86×10^{-2} |
| $\nu' (\cdot)$ | 2.52×10^{-3} | 1.78×10^{-2} | 4.58×10^{-3} | 1.71×10^{-2} | 8.38×10^{-3} | 5.22×10^{-7} |

Table 8.4: Parameters for PMMA CL.

| | | | | | |
|--------------------------------|-----------------------------------------|-----------------------------------------|-----------------------------------------|-----------------------|-----------------------|
| $\dot{\epsilon}_{eq} (s^{-1})$ | 1.56×10^{-6} | 1.61×10^{-4} | 1.59×10^{-2} | 1.83 | 255 |
| $Ns_1^* (MPa/mm^3)$ | 1.56 | 1.79 | 3.18 | 52.71 | 174.36 |
| $Nc_1^* (MPa/mm^3)$ | 2.17×10^{-2} | 2.51×10^{-2} | 2.42×10^{-2} | 2.01×10^{-2} | 1.93×10^{-2} |
| $Z (-)$ | 10.78 | 10.58 | 10.16 | 98.25 | 1664.28 |
| $p1 (-)$ | 1.13 | 1.16 | 1.51 | 1.78 | 2.16 |
| $Ns_2^* (MPa/mm^3)$ | 5.56×10^{-1} | 5.76×10^{-1} | 6.55×10^{-1} | 9.38×10^{-1} | 1.35 |
| $\alpha_2^2 (\cdot)$ | 2.27×10^{-3} | 1.24×10^{-3} | 1.23×10^{-3} | 3.02×10^{-2} | 4.80×10^{-2} |
| $\tau_s (\cdot)$ | 5.18×10^{-6} | 8.38×10^{-6} | 7.65×10^{-6} | 5.40×10^{-5} | 4.08×10^{-4} |
| $\xi (\cdot)$ | 1.25 | 1.42 | 1.65 | 1.37 | 1.42×10^{-6} |
| $\nu (\cdot)$ | 2.90×10^{-4} | 2.09×10^{-4} | 8.16×10^{-6} | 9.26×10^{-2} | 1.42×10^{-2} |
| $\nu' (\cdot)$ | 2.19×10^{-5} | 3.52×10^{-5} | 2.87×10^{-5} | 1.09×10^{-5} | 8.08×10^{-6} |

8.10 Parameters Evolution

Next, we present the phenomenological approach for describing the evolution of the internal state variables with the equivalent strain rate:

PMMA 80

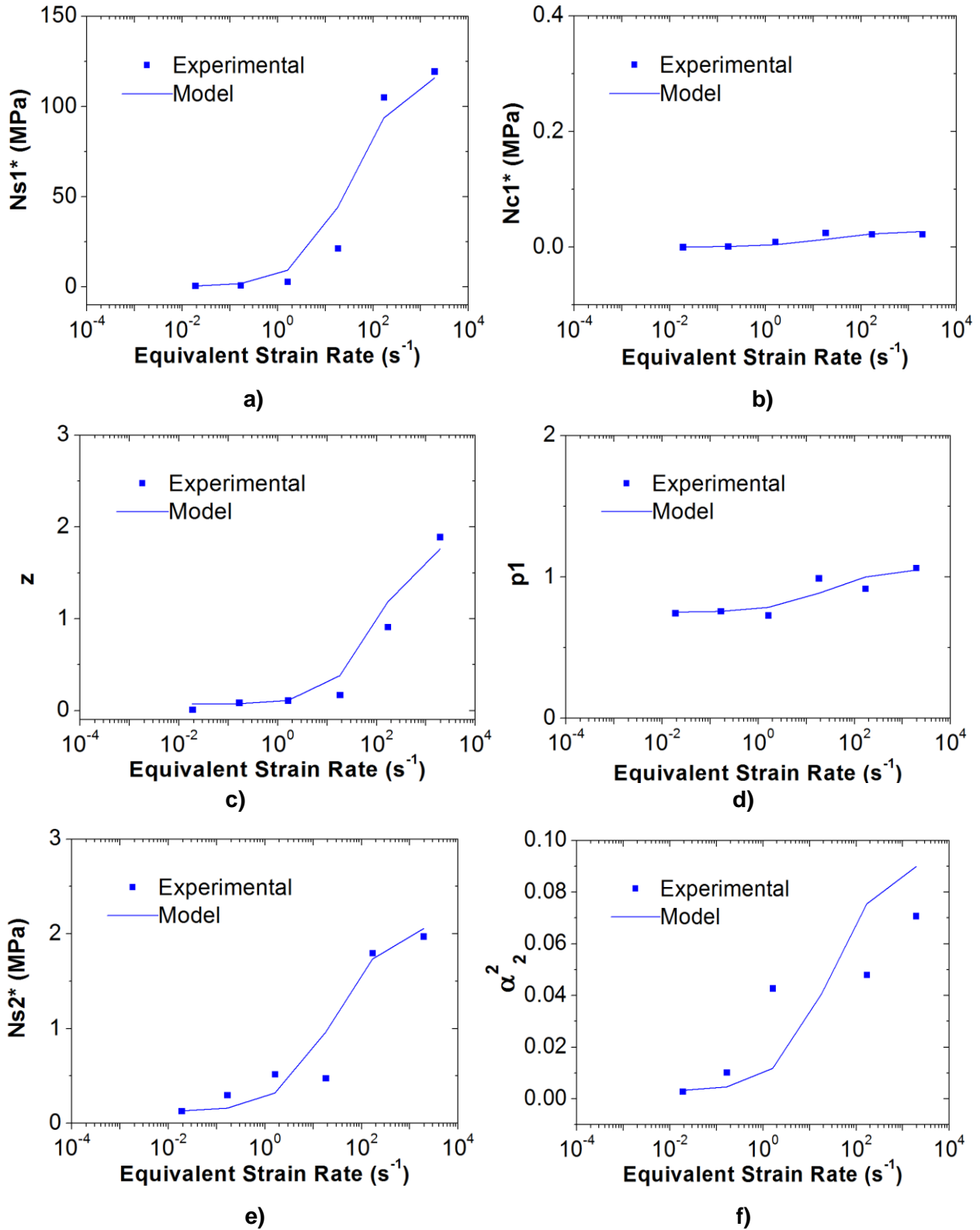


Figure 8.11: Internal state variables evolution with the equivalent strain rate for PMMA 80: a) Ns_1^* , b) Nc_1^* , c) z , d) p_1 , e) Ns_2^* and f) α_2^2 .

PMMA 3500

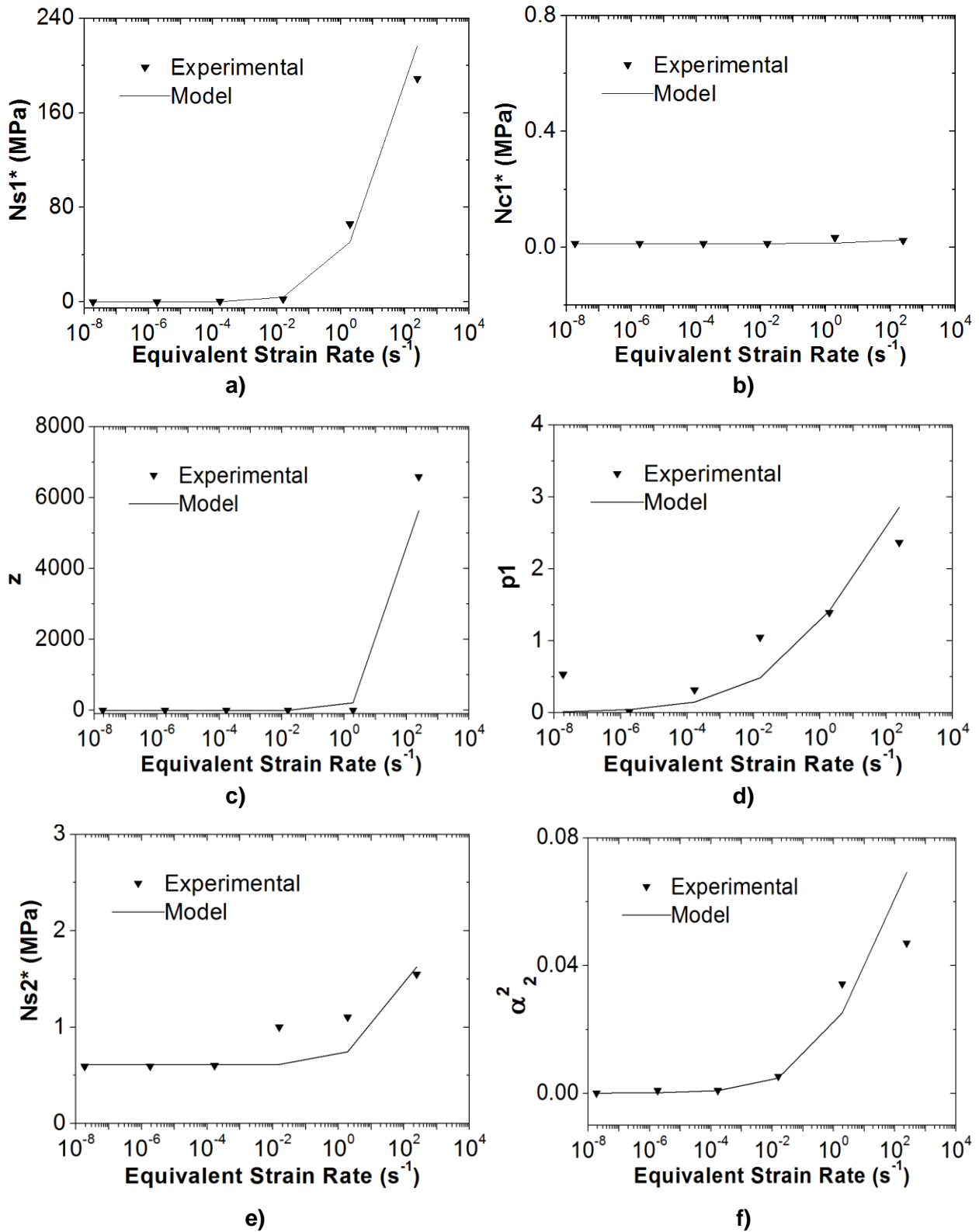


Figure 8.12: Internal state variables evolution with the equivalent strain rate for PMMA 3500: a) Ns_1^* , b) Nc_1^* , c) z , d) p_1 , e) Ns_2^* and f) α_2^2 .

PMMA CL

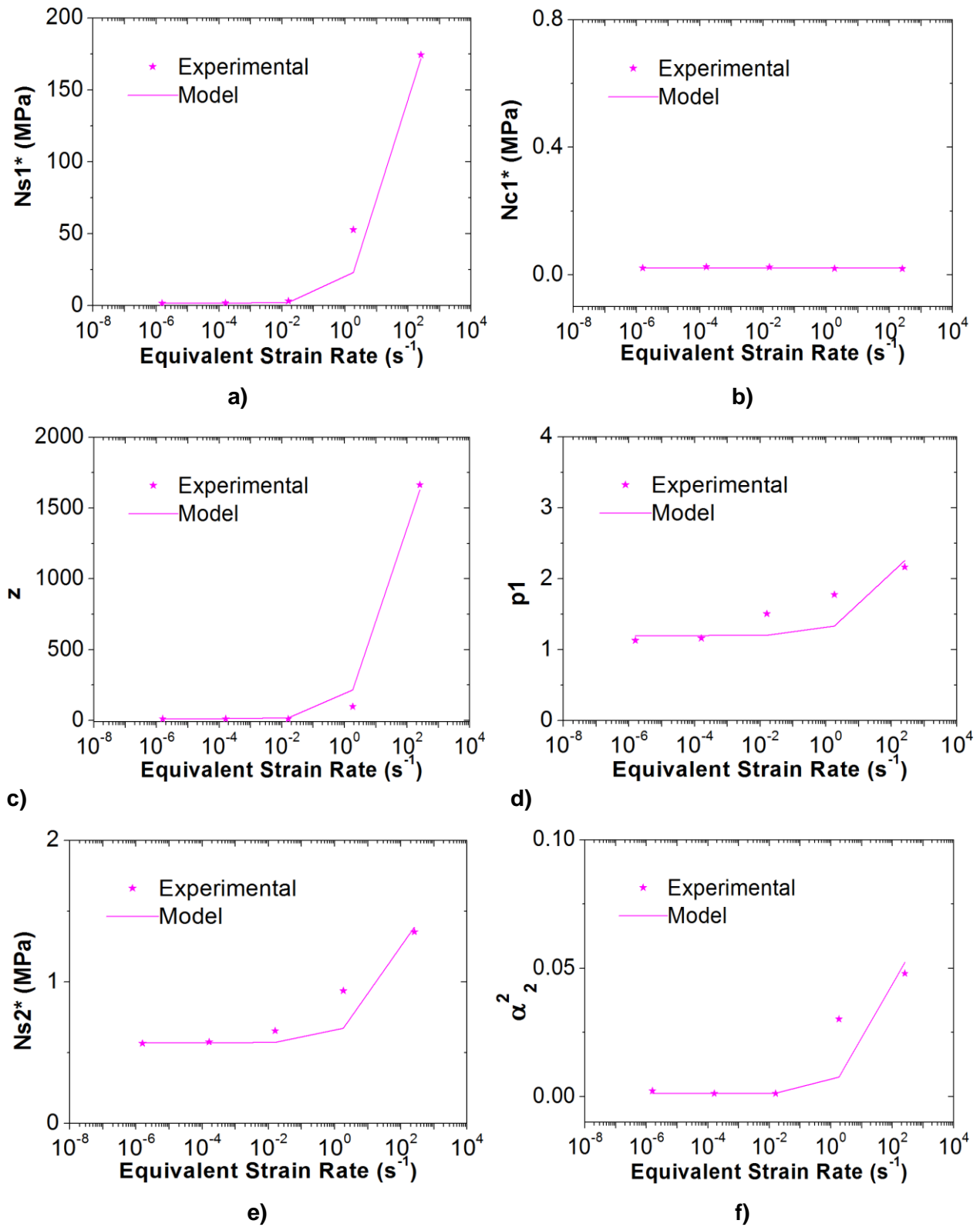


Figure 8.13: Internal state variables evolution with the equivalent strain rate for PMMA CL: a) Ns_1^* , b) Nc_1^* , c) z , d) $p1$, e) Ns_2^* and f) α_2^2 .

Résumé

L'objectif de cette thèse est de proposer une stratégie simplifiée et précise pour caractériser et modéliser le comportement mécanique des polymères amorphes de l'état quasi-fluide à l'état solide.

L'étude a été réalisée sur des PMMA de masses molaires et de degré de réticulations différentes.

D'abord, le comportement mécanique dans le domaine viscoélastique linéaire est étudié à l'aide de tests DMTA et rhéologiques. Il ressort de l'étude que l'augmentation de la masse molaire et du degré de réticulation augmentait les modules de stockage et de perte en tant que la transition α . En parallèle, l'utilisation du principe de superposition temps-température a permis de déterminer «des vitesses de déformation équivalentes à la température de référence».

Ensuite, le comportement mécanique à grande déformation est étudié par essais cycliques en traction uni-axial et de cisaillement à haute température et couplés à la DIC. De plus, les effets de la vitesse de déformation et de la température ont été couplés grâce à "vitesse de déformation équivalent à la température de référence" extrait des observations dans le domaine linéaire. Les résultats ont montré que cibler la même vitesse de déformation équivalente conduira aux mêmes courbes contrainte-déformation, c'est-à-dire la même réponse mécanique. Ceci permet de réduire le nombre de tests expérimentaux nécessaires pour caractériser le comportement mécanique des polymères amorphes.

Enfin, un modèle basée dans un cadre thermodynamique a été utilisée pour reproduire la réponse mécanique des PMMA à grande déformation. Le modèle présentait un bon accord avec les données expérimentales, étant capable de reproduire des comportements visco-élasto-plastiques, viscoélastiques, hyperélastiques et visco-hyperélastiques pour la traction cyclique.

Mots Clés

Poly(méthyle méthacrylate), principe de superposition temps-température, DIC, comportement mécanique, masse molaire, viscohyperélasticité

Abstract

The present PhD thesis proposes a simplified and accurate strategy for characterising and modelling the mechanical behaviour of amorphous polymers from the quasi-fluid state up to the solid state.

The study was carried out on PMMAs with different molar masses and crosslinking degree.

First, we addressed the mechanical behaviour in the linear viscoelastic domain using DMTA and rheological tests. Results showed that increasing the molar mass and crosslinking degree increased the elastic and loss moduli as the α -transition. In parallel, using the time-temperature superposition principle allowed determining "equivalent strain rates at reference temperature".

Then, we performed uniaxial tensile and shear unloading-unloading tests at high temperature and coupled with DIC, to characterise the mechanical behaviour at large strain. Additionally, strain rate and temperature effects were coupled by means of the "equivalent strain rate at reference temperature" extracted from observations in the linear domain. Results showed that targeting the same equivalent strain rate lead to the same stress-strain curves, i.e. same mechanical response. This allows reducing the number of experimental tests needed to characterise the mechanical behaviour of amorphous polymers.

Finally, a constitutive modelling based in a thermodynamics framework, was used to reproduce the mechanical response of the PMMAs at large deformation. The model presented a good agreement with the experimental data, being able to reproduce viscoelastoplastic, viscoelastic, hyperelastic and viscohyperelastic behaviours for cyclic loading tensile.

Keywords

Poly(methyl methacrylate), time-temperature superposition principle, DIC, mechanical behaviour, molar mass, viscohyperelasticity